ANION PHOTOELECTRON SPECTROSCOPY: LESSONS LEARNED

By

Zhang, Xinxing

A dissertation submitted to Johns Hopkins University in conformity with the requirements for the degree of Doctor of Philosophy

Baltimore, Maryland

Sepetember, 2015

ABSTRACT

A combination of various ion sources, a reaction cell, mass spectrometry, anion photoelectron spectroscopy and theoretical calculations has been utilized to study cluster anions belonging to a variety of categories. Emphasis has been placed on the rich information and potential applications that one can obtain from these techniques. Obtaining as much information as possible, pushing the boundary of chemistry, designing materials and studying reaction mechanisms are the aspects that one can learn from these experiments and calculations, which are discussed in the introduction and five chapters of this thesis.

In Chapter 1, cluster anions showing very special bonding between TM and hydrogen are discussed. The interaction between transition metals (TM) and hydrogen has always been an intriguing research topic for such applications as hydrogen storage and catalysis of hydrogenation and dehydrogenation reactions. Special bonding features between TM and hydrogen other than the simple M-H σ bond are interesting not only because they are scarcely reported but also because they could help to discover and understand the nature of chemical bonding.

In chapter 2, by inserting a reaction cell between the ion sources and the Wiley-McLaren region of the time-of-flight mass spectrometer, various reactions between cluster anions and neutral molecules have been studied. The oxidation reactions of aluminum hydride cluster anions and boron aluminum hydride cluster anions give insights about their potential applications as highly energetic materials. The reactions between aluminum hydride cluster anions and commonly used organic ligands shed light on the synthesis of never-existed low oxidation state aluminum containing materials.

Chapter 3 discusses the mechanism of CO_2 activation and fixation by coinage metal anions and platinum hydride cluster anions. Recycling CO_2 is a hot topic by itself, however, our focus has been put on the mechanism of the interactions and reactions.

Chapter 4 further stretches the material designing efforts into group 13 elements, aluminum and boron. Study on stable aluminum hydride cluster cations (4.1), o-carborane anions (4.5) and carbon aluminum hydride cluster anions (4.6) promises potential energetic materials. The derivative of AlH_4^-, $AlH_2Cp^*Cl^-$, can be used as a building block for ionic liquid or salt (4.2). $Li_2Al_3H_8^-$ in section 4.3 shows an unprecedented homocatenated chain, Al-Al-Al. By obtaining electron from Li, Al transmutates into C, and the $Al_3H_8^{3-}$ kernel mimics propane. This discovery sheds light on the synthesis of a new salt, $Li_3Al_3H_8$, an extension of an existing salt, $LiAlH_4$. In section 4.4, a new precursor, $Al^+Ph_2CO^-$, for synthesizing low oxidation state Al containing compounds is discussed. $Al^+Ph_2CO^-$ is similar to the famous monovalent AlCl, but the synthesis should be much simpler.

Chapter 5 presents the very special chemical bonding features of $LiOH_2^-$ cluster anion, known as the double Rydberg anion. In history, $LiOH_2^-$ is the second experimentally observed double Rydberg anion only after the $NH_4^-(NH_3)_n$ family. This finding, essentially a new type of chemical bonding, is viewed to have pushed the boundary of chemistry.

Research Advisor: Dr. Kit H. Bowen

Committee: Dr. Kit H. Bowen

Dr. Paul J. Dagdigian

Dr. Howard Fairbrother

ACKNOWLEDGEMENT

TABLE OF CONTENTS

INTRODUCTION

Since the magnetic bottle type anion photoelectron spectrometer (aPES) came to birth in 1987,[1] its research areas have expanded to many aspects of chemistry, physics and biology. As a well-established and sophisticated physical chemistry research technique, the influence of aPES remains significant after decades. In this introduction, four important lessons learnt from aPES will be discussed from the perspective of the Bowen Research Lab, and examples of these four lessons will be presented in detail in this thesis.

Lesson 1. Obtain as much information as possible. aPES is able to provide a large variety of information. By nature, aPES detects the electronic structures of the systems studied. Via photodetachment, an anion can be excited to the ground and excited states of the neutral. Therefore, even though an anion is made at the first place, the most information that we can obtain is about the neutral. Furthermore, when transitions within a neutral, for example, from a singlet state to a triplet state, are forbidden, aPES does not have this problem, as long as the photodetachment photon energy is high enough, all electronic states of the neutral can be detected. When there is enough Franck-Condon overlap between the anion and the neutral and when there are not many hot band features, the threshold of the spectrum is the electron affinity (EA). EA is a basic and intrinsic property of all the neutral systems, and by far aPES is the most effective technique that measures EA. The peak position of the spectrum corresponds to another intrinsic property of the anion, the vertical detachment energy (VDE). If the neutral is a closed-shell system, the spacing between the first and the second PES peaks corresponds to the HOMO-LUMO gap. When the temperature of a studied system is low enough and the structural difference between the anion and the neutral is big enough, one could also be able to observe vibrational progressions of the neutral.

Sometimes vibrational frequencies can be used as a way of isotope tagging to detect the structure of the molecules.

The above is just the most direct information provided by aPES. If one looks deeper into various experiments, much more information can be obtained.

Isomers that are close in energy might co-exist in the ion beam, however, they cannot be identified by mass spectrometry. By aPES, photoelectrons detached from different isomers can be distinguished. By changing source conditions, the photoelectron intensities from different isomers can be varied to further confirm the co-existence of isomers. Chapter 4.4 presents an example of anionic isomers.

Kinetics information such as reaction rate can be calculated from the mass spectra before and after reaction because the ion intensity is directly proportional to the area below the mass peak. No surprise about it. However, in our lab, for the first time in the world, reaction rate was also calculated from photoelectron spectra. In two separate experiments, isomers $Pt(H_2O)^-$ and $HPtOH^-$, isomers $Pt(D_2O)^-$ and $DPtOD^-$ were found to co-exist in the mass spectra. The following reactions: $Pt(H_2O)^- \rightarrow HPtOH^-$ and $Pt(D_2O)^- \rightarrow DPtOD^-$ were believed to have occurred, and the relative PES intensity of $DPtOD^-$ compared to $Pt(D_2O)^-$ is lower than that of $HPtOH^-$ compared to $Pt(H_2O)^-$, which is due to the activation energy difference caused by the zero-point energy difference. The isotope-caused zero-point energy difference can be so high that it will significantly affect the reaction rate. With the help of the calculated activation energies and Arrhenius equation, we calculated the reaction rates of the reactions $Pt(H_2O)^- \rightarrow HPtOH^-$ and $Pt(D_2O)^- \rightarrow DPtOD^-$. This phenomenon called kinetic isotope effect in turn proves that there is really water activation reactions occurring in the source region, but not "the ion source simply made the isomers". Appendix A will discuss this new finding in detail.

Even though it is well known that aPES can give rich information about the electronic structures of the neutral, sometimes the electronic structural information of the anion can also be obtained. For example, hot bands are actually the vibrationally excited states of the anion. Sometimes when the source condition is not cold enough, there also might be transitions from the excited electronic states of the anion to different neutral states. More interestingly, when the anion has resonance (either shape resonance or Feshbach resonance) with the photon energy used for photodetachment, the anion will be pumped to its excited states and then undergo an autodetachment process. The apparatus will record these autodetached electrons as photoelectrons, and slightly changing the photon energy will slightly change the "EBE" of the resonant peak. In my point of view, to better study anionic resonance, time-resolved aPES should be the key. Firstly, one can use the first photon to pump the anion to the resonant state, after a few femtoseconds, the second probe photon can be fired to photo detach the excited anion. Without a femtosecond laser, our apparatus is already able to achieve a lot of information. In appendix A, the example of azobenzene parent anion is presented.

By simply looking at an anion photoelectron spectrum, a lot of other non-quantitative information can be predicted. For example, a very low EA implies the low stability of the anion, a very large HOMO-LUMO gap indicates the high stability of the neutral, a very wide PES peak reveals a large structural difference between the anion and the neutral while a sharp one means less structural difference, a spectrum with very few features implies that the cluster has high symmetry, a spectrum with small splitting might involve spin-orbital coupling or degenerate molecular orbitals, two very similar but only shifted spectra presents the possibility of solvation effects…

Lesson 2. Push the boundary of chemistry. Chemistry aims to understand the nature of substances. What kind of discovery can be regarded as "pushing the boundary of chemistry"? Those which discover new intrinsic properties of substances, new ways how substances exist, can be viewed as having pushed the boundary of chemistry. Discovering new oxidation states or new forms of chemical bonds falls into this category. For example, the highest oxidation state that human beings have ever known is +8 of Xe in XeO_4.[2] In 2014, Dr. Mingfei Zhou refreshed the record of highest oxidation state to be +9 of Ir in IrO_4^+, this discovery is one good example of pushing the boundary of chemistry. As for discovering new chemical bonds, for example, B has three valence electrons, surprisingly, all of them can be used to form a very special B-B triple bond. The valence vacancies of the boron dimer further are stabilized by two CO ligands from the two ends and in all it makes a stable cluster OCBBCO.[4] This work is also from Dr. Mingfei Zhou.

In this thesis, examples of discovering unprecedented chemical bonds are presented. In Chapters 1.2 and 1.3, I report a $PtZnH_5^-$ cluster which possesses a planar pentagonal coordination between the H_5^- moiety and Pt and exhibits special σ-aromatic character. Afterwards, we extend this work to the isoelectronic and isostructural cluster $PtMgH_5^-$ in which similar bondings are also found. In these clusters, the H_5^- kernel as a whole can be viewed as a η^5-H_5 ligand for Pt, and it is in turn stabilized by the Pt atom. As for the Pt atom, a penta-coordination was never reported before.

In Chapters 1.1 and 1.3, I present very special structures of PdH_3^- and $PtMgH_3^-$ where an H_2 molecule forms a η^2-H_2 type of ligation to Pd and Pt, and the H-H bond length is lengthened comparing to the free H_2 molecule. Detailed molecular orbital analysis reveals that the back donation from a *d*-type orbital of Pd and Pt to the σ* orbital of H_2 causes the H-H elongation, and

hence, activation. The H_2 binding energy is unusually as high as 80-100 kJ/mol, even higher than that between CO and Pd.

In Chapter 5, I present a very unique double Rydberg anion (DRA), $LiOH_2^-$, where there is a pair of electrons which occupy a very diffusive molecular orbital and surround a stable $LiOH_2^+$ core. In history, this special doubly occupied Rydberg orbital in a DRA was discovered experimentally only once in the DRA NH_4^-.[5] For years researchers have been exploring the DRA H_3O^-, however, no positive results have been reported other than theoretical predictions. By substituting one H atom in H_3O^- with a Li atom, we successfully designed and obtained a DRA $LiOH_2^-$ via anion photoelectron spectroscopy and theoretical calculations.

Group 13 elements are very rarely observed to catenate into linear chains and experimental observation of such species is challenging. In the well-known aluminium hydride cluster anions, even though a certain structure tends to form a chain, the chain is bridged by H atoms but not formed by Al-Al bonds.[6] In Chapter 4.3, I report unique results obtained via combined photoelectron spectroscopy and ab initio studies of the $Li_2Al_3H_8^-$ cluster that confirm the formation of Al-Al-Al chain surrounded by hydrogen atoms in a very particular manner. This unique chemical bonding of Al atoms mimics the ubiquitous C-C bonds.

Lesson 3. Design new materials. We can hardly synthesize a beaker of materials, but we can help design materials. By characterizing a certain cluster that has unusual stability, we are always hoping that this cluster can be further synthesized as materials, or synthesized as a building block of other materials in the bulk. These cluster are often called "magic clusters". In history, C_{60} is a great example of discovering and understanding a new material from an ion beam.[7] Nowadays

C_{60} can be produced in large quantities. Other examples include the discovery of very stable Al_4H_6 clusters in the gas phase,[8] instructed by which the $Al_4(P'Bu_2)_6$ derivative was synthesized afterwards.[9] Al_{13}^-, with 40 valence electrons, is stable and considered to be a super anion of Cl^-.[10] Using it as a building block of salt promises novel materials such as KAl_{13}.[11] However, synthesis of KAl_{13} in the bulk is still absent. Castleman's metcars (M_8C_{12}),[12] Laisheng Wang's Au_{20}[13] and borophene[14] are all examples of very stable clusters discovered in the beam and are promising for bulk synthesis. Successful attempts of synthesizing ligand protected Au_{20} clusters have been made.[15]

In this thesis, efforts towards designing new materials are presented. $LiAlH_4$, known as a famous reductant, is widely used in synthetic chemistry. Its anion part, AlH_4^-, is isoelectronic to methane, which makes it highly stable. We have characterized AlH_4^- with aPES.[16] Enlightened by this, synthesizing $Li_2Al_2H_6$ and $Li_3Al_3H_8$ as bulk materials are also feasible, where the $Al_2H_6^{2-}$ and $Al_3H_8^{3-}$ kernels mimic ethane and propane, respectively. In Chapter 4.3, I present the aPES study of $Li_2Al_3H_8^-$, where $Al_3H_8^{3-}$ indeed has the structure of propane. Our collaborators who are experts in inorganic synthesis are promptly synthesizing these new materials.

In Chapter 4.2, a tetra-coordinated Al containing cluster anion, $AlCp*H_2Cl^-$, which can be viewed as a derivative of AlH_4^- is discussed. Its high stability promises the potential application as a building block of salts and ionic liquids, just as AlH_4^- already does.

In Chapter 4.4, aPES has been utilized to study neutral and anionic $Ph_2CO^-Al^+$. The comparisons between the experimental and theoretical vertical detachment energies (VDE) of both the anion isomers are made, and excellent agreement is found. Natural population analysis (NPA) show that in $Ph_2CO^-Al^+$, Al is positively charged by $+0.81$ e, indicating a highly ionic bond between Al and Ph_2CO, which is comparable to the case of AlCl. Similarly to aluminum

monohalide,[17-19] this Al(I) containing molecule $Ph_2CO^-Al^+$ could further be utilized as a precursor of low oxidation state Al chemistry. Our collaborator Bryan Eichhorn is actively working on synthesizing it.

Lesson 4. Explore reaction mechanism. The advantages of aPES in exploring reaction mechanisms and building models for catalytic reactions are that these experiments are performed at the atomic level and there is no complicated environment involved. Catalytic reactions are mostly performed in much more complicated environments such as solutions, which makes the fine control of each molecule difficult.

A transition metal hydride is excellent in CO_2 hydrogenation.[20] The critical step of the reduction involves the insertion of C=O into the M-H bond to produce a formate-metal adduct, L_nM-OC(O)H, which can generate the reduction product formate in the solution or be further reduced to other ultimate products by additional metal hydrides. In Chapter 3.2, we present the experimental results of the reactions between the platinum hydride cluster anions PtH_n^- and CO_2. Two products, $PtCO_2H_{1,3}^-$ were identified by mass spectrometry and characterized by anion photoelectron spectroscopy. For $PtCO_2H^-$, its structure can be written as $HPtCO_2^-$ where CO_2 is in the form of being bent and activated. For $PtCO_2H_3^-$, its structure can be written as $H_2Pt(formate)^-$ where CO_2 has been hydrogenated. *Ab initio* calculations were performed to reveal the reaction mechanism. How CO_2 was activated and hydrogenated in the current case has been explained in great details at the atomic level.

The negatively charged surface or a negatively charged site of a neutral catalyst are believed to be able to bind and activate CO_2. In Chapter 3.1, photoelectron spectroscopic and computational studies were performed for $(M-CO_2)^-$ (M= Au, Ag, Cu) anionic complexes. We show that $(Au-CO_2)^-$ forms both the chemisorbed and physisorbed isomers, $AuCO_2^-$ and $Au^-(CO_2)$,

7

respectively; that $(Ag\text{-}CO_2)^-$ forms only the physisorbed isomer, $Ag^-(CO_2)$; and that $(Cu\text{-}CO_2)^-$ forms only the chemisorbed isomer, $CuCO_2^-$. The two chemisorbed complexes, $AuCO_2^-$ and $CuCO_2^-$ are covalently-bound, formate-like anions, in which their CO_2 moieties are significantly reduced. These two species are examples of electron-induced CO_2 activation. The two physisorbed complexes, $Au^-(CO_2)$ and $Ag^-(CO_2)$ are electrostatically and thus weakly bound. These cluster anions provide very good models for understanding the mechanism of CO_2 activation in catalysis.

Please note that not all of the contents in this thesis are categorized into these four lessons in the introduction. Similar systems have been written in the same chapters, even though different lessons can be learnt from them. Most of the work in this thesis has not been published elsewhere.

References

1. O. Cheshnovsky, S. H. Yang, C. L. Pettiette, M. J. Craycraft, and R. E. Smalley, *Rev. Sci. Instrum.* **58**, 2131 (1987).

2. H.Selig, J. G. Malm, H. H. Claassen, C. L. Chernick, and J. L. Huston, *Science* **143**, 1322 (1964).

3. G. Wang, M. Zhou, J. T. Goettel, G. J. Schrobilgen, J. Su, J. Li, T. Schlöder, and S. Riedel, *Nature* **514**, 475 (2014).

4. M. Zhou, N. Tsumori, Z. Li, K. Fan, L. Andrews, and Q. Xu, *J. Am. Chem. Soc.* **124**, 12936 (2002).

5. J. T. Snodgrass, J. V. Coe, C. B. Freidhoff, K. M. McHugh, and K. H. Bowen, *Faraday Discuss. Chem. Soc.* **86**, 241 (1988).

6. X. Li, A. Grubisic, K. H. Bowen, A. K. Kandalam, B. Kiran, G. F. Gantefoer, and P. Jena, *J. Chem. Phys.*, **132**, 241103 (2010).

7. H. W. Kroto, J. R. Heath, S. C. O'Brien, R. F. Curl, and R. E. Smalley, *Nature*, **318**, 162 (1985).

8. X. Li, A. Grubisic, S. T. Stokes, J. Cordes, G. F. Gantefoer, K. H. Bowen, B. Kiran, M. Willis, P. Jena, R. Burgert, and H. Schnoeckel, *Science*, **315**, 356-358 (2007).

9. P. Henke, M. Huber, J. Steiner, K. Bowen, B. Eichhorn, and H. Schnockel, *J. Am. Chem. Soc.*, **131**, 5698-5704 (2009).

10. S. N. Khanna and P. Jena, *Chem. Phys. Lett.* **219**, 479 (1994).

11. W. -J. Zheng, O. C. Thomas, T. P. Lippa, S. -J. Xu, and K. H. Bowen, *J. Chem. Phys.* **124**, 144304 (2006).

12. B. C. Guo, K. P. Kerns, and A. W. Castleman, *Science* **255**, 1411 (1992).

13. J. Li, X. Li, H. J. Zhai, and L. S. Wang, *Science* **299**, 864-867 (2003).

14. W. L. Li, Q. Chen, W. Tian, H. Bai, Y. F. Zhao, H. S. Hu, J. Li, H. J. Zhai, S. D. Li, and L. S. Wang, *J. Am. Chem. Soc.* **136**, 12257 (2014).

15. Jing Chen, Qian-Fan Zhang, P. G. Williard, and L. S. Wang, *Inorg. Chem.* **53**, 3932 (2014).

16. J. D. Graham, A. M. Buytendyk, X. Zhang, E. L. Collins, K. Boggavarapu, G. Gantefoer, B. W. Eichhorn, G. L. Gutsev, S. Behera, P. Jena, and K. H. Bowen, *J. Phys. Chem. A* **118**, 8158 (2014).

17. M. Tacke and H. Schnöckel, *Inorg. Chem.* **28**, 2896 (1989).

18. M. Mocker, C. Rob and H. Schnöckel, *Angew. Chem.* **106**, 1860 (1994).

19. A. Ecker and H. Schnöckel, *Z. Anorg. Allg. Chem.* **622**, 149 (1996).

20. P. G. Jessop, T. Ikariya, and R. Noyori, *Chem. Rev.* **95**, 259 (1995).

CHAPTER 1. Photoelectron Spectroscopy of Transition Metal Hydrides

The interaction between transition metals (TM) and hydrogen has always been an intriguing research topic for such applications as hydrogen storage and catalysis of hydrogenation and dehydrogenation reactions. Special bonding features between TM and hydrogen other than the simple M-H σ bond are interesting not only because they are scarcely reported but also because they could help to discover and understand the nature of chemical bonding. In this chapter, cluster anions showing very special bonding between TM and hydrogen will be discussed.

In section 1.1, we present that in the structure of PdH_3^-, two H atoms form a η^2-H_2 type of ligation to Pd, and the H-H bond length is lengthened comparing to the free H_2 molecule. Detailed molecular orbital analysis of PdH^-, H_2 and PdH_3^- reveals that the back donation from a d-type orbital of PdH^- to the σ^* orbital of H_2 causes the H-H elongation, and hence, activation. The H_2 binding energy to PdH^- is unusually as high as 89.2 kJ/mol, even higher than that between CO and Pd. In Section 1.2, we discovered a $PtZnH_5^-$ cluster which possessed an unprecedented planar pentagonal coordination between the H_5^- moiety and Pt, and exhibited special σ-aromatic character. The H_5^- kernel as a whole can be viewed as a η^5-H_5 ligand for Pt, and it is in turn stabilized by the Pt atom. Afterwards, in section 1.3 we extended this work to $PtMgH_{3,5}^-$ in which bonding features similar to those of PdH_3^- and $PtZnH_5^-$ were also found. Finally in section 1.4, other TM-H data without detailed interpretations are presented.

1.1 Photoelectron Spectroscopic and Theoretical Study of the [HPd(η²-H₂)]⁻ Cluster Anion

Xinxing Zhang, [1] Paul J. Robinson, [2] Anastassia Alexandrova [2,3] and Kit H. Bowen [1*]

[1] *Departments of Chemistry and Materials Science, Johns Hopkins University, Baltimore, Maryland 21218, USA*

[2] *Department of Chemistry and Biochemistry, University of California, Los Angeles, Los Angeles, California 90095-1569, USA*

[3] *California NanoSystems Institute, 570 Westwood Plaza, Building 114, Los Angeles, California 90095, USA*

*Electronic addresses: kbowen@jhu.edu, Telephone: 001-410-516-8425

Abstract

Anion photoelectron spectroscopic and theoretical studies were performed for the PdH⁻ and PdH₃⁻ cluster anions. Experimentally observed electron affinities (EAs) and vertical detachment energies (VDEs) agree very well with theoretical predictions. In the structure of PdH₃⁻, two H atoms form a η²-H₂ type of ligation to Pd, and the H-H bond length is lengthened comparing to the free H₂ molecule. Detailed molecular orbital analysis of PdH⁻, H₂ and PdH₃⁻ reveals that the back donation from a *d*-type orbital of PdH⁻ to the σ* orbital of H₂ causes the H-H elongation, and hence, activation. The H₂ binding energy to PdH⁻ is 89.2 kJ/mol, even higher than that between CO and Pd. The unusually high binding energy as well as the H-H bond activation can be appreciated in practical applications such as hydrogen storage and catalysis.

Introduction

The interaction between transition metals (TM) and hydrogen has always been an intriguing research topic for such applications as hydrogen storage[1-3] and catalysis[4, 5] of hydrogenation and dehydrogenation reactions. Special bonding features between TM and hydrogen other than the simple M-H σ bond are interesting not only because they are scarcely reported but also because they could help to discover and understand the nature of chemical bonding. Very recently, the same experimental and theoretical team as the current paper discovered a $PtZnH_5^-$ cluster which possessed an unprecedented planar pentagonal coordination between the H_5^- moiety and Pt, and exhibited special σ-aromatic character.[6] Afterwards, we extended this work to the isoelectronic and isostructural cluster $PtMgH_5^-$ in which similar bondings were also found.[7] In these clusters, the H_5^- kernel as a whole can be viewed as a η^5-H_5 ligand for Pt, and it is in turn stabilized by the Pt atom. Besides H_5^-, free H_2 molecule was also found to act as a ligand in the η^2-H_2 manner. In 1991, via IR spectroscopy and theoretical calculations, Hansgeorg Schnöckel discovered a $[Cu(\eta^2$-$H_2)Cl]$ cluster in which a H_2 molecule was ligated to Cu from the opposite side of Cl and formed a C_{2v} structure. The H-H bond of the H_2 ligand is slightly elongated comparing to a free H_2 molecule.[8] Then, Stewart Novick performed the study of the $[Cu(\eta^2$-$H_2)F]$ and $[Ag(\eta^2$-$H_2)Cl]$ clusters with microwave spectroscopy,[9, 10] where they pointed out that it is a back-donation from a *d*-type orbital of the transition metal to the unoccupied σ* orbital of H_2 that causes the elongation of the H-H bond. The occupied σ orbital of H_2 acts as a lone pair and inserts into the lowest unoccupied molecular orbital (LUMO) of the metal halide. In all of these three cases, the geometry of the H_2 moiety does not deviate too much from that of the free H_2, however the binding energies of H_2 to the transition metals (80 - 110 kJ/mol) are much greater than typical van der Waals interaction energies. Other η^2-H_2 ligation examples were discovered in

much more complicated transition metal complexes such as those protected by N, P or O based ligands or π-acceptor ligand CO. [3, 11-15]

In the present paper we report the anion photoelectron spectroscopic (PES) study of the PdH_3^- cluster anion in which a H_2 molecule acts as a ligand to Pd. Ab initio calculations closely reproduce the experimental data, confirming the structure of the anion seen in the experiment. In order to understand the details of the bonding between H_2 and PdH^-, experimental data of PdH^- as well as the molecular orbital (MO) analysis of PdH^-, PdH_3^- and H_2 are also presented. The H-H bond in PdH_3^- is lengthened comparing to the free H_2 molecule due to the back donation from a d-type orbital of PdH^- to the LUMO (the σ^* orbital) of H_2, which is similar as in the previously published studies. The additional interactions of H_2 and PdH^- come from the bonding and antibonding combinations of the highest occupied molecular orbital (HOMO, the σ orbital) of H_2 and the σ bonding orbital of PdH^-, together giving a zero bonding effect. We conclude that the strong bonding between H_2 and PdH^- is nearly exclusively due to back donation.

Experimental and Theoretical Methods

The present work utilized anion photoelectron spectroscopy (PES) as its primary probe. Anion PES is conducted by crossing a mass-selected beam of negative ions with a fixed-energy photon beam and energy analyzing the resulting photodetached electrons. This technique is governed by the energy conservation relationship, $h\nu = EBE + EKE$, where $h\nu$, EBE, and EKE are the photon energy, electron binding (transition) energy, and the electron kinetic energy, respectively. Our photoelectron spectrometer, which has been described in ref 16, consists of one of several ion sources, a linear time-of-flight mass spectrometer, a mass gate, a momentum decelerator, a neodymium-doped yttrium aluminum garnet (Nd:YAG) laser for photodetachment,

and a magnetic bottle electron energy analyzer having a resolution of 35 meV at EKE = 1 eV. Photoelectron spectra were calibrated against the well-known photoelectron spectrum of Cu$^-$.[17] The PdH$_{1,3}$$^-$ anions were generated using a pulsed arc cluster ionization source (PACIS), which has been described in detail elsewhere.[18] In brief, a ~30 μs long 180 V electrical pulse applied across the anode and sample cathode of the discharging chamber vaporizes the Pd atoms. The sample cathode was prepared by firmly pressing Pd powders onto a copper rod. Almost simultaneously, 200 psi of ultrahigh purity hydrogen gas was injected into the discharge region, where it was dissociated into hydrogen atoms. The resulting mixture of atoms, ions, and electrons then reacted and cooled as it flowed along a 15 cm tube before exiting into high vacuum. The resulting anions were then extracted and mass-selected prior to photodetachment.

Density functional theory calculations were conducted by applying PBEPBE functional[19] using the Gaussian09 software package[20] to determine the geometries of the anionic and neutral clusters. The 6-311++G (3df, 3pd) basis set[21] on H, Stuttgart Dresden (SDD) basis set[22] on Pd were used. The PdH, PdH$^-$, PdH$_3$, and PdH$_3$$^-$ clusters were all initially treated with ROHF SCF with the aug-CC-pVTZ-PP[23] basis set on the Pd atom, and the ATZP[24] basis set on H atoms. The wavefunctions were then read in the CCSD(T)[25] and EOM-CCSD(T)[26] calculations. The adiabatic detachment energy (ADE) is the energy difference between the anion and the neutral relaxed to the anion's nearest local minimum. If the local minimum is also the global minimum, the ADE is actually the electron affinity (EA). The vertical detachment energy (VDE) was obtained by a simply subtracting the energy of the neutral cluster calculated at the geometry of the anion from the energy of the anion. Deeper transitions were calculated by adding the electronic excitation energies of the neutral to the VDE. We note that the agreement with the experimental spectrum improved dramatically with the increase of the basis sets, and also the inclusion of the perturbative-

triple excitations in CCSD(T) (EOM-CCSD was insufficient). All calculations were carried out using NW Chem software[27] and all visualizations of orbitals were generated with VMD.[28] Atomic charges were calculated using Natural Population Analysis (NPA)[29] in Gaussian 09 with SDD basis set on Pd and TZVP[30] basis set on H. The NPA method has been found to be satisfactory in calculating the charge distribution within a cluster.[31, 32] Density functional theory was implemented using the B3LYP[33] hybrid functional.

Results and discussion

Figure 1.1.1 presents the resultant mass spectrum containing $PdH_{1, 3}^-$. Due to the complication caused by the isotopes of Pd, the simulated isotopic distributions of PdH^- and PdH_3^- are displayed below the experimental data for comparison. The absence of ion intensity at mass = 110 gives evidence that there is no Pd^- or PdH_2^- in the ion beam and $PdH_{1,3}^-$ are the only species obtained. The photoelectron spectrum of PdH^- was taken at mass = 106, and the photoelectron spectrum of PdH_3^- was taken at mass = 108 and 113 in order to avoid mutual contamination. The lack of other PdH_n^- in the mass spectrum indicates the special stability of $PdH_{1, 3}^-$. Figure 1.1.2 exhibits the photoelectron spectra of $PdH_{1, 3}^-$. For PdH^-, several distinct peaks can be observed, the positions of the first three peaks marked by X, A and B are tabulated in Table 1.1.1 for comparison with the calculated spectra. The X peak located at 1.29 eV corresponds to the VDE. The A peak shows splitting, which might be owing to the double degeneracy of this feature, as shown theoretically (Figure 1.1.3). The peaks of PdH^- are relatively sharp, in consistency with the fact that the structural difference between the anion and neutral is small (Figure 1.1.3) and therefore a large Frank-Condon overlap. The electron affinity (EA), defined to be the energy difference of the ground state of the anion and the ground state of the neutral, is estimated by the threshold of the

first EBE band. The EA of PdH is estimated to be ~1.2 eV. The calculated ADE value is 1.288 eV (Table 1.1.1), in good consistency with the experimental value. Therefore, ADE and EA are actually one and same value. For PdH_3^-, one major broad EBE band X starts from around ~1.7 eV (EA) and peaks at 1.94 eV (VDE). Other features can be observed on the higher EBE end, but they are not well-resolved. We tentatively mark a peak A at EBE = 2.9 eV, but there might be more than one transition hiding underneath these features, as indeed is supported by calculations. The relatively broad peak of PdH_3^- indicates a large structural difference between the anion and the neutral (Figure 1.1.4). The calculated ADE value is 1.784 eV, agrees very well with experiment. Again, ADE and EA are one and the same in this case. An excellent agreement between experimental and theoretical values can be observed (Table 1.1.1). The final electron configurations corresponding each peak after photodetachment are also displayed in Table 1.1.1, and the MOs from which the corresponding electron detachments take place are depicted in Figures 1.1.3 and 1.1.4.

The calculated results of $PdH^{-/0}$ and $PdH_3^{-/0}$, including bond lengths (Å, in black), NPA charge distributions (*e*, in red) and molecular orbitals (MO) are displayed in Figure 1.1.3 and 1.1.4. For PdH^-, the Pd-H bond distance is 1.538 Å, very close to that of the neutral (1.530 Å). The Pd atom takes most of the negative charge. The HOMO-5 and HOMO are the bonding and anti-bonding orbitals of the Pd-H single bond from the combination of d_z^2 orbital of Pd and *s* orbital of H. The HOMO-1 to HOMO-4 are the non-bonding *d* orbitals of Pd, and the HOMO-6, HOMO-7 are the non-bonding *p* orbitals of Pd. For PdH_3^-, the Pd-H bond length is 1.660 Å, slightly longer than that of PdH^-, and the H-H moiety clearly shows a η^2 type of ligation. At this stage, we can formally write PdH_3^- as $[HPd(\eta^2-H_2)]^-$ as it appears in the title. The H-H bond length is 0.897 Å, 20% longer than free H_2 molecule (0.747 Å), indicating that the H-H bond is activated. The NPA

charge distribution shows that the H-H moiety is partially negatively charged, which is consistent with the bond elongation and back-donation from the Pd atom. In neutral PdH_3, the H_2 molecule is further away from the PdH moiety and the H-H bond length is closer to free H_2, indicating a weaker interaction between H_2 and PdH. The charge on Pd is positive, thus, the back donation from Pd to H_2 is smaller, causing the positive charge on H_2 moiety. Figure 1.1.5 is the correlation diagram depicting how the MOs of $[HPd(\eta^2-H_2)]^-$ are formed from the combinations of the MOs of PdH^- and H_2. The HOMO-4, a d-type orbital of PdH^-, back donates into the LUMO of H_2 and forms the HOMO-3 of $[HPd(\eta^2-H_2)]^-$. This is the combination that causes the H-H bond elongation, charge transfer to H_2 and its activation. HOMO-5 of PdH^- combines with the HOMO of H_2 and splits into HOMO-4 and HOMO-6 of PdH_3^-. HOMO-4 represents the anti-bonding orbital between H_2 and PdH^-, and HOMO-6 is the bonding orbital. HOMO, HOMO-1, HOMO-2 and HOMO-5 of PdH_3^- are now the non-bonding orbitals belonging only to PdH^-, which are displayed in Figure 1.1.4. Note that the degenerate HOMO-1 and HOMO-2 of PdH^- loose degeneracy in PdH_3^- due to symmetry break.

The binding energy, D_0, of the η^2-H_2 moiety to the PdH^- ion is calculated from the following formula with the CCSD(T) level of theory: $D_0 = E(PdH^-) + E(H_2) - E(PdH_3^-) = 89.2$ kJ/mol. This number is comparable to the binding energies between H_2 and transition metal halides [8-10] and higher than the binding energy between the much more commonly used ligand CO and Pd.[34,35]

Concluding remarks

PdH^- is isoelectronic to CuCl, CuF and AgCl, so it is not surprising that H_2 binds to them in similar manners.[8-10] However, the existence of highly electron-withdrawing halide atoms in these complexes reduces the electron density on the transition metal atom and limits the back

donation to H_2. Therefore, the H atoms are negatively charged in PdH_3^-, unlike others which often exhibit cationic features.[3] Negatively charged H is the key to, for example, CO_2 hydrogenation.[36] The H-H bond length in the current study is calculated to be 20.0% longer than free H_2 molecule and around 12.5% longer than those reported in references 8-10, which means the H-H bond is much more activated in our case. The H-H bond length and charge distribution differences between PdH_3^- and PdH_3 are also examples of the extent of back-donation, i.e. in neutral PdH_3 the H_2 moiety is less activated than the anionic PdH_3^- but similar to those in references 8-10. Therefore, this cluster anion might find its role in catalysis. Actually our lab has started the research using TM polyhydride cluster anions as H source for CO_2 hydrogenation and observed the formation of formate from the reaction between platinum hydride cluster anions and CO_2. These results will be published in the near future.

Moreover, when Pd is used as hydrogen storage material, the best stoichiometry that has been achieved is $PdH_{0.6}$, with a hydrogen mass density of 0.56%.[1] In the current study, if we view the H_2 ligand as the stored hydrogen, the H mass density is increased to 1.86%. Therefore, when people pursue Pd as hydrogen storage materials in the future, anionic clusters might be a good direction and the cluster in the current paper provides a good model of it.

Acknowledgement

References

1. L.Schlapbach and A. Züttel, *Nature*, **414**, 353 (2001).

2. W. Grochala and P. P. Edwards, *Chem. Rev.* **104**, 1283 (2004).

3. G. J. Kubas, *Chem. Rev.* **107**, 4152 (2007).

4. J. A. Widegren, R. G. Finke, J. *Mol. Catal. A* **191**, 187 (2003).

5. G. E. Dobereiner and R. H. Crabtree, *Chem. Rev.* **110**, 681 (2010).

6. X. Zhang, G. Liu, G. Gantefoer, K. H. Bowen, and A. N. Alexandrova, *J. Phys. Chem. Lett.* **5,** 1596 (2014).

7. Unpublished work. To be published soon.

8. H. S. Plitt, M. R. Bär, R. Ahlrichs, and H. Schnöckel, *Angew. Chem. Int. Ed.* **30**, 832 (1991).

9. G. S. Grubbs II, D. A. Obenchain, H. M. Pickett, and S. E. Novick, *J. Chem. Phys.* **141**, 114306 (2014)

10. D. J. Frohman, G. S. Grubbs, II, Z. Yu, and S. E. Novick, *Inorg. Chem.* **52**, 816 (2013).

11. B. Chaudret, G. Chung, O. Eisenstein, S. A. Jackson, F. J. Lahoz, and J. A. Lopez, *J. Am. Chem. Soc.* **113**, 2315 (1991).

12. M. L. Christ, S. Sabo-Etienne, and B. Chaudret, *Organometallics* **13**, 3800 (1994).

13. G. J. Kubas, R. R. Ryan, B. I. Swanson, P. J. Vergamini, and H. J. Wasserman, *J. Am. Chem. Soc.* **106**, 452 (1984).

14. N. Aebischer, U. Frey, and A. E. Merbach, *Chem. Commun.***1998**, 2303 (1998).

15. S. L. Matthews, V. Pons, and D. M. Heinekey, *J. Am. Chem. Soc.* **127**, 850 (2005).

16. M. Gerhards, O. C. Thomas, J. M. Nilles, W. J. Zheng, and K. H. Bowen, *J. Chem. Phys.* **116**, 10247 (2002).

17. J. Ho, K. M. Ervin, and W. C. Lineberger, *J. Chem. Phys.* **93**, 6987 (1990).

18. X. Zhang, Y. Wang, H. Wang, A. Lim, G. Gantefӧr, K. H. Bowen, J. U. Reveles and S. N. Khanna, *J. Am. Chem. Soc.* **135,** 4856 (2013).

19. J. P. Perdew, K. Burke, and M. Ernzerhof, *Phys. Rev. Lett.* **77**, 3865 (1996).

20. M. J. Risch, G. W. Trucks, H. B. Schlegel, G. E. Scuseria, M. A. Robb, J. R. Cheeseman, G. Scalmani, V. Barone, B. Mennucci, G. A. Petersson, et al. Gaussian 09, revision A.1; Gaussian, Inc.:Wallingford, CT, 2009

21. R. Krishnan, J. S. Binkley, R. Seeger, and J. A. Pople, *J. Chem. Phys.* **72**, 650 (1980).

22. M. Dolg, H. Stoll, H. Preuss, R.M. Pitzer, J. Phys. Chem. **97**, 5852 (1993).

23. K. A. Peterson, D. Figgen, M. Dolg, and H. Stoll, *J. Chem. Phys.* **126**, 124101 (2007).

24. P. A. Fantin, P. L. Barbieri, A. C. Neto, and F. E. Jorge, *J. Mol. Struct.* **810**, 103 (2007).

25. K. Raghavachari, G. W. Trucks, J. A. Pople, and M. Head-Gordon, *Chem. Phys. Lett.* **157**, 479 (1989).

26. J. D. Watts and R. J. Bartlett, *Chem. Phys. Lett.* **233**, 81 (1995).

27. M. Valiev, E. J. Bylaska, N. Govind, K. Kowalski, T. P. Straatsma, H. J. J. van Dam, D. Wang, J. Nieplocha, E. Apra, T. L. Windus, and W. A. de Jong, *Comput. Phys. Commun.* **181**, 1477 (2010).

28. W. Humphrey, A. Dalke, and K. J. Schulten, *Molec. Graphics*, **14**, 33 (1996).

29. A. E. Reed, R. B. Weinstock, and F. Weinhold, *J. Chem. Phys.* **83**, 735 (1985).

30. N. Godbout, D. R. Salahub, J. Andzelm, and E. Wimmer, *Can. J. Chem.* **70**, 560 (1992).

31. H. Wang, X. Zhang, J. Ko, A. Grubisic, X. Li, G. Gantefӧr, H. Schnӧckel, B. Eichhorn, M. Lee, P. Jena, A. Kandalam, B. Kiran, and K. H. Bowen, *J. Chem. Phys.* **140**, 054301 (2014).

32. H. Wang, Y. Ko, X. Zhang, G. Gantefoer, H. Schnoeckel, B. W. Eichhorn, P. Jena, B. Kiran, A. K. Kandalam, and K. H. Bowen, *J. Chem. Phys.* **140**, 124309 (2014).

33. A. D. Becke, *J. Chem. Phys.* **98**, 5648 (1993).

34. J. Li, G. Schreckenbach, and T. Ziegler, *J. Am. Chem. Soc.* **117**, 486 (1995).

35. V. Jonas and W. Thiel, *J. Chem. Phys.* **102**, 8474 (1995).

36. H. K. Gerardi, A. F. DeBlase, X. Su, K. D. Jordan, A. B. McCoy, and M. A. Johnson, *J. Phys. Chem. Lett.* **2**, 2437 (2011).

Table 1.1.1 The experimental photoelectron spectra comparing to those from calculations (eV). Peak X denotes the vertical detachment energy (VDE). Peaks A and B denote photodetachment from deeper MOs. The final electron configurations after photodetachment are also presented.

Species	Expt.	Theo.[a]	Final configuration
PdH$^-$	EA ~1.2	ADE 1.288	N/A
	X 1.29	1.29	...$1\Sigma+^2, \Pi^4, \Delta^4, 2\Sigma^1$
	A 2.04	2.07 [b]	...$1\Sigma+^2, \Pi^4, \Delta^3, 2\Sigma^2$
	B 2.22	2.39 [b]	...$1\Sigma+^2, \Pi^3, \Delta^4, 2\Sigma^2$
PdH$_3^-$	EA ~1.7	ADE 1.784	N/A
	X 1.94	1.97	...$2a_1^2 2b_2^2 1a_2^2 3a_1^2 4a_1^1$
	A ~2.9	2.81	...$2a_1^2 2b_2^2 1a_2^2 3a_1^1 4a_1^2$
		2.81	...$2a_1^2 2b_2^2 1a_2^1 3a_1^2 4a_1^2$
		2.82	...$2a_1^2 2b_2^1 1a_2^2 3a_1^2 4a_1^2$
		3.19	...$2a_1^1 2b_2^2 1a_2^2 3a_1^2 4a_1^2$

[a] aug-CC-pVTZ-PP[23] basis set was used for Pd, ATZP basis set was used for H.

[b] Indicates doubly degenerate features.

Figure Captions

Figure 1.1.1. The epxperimental mass spctrum containing $PdH_{1,3}^-$ and the simulated isotopic distributions of PdH^- and PdH_3^-.

Figure 1.1.2. The Photoelectron Spectra of PdH^- and PdH_3^- taken with 3.49 eV laser.

Figure 1.1.3. The strucutres and MOs of $PdH^{-/0}$.

Figure 1.1.4. The strucutres and MOs of $PdH_3^{-/0}$.

Figure 1.1.5. Correlation diagram for the valence MOs.

Figure 1.1.1 The epxperimental mass spctrum containing PdH$_{1,3}^-$ and the simulated isotopic distributions of PdH$^-$ and PdH$_3^-$.

Figure 1.1.2 The Photoelectron Spectra of PdH⁻ and PdH₃⁻ taken with 3.49 eV laser.

Figure 1.1.3 The strucutres and MOs of PdH$^{-/0}$.

Figure 1.1.4 The strucutres and MOs of PdH$_3^{-/0}$.
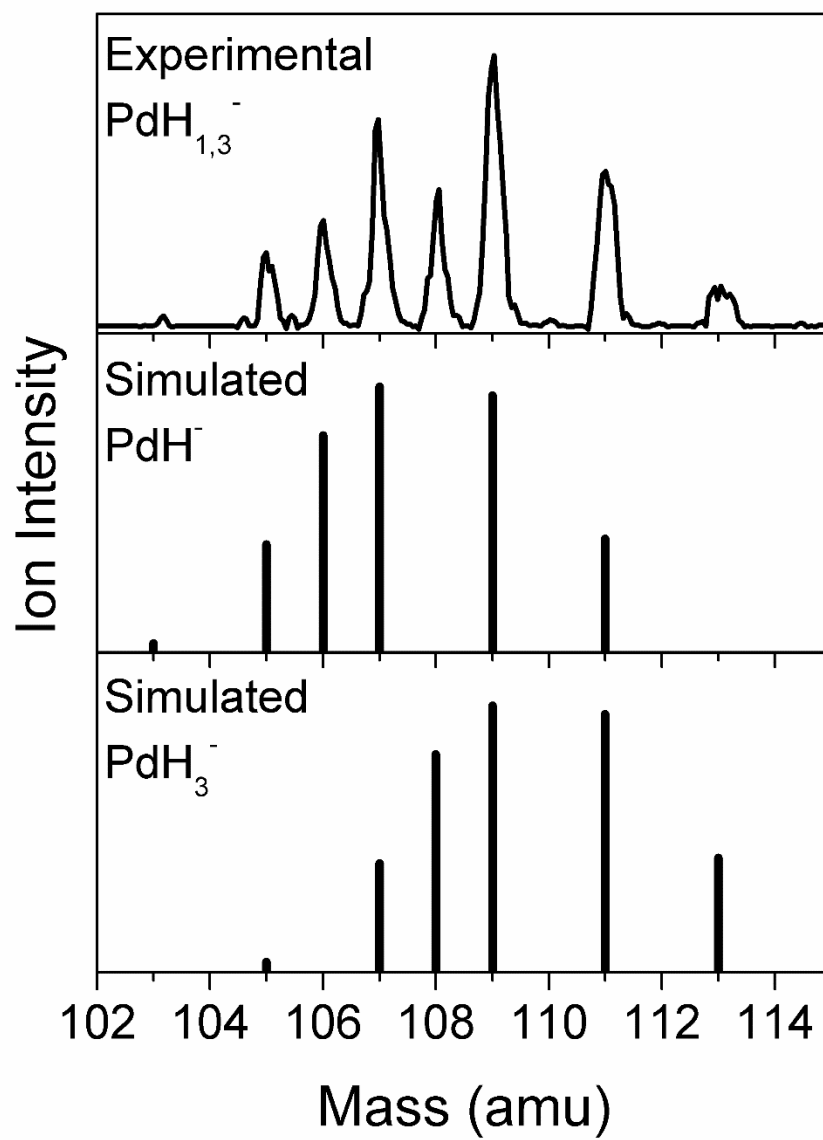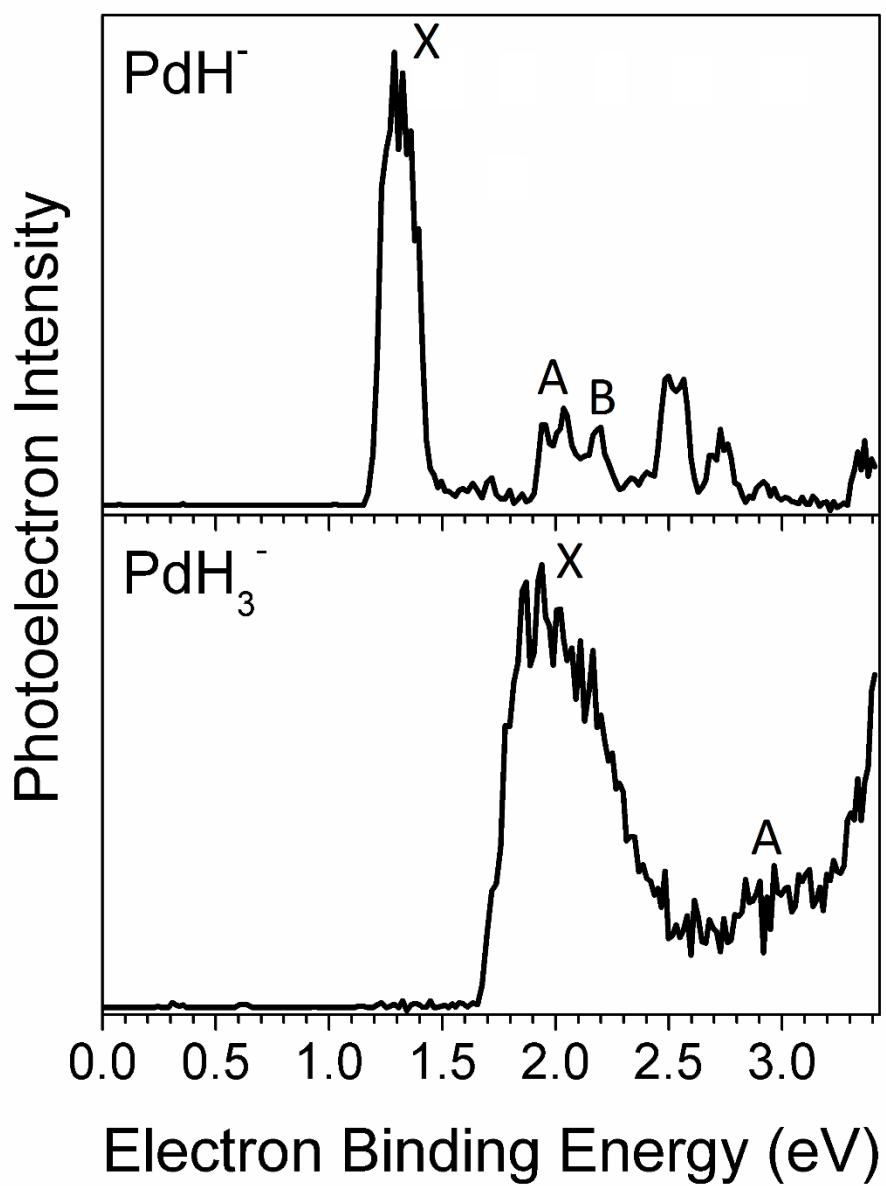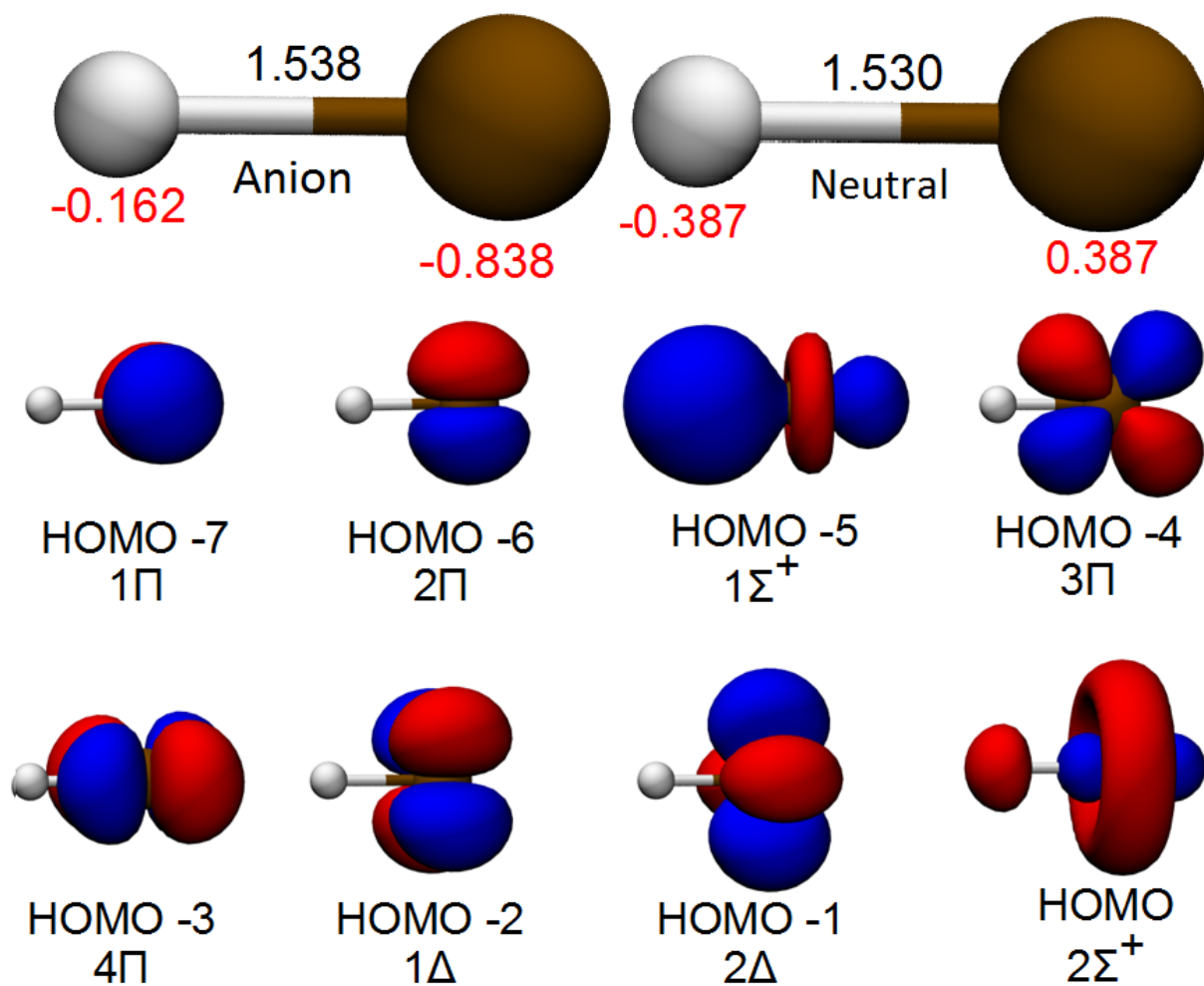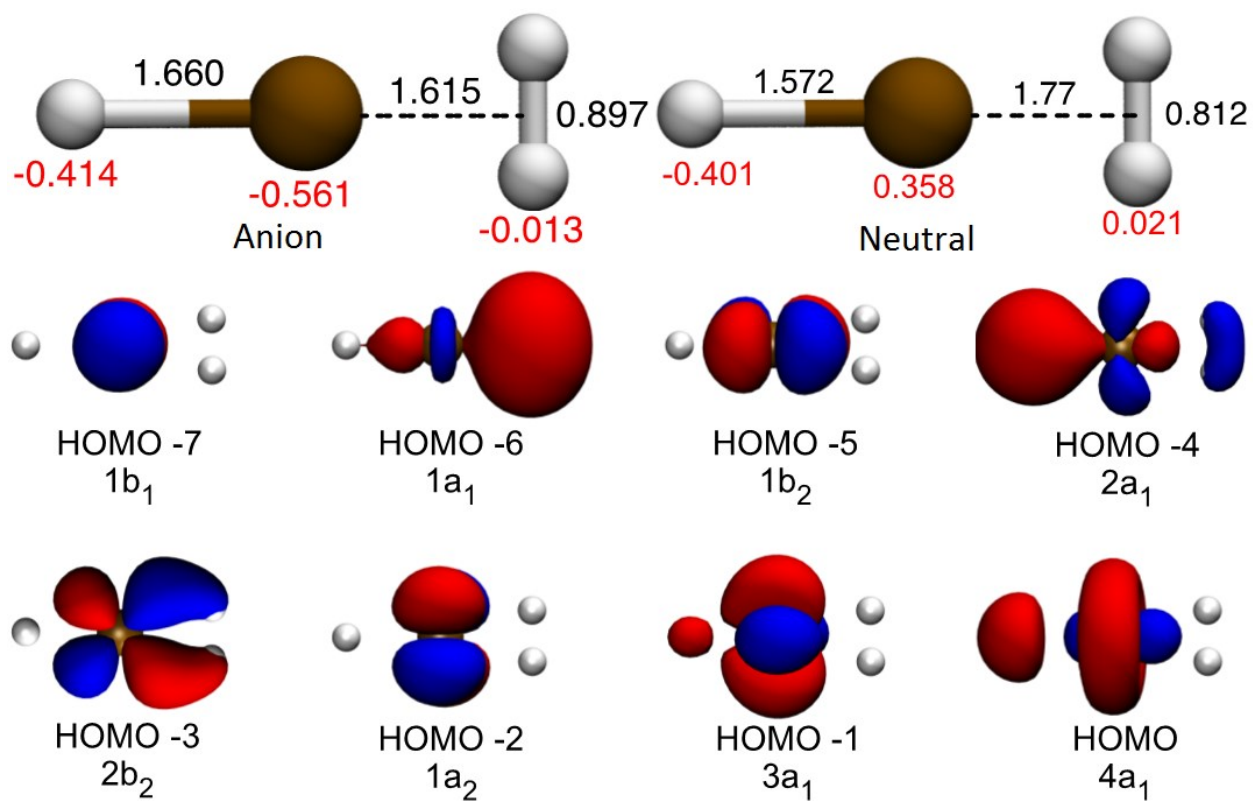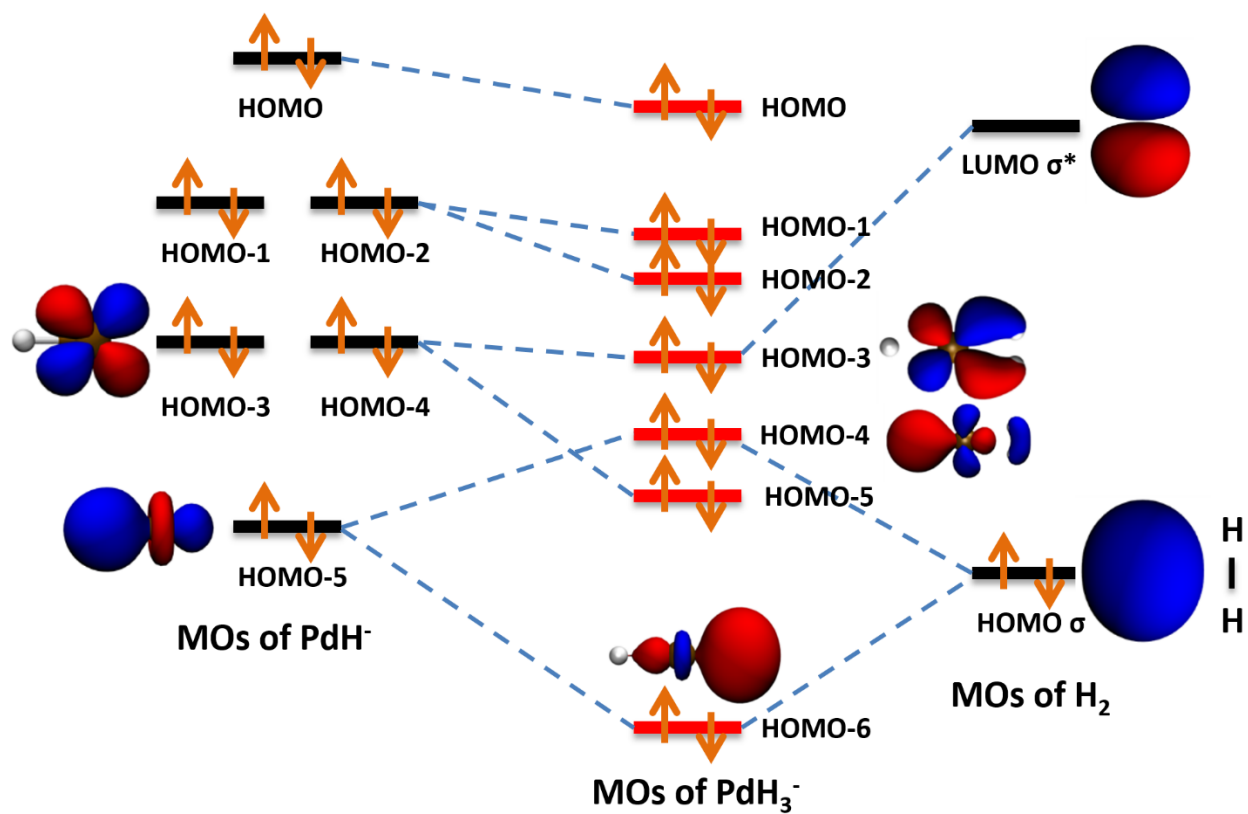
Figure 1.1.5 Correlation diagram for the valence MOs.

1.2 PtZnH$_5^-$, A σ-Aromatic Cluster

Xinxing Zhang,[1] Gaoxiang Liu,[1] Gerd Ganteför,[1] Kit H. Bowen,[1] and Anastassia N. Alexandrova[2,3]

1 Department of Chemistry and Materials Science, Johns Hopkins University, Baltimore, Maryland 21218, United States

2 Department of Chemistry and Biochemistry, University of California, Los Angeles, Los Angeles, California 90095-1569, United States

3 California NanoSystems Institute, 570 Westwood Plaza, Building 114, Los Angeles, California 90095, United States

Abstract

We report a joint photoelectron spectroscopic and theoretical study of the PtZnH$_5^-$ cluster anion. This cluster exhibited an unprecedented planar pentagonal coordination for Pt and an unusual stability and high intensity in the mass spectrum. Both are due to the σ-aromaticity found in the H$_5$-cycle supported by the 5d orbitals on the Pt atom. σ-Aromaticity in all-H systems has been predicted in the past but never found in experimentally observed species. Besides fundamental importance, mixed transition-metal hydrides can be found as intermediates in catalytic processes, and thus, the unexpected stability facilitated by σ-aromaticity can be appreciated also in practical applications.

Introduction

Aromaticity, one of the most significant concepts in modern chemistry, continues to gain appreciation as it is one of the stabilizing chemical bonding effects that leads to remarkable symmetries and stabilities of clusters and molecules.[1-16] Many all-metal clusters were reported to exhibit multiple types of aromaticity, including σ-, π-, and δ-type or a combination of these three types. σ-Aromaticity in particular has been a concept first subjected to debates and prosecution and then accepted and widely explored. The simplest systems in which σ-aromaticity can be found are clusters of H, where the bonding overlap of the 1s atomic orbitals (AOs) on atoms gives rise to this phenomenon. The peculiar example of this sort is the H_3^+ cluster, a highly abundant species in the interstellar space. Species decorated with multiple hydrides also occur in heterogeneous catalysis, and there, every bit of stability (whether or not due to aromaticity) counts toward or against the kinetics of the catalytic processes. Intriguingly, in 2003, Tsipis et al. theoretically predicted the existence of aromatic metal hydride clusters M_nH_n (M = Cu, Ag, Au; n = 3–6);[17-20] however, their experimental evidence is still absent. It would be exciting to see if the simplest possible type of aromaticity and antiaromaticity (σ-type) could be present in metal hydrides and govern their stability, in particular, if one day this could be explored in catalytic processes.

In this work, we study mixed Pt–Zn hydrides at the subnano scale. The Pt–Zn bimetallic systems are used as catalysts for various reactions, such as hydrogenation/dehydrogenation and fuel cell oxidation.[21-26] Doping precious metal catalysts in general is an amendable strategy for manipulating and tuning the electronic structure and thus properties of the catalyst and potentially reducing the cost. However, the research is still within the nanoregime, and subnano bimetallic Pt–Zn clusters containing only several atoms have not been studied but pose a great interest in

view of the observation that small clusters are actually the sites where the majority of catalytic processes occur.[27-29] Hydrides of these small clusters are thus of interest.

We present a combined experimental and theoretical study of a σ-aromatic cluster, $PtZnH_5^-$, and also of $PtZnH_3^-$ and $PtZnH_4^-$. These anionic hydrides are generated in the gas phase and investigated using negative ion photoelectron spectroscopy (PES). The experimental photoelectron spectra are compared with theoretical predictions for the found global minimum structures. $PtZnH_5^-$ is found to have an unusual structure, high stability manifested in the abundance in the mass spectrum, and σ-aromaticity.

Experimental Methods

The present work utilized negative ion PES as its primary probe. Anion PES is conducted by crossing a mass-selected beam of negative ions with a fixed-energy photon beam and energy analyzing the resulting photodetached electrons. This technique is governed by the energy-conservation relationship, $hv = EBE + EKE$, where hv, EBE, and EKE are the photon energy, electron binding (transition) energy, and the electron kinetic energy, respectively. Our photoelectron spectrometer, which has been described in ref 30, consists of one of several ion sources, a linear time-of-flight mass spectrometer, a mass gate, a momentum decelerator, a neodymium-doped yttrium aluminum garnet (Nd:YAG) laser for photodetachment, and a magnetic bottle electron energy analyzer having a resolution of 35 meV at EKE = 1 eV. Photoelectron spectra were calibrated against the well-known photoelectron spectrum of Cu^-.[36] The $PtZnH_5^-$ anions were generated using a pulsed arc cluster ionization source (PACIS), which has been described in detail elsewhere.[37] In brief, a ~30 μs long 150 V electrical pulse applied across the anode and sample cathode of the discharging chamber vaporizes the Pt and Zn atoms.

The sample cathode was prepared in a nitrogen-protected glovebox, where fresh Zn and Pt powders were mixed and firmly pressed onto a zinc rod. Almost simultaneously, 250 psi of ultrahigh purity hydrogen gas was injected into the discharge region, where it was dissociated into hydrogen atoms. The resulting mixture of atoms, ions, and electrons then reacted and cooled as it flowed along a 20 cm tube before exiting into high vacuum. The resulting anions were then extracted and mass-selected prior to photodetachment. The $PtZnH_5^-$ cluster anion has several isotopes; therefore, photoelectron spectra were taken from all of the isotopic peaks to confirm that there were no impurities in the mass spectrum.

Computational Methods

The search for the global minima of the studied cluster anions was done using the gradient embedded genetic algorithm (GEGA),[38] with the population size of 20, and the UPBEPBE[39]/LANL2DZ[40] method. Separate searches for several spin states were performed. The lowest-energy isomers were characterized at higher levels of theory, UPBEPBE/aug-cc-pvTZ+pp,[41] UM06,[42] single-point CCSD[43]//UPBE, and CASSCF(m,n),[44] with (m,n) being as large as (12,12), with the same basis set. It was found that the perturbation theory fails for the studied systems, and for this reason, MP-based methods and CCSD(T) were not used. The combination of Pople's 6-311++G**[45] basis for Zn and H and the LANL2DZ basis for Pt were also used to make sure that there is no unhealthy dependence on the choice for the basis set. For calculations of photoelectron spectra, linear response time-dependent DFT, TD-UPBEPBE, with different basis sets, and also CCSD/aug-cc-pvTZ+pp//UPBEPBE/aug-cc-pvTZ+pp were used. TD-DFT was used for calculations of the excited states of the neutral clusters, and then, the excitation energies were

added to the value of the first vertical detachment energy (VDE_1) to produce VDE_2, VDE_3, and so forth. All calculations were done with Gaussian 09.[46]

Experimental Results

The mass spectrum of the $PtZnH_5^-$ cluster anion is presented in Figure 1.2.1A. One can observe several major isotopic peaks ranging from 261 to 271. In order to make sure that the spectrum has no impurities from other hydrides, that is, $PtZnH_n^-$, we plotted the simulated isotopic distribution of $PtZnH_5^-$ in Figure 1.2.1 B. One can observe that both spectra match very well not only in distribution but also in relative intensity. This phenomenon is uncommon for mass spectrometric study of metal hydrides; typically, there are different numbers of hydrogen atoms attached to the metal atom. Thus, the triumph of $PtZnH_5^-$ from the $PtZnH_n^-$ series indicates its special stability.

Figure 1.2.2 presents the photoelectron spectrum of $PtZnH_5^-$ taken with a 355 nm (3.496 eV) laser. We took spectra from all of the isotopic peaks, and all of them were identical, which is another confirmation that there is no contamination in the mass spectrum. One observes a major EBE band ranging from 2.4 to 3.2 eV and peaked at 2.75 eV, with the resolution being better than 50 meV. The electron binding energy (EBE) value corresponding to the intensity maximum in the observed band is its vertical detachment energy (VDE), the transition energy at which the Franck–Condon overlap between the wave functions of the anion and its neutral counterpart is maximal. The adiabatic electron affinity (EA) is the energy difference between the lowest energy vibronic state of the anion and the lowest energy vibronic state of its neutral counterpart. We have estimated the EA of $PtZnH_5$ to be 2.5 eV by extrapolating the low EBE side, with the corresponding EBE value there being taken as the EA.

Cluster Structures

Figure 1.2.3 shows the found global minima of considered clusters, $PtZnH_3^-$, $PtZnH_4^-$, and $PtZnH_5^-$; for $PtZnH_5^-$, we show the global minimum and the second competing isomer. All clusters bind atomic H, which indicates that they would likely dissociate H_2, should it bind to them as a molecule, for example, in a catalytic process. Indeed, Pt is a typical catalyst for dehydrogenation, in the form of extended surfaces, nanoparticles, and nanoislands, even though catalysis of really small clusters was hardly ever explored. For $PtZnH_3^-$, the global minimum is a C_1 (^1A) structure, with all three H atoms bound to the Pt atom. For $PtZnH_4^-$, it is the C_{2v} ($^1A_1$) structure, with two of the four H atoms bridging between Pt and Zn and the remaining two bound to Pt. For $PtZnH_5^-$, there are two isomers relatively close in energy. Most theoretical methods predict isomer II (C_{2v} ($^1A_1$)) to be more stable by ~4 kcal/mol. One exception is the CASSCF(12,12) method, which predicts isomer I (C_{5v} ($^1A_1$)) to be more stable. Considering the expected error in the performance of the ab initio method in use, it is fair to say that these two isomers are isoenergetic.

Theoretical Interpretation of the Photoelectron Spectrum of $PtZnH_5^-$

In this work, we focus on $PtZnH_5^-$ because of its unusually high abundance in the mass spectrum as compared to the two lighter hydrides. We expect it to exhibit unusual structure and bonding characteristics. Table 1.2.1 shows calculated photoelectron spectra of the two isomers of $PtZnH_5^-$. The agreement across different theoretical methods is apparent. The simulated spectrum of isomer II does not agree with the experiment, with VDE_1, being ~1 eV off, and that rules out the possibility of the isomer II being observed in the experiment. On the other hand, the theoretical spectrum of isomer I is in close agreement with the experiment. All experimental features are

successfully assigned to single-electron processes of electron detachment from the valence molecular orbitals (MOs) shown in Figure 1.2.4A. The fact that isomer I is predicted to be less stable but is the one observed experimentally indicates either the inadequate performance of theoretical methods or the kinetic stabilization of the metastable isomer I in the beam. The predicted adiabatic detachment energy (ADE) is close to the VDE (Table 1.2.1), and in the experiment, the observed EA, 2.5 eV, and the theoretical ADE are effectively the same quantities in this case. The electron detachment from the completely symmetric HOMO of the cluster leads to a small geometric change upon relaxation, hence resulting in a small difference between the VDE and ADE.

Aromaticity of PtZnH$_5^-$.

Figure 1.2.4 addresses the chemical bonding in the C_{5v} ($^1A_1$) isomer I of PtZnH$_5^-$. First of all, its structure is highly unusual due to its high symmetry and an anomalous coordination of the Pt atom, pentagonal pyramidal. Pt is often found to be square planar, but here, we have a five-coordinated arrangement in-plane and an additional Zn atom on the axial position. To the best of our knowledge, such coordination for Pt was never observed before. What leads to the stabilization of this unusual structure and the high abundance of this species in the mass spectrum of PtZn hydride anions? Valence MOs of the cluster are shown in Figure 1.2.4A, and a sketch of how they are formed from AOs is presented in Figure 1.2.4B. Some of the MOs of the cluster are clearly pure d lone pairs of Pt (HOMO–1 and HOMO–4) and Zn (HOMO–6, HOMO–7, and HOMO–8) that do not contribute to the bonding in the cluster. The HOMO and HOMO–3 correspond to σ-bonding between Pt and Zn. These MOs are mainly the bonding and antibonding combinations of the 4s AO on Zn and 5d$_z^2$ AO on Pt. The Pt–Zn bond is partially ionic, with the partial charges on

atoms being $+0.011$ on Zn and -1.355 on Pt (natural population analysis[31]). Importantly, removal of Zn from the cluster results in the PtH_5^- species, which is a planar D_{5h} structure (at least in the local minimum form), and the bonding within this fragment is analogous to that in the PtH_5^- unit within the $PtZnH_5^-$ hydride. Thus, Zn is merely a spectator in the system where Pt exhibits an unusual coordination.

The most interesting MOs are the doubly degenerate HOMO–2 and the HOMO–5 (Figure 1.2.4A). These are σ-MOs, mostly formed by the five 1s AOs on hydrides. They mix with the 6p and 6s AOs on Pt, as allowed by symmetry (Figure 1.2.4B). For simplicity, first consider just the isolated (hypothetic) H_5 pentagon. The five 1s AOs would form five MOs that are shown schematically in Figure 1.2.4C. The three lowest-energy ones correspond nicely to the valence HOMO–2 and HOMO–5 of $PtZnH_5^-$ in terms of contributions from hydrides. Hence, they are depicted populated in the scheme in Figure 1.2.4C. Populated by six electrons, the HOMO–2 and HOMO–5 make the cluster σ-aromatic,[11,32] in accord with the $(4n + 2)$ Hückel's electron counting rule for aromatic compounds with $n = 1$. Remarkably, σ-aromaticity was predicted for the isolated H_5^- (D_{5h}) cluster, but it was found to be a saddle point on the potential energy surface.[33] With the additional support of the 6s and 6p AOs on Pt, the aromatic all-H cycle is stabilized in the studied hydride. Pt is capable of sustaining the five-fold coordination in-plane because it is not really a five-fold coordination; it is a coordination to the H_5 pentagon (the complex can be described as $[Zn–Pt(\eta_5\text{-}H_5)]^-$), and the bonding within this unit is delocalized. Notably, transition metals can coordinate to five-membered ring structures, for example, in metallocenes, but there, the coordination is not in one plane. In $PtZnH_5^-$, Pt takes the central position in the ring to match the σ-MOs on H_5.

Besides the electron counting rule, we wished to gain an additional confirmation of aromaticity in this hydride. The calculation of the nucleus-independent chemical shifts (NICS)[34] index at the center of the pentagonal aromatic unit produces meaningless results because the geometric center coincides with the Pt atom and the contribution of the aromatic ring to the chemical shift is convoluted by the contributions from the AOs on Pt. We also applied the AdNDP[35] procedure, allowing for the maximal electron localization while preserving the electron pair paradigm. Two possible bonding pictures emerged from this analysis. One of them describes the H_5 arrangement σ-aromatic, with three localized AdNDP orbitals that look nearly identical to the HOMO–2 and HOMO–5 in Figure 1.2.4A. The contributions from Pt in this case were separated out to be lone pairs with fairly low population numbers of ~1.6 e. The alternative picture produced five 2c–2e Pt–H bonds with population numbers of ~1.9 e. Both pictures are valid from the AdNDP standpoint, and it is possible that there is a resonance between the two localized solutions. However, the presence of five covalent bonds in the plane mismatches the mutual orientations of the lobes of the AOs on Pt, making the picture counterintuitive. On the other hand, if one assumes the complete population of the 5d set and the 6s AOs and their overall spherical symmetry, then the H and Zn atoms would form an octahedral arrangement around Pt, not the pentagonal pyramidal arrangement. Thus, the five covalent bonds AdNDP picture is confusing. We therefore prefer the σ-aromaticity view of the studied hydride.

Aromaticity is a highly stabilizing effect, also responsible for high symmetry of the system. Therefore, we attribute the high abundance of the studied cluster in the mass spectrum and the apparent stability to σ-aromaticity. Our observation of the σ-aromatic arrangement of hydrides bound to metal clusters is important for catalysis applications. One may imagine that a cluster capable of hosting multiple H atoms that hold just the right charge may exhibit aromaticity and

thus be unusually stable on the reaction profiles of the catalyzed reaction of dehydrogenation. This, however, remains to be demonstrated.

Acknowledgment

References

1. Li, X.; Kuznetsov, A. E.; Zhang, H. F.; Boldyrev, A. I.; Wang, L. S. *Science* 2001, **291**, 859.

2. Li, X.; Zhang, H. F.; Wang, L. S.; Kuznetsov, A. E.; Cannon, N. A.; Boldyrev, A. I. *Angew. Chem., Int. Ed.* 2001, **113**, 1919.

3. Kuznetsov, A. E.; Boldyrev, A. I.; Li, X.; Wang, L. S. *J. Am. Chem. Soc.* 2001, **123**, 8825.

4. Boldyrev, A. I.; Kuznetsov, A. E. *Inorg. Chem.* 2002, **41**, 532.

5. Kuznetsov, A. E.; Boldyrev, A. I.; Zhai, H. J.; Li, X.; Wang, L. S. *J. Am. Chem. Soc.* 2002, **124**, 11791.

6. Kuznetsov, A. E.; Boldyrev, A. I. *Struct. Chem.* 2002, **13**, 141.

7. Alexandrova, A. N.; Boldyrev, A. I. *J. Phys. Chem. A* 2003, **107**, 554.

8. Tanaka, H.; Neukermans, S.; Janssens, E.; Silverrans, R. E.; Lievens, P. *J. Am. Chem. Soc.* 2003, **125**, 2862.

9. Boldyrev, A. I.; Wang, L. S. *Chem. Rev.* 2005, **105**, 3716.

10. Alexandrova, A. N. *Chem. Phys. Lett.* 2012, **533**, 1.

11. Alexandrova, A. N.; Boldyrev, A. I.; Li, X.; Sarkas, H. W.; Hendricks, J. H.; Arnold, S. T.; Bowen, K. H. *J. Chem. Phys.* 2011, **134**, 044322.

12. Li, Z. H.; Moran, D.; Fan, K. N.; Schleyer, P. v. R. *J. Phys. Chem. A* 2005, **109**, 3711.

13. Zhang, J.; Alexandrova, A. N. *J. Phys. Chem. Lett.* 2012, **3**, 751.

14. Zubarev, D. Y.; Averkiev, B. B.; Zhai, H. J.; Wang, L. S.; Boldyrev, A. I. *Phys. Chem. Chem. Phys.* 2008, **10**, 257.

15. Galeev, T. R.; Boldyrev, A. I. *Annu. Rep. Prog. Chem., Sect. C* 2001, **107**, 124.

16. Kuznetsov, A. E.; Birch, K. A.; Boldyrev, A. I.; Li, X.; Zhai, H. J.; Wang, L. S. *Science* 2003, **300**, 622.

17. Tsipis, A. C.; Tsipis, C. A. *J. Am. Chem. Soc.* 2003, **125**, 1136.

18. Tsipis, C. A.; Karagiannis, E. E.; Kladou, P. F.; Tsipis, A. C. *J. Am. Chem. Soc.* 2004, **126**, 12916.

19. Tsipis, A. C.; Tsipis, C. A. *J. Am. Chem. Soc.* 2005, **127**, 10623.

20. Tsipis, A. C.; Stalikas, A. V. *New J. Chem.* 2007, **31**, 852.

21. Kang, Y. J.; Pyo, J. B.; Ye, X. C.; Gordon, T. R.; Murray, C. B. *ACS Nano* 2012, **6**, 5642.

22. Miura, A.; Wang, H.; Leonard, B. M.; Abruna, H. D.; DiSalvo, F. *J. Chem. Mater.* 2009, **21**, 2661.

23. Galloway, E.; Armbrüster, M.; Kovnir, K.; Tikhov, M. S.; Lambert, R. M. *J. Catal.* 2009, **261**, 60.

24. Rossmeisl, J.; Karlberg, G. S.; Jaramillo, T.; Norskov, J. K. *Faraday Discuss.* 2009, **140**, 337.

25. Martono, E.; Vohs, J. M. *J. Phys. Chem. C* 2013, **117**, 6692.

26. McManus, J. R.; Martono, E.; Vohs, J. M. *ACS Catal.* 2013, **3**, 1739.

27. Lee, S.; Fan, C.; Wu, T.; Anderson, S. L. *J. Am. Chem. Soc.* 2004, **126**, 5682.

28. Fu, Q.; Saltsburg, H.; Flytzani-Stephanopoulos, M. *Science* 2003, **301**, 935.

29. Herzing, A. A.; Kiely, C. J.; Carley, A. F.; Landon, P.; Hutchings, G. J. *Science* 2008, **321**, 1331.

30. Gerhards, M.; Thomas, O. C.; Nilles, J. M.; Zheng, W. L.; Bowen, K. H. *J. Chem. Phys.* 2002, **116**, 10247.

31. (a) Carpenter, J. E.; Weinhold, F. *J. Mol. Struct.: THEOCHEM* 1988, **169**, 41; (b) Carpenter, J. E. Ph.D. Thesis, University of Wisconsin, Madison, WI, 1987; (c) Foster, J. P.; Weinhold, F. *J. Am. Chem. Soc.* 1980, **102**, 7211; (d) Reed, A. E.; Weinhold, F. *J. Chem. Phys.* 1983, **78**, 4066; (e) Reed, A. E.; Curtiss, L. A.; Weinhold, F. *Chem. Rev.* 1988, **88**, 899.

32. Alexandrova, A. N.; Boldyrev, A. I. *J. Phys. Chem. A* 2003, **107**, 554.

33. Jiao, H.; Schleyer, P. v. R.; Glukhovtsev, M. N. *J. Phys. Chem.* 1996, **100**, 12299.

34. Schleyer, P. V. R.; Maerker, C.; Dransfeld, A.; Jiao, H.; Hommes, N. E. R. v. E. *J. Am. Chem. Soc.* 1996, **118**, 6317.

35. Zubarev, D. Yu.; Boldyrev, A. I. *Phys. Chem. Chem. Phys.* 2008, **10**, 5207.

36. Ho, J.; Ervin, K. M.; Lineberger, W. C. *J. Chem. Phys.* 1990, **93**, 6987.

37. Li, X.; Grubisic, A.; Stokes, S. T.; Cordes, J.; Gantefoer, G. F.; Bowen, K. H.; Kiran, B.; Willis, M.; Jena, P.; Burgert, R.; Schnoeckel, H. *Science* 2007, **315**, 356.

38. (a) Alexandrova, A. N. *J. Phys. Chem. A* 2010, **114**, 12591; (b) Alexandrova, A. N.; Boldyrev, A. I. *J. Chem. Theory. Comput.* 2005, **1**, 566; (c) Alexandrova, A. N.; Boldyrev, A. I.; Fu, T. J.; Yang, X.; Wang, X. B.; Wang, L. S. *J. Chem. Phys.* 2004, **121**, 5709.

39. Perdew, J. P.; Burke, K.; Ernzerhof, M. *Phys. Rev. Lett.* 1996, **77**, 3865.

40. (a) Hay, P. J.; Wadt, W. R. *J. Chem. Phys.* 1985, **82**, 270; (b) Hay, P. J.; Wadt, W. R. *J. Chem. Phys.* 1985, **82**, 284; (c) Hay, P. J.; Wadt, W. R. *J. Chem. Phys.* 1985, **82**, 299.

41. Peterson, K. A.; Puzzarini, C. *Theor. Chem. Acc.* 2005, **114**, 283.

42. Zhao, Y.; Truhlar, D. G. *Theor. Chem. Acc.* 2008, **120**, 215.

43. (a) Cizek, J. *Adv. Chem. Phys.* 1969, **14**, 35; (b) Purvis, G. D., III; Bartlett, R. L. *J. Chem. Phys.* 1982, **76**, 1910; (c) Scuseria, G. E.; Janssen, C. L.; Schaefer, H. F., III. *J. Chem. Phys.* 1988, **89**, 7382; (d) Scuseria, G. E.; Schaefer, H. F., III. *J. Chem. Phys.* 1989, **90**, 3700.

44. (a) Pople, J. A.; Head-Gordon, M.; Raghavachari, K. J. A. *J. Chem. Phys.* 1987, **87**, 5968; (b) Hegarty, D.; Robb, M. A. *Mol. Phys.* 1979, **38**, 1795; (c) Eade, R. H. A.; Robb, M. A. *Chem. Phys. Lett.* 1981, **83**, 362; (d) Bernardi, F.; Bottini, A.; McDougall, J. J. W.; Robb, M. A.; Schlegel, H. B. *Faraday Symp. Chem. Soc.* 1984, **19**, 137; (f) Frisch, M. J.; Ragazos, I. N.; Robb, M. A.; Schlegel, H. N. *Chem. Phys. Lett.* 1992, **189**, 524; (g) Yamamoto, N.; Vreven, T.; Robb, M. A.; Frisch, M. J.; Schlegel, H. B. *Chem. Phys. Lett.* 1996, **250**, 373.

45. (a) Clark, T.; Chandrasekhar, J.; Spitznagel, C. W.; Schleyer, P. v. R. *J. Comput. Chem.* 1983, **4**, 294; (b) Frisch, M. J.; Pople, J. A.; Binkley, J. S. *J. Chem. Phys.* 1984, **80**, 3265.

46. Frisch, M. J.; Trucks, G. W.; Schlegel, H. B.; Scuseria, G. E.; Robb, M. A.; Cheeseman, J. R.; Scalmani, G.; Barone, V.; Mennucci, B.; Petersson, G. A.; Gaussian 09, revision A.1; Gaussian, Inc.: Wallingford, CT, 2009.

Table 1.2.1 Calculated photoelectron spectra of ZnPtH$_5^-$ isomers **I** and **II**, in eV.

Peak	Exper	MO	Resultant e-configuration	TD-UPBEPBE[a]	TD-UPBEPBE[b]	CCSD(T)
			Isomer I			
X	2.75	HOMO	$\ldots 2a_1{}^2 2e_2{}^4 3a_1{}^2 2e_1{}^4 3e_1{}^4 4a_1{}^1$	2.71	2.70	2.50[c]
		HOMO-1	$\ldots 2a_1{}^2 2e_2{}^4 3a_1{}^2 2e_1{}^4 3e_1{}^3 4a_1{}^2$	4.48*	4.50*	
		HOMO-2	$\ldots 2a_1{}^2 2e_2{}^4 3a_1{}^2 2e_1{}^3 3e_1{}^4 4a_1{}^2$	4.93*	4.92*	
		HOMO-3	$\ldots 2a_1{}^2 2e_2{}^4 3a_1{}^1 2e_1{}^4 3e_1{}^4 4a_1{}^2$	5.83	5.91	
		HOMO-4	$\ldots 2a_1{}^2 2e_2{}^3 3a_1{}^2 2e_1{}^4 3e_1{}^4 4a_1{}^2$	7.12*	7.13*	
			Isomer II			
X	2.75	HOMO	$\ldots 5a_1{}^2 6a_1{}^2 3b_2{}^2 2b_1{}^2 2a_2{}^2 7a_1{}^1$	3.68	3.65	3.84[c]
		HOMO-1	$\ldots 5a_1{}^2 6a_1{}^2 3b_2{}^2 2b_1{}^2 2a_2{}^1 7a_1{}^2$	3.97	4.02	
		HOMO-2	$\ldots 5a_1{}^2 6a_1{}^2 3b_2{}^2 2b_1{}^1 2a_2{}^2 7a_1{}^2$	4.17	4.19	
		HOMO-3	$\ldots 5a_1{}^2 6a_1{}^2 3b_2{}^1 2b_1{}^2 2a_2{}^2 7a_1{}^2$	4.46	4.67	
		HOMO-4	$\ldots 5a_1{}^2 6a_1{}^1 3b_2{}^2 2b_1{}^2 2a_2{}^2 7a_1{}^2$	4.70	5.17	

[a] The aug-cc-pvTZ-pp basis set was used.

[b] The 6-311++G** basis was used for Zn and H, and LANL2DZ(+f) was used for Pt.

[c] At the geometry of the anion optimized using MP2/aug-cc-pvTZ-pp.

* Indicates doubly-degenerate features

Figure Captions

Figure 1.2.1. Experimental (A) and simulated (B) mass spectrum of $PtZnH_5^-$.

Figure 1.2.2. Photoelectron spectra of $PtZnH_5^-$ recordedusing 355 nm (3.49 eV) photons.

Figure 1.2.3. Calculated global minima of $ZnPtH_{3,4}^-$ and two competing isomers of $ZnPtH_5^-$.

Figure 1.2.4. Chemical bonding in $PtZnH_5^-$: (A) valence MOs, with the ones outlined in red corresponding to the sigma-aromatic unit. (B) Correlation diagram for the valence MOs; the MOs outlined in red in (A) are highlighted. (C) A qualitative scheme for the formation of sigma-MOs from five 1s-AOs on H atoms in a pentagonal arrangement; the lowest energy three MOs are analogous to those populated in the cluster; their population makes the cluster obey the $(4n+2)$ Hückel's rule for aromatic compounds, with $n=1$.
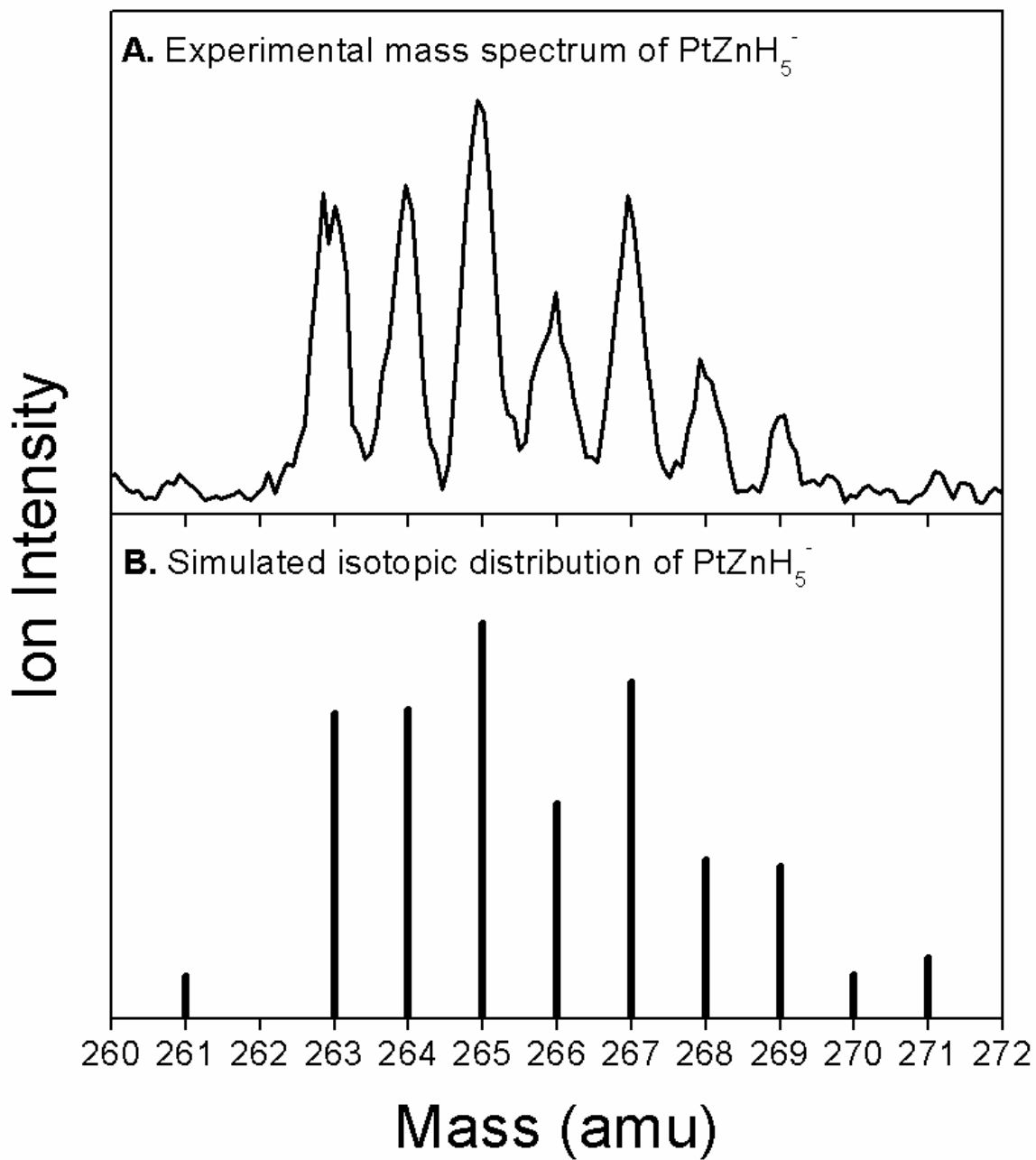
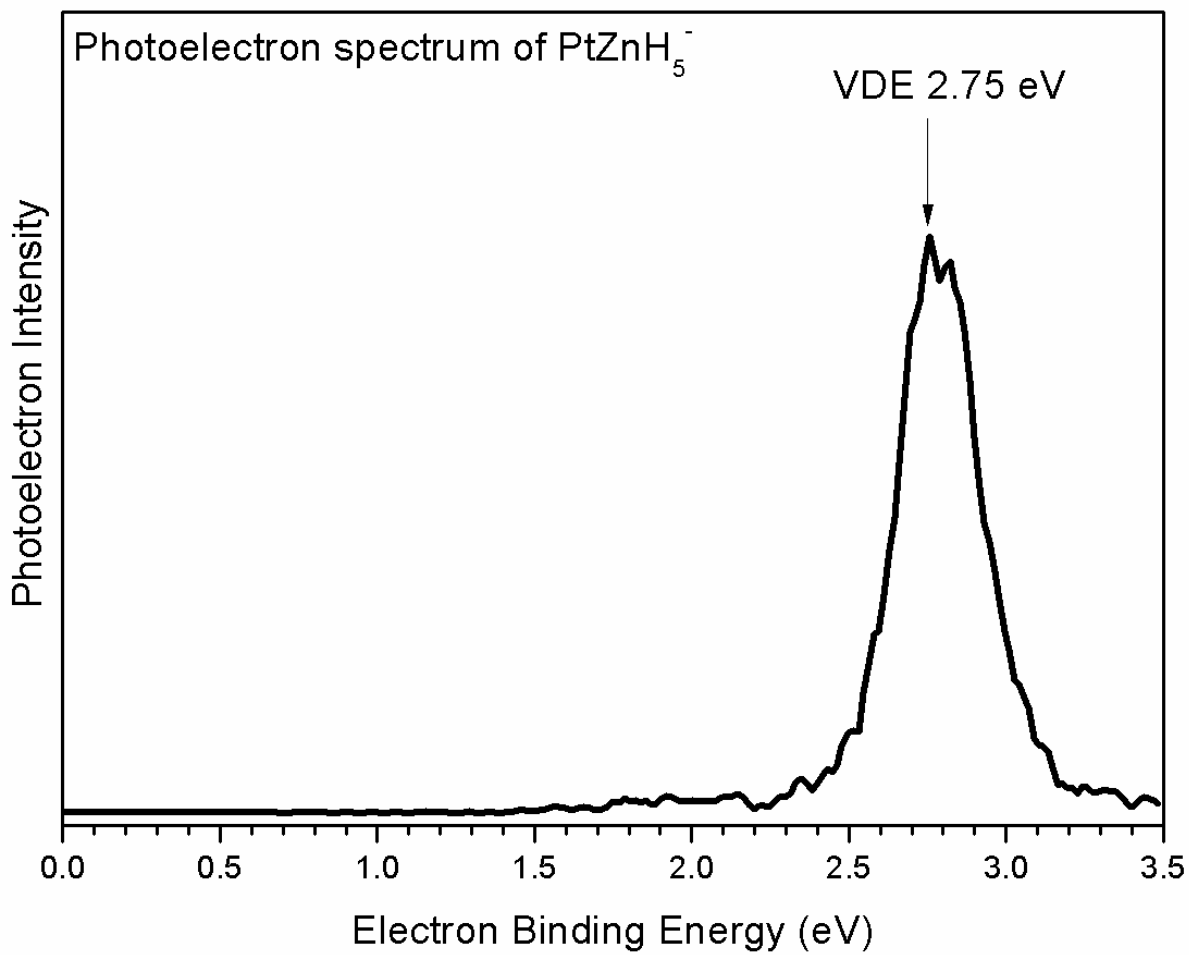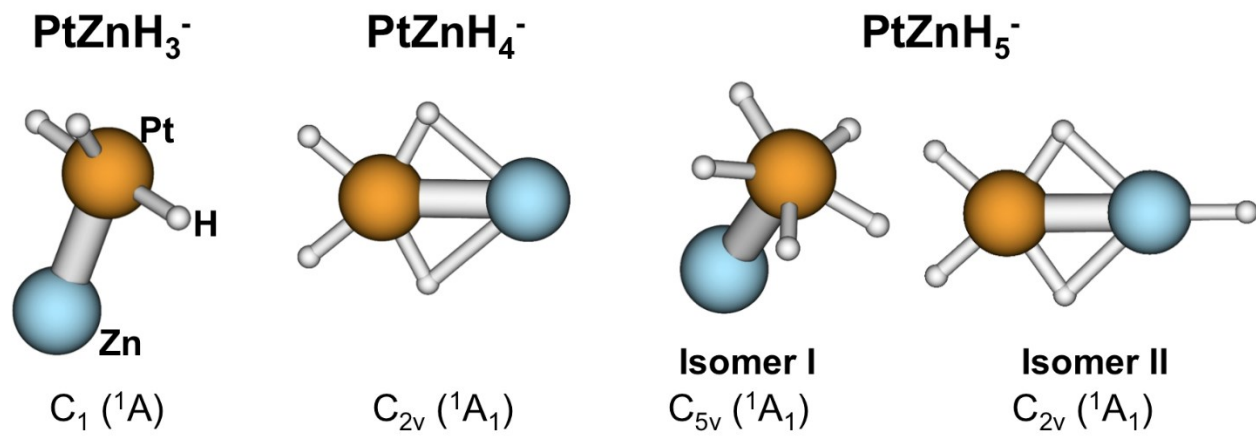**A.** Experimental mass spectrum of PtZnH$_5^-$

B. Simulated isotopic distribution of PtZnH$_5^-$

Mass (amu)

Ion Intensity

Figure 1.2.1

Figure 1.2.2

PtZnH₃⁻ **PtZnH₄⁻** **PtZnH₅⁻**

C_1 (^1A) C_{2v} ($^1A_1$) **Isomer I** **Isomer II**
                                   C_{5v} ($^1A_1$) C_{2v} ($^1A_1$)

Figure 1.2.3
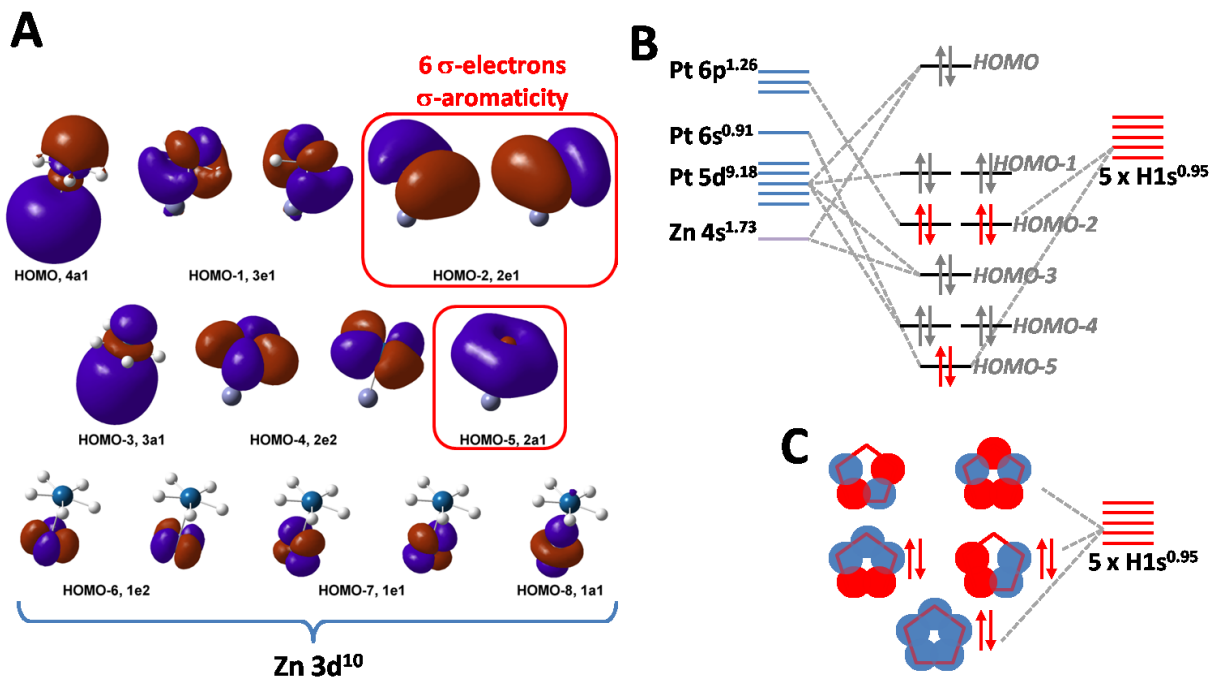
Figure 1.2.4

1.3 Photoelectron Spectroscopic and Theoretical Study of PtMgH$_{3,\,5}^{-}$ Cluster Anions

Xinxing Zhang, [1] Hansgeorg Schnoeckel [2] and Kit Bowen[1], a)

[1] *Department of Chemistry, Johns Hopkins University, Baltimore, Maryland 21218, USA*

[2] *Institute of Inorganic Chemistry, Karlsruhe Institute of Technology, 76128 Karlsruhe, Germany*

a) Electronic mail: kbowen@jhu.edu

Abstract

Two exotic clusters, PtMgH$_3^-$ and PtMgH$_5^-$, are studied by photoelectron spectroscopy and theoretical calculations. Experimentally measured electron affinity (EA) and vertical detachment energy (VDE) values are compared with those obtained from theory and excellent agreements are found. For PtMgH$_3^-$, a very special η_2-bonded H$_2$ moiety is observed in its structure. For PtMgH$_5^-$, an all-hydrogen, five-member, σ-aromatic ring is found, which is accountable for its special stability. These mixed-metal hydride clusters may have potential application in catalytic processes.

Introduction

The interaction between hydrogen and small bimetallic clusters containing precious metal elements has drawn great attention in catalysis, such as in hydrogenation and dehydrogenation. [1-7] Doping commonly used hydrogenation or dehydrogenation catalysts, such as Ni, Pd, Pt with another metal is a good way of fine-tuning their catalytic activity, such as lowering the H-H bond activation barrier. However, the studies to explore why they are better than single element catalyst, to understand the catalytic mechanism, and to further design such catalysts are scarce. J. Rossmeisl and coworkers suggested that doping can tune the electronic structure by adjusting the position of the d-band center. [8] A theoretical study on H_2 dissociation on doped Ni clusters showed that dopants such as Rh, Pd, Pt, and Au could lower the H_2 activation barrier. [2] A density functional theory study observed that the adsorption of H_2 on Au_nCu_m clusters enhanced the stability of the whole cluster. [4] A comparative study of CH_3OH dehydrogenation on Pt_7 and Pt_5Ni_2 presented that there charge transfer from Ni to Pt increased the electron density of Pt's 5d orbital and improved the catalytic activity of the bimetallic cluster. [5] More recently, our group reported that an exotic cluster, $PtZnH_5^-$, had a special planar five-coordinated structure and unusual stability due to its σ-aromaticity. [1] We suggested that its unusual stability might have potential applications in H-related catalysis.

In this work, we extend the study on the interaction between hydrogen and bimetallic cluster with two newly found cluster anions, $PtMgH_{3,\ 5}^-$ via a combined research of anion photoelectron spectroscopy and theoretical calculations. Their electronic structures are characterized. We discovered that both clusters had very unique bonding features between H and the metal center.

Experimental and Theoretical Methods

The present work utilized anion photoelectron spectroscopy (PES) as its primary probe. Anion PES is conducted by crossing a mass-selected beam of negative ions with a fixed-energy photon beam and energy analyzing the resulting photodetached electrons. This technique is governed by the energy conservation relationship, hv = EBE + EKE, where hv, EBE, and EKE are the photon energy, electron binding (transition) energy, and the electron kinetic energy, respectively. Our photoelectron spectrometer, which has been described in ref 9, consists of one of several ion sources, a linear time-of-flight mass spectrometer, a mass gate, a momentum decelerator, a neodymium-doped yttrium aluminum garnet (Nd:YAG) laser for photodetachment, and a magnetic bottle electron energy analyzer having a resolution of 35 meV at EKE = 1 eV. Photoelectron spectra were calibrated against the well-known photoelectron spectrum of Cu^-.[10] The $PtMgH_{3,5}^-$ anions were generated using a pulsed arc cluster ionization source (PACIS), which has been described in detail elsewhere.[11] In brief, a ~30 μs long 150 V electrical pulse applied across the anode and sample cathode of the discharging chamber vaporizes the Pt and Mg atoms. The sample cathode was prepared in a nitrogen-protected glovebox, where fresh Mg and Pt powders were mixed and firmly pressed onto a copper rod. Almost simultaneously, 200 psi of ultrahigh purity hydrogen gas was injected into the discharge region, where it was dissociated into hydrogen atoms. The resulting mixture of atoms, ions, and electrons then reacted and cooled as it flowed along a 15 cm tube before exiting into high vacuum. The resulting anions were then extracted and mass-selected prior to photodetachment.

Density functional theory calculations were conducted by applying PBEPBE functional[12] using the Gaussian09 software package[13] to determine the geometries of both neutral and anionic clusters, the electron affinity (EA) and vertical detachment energy (VDE) values, and the charge

distribution. All geometries, including that of the anion and its corresponding neutral molecule, were fully optimized without any geometrical constraints using the 6-311++G (3df, 3pd) basis set[14] for Mg and H, LANL2DZ effective core potentials [15-17] for Pt. The EA value is the energy difference between the ground state of the neutral and the ground state of the anion with zero point energy correction. The VDE is the energy difference between the ground state of the anion and the neutral with the same structure as the anion. Natural population analysis (NPA), as implemented in the Gaussian09 code, was also carried out to determine the charge distribution of the anion. The NPA method has been found to be satisfactory in calculating the charge distribution within a cluster. [18, 19]

Results and discussion

Figure 1.3.1 presents the simulated and experimental isotopic distributions of $PtMgH_{3, 5}$. One can observe that $PtMgH_3^-$ and $PtMgH_5^-$ coexist in the ion beam. To avoid isotopic contamination, the photoelectron spectrum of $PtMgH_3^-$ was taken at mass = 221 and 222, and the spectrum of $PtMgH_5^-$ was taken at mass = 226 and 227. By making careful analysis of all the photoelectron spectra, we made sure there was no $PtMgH_4^-$ in the ion beam. The higher intensity of $PtMgH_5^-$ than that of $PtMgH_3^-$, together with the fact that there is no other $PtMgH_n^-$ clusters in the beam, indicate its unusual stability. The resulted photoelectron spectra are shown in Figure 1.3.2. For $PtMgH_3^-$, one can observe a wide EBE band starts from 1.45 eV and peaks at 1.80 eV. For $PtMgH_5^-$, the peak is sharper, starts from 1.85 eV and peaks at 2.05 eV. If there is sufficient Franck-Condon overlap between the ground state of the anion and the ground state of the neutral and there is not much hot band signal, the threshold of the first EBE band should be the electron affinity (EA). The peak position of the first EBE band is corresponding to the experimental vertical

detachment energy (VDE). The experimental EA and VDE values of both clusters are tabulated in Table 1.3.1 and compared with those obtained from theory, and excellent agreement can be observed.

Figure 1.3.3 presents the calculated structures of anionic and neutral $PtMgH_{3,5}^-$. The bond lengths are marked with red numbers. $PtMgH_3^-$ has a planar structure, in which there is an H-H moiety attaches to the Pt atom. The bond length between these two H atoms is 0.98 Å, longer than that of free H_2 molecule (0.74 Å), indicating that the H_2 moiety is slightly activated. The neutral $PtMgH_3$, which is very different from its anion counterpart, has a 3-D *Cs* structure. Due to this large structural difference, one would expect a relatively small Franck-Condon overlap between the anion and the neutral, which is consistent with the observed broad EBE band. $PtMgH_5^-$, on the other hand, has a C_{5v} umbrella-like structure, all the H atoms attaches to Pt and forms an all-hydrogen, five-member ring. Pt is often found to be tetra-coordinated square planar, but here, we have a five-coordinated arrangement in-plane and Mg atom on the axial position. To the best of our knowledge, such a structure was only found once in our previously reported cluster, $PtZnH_5^-$.[1] Its neutral counterpart is very similar to the anion, and only the Pt-Mg bond length is relatively shorter, therefore, due to this smaller structural difference, the observed EBE band is much sharper. The coordinates of all of these clusters are reported in the supporting information.

The charge distributions of each atom in the anions obtained from natural population analysis are marked in blue in Figure 1.3.3. In $PtMgH_3^-$, Pt atom draws most of the negative charge, which is due to its high electronegativity. The radially bonded H atom has a negative charge of -0.23 *e*, but the H atoms in the H-H moiety are almost neutral, indicating that it still keeps feature of free H_2 molecule. Therefore, the $PtMgH_3^-$ cluster can be viewed as a η_2-H_2 molecule attaches to a $PtMgH^-$ moiety. η_2-bonded H_2 were observed in $M(CO_3)(Pr_3)_2(H_2)$ [20] as single crystal and Cl-

Cu(η_2-H$_2$) cluster in Ar matrix, [21] in which significant binding energies was found between H$_2$ and the rest of the cluster. Figures 1.3.4(a) shows the three-center molecular orbital of the Pt(η_2-H$_2$) bond, which is very similar to the corresponding molecular orbital in Cl-Cu(η_2-H$_2$) extracted from ref. 20 (Figure 1.3.4(b)). Please note that the charge on Mg atom is almost neutral, therefore, Mg is just a spectator in the system. The rest of the cluster, [H-Pt(η_2-H$_2$)]$^-$, is actually isoelectronic to Cl-Cu(η_2-H$_2$), thus, it is not surprising that similar chemical bonding are observed in these two systems. The dissociation energy D of η_2-bonded H$_2$ is calculated from the following formula: D = E (PtMgH$^-$) + E (H$_2$) – E (PtMgH$_3^-$). The resulting value is 101 kJ/mol, indicating that the binding is quite strong. This number is comparable to the value of Cl-Cu(η_2-H$_2$), 84 kJ/mol.

Next we will discuss the chemical bonding of PtMgH$_5^-$. Since both Mg and Zn have two valence electrons, one would expect PtMgH$_5^-$ and PtZnH$_5^-$ (Reference 1) to show similar structure and bonding features. Figure 1.3.5(a) shows the valence molecular orbitals (MOs) of PtMgH$_5^-$, with the ones outlined in red corresponding to the σ-aromatic MOs. Figure 1.3.5(b) shows how the MOs are formed from the combination of atomic orbitals, with those highlighted in red corresponding to the σ-aromatic MOs in Figure 1.3.5(a). Apparently HOMO-1 and HOMO-4 are the d lone pairs of Pt, HOMO-6 and HOMO-7 are the p orbitals of Mg. HOMO and HOMO-2 are corresponding to the σ bond between Pt and Mg. These MOs are bonding and antibonding combinations of the 5d$_z^2$ atomic orbital of Pt and 3s atomic orbital of Mg. The most interesting MOs are doubly degenerate HOMO-3 and HOMO-5, they are the σ-aromatic units. These orbitals are formed from the combination of the five 1s atomic orbitals of the five H atoms and 6p and 6s atomic orbitals of Pt. Occupied by total six electrons, the HOMO-3 and HOMO-5 make the σ-aromaticity, [22, 23] which fulfills the 4n + 2 Hückel rule, where n = 1. Similarly to PtZnH$_5^-$, PtMgH$_5^-$ can also be described as a coordination between Pt and an H$_5$ pentagon, and written as [Mg-Pt(η_5-

$H_5)]^-$. It is this special σ-aromaticity that makes $PtMgH_5^-$ an unusually stable cluster and explains its high abundance in the mass spectrum. Besides the σ-aromaticity, a simple electron counting rule can be applied to this cluster: Pt has 10 valences electrons, Mg has 2, five H have 5, and there is 1 from the negative charge, therefore, totally there are $10 + 2 + 5 + 1 = 18$ valence electrons. These 18 electrons occupy the first 9 MOs (from HOMO to HOMO-5) in Figure 1.3.5. Therefore, besides the σ-aromaticity, the 18-electron rule also makes this cluster unusually stable. Similarly, this electron counting rule can also be applied to our previously reported $PtZnH_5^-$. [1]

Conclusion

Two exotic cluster anions, $PtMgH_3^-$ and $PtMgH_5^-$ are produced by our unique PACIS ion source. Their experimental EA values are estimated to be 1.45 eV and 1.85 eV, respectively, and VDE values are 1.80 eV and 2.05 eV, respectively. All of these numbers have great agreement with theoretical calculations. Both of these clusters have very special structures. For $PtMgH_3^-$, a η_2-bonded H_2 moiety is found, and its MO analysis shows that this is a very strong three-center bond, very similar to a previously reported cluster, $Cl-Cu(\eta_2-H_2)$. The H_2 moiety is strongly bonded to the rest of the cluster with a dissociation energy of 101 kJ/mol. For $PtMgH_5^-$, there is a coordination between Pt and an σ-aromatic H_5 pentagon. With the support from its 6s and 6p atomic orbitals, Pt is able to stabilize this special in-plane, five-coordinated structure. Electron counting shows that this cluster has 18 valence electrons distributed in 9 different MOs. In all, it is the σ-aromaticity and 18-electron rule that make this cluster unusually stable.

Acknowledgement

References

1. X. Zhang, G. Liu, G. Gantefoer, K. H. Bowen, and A. N. Alexandrova, *J. Phys. Chem. Lett.* **5,** 1596 (2014)

2. N. S. Venkataramanan, A. Suvitha, H. Mizuseki, and Y. Kawazoe, *Int. J. Quantum Chem.* **113**, 1940 (2013)

3. L. B. Ortiz-Soto, J. R. Monnier, and M. D. Amiridis, *Catal. Lett.* **107**, 13 (2006)

4. S. Zhao, X. Tian, J. Liu, Y. Ren, Y. Ren, and J. Wang, *J. Clust. Sci.* **26**, 491 (2015)

5. W. Guo, W. Tian, X. Lian, F. Liu, M. Zhou, P. Xiao, and Y. Zhang, *Comput. Theo. Chem.* **1032**, 73 (2014)

6. H. Liu, *J. Quantum Matter*. **3**, 119 (2014)

7. X. Zhang, G. Gantefoer, K.H. Bowen, and A. Alexandrova , *J. Chem. Phys.* **140**, 164316 (2014)

8. J. Rossmeisl, G. S. Karlberg, T. Jaramillo, and J. K. Norskov, *Faraday Discuss.* **140**, 337 (2009)

9. M. Gerhards, O. C. Thomas, J. M. Nilles, W. J. Zheng, K. H. Bowen, *J. Chem. Phys.* **116**, 10247 (2002)

10. J. Ho, K. M. Ervin, and W. C. Lineberger, *J. Chem. Phys.* **93**, 6987 (1990)

11. X. Zhang, Y. Wang, H. Wang, A. Lim, G. Ganteför, K. H. Bowen, J. U. Reveles and S. N. Khanna, *J. Am. Chem. Soc.* **135,** 4856 (2013)

12. J. P. Perdew, K. Burke, and M. Ernzerhof, *Phys. Rev. Lett.* **77**, 3865 (1996)

13. M. J. Risch, G. W. Trucks, H. B. Schlegel, G. E. Scuseria, M. A. Robb, J. R. Cheeseman, G. Scalmani, V. Barone, B. Mennucci, G. A. Petersson, et al. Gaussian 09, revision A.1; Gaussian, Inc.:Wallingford, CT, 2009

14. R. Krishnan, J. S. Binkley, R. Seeger, and J. A. Pople, *J. Chem. Phys.* **72**, 650 (1980).

15. P. J. Hay and W. R. Wadt, *J. Chem. Phys*. **82**, 270 (1985)

16. P. J. Hay and W. R. Wadt, *J. Chem. Phys*. **82**, 284 (1985)

17. P. J. Hay and W. R. Wadt, *J. Chem. Phys*. **82**, 299 (1985)

18. H. Wang, X. Zhang, J. Ko, A. Grubisic, X. Li, G. Ganteför, H. Schnöckel, B. Eichhorn, M. Lee, P. Jena, A. Kandalam, B. Kiran, and K. H. Bowen, *J. Chem. Phys.* **140,** 054301 (2014)

19. H. Wang, Y. Ko, X. Zhang, G. Gantefoer, H. Schnoeckel, B. W. Eichhorn, P. Jena, B. Kiran, A. K. Kandalam, and K. H. Bowen, *J. Chem. Phys.* **140,** 124309 (2014)

20. G. J. Kubas, R. R. Ryan, B. I. Swanson, P. J. Vergamini, and H. J. Wasserman, *J. Am. Chem. Soc.* **106**, 452 (1984)

21. Von H. S. Plitt, M. R. Bar, R. Ahlrichs and H. Schnockel, *Angew. Chem.* **103**, 848 (1991)

22. A. N. Alexandrova, A. I. Boldyrev, X. Li, H. W. Sarkas, J. H. Hendricks, S. T. Arnold and K. H. Bowen, *J. Chem. Phys.* **134**, 044322 (2011)

23. A. N. Alexandrova and A. I. Boldyrev, *J. Phys. Chem. A* **107**, 554 (2003)

Table 1.3.1. Experimental and theoretical EA and VDE values. All the numbers are in eV.

Clusters	Expt. EA	Theo. EA	Expt. VDE	Theo. VDE
$PtMgH_3^-$	1.45	1.48	1.80	1.73
$PtMgH_5^-$	1.85	1.93	2.05	2.03

Figure Captions

Figure 1.3.1. Simulated and experimental isotopic distributions of $PtMgH_{3,5}^{-}$

Figure 1.3.2. Photoelectron Spectra of $PtMgH_{3,5}^{-}$ taken with 355 nm laser.

Figure 1.3.3. Calculated structures of $PtMgH_{3,5}^{-/0}$. The bond lengths are mark in red and the charge distributions in blue.

Figure 1.3.4. The MO of $PtMgH_3^{-}$ showing the $Pt(\eta_2-H_2)$ bond (a) and the similar MO of $CuCl(H_2)$ showing the $Cu(\eta_2-H_2)$ bond (b). (b) is extracted from ref. 20.

Figure 1.3.5. Chemical bonding in $PtMgH_5^{-}$. Valence MOs, with the ones outlined in red corresponding to the σ-aromatic MOs (a). Correlation diagram for the valence MOs (b).
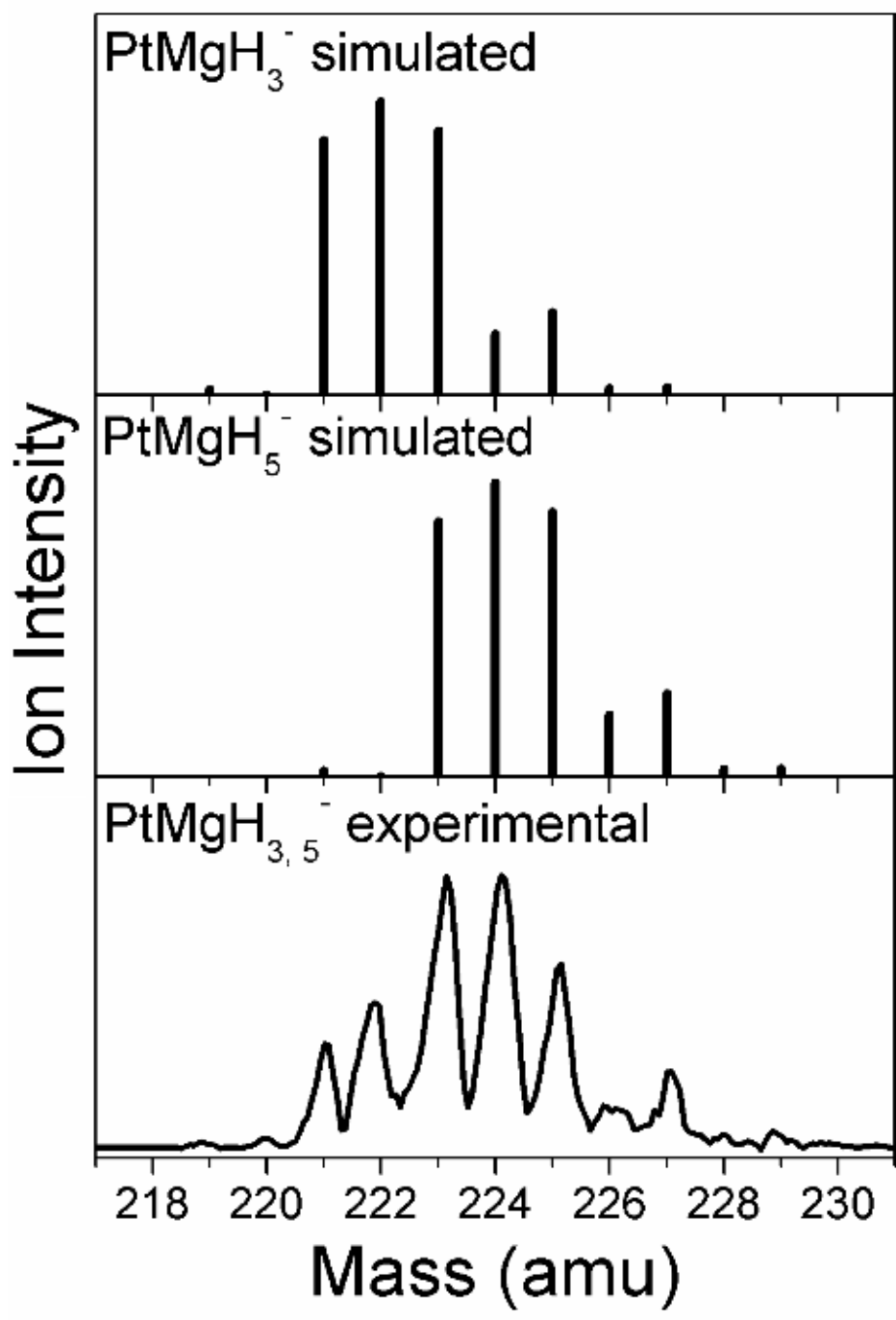
Figure 1.3.1
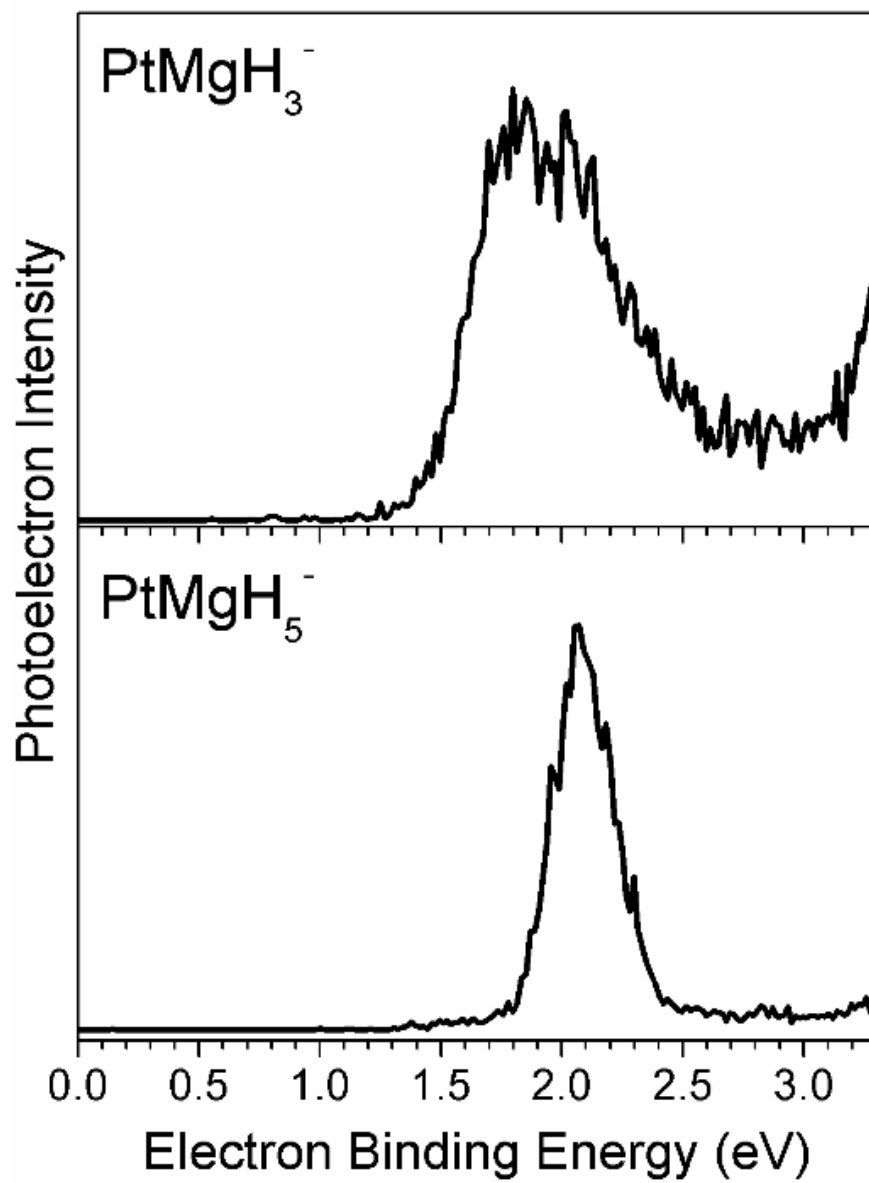
Figure 1.3.2
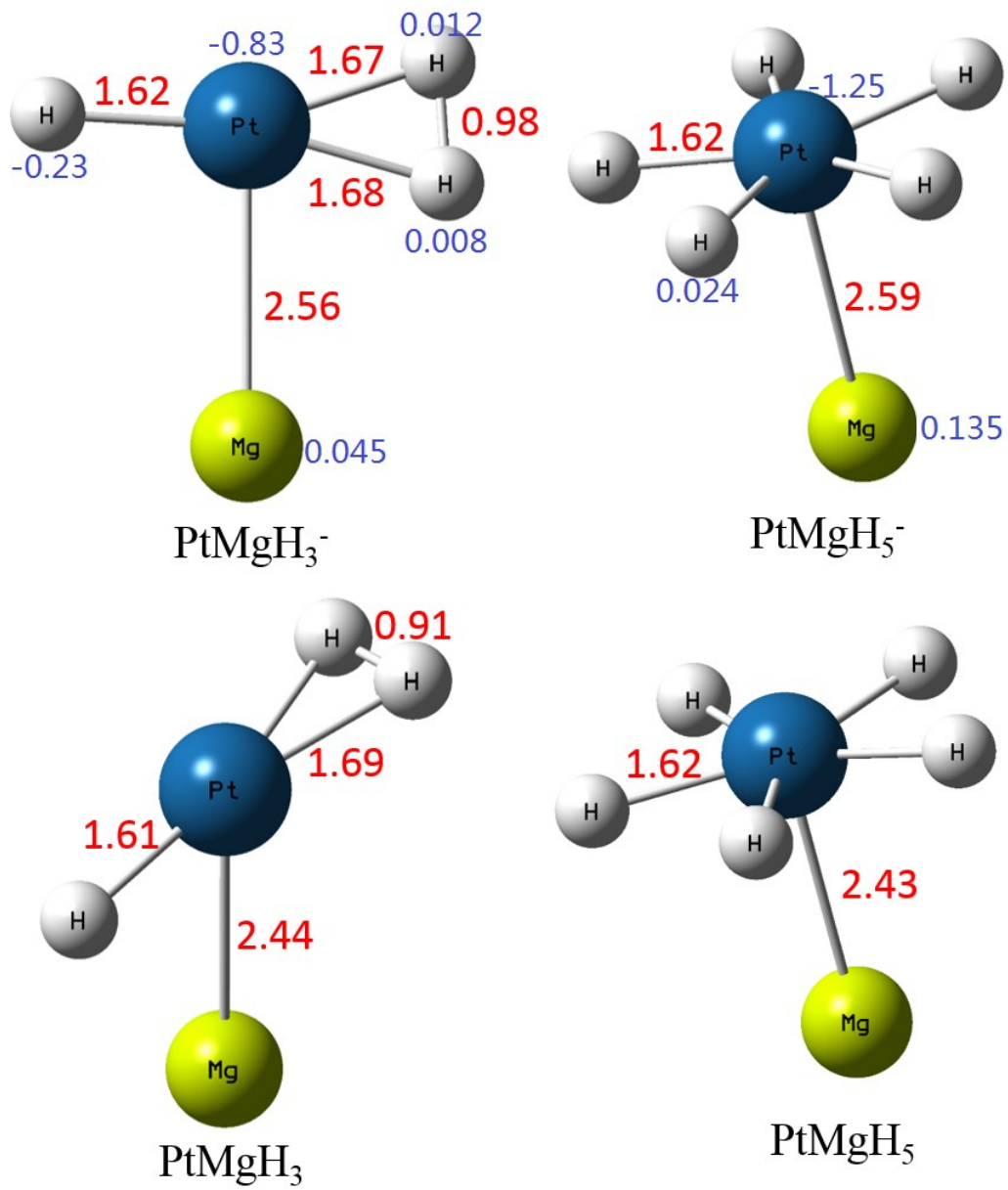
Figure 1.3.3
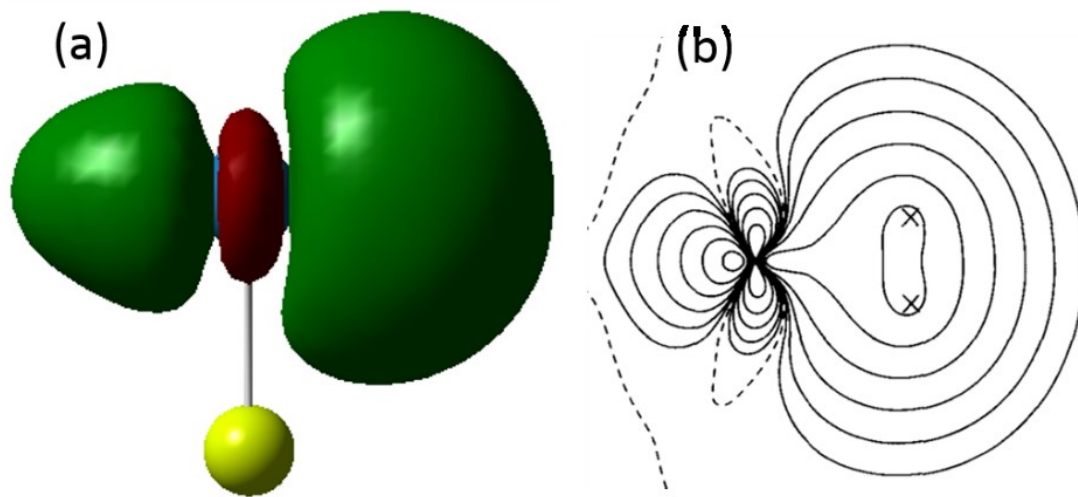
Figure 1.3.4
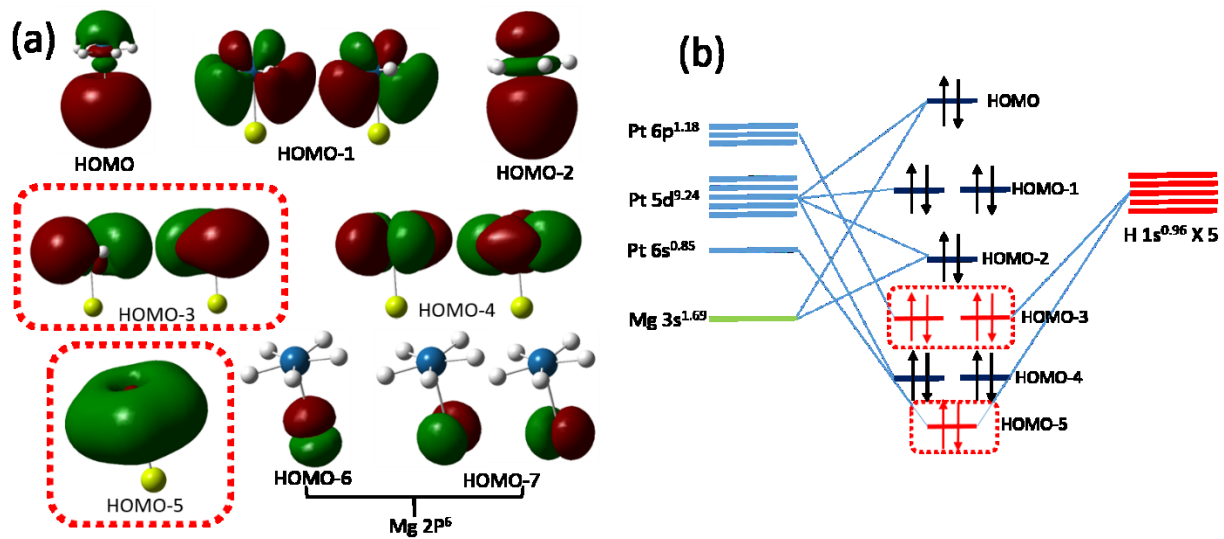
Figure 1.3.5

1.4 Photoelectron Spectroscopic Study of Other Transition Metal Hydride Cluster Anions

Xinxing Zhang and Kit Bowen

Introduction

In this section, experimental results of some transition metal hydride cluster anions which have not been interpreted will be presented. TM hydrides cluster anion is a gold mine (platinum mine, palladium mine…) worth exploiting. With our unique pulsed arc cluster ion source, these experiments can be easily done. After my opening this set of experiments, I hope that more experiments can be done in the future.

Figure Captions

Figure 1.4.1. Mass spectrum and photoelectron spectra of PtH_n^- (n = 0-3, 5). Please note that there is photon-induced dissociation involved in the PES. Therefore, each PES peak is marked by the number of H atoms in order to clarify its origin. PtH_5^- is similar to $PtZnH_5^-$ in which H_5^- shows sigma aromaticity. PtH_5^- has a planar pentagon structure. PtH_3^- is similar to PdH_3^- which has η^2-H_2 type of bond.

Figure 1.4.2. Mass spectrum and photoelectron spectra of $PdAlH_5^-$.

Figure 1.4.3. Mass spectrum and photoelectron spectra of $PdBH_5^-$.

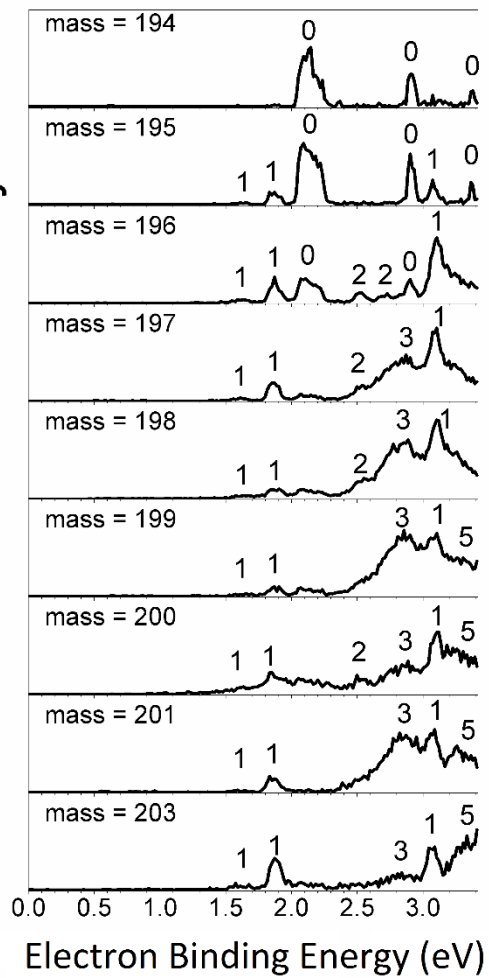Figure 1.4.4. PES of $PtMg_{1-3}H_5^-$. The calculated structure is embedded.
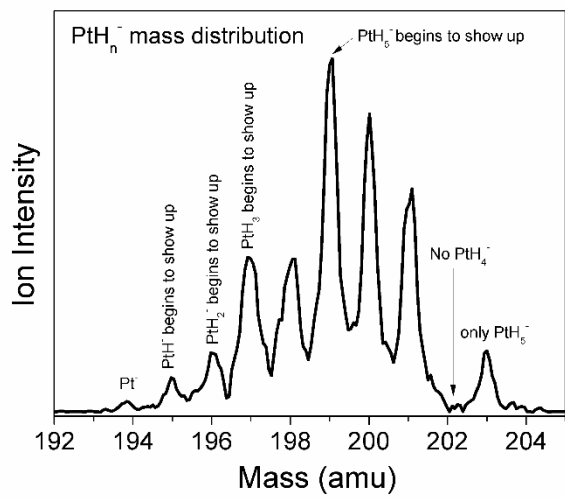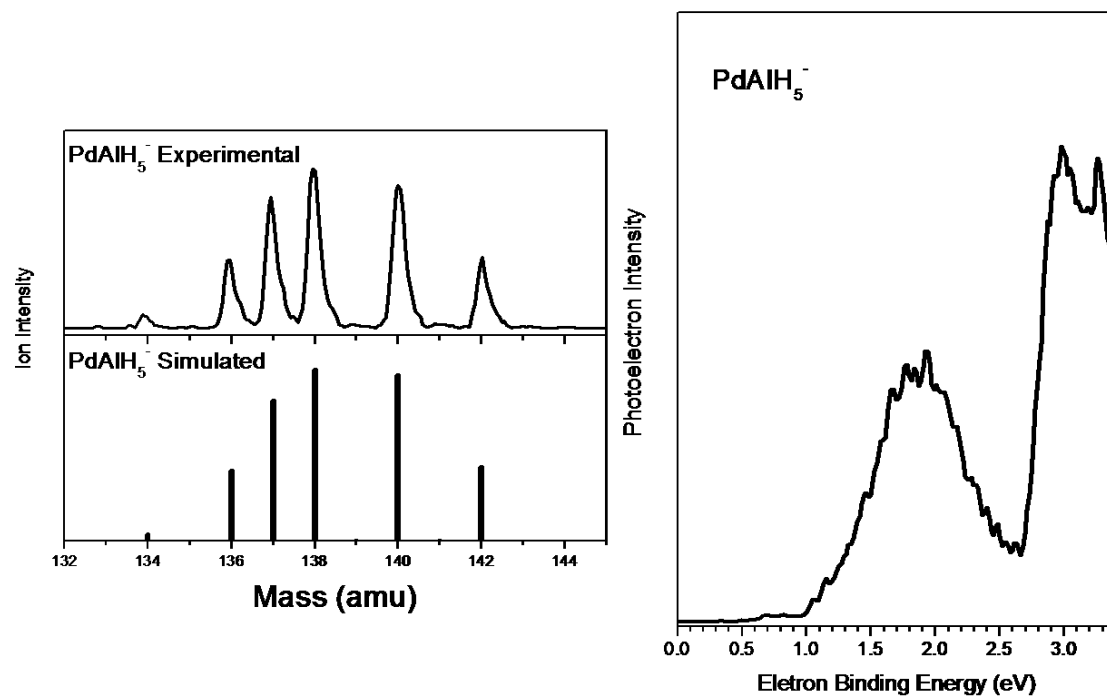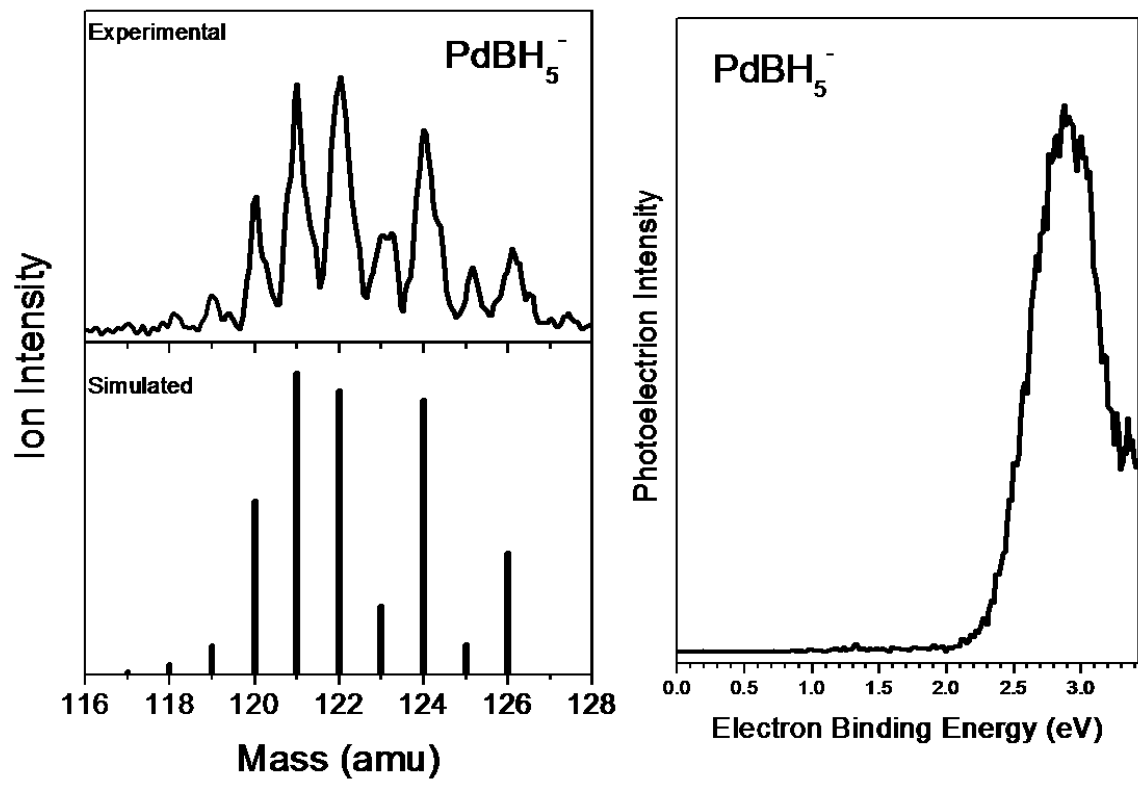
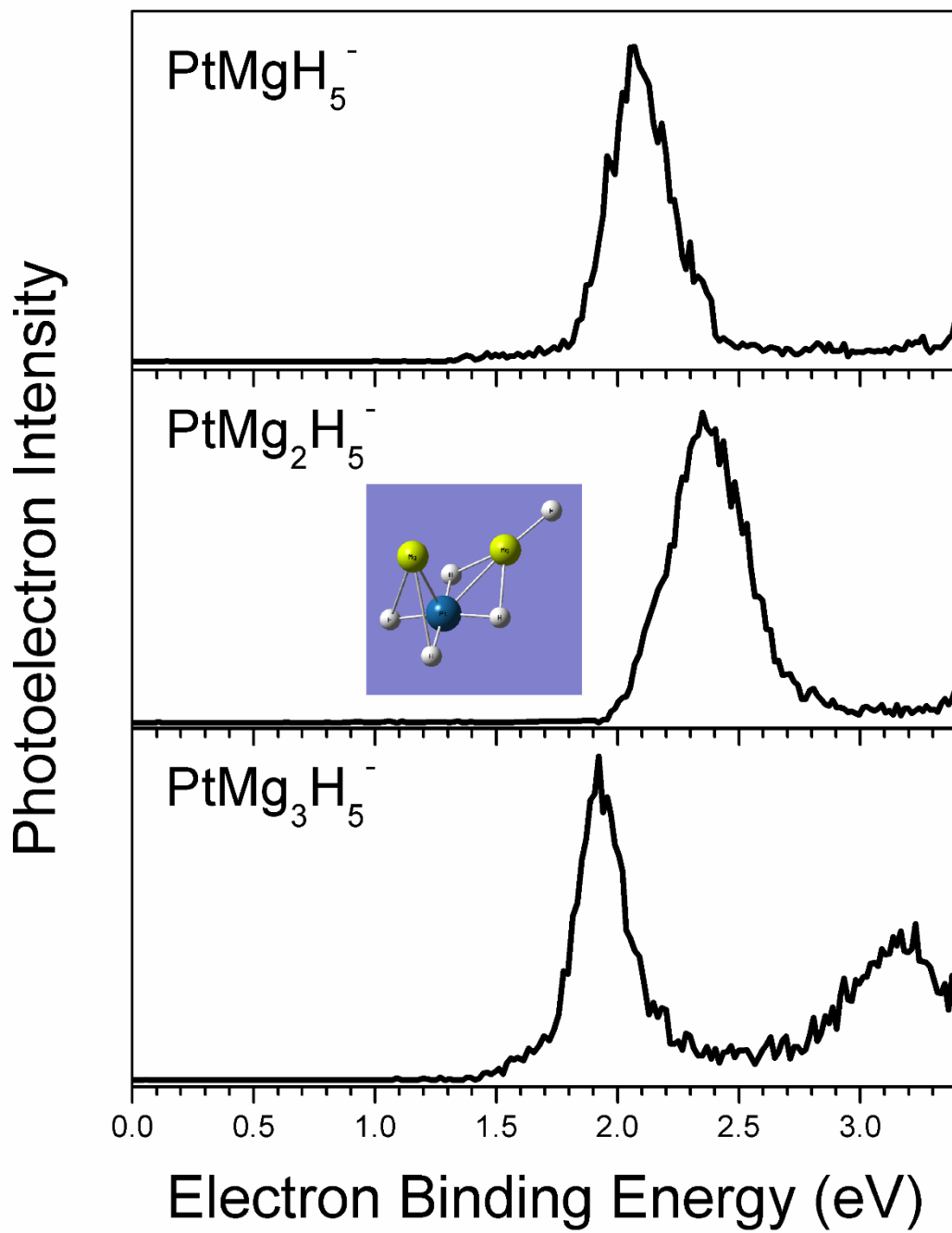Figure 1.4.1

Figure 1.4.2

Figure 1.4.3

Figure 1.4.4

CHAPTER 2. Reactions between Cluster Anion Beam and Neutral Molecules: The Utilization of a Reaction Cell

By inserting a reaction cell between the ion sources and the Wiley-McLaren region of the TOF mass spectrometer, various reactions between different cluster anions and neutral molecules were studied.

In section 2.1, the reaction between oxygen and aluminum hydride cluster anions, and the reaction between oxygen and boron aluminum hydride cluster anions are reported. Unlike boranes which cannot be burnt thoroughly due to the formation of stable HOBO-type products, aluminum hydride and boron aluminum hydride cluster anions showed very good properties in the oxidation reactions with O_2. The results are pointing towards the direction that these cluster anions can be developed as excellent energetic materials.

In section 2.2, the reaction between aluminum hydride cluster anions and a commonly used ligand Cp*H is reported. From this reaction, several low oxidation state Al containing clusters were observed for the first time.

In section 2.3, reactions between aluminum hydride cluster anions and several other ligands are presented. However, there is no detailed interpretation in this section yet.

2.1 Oxidative Reactions of Aluminum Hydride Cluster Anions and Boron Aluminum Hydride Cluster Anions

Xinxing Zhang, [1] Haopeng Wang, [1] Gerd Ganteför, [2] Bryan W. Eichhorn, [3] Hansgeorg

Schnoeckel, [4] and Kit Bowen[1]*

[1] *Department of Chemistry, Johns Hopkins University, Baltimore, MD 21218*

[2]*Facultat für Physik, Universität Konstanz, 78457 Konstanz, Germany*

[3] *Department of Chemistry, University of Maryland at College Park, College Park, MD 20742*

[4] *Institute of Inorganic Chemistry and Center for Functional Nanostructures, Karlsruhe Institute*

of Technology 76128 Karlsruhe, Germany

*Electronic mail: kbowen@jhu.edu

Abstract

The reactions between aluminum hydride cluster anions and oxygen, boron aluminum hydride cluster anions and oxygen are reported in this paper. Both the anionic reactants and anionic products were identified by time-of-flight mass spectrometer. Some of the products were also calculated by density functional theory. Unlike the boranes which cannot be burnt completely due to the "HOBO problem", most of the products in this study were fully oxidized clusters. Only two major HOBO-type products, $H_2AlO_4^-$ and $HAl_2O_4^-$ were observed, but their intensities were very low. Therefore, both aluminum hydrides and boron aluminum hydrides have potential applications to be excellent energetic materials.

Introduction

One potential application for the large variety of boranes [1-3] is utilizing them as energetic materials [4-13] such as rocket propellants and explosives. However, the highly exothermic reaction, for example, $B_2H_6 + 3O_2 \rightarrow B_2O_3$ (s) $+ 3H_2O$ (g); $\Delta H^0{}_{298}= -482.9$ kcal [14] cannot be achieved due to the stable hydrogen-containing compounds formed during the combustion. Therefore, the actual energy released in the reaction is much lower than the full oxidation process. For instance, J. F. Ditter *et al.* reported that the oxidation of pentaborane produced stable H, B, O containing products,[4] among which $H_2B_2O_3$ showed the highest intensity. As the second intense product, HBO_2 (or HOBO)'s intensity was 54.8% of that of $H_2B_2O_3$, and the intensity of B_2O_3 was only 11.1%. W. Bauer *et al.* also observed that the oxidation products of pentaborane were HBO, HOBO, and $H_2B_2O_3$.[5] H. C. Baden and coworkers' research reported that the slow oxidation of pentaborane formed diborane, hydrogen, and a white solid which could be HOBO or B_2O_3.[6] A. T. Whatley *et al.* claimed that in the oxidation of diborane, "a pyrolysis product is normally involved."[7] W. Roth *et al.*'s research on the oxidation of diborane also showed that HOBO was the main product.[8] The oxidation mechanism was proposed as a chain reaction,[9] and the step that forms HOBO was the chain breaking step, which suggested that HOBO stops the reaction. In sum, boranes never reached a major impact as energetic materials due to this "HOBO problem".

As boron's sister element, aluminum, both its micron-sized particles and nanoparticles have been used as energetic materials because of the high combustion enthalpy.[15-19] More interestingly, aluminum hydrides ("alane"), with the formula of AlH_3, seem to work even better than aluminum. The specific impulse of an AP/HTPB rocket propellant filled with alane was calculated to be 100 N s kg^{-1} higher compared to the same concentration of aluminum.[20] Furthermore, the flame temperature of alane-containing propellants was 15% lower than that of

aluminum-containing propellants, resulting in a lower need for thermal protection of the rocket. [21]The mechanism of alane combustion was proposed as follows: $AlH_3 \rightarrow Al + 3/2\ H_2$ (dehydrogenation), $Al + 3/4O_2 \rightarrow 1/2Al_2O_3$ (oxidation).[22] The hydrogen release temperature was 650K and the starting ignition temperature was 933K, even lower than the aluminum melting point. [21] More importantly, the combustion of alanes does not have the "HOBO problem". However, because of the difficulty of obtaining high grade sample, alane does not have significant application yet. Alane has been the only aluminum hydride that is ever studied in the field of combustion. The studies of other aluminum hydrides' oxidation behavior are scarce. Al_4H_6 cluster was proven to have unexpected stability, and the heat of combustion of resulting in Al_2O_3 and water was calculated to be 438 kcal/mol, ~2.6 times greater than that of methane.[23] P. J. Roach *et al.* studied the oxidation behavior of $Al_4H_x^-$ cluster anions and observed that the clusters with an even number of hydrogen atoms had higher reactivity,[24] but no products were shown in that work. Since 2007, our group has discovered hundreds of aluminum hydride cluster anions ($Al_xH_y^-$) generated by the pulsed arc cluster ionization source (PACIS).[23, 25-30] Therefore, it would be very interesting to investigate that whether or not these aluminum hydrides can be fully oxidized to aluminum oxides and bypass the borane counterparts' HOBO problem. Other than aluminum hydride cluster anions, we also produced around 80 new boron aluminum hydride cluster anions, [31] therefore, another interesting question is that can boron aluminum hydrides also bypass the HOBO problem due to the presence of aluminum?

In the present paper, we report the reactions between aluminum hydride cluster anions ($Al_xH_y^-$) and pure oxygen, boron aluminum hydride cluster anions ($B_xAl_yH_z^-$) and pure oxygen using a reaction cell attached to our PACIS source. In both cases, we observed various oxidation

products $Al_xO_y^-$ in the mass spectrum. Unlike the HOBO problem, almost all the clusters can be fully oxidized. Only very few hydrogen containing products were observed.

Methods

Experimental

Aluminum hydride and boron aluminum hydride cluster anions were generated by a pulsed arc cluster ionization source (PACIS), which has been described in detail elsewhere.[32] In brief, a ~30 μs long 150 V electrical pulse applied across anode and sample cathode of the discharging chamber vaporizes the sample atoms and forms plasma. In this case, the sample cathode is a 0.5" diameter pure Al rod or a boron and aluminum powder mixture firmly pressed onto an Al rod. About 200 psi of ultrahigh purity hydrogen gas was then injected into the arc region by the first pulsed valve, broken into H atoms and then flushed the plasma mix down in a 3 cm flow tube, where it reacted, formed clusters and cooled.

Anions generated by this method then passed through a 2 mm-wide gap and entered the reaction cell. The reaction cell is a 10 cm long, 1 cm diameter tube. On both ends of the cell, there is a small aperture that is 2 mm in diameter. The small apertures were used to contain a relatively high concentration of oxygen and to prevent the back flow of oxygen. 50 Psi of pure oxygen was injected by a second pulsed valve from the side of the reaction cell. The amount of oxygen injected was controlled by changing the firing period of the pulsed valve in each pulse. The resultant reactants $Al_xH_y^-$, $B_xAl_yH_z^-$ and the reaction products were further identified by time-of-flight mass spectrometer.

Theoretical

Density functional theory calculations were conducted by applying Becke's three-parameter hybrid functional (B3LYP)[21-23] using the Gaussian09 software package[24] to determine the geometries of anionic $H_2AlO_4^-$ and $HAl_2O_4^-$. All geometries were fully optimized using the 6-311++G (3df, 3pd) basis set. The vertical detachment energy is the energy difference between the ground state of the anion and the neutral with the same structure as the anion.

Results

The resultant mass spectra of aluminum hydride cluster anions and their oxidation products are shown in Figure 2.1.1(a) and 2.1.1(b), respectively. Figure 2.1.1(a) presents the typical mass spectrum of $Al_xH_y^-$ where x = 2 - 7, y ranges from 0 to different numbers. This spectrum was repeated many times, and we are very confident that there is no contamination especially no aluminum oxides. Figure 2.1.1(b) shows the mass spectrum after adding a small amount of oxygen into the reaction cell. A lot of products showed up, such as AlO^-, AlO_2^-, $H_{0-2}AlO_3^-$, $H_{0,1}Al_2O_2^-$, $H_2AlO_4^-$, $H_{0,1}Al_2O_3^-$, $H_{0,1}Al_2O_4^-$, $Al_3O_3^-$, $Al_2O_5^-$, $Al_3O_5^-$, in which $Al_3O_3^-$ is the most intense. We set the intensity of $Al_3O_3^-$ as 100%, and the relative intensities of all the rest products are tabulated in Table 2.1.1. This spectrum has been repeated many times, and the relative intensities of these products are consistent in these repeated experiments. The other unmarked peaks are the unreacted aluminum hydride cluster anions, all of which have very low intensity. In Table 2.1.1, the most abundant HOBO-type products are $H_2AlO_4^-$ and $HAl_2O_4^-$, which are only 19.0% and 12.3% of the major product, respectively.

Similarly, Figure 2.1.2(a) and 2.1.2(b) present the mass spectra of boron aluminum hydride cluster anions and their oxidation products. Figure 2.1.2(a) shows the coexistence of $Al_xH_y^-$ and $B_{2,3}Al_yH_z^-$. The details of these boron aluminum cluster anions are described in Ref. 31. $B_{2,3}Al_yH_z^-$

are the dominant peaks in Figure 2.1.2(a). Because of the aluminum hydride cluster anions in the ion beam, despite very low intensity, one would expect similar products as appeared in Figure 2.1.1. Figure 2.1.2(b) presents the products including cluster anions such as BO_2^-, AlO^-, AlO_2^-, $H_2AlO_4^-$, $Al_2O_3^-$, $H_{0,1}Al_2O_4^-$, $Al_3O_3^-$, $Al_2O_5^-$, $Al_3O_4^-$, $Al_3O_5^-$. Again, $Al_3O_3^-$ has the highest intensity, and the relative intensities of all of these products are shown in Table 2.1.2. All the other unmarked peaks are the unreacted clusters. The most abundant HOBO-type products are also $H_2AlO_4^-$ and $HAl_2O_4^-$, which are only 10.2% and 14.4% of the major product, respectively.

One complication is that the molar mass of ^{11}BO is the same as Al. In order to search for the existence of B, we carefully examined the presence of ^{10}B in Figure 2.1.2(b). For example, the peak at mass = 43 could be AlO^- and $^{11}BO_2^-$, but the peak at mass = 42 ($^{10}BO_2^-$) confirmed the coexistence of BO_2^- and AlO^-. The natural abundance of ^{10}B is 24.7% of that of ^{11}B. Details are shown in the imbedded spectrum in Figure 2.1.2(b). Another example, the mass of AlO_2^- is the same as $^{11}BO_3^-$, but $^{10}BO_3^-$ is not observed, so we assign the peak at mass = 59 to be pure AlO_2^-. However, some other peaks are surrounded by unreacted clusters, such as those located at mass = 93, 102, 118, 119, so we are not certain that there is no B in these clusters. We tentatively assign them to only contain Al but not B, but please note that there might be B element hidden in these peaks. The bottom line is that we did not observe any H, B, O containing clusters.

The calculated structures of the two HOBO-type cluster anions are presented in Figure 2.1.3. All the bond lengths are marked in Å. $H_2AlO_4^-$ has a tetrahedral structure, where two hydroxyl groups and a peroxide moiety are attached to the center Al atom. Its vertical detachment energy is calculated to be 3.73 eV. $HAl_2O_4^-$ is planar, two Al atoms are connected by two bridge O atoms, and the other two O atoms form radial bonds with the two Al atoms respectively. Its vertical detachment energy is calculated to be 3.78 eV.

Discussion

The major products from both reactions are aluminum oxide cluster anions, by producing which we believe that a lot of heat is released during the reaction. The electronic and geometric structures of these aluminum oxide cluster anions were reported in references 37 and 38. In BO_2^-, AlO_2^-, AlO_3^-, $Al_2O_3^-$, $Al_2O_4^-$, $Al_2O_5^-$, and $Al_3O_5^-$, both Al and B reach their highest oxidation states, +3, The most abundant product, $Al_3O_3^-$, can be viewed as $(Al_3)^{5+} (O^{2-})_3^-$,[33] in which Al is not oxidized to +3. However, it is a very stable product due to its very stable six member ring structure.

Next we discuss the two hydrogen containing products $H_2AlO_4^-$ and $HAl_2O_4^-$. In both of the clusters, the Al atom reaches the +3 oxidation state. Their vertical detachment energies are both very high, indicating the special stability. Even though these two products can be viewed as the HOBO counterparts, their intensities are much lower than those HOBO species in the borane combustion reactions. Therefore, we conclude that the oxidation reactions of aluminum hydride and boron aluminum hydride cluster anions give much better results than the boranes.

For the reactions of boron aluminum hydride cluster anions, an obvious question is that where does the B element go after the reaction? One answer is that the B atoms are in the form of neutral products, however, detecting neutral products is beyond the scope of the current study. Another possibility is that due to the mass coincidence described above (^{11}BO has the same mass as Al), it might be hidden under those peaks marked by Al. Nevertheless, our goal is that by doping aluminum to boron hydrides, we can bypass the "HOBO problem" that boranes encountered. Apparently we are not observing any HOBO related clusters in this reaction.

Conclusion

Boranes cannot be fully oxidized in combustion because of an unanticipated kinetic trap that prevented boranes from undergoing complete combustion, robbing the oxidation reaction of its full energy release. The species that terminated the reaction mechanism were various hydrogen boron oxides, known collectively as HOBO. The conventional wisdom, based on their presumed reactivity relative to boranes, is that aluminum hydride clusters/molecules would burn completely without encountering an equivalent HOBO problem. Another route is doping Al to boranes to make boron aluminum hydride, and the presence of Al would also help these compounds burn completely. In this paper, we studied the oxidation reactions of aluminum hydride and boron aluminum hydride cluster anions, and found that most of the products are aluminum oxides. Two HOBO-type products $H_2AlO_4^-$ and $HAl_2O_4^-$ were observed, however, their intensities are very low comparing to other major products. Therefore, we conclude that both aluminum hydrides and boron aluminum hydrides could potentially be excellent energetic materials.

Acknowledgement

References

1. W. N. Lipscomb, *Boron Hydrides* (W. A. Benjamin Inc., New York, 1963).

2. N. Greenwood, *A. E. Chemistry of the Elements*, 2nd ed. (Elsevier Science, Amsterdam, The Netherlands, 1997).

3. A. Stock and C. Massenez, *Ber. Dtsch. Chem. Ges.* **45,** 3539 (1912).

4. J. F. Ditter and I. Shapiro, *J. Am. Chem. Soc.* **81**, 1022 (1959).

5. W. H. Bauer and S. Wiberley, In Borax To Boranes, Advances in Chemistry American Chemical Society: Washington, DC, 1961.

6. H. C. Baden, S. E. Wiberley and W. H. Bauer, *J. Phys. Chem.* **59**, 287 (1955).

7. A. T. Whatley and R. N . Pease, *J. Am. Chem. Soc,* **76**, 1997 (1954).

8. W. Roth and W. H. Bauer, *J. Phys. Chem,* **60**, 639 (1956).

9. W. Roth, and W. H. Bauer, "Fifth Symposium on Combustion," p. 710, Reinhold, New York, 1955.

10. F. P. Price, *J. Am. Chem. Soc.* **72**, 5361 (1950).

11. H. C . Baden, W. H . Bauer and S. E. Wiberley, *J. Phys. Chem.* **62**, 331 (1958).

12. F. P. Price, *J. Am. Chem. Soc.* **73**, 2141(1951).

13. E. Gobbett and J. W. Linnett, *J. Chem. Soc.* **1962**, 2893 (1962).

14. F. D. Rossini. "Selected Values of Chemical Thermodynamic Properties," *Natl. Bur. Standards Circular No. 300* (1952).

15. A. Rai, D. Lee, K. Park, and M. R. Zachariah, *J. Phys. Chem. B* **108**, 14793 (2004).

16. A. Rai, K. Park, L. Zhou and M. R. Zachariah, *Combust. Theor. Model*. **10**, 843 (2006).

17. G. V. Ivanov, F. Tepper, *4th Int. Symp. Spec. Top. Chem. Propul*. 636 (1997).

18. C. E. Aumann, G. L. Skofronick, J. A. Martin, *J. Vac. Sci. Technol. B* **13**, 1178 (1995).

19. T. Bazyn, H. Krier, and N. Glumac, *Combust. flame*, **145**, 703 (2006).

20. V. Weiser, N. Eisenreich, A. Koleczko, E. Roth, *Propell. Explos. Pyrot*. 32, (2007).

21. G. Young, N. Piekiel, S. Chowdhury, and M. R. Zachariah, *Combust. Sci. and Tech.,* **182**, 1341 (2010).

22. T. Bazyn, R. Eyer, H. Krier, and N. Glumac, *J. Propul. Power,* **20**, 427 (2004).

23. X. Li, A. Grubisic, S. T. Stokes, J. Cordes, G. F. Gantefoer, K. H. Bowen, B. Kiran, M. Willis, P. Jena, R. Burgert, and H. Schnoeckel, *Science* **315**, 356 (2007).

24. P. J. Roach, A. C. Reber, W. H. Woodward, S. N. Khanna, and A. W. Castleman, Jr. *P. Natl. Acad. Sci.,* **104**, 14565 (2007).

25. B. Kiran, P. Jena, X. Li, A. Grubisic, S. T. Stokes, G. F. Gantefoer, K. H. Bowen, R. Burgert, and H. Schnoeckel, *Phys. Rev. Lett.* **98,** 256802/1 (2007).

26. A. Grubisic, X. Li, G. F. Gantefoer, K. H. Bowen, B. Kiran, P. Jena, R. Burgert, and H. Schnoeckel, *J. Am. Chem. Soc.* **129,** 5969 (2007).

27. A. Grubisic, X. Li, S. T. Stokes, K. Vetter, G. F. Gantefoer, K. H. Bowen, P. Jena, B. Kiran, R. Burgert, and H. Schnockel, *J. Chem. Phys*. **131,** 121103 (2009).

28. X. Li, A. Grubisic, K. H. Bowen, A. K. Kandalam, B. Kiran, G. F. Gantefoer, and P. Jena, *J. Chem. Phys*. **132,** 241103 (2010).

29. X. Zhang, H. Wang, E. Collins, A. Lim, G. Ganteför, B. Kiran, H.Schnöckel, B. Eichhorn, and K.H. Bowen , *J. Chem. Phys.* **138**, 124303 (2013).

30. J. D. Graham , A. M. Buytendyk , X. Zhang , E. L. Collins , K. Boggavarapu , G. Gantefoer , B. W. Eichhorn , G. L. Gutsev , S. Behera , P. Jena , and K. H. Bowen, *J. Phys. Chem. A,* **118**, 8158 (2014).

31. H. Wang, X. Zhang, Y. Ko, G. F. Ganteför, K. H. Bowen, X. Li, K. Boggavarapu, and A. Kandalam , *J. Chem. Phys.* **140**, 164317 (2014).

32. X. Zhang, Y.Wang, H. Wang,A. Lim,G. Ganteför, K.H. Bowen,J. U. Reveles, and S. N. Khanna, *J. Am. Chem. Soc.,* **135**, 4856 (2013).

33. A. D. Becke, *Phys. Rev. A* **38,** 3098 (1988).

34. A. D. Becke, *J. Chem. Phys.* **98,** 5648 (1993).

35. C. Lee, W. Yang and R. G. Parr, *Phys. Rev. B* **37,** 785 (1988).

36. M. J. Risch, G. W. Trucks, H. B. Schlegel, G. E. Scuseria, M. A. Robb, J. R. Cheeseman, G. Scalmani, V. Barone, B. Mennucci, G. A. Petersson, et al. Gaussian 09, revision A.1; Gaussian, Inc.:Wallingford, CT, 2009

37. H. Wu, X. Li, X. Wang, C. Ding, and L. Wang, *J. Chem. Phys.,***109**, 449 (1998).

38. S. R. Desai, H. Wu, C. M. Rohlfing,and L. Wang, *J. Chem. Phys.,***106**, 1309 (1997).

Table 2.1.1. The relative intensities of the major products from the reaction between aluminum cluster anions and oxygen. The intensity of $Al_3O_3^-$ is set to be 100%.

Species	Mass (amu)	Relative Intensity (100%)
$Al_3O_3^-$	129	100.0
AlO_2^-	59	43.9
$H_2AlO_4^-$	93	19.0
$Al_2O_5^-$	134	17.9
$Al_2O_3^-$	102	13.1
$HAl_2O_4^-$	119	12.3
$Al_3O_5^-$	161	9.2
$HAl_2O_2^-$	87	6.4
$Al_2O_2^-$	86	5.0
$HAl_2O_3^-$	103	4.8
$H_2AlO_3^-$	77	3.9
$Al_2O_4^-$	118	3.6
AlO_3^-	75	2.2
$HAlO_3^-$	76	2.0
AlO^-	43	1.1

Table 2.1.2. The relative intensities of the major products from the reaction between boron aluminum cluster anions and oxygen. The intensity of $Al_3O_3^-$ is set to be 100%.

Species	Mass (amu)	Relative Intensity (100%)
$Al_3O_3^-$	129	100.0
$Al_2O_5^-$	134	58.2
AlO_2^-	59	56.4
$Al_3O_5^-$	161	28.4
$Al_2O_3^-$	102	26.1
$HAl_2O_4^-$	119	14.4
$Al_2O_4^-$	118	13.7
$Al_3O_4^-$	145	13.3
$H_2AlO_4^-$	93	10.2
AlO^-	43	3.2
BO_2^-	42 and 43	2.9

Figure Captions

Figure 2.1.1. Typical mass spectrum of $Al_xH_y^-$ (a) and their oxidation products (b).

Figure 2.1.2. Typical mass spectrum of $B_xAl_yH_z^-$ (a) and their oxidation products (b). The embedded spectrum in Figure 2(b) shows the coexistence of BO_2^- and AlO^-.

Figure 2.1.3. Calculated structures of $H_2AlO_4^-$ and $HAl_2O_4^-$. All the bond lengths are marked in Å.
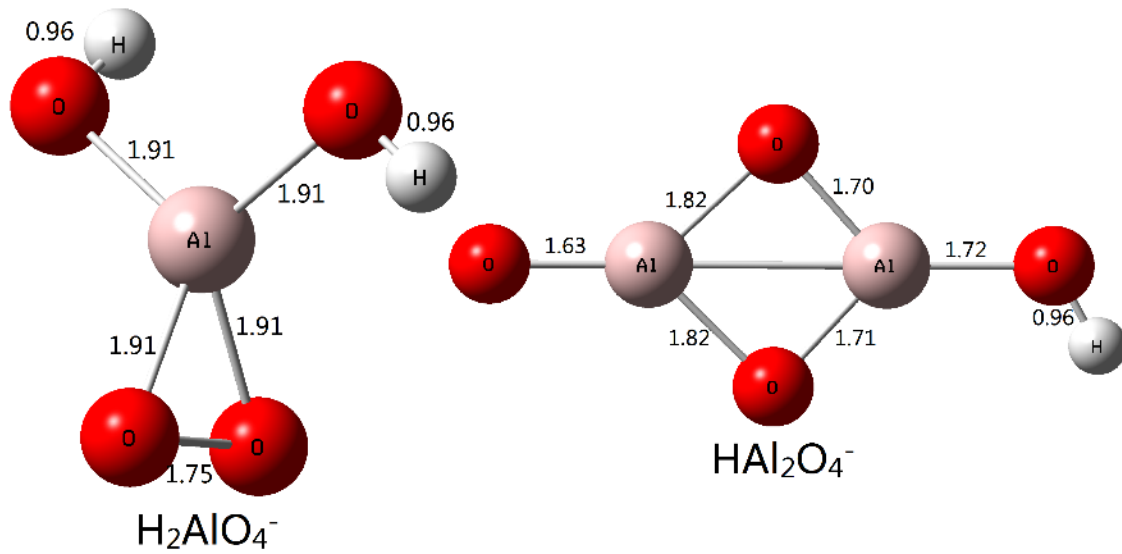
Figure 2.1.1

85
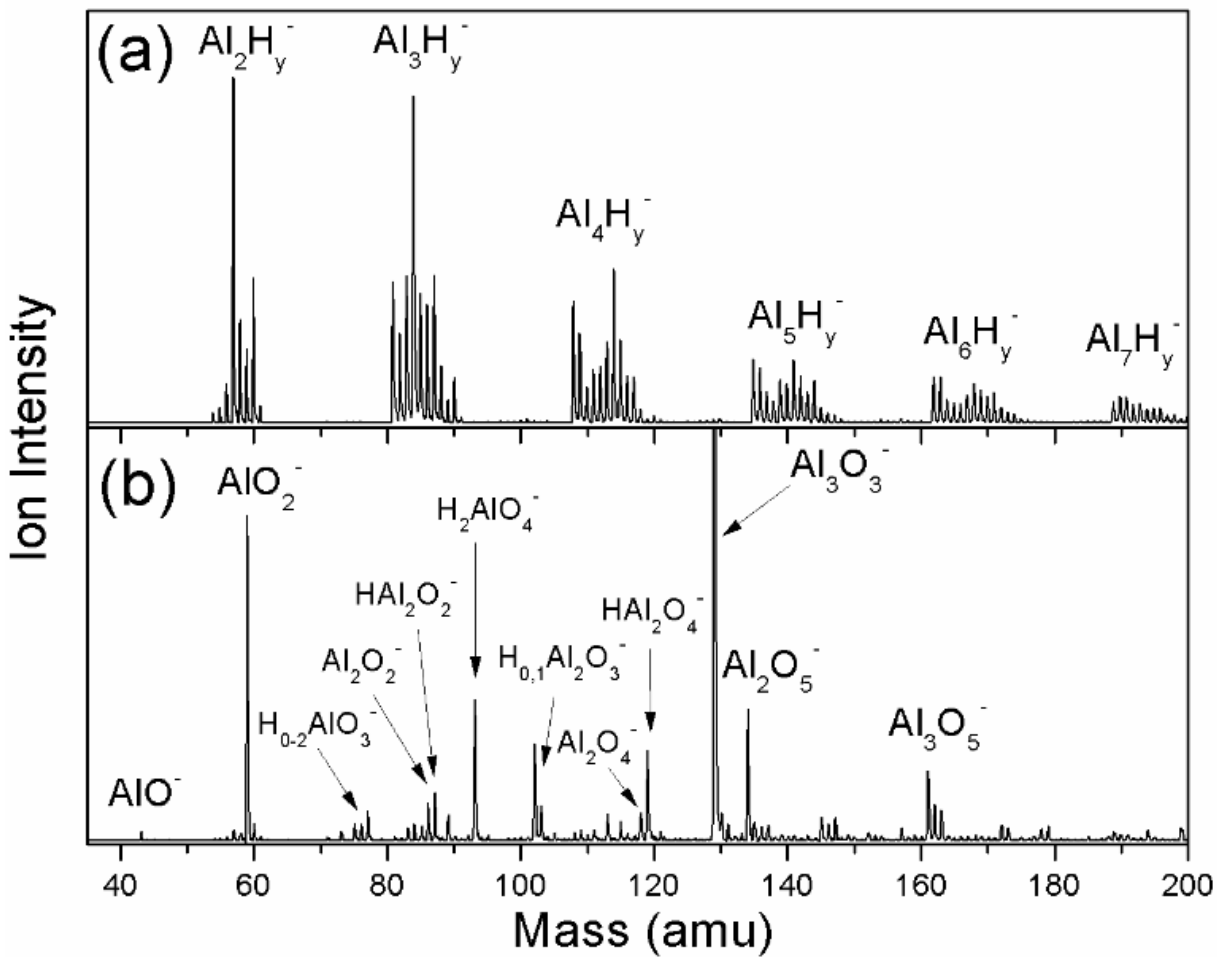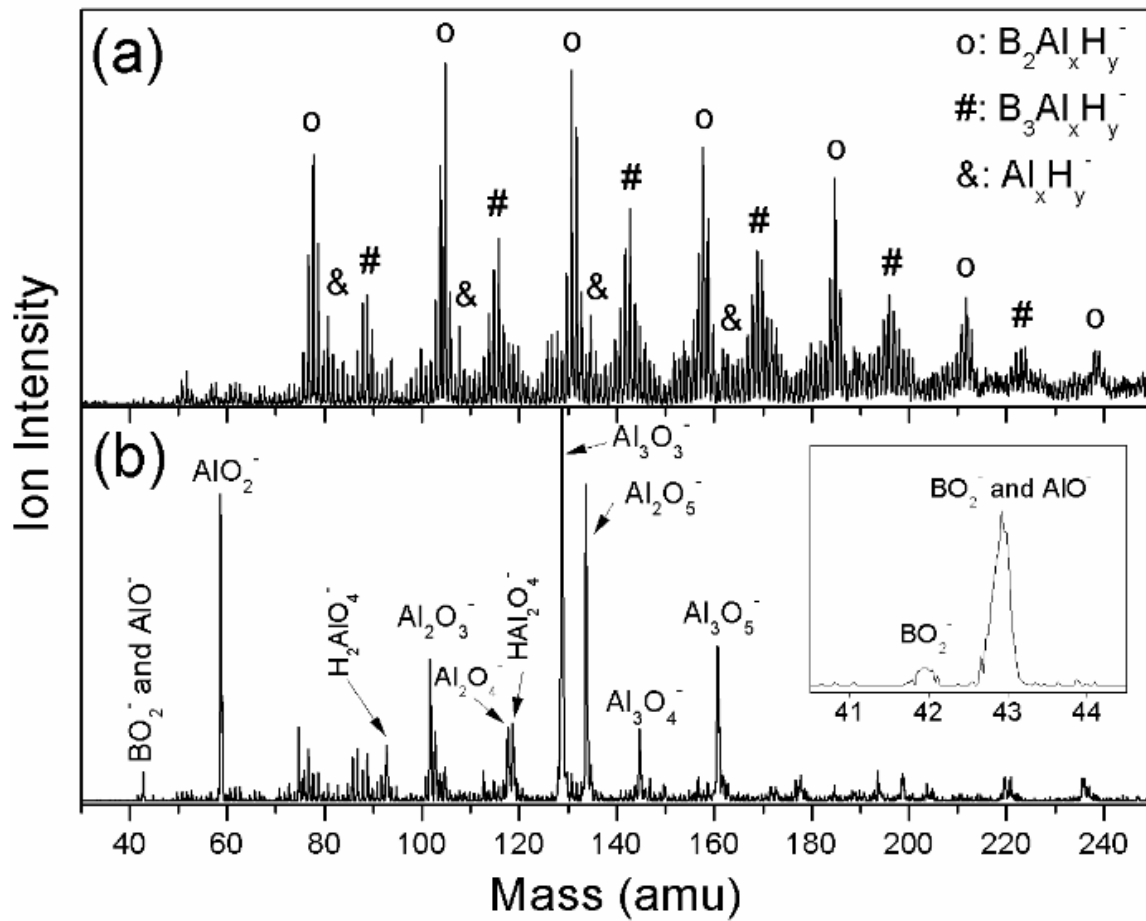
Figure 2.1.2

Figure 2.1.3

2.2 The Reaction between Aluminum Hydride Cluster Anions and Cp*H: Production of New Low Oxidation State Al Clusters

Xinxing Zhang, [1] Dennis H. Mayo, [2,3] Byran Eichhorn,[2] William. H. Sawyer[4], Ann F. Gill,[4] Anil K. Kandalam[4], and Kit Bowen[1*]

[1] *Department of Chemistry, Johns Hopkins University, Baltimore, MD 21218*

[2] *Department of Chemistry, University of Maryland at College Park, College Park, MD 20742*

[3] *Research Department, Indian Head EOD Technology Division, Naval Surface Warfare Center, Indian Head, MD 20640, USA*

[4]*Department of Physics, West Chester University of PA, West Chester, PA 19383*

* Corresponding author: kbowen@jhu.edu

Phone: 001-410-516-8425

Abstract

Three new low oxidation state Al containing cluster anions, $Cp*Al_{1-3}H^-$, have been produced via the reaction between aluminum hydride cluster anions and Cp*H and characterized by mass spectrometry and photoelectron spectroscopy. The structures, electron affinities (EAs) and vertical detachment energies (VDEs) were obtained by density functional theory (DFT) based calculations and compared with experimental values. Good agreement was found. The reactions open up a new path of synthesizing ligand-protected, low oxidation state Al clusters, which may further be utilized as novel energetic materials.

Introduction

In recent years aluminum chemistry has experienced a renaissance as a result of an increased interest in the reactivity of its low oxidation state.[1, 2] Since Schnöckel first synthesized a metastable AlCl solution and its solid more than 30 years ago, [3,4] AlCl has become the basis from which a variety of aluminum containing compounds have been synthesized.[1-2, 5-13] Among these there is a fascinating cluster $(Cp^*Al)_4$ (Cp^* = pentamethylcyclopentadienyl) which was obtained from the reaction of an AlCl solution and Cp^*_2Mg. [11-13] $(Cp^*Al)_4$ has a unique chemistry resulting from its +1 oxidation state.[14-23] It dissociates into monomeric Cp^*Al in both solution and gas phase.[14] This monomer has a lone pair of electrons on the Al side so it can be used as a ligand in transition metal complexes. [16-20] $(Cp^*Al)_4$ can also react with main group element compounds to form clusters with different structures, such as rings and cages.[21-23]

Historically $(Cp^*Al)_4$ has been the most studied but not the only cluster that contains Al-Cp^*. An Al-rich metalloid cluster $Al_{50}Cp^*_{12}$ was prepared using AlBr as precursor. [24] Its energy content was calculated by Hooper and his coworkers to estimate its potential as an energetic material.[25] When $(Cp^*Al)_4$ was used in a series of MALDI experiments another Al-rich cluster $Al_8Cp^*_4$ was observed. [26] Additionally, $[Cp^*AlH_2]_3$ and Cp^*_2AlH were prepared and used to react with Cp^*H to form Cp^*Al. [27]

In the present work, we extend the Al-Cp^* study into the gas phase. We report the formation and the anion photoelectron spectroscopy of three new cluster anions: $Cp^*Al_{1-3}H^-$ resulting from a reaction cell experiment using aluminum hydride cluster anions $Al_xH_y^-$ and Cp^*H. Density functional theory (DFT) based calculations were carried out on neutral and negatively charged Cp^*AlH and Cp^*Al_2H systems to identify their lowest energy structures. The calculated

vertical detachment energies (VDE) and adiabatic detachment energies (ADE) were compared to the corresponding measured values.

Methods

Experimental

Aluminum hydrides were generated by a pulsed arc cluster ionization source (PACIS), which has been described in detail elsewhere.[28] In brief, a ~30 μs long 150 V electrical pulse was applied between the anode and the sample cathode of the discharging chamber vaporizing the aluminum atoms and forming plasma. In this case, the sample cathode was a 0.5" diameter pure aluminum rod. About 200 psi of ultrahigh purity hydrogen gas was then injected into the arc region by the first pulsed valve. The flowing hydrogen, dissociated in the plasma, flushed the aluminum, H plasma mix into a 3 cm flow tube, where it reacted, formed clusters and cooled.

Anions generated by this method then passed through a 5 mm-wide gap and entered the reaction cell. The reaction cell was a 10 cm long, 1 cm diameter tube. On both ends of the cell, there was a small aperture 2 mm in diameter. These apertures were used to contain a higher concentration of the reactant and to prevent the back flow of the Cp*H. 50 Psi of ultra high purity Cp*H seeded He was injected through an aperture in the side of the reaction cell using a second pulsed valve. The side aperture was mounted on the downstream end of the cell in order to reduce the probability of black flow. The amount of Cp*H injected into the cell was controlled by varying the valve's pulse duration from 50 μs to 250 μs The resulting $Al_xH_y^-$ and the reaction products were further identified by time-of-flight mass spectrometry followed by photoelectron spectrometry.

Anion photoelectron spectroscopy is conducted by crossing a mass-selected, negative ion beam with a fixed-energy photon beam and analyzing the energies of the resultant photo-detached electrons. This technique is governed by the well-known energy-conserving relationship, hv=EBE+EKE, where hv, EBE, and EKE are the photon energy, electron binding energy (transition energy), and the electron kinetic energy, respectively.

Our photoelectron instruments, which have been described elsewhere, [29] consist of an ion source, a linear time-of- flight mass spectrometer, a mass gate, a momentum decelerator, a neodymium-doped yttrium aluminum garnet (Nd:YAG) laser operated in the third harmonic (355 nm) for photodetachment, and a magnetic bottle electron energy analyzer with a resolution of 35 meV at EKE=1 eV. The photoelectron spectra were calibrated against the well-known photoelectron spectrum of Cu^-. [30]

Theoretical

The lowest energy structures of neutral and negatively charged $Cp^*Al_{1-3}H$ systems were obtained by density functional theory (DFT) based electronic structure calculations. The gradient corrected Becke's exchange[31] functional combined with Perdew-Wang correlation[32] functional (BPW91), along with 6-311+G** basis set was used for all the calculations. All of the calculations were carried out using the Gaussian 09 software package[33]. Several structural configurations of neutral and anionic $Cp^*Al_{1-3}H$ were optimized without any symmetry constraints. In the geometry optimization procedure, the convergence criterion for energy was set to 10^{-9} Hartree, while the gradient was converged to 10^{-4} hartree/Å. The reliability and accuracy of the functional form used in this study in predicting the lowest energy structures of metal organic systems has been established in our earlier studies on metal-organic complexes [34-38].

The vertical detachment energies (VDE) and the higher energy transitions obtained from the theoretical calculations were compared with the corresponding measured values. The vertical detachment energy (VDE) is the energy between the ground state anion and its corresponding neutral at the geometry of the anion. The calculated adiabatic detachment energy (ADE) of the lowest energy isomers of anion were also compared to the onset (threshold) region of the lowest electron binding energy of the PES spectrum. The ADE is calculated as the energy difference between the lowest energy geometry of the anionic cluster and the structurally similar/identical isomer (nearest local minimum) of its neutral counterpart.

Results and Discussion

Figure 2.2.1 (a) and (b) present the anion mass spectra before and after a reaction. In Figure 2.2.1 (a), several homologous aluminum hydride cluster series are observed, i.e., those based on 2-8 aluminum atoms per cluster. After pulsing the second valve to inject Cp*H seeded He into the reaction cell we observed the spectrum presented in Figure 2.2.1 (b); here a small amount of unreacted aluminum hydride clusters can still be seen together with three high intensity product peaks. After careful mass coincidence examination, we determined the three peaks to be $Cp*Al_{1-3}H^-$. Unit mass resolution was attained for all the species we studied.

In Figure 2.2.2 (a), (b), and (c), we present the photoelectron spectra (PES) of $Cp*Al_{1-3}H^-$ respectively taken with a 3.49 eV laser. The EBE value corresponding to the intensity maximum in the observed band is its vertical detachment energy, VDE, the transition energy at which the Franck Condon overlap between the wave functions of the anion and its neutral counterpart is maximal. The electron affinity, EA, is the energy difference between the lowest energy state of the anion and the lowest energy state of its neutral counterpart. When significant Franck-Condon overlap exists between $v = 0$ of the anion and $v' = 0$ of its corresponding neutral (the origin

transition) and when no vibrational hot bands (photoelectrons from vibrationally excited anions) are present, the EA value corresponds to the EBE of the intensity threshold. Therefore, we assign the EA values by extrapolating the low EBE side of each band to zero. All the experimental and theoretical VDE and ADE/EA values are tabulated in Table 2.2.1.

The spectrum of Cp*AlH⁻ (Figure 2.2.2 (a)) begins with a broad band between 1.0 and 2.0 eV of EBE, followed by several smaller peaks at higher EBE values. The EA value of Cp*AlH is estimated to be 1.0 ± 0.1 eV, while the VDE of Cp*AlH⁻, the EBE of the intensity maximum in the lowest EBE band, is 1.6 ± 0.1 eV. The calculated ground state structure of Cp*AlH⁻ is shown in Figure 2.2.3 (a). The Al atom binds to two carbon atoms (η^2 coordination) of the Cp* ring with an average Al-C bond length of 2.41 Å, while the hydrogen atom bound radially with the Al atom. The calculated VDE of this anionic structure is 1.60 eV, which is in agreement with the measured value of 1.6 ± 0.1 eV. In the case of the neutral Cp*AlH, the Al atom prefers to bind with a η^5 coordination with the carbon atoms of Cp* ring (see Figure 2.2.3(b)), with an average Al – C bond length of 2.33 Å. The η^2 coordinated structure, the ground state of anion, was not found to be a minimum on for the neutral system. The calculated EA value of Cp*AlH is 0.85 eV, which is in agreement with the measured value. The large difference between EA and VDE values of this system can be attribute to the differences in the Al atom coordination with the Cp* ring.

The PES of Cp*Al₂H⁻ (Figure 2.2.2(b)) has a broad feature between EBE = 0.8 and 1.3 eV, followed by a higher EBE broader band between 1.7 and 3.0 eV. The VDE of the Cp*Al₂H⁻ is 1.2 ± 0.1 eV. Our theoretical calculations show that there are three stable and energetically almost degenerate structures (ΔE_{max}= 0.30 eV) for Cp*Al₂H⁻ system (see Fig 2.2.3(c), (d), and (e)), with a spin multiplicity of doublet (2S+1 =2). The common structural feature among these three isomers is that the aluminum atoms dimerize, with only one of the metal atoms of the dimer interacting

directly with the Cp* ring. In the lowest energy isomer (Figure 2.2.3(a)), the proximal Al atom has η^4 coordination with the Cp* ring, while the next higher energy ($\Delta E = 0.09$ eV) isomer has η^5 coordination (Figure 2.2.3(d)), while the third isomer has η^2 coordination (Figure 2.2.3(e)). Another notable structural difference between these isomers is the interaction of hydrogen atom with the Al_2 dimer. In the lowest energy isomer (Figure 2.2.3(c)), the hydrogen atom is bound to the terminal aluminum atom with a weak interaction with the proximal aluminum atom as well, while in the second isomer (Figure 2.2.3(d)), the hydrogen atom is bound strongly to the terminal aluminum atom, whereas in the last isomer (Figure 2.2.3(e)), the hydrogen atom is bound to the proximal aluminum atom only. Since, the energy differences between these three isomers are close, we have calculated the vertical detachment energies for all three isomers. The calculated VDE values of the first isomer (Figure 2.2.3(c)), second isomer (Figure 2.2.3(d)), and the third isomers (Figure 2.2.3(e)) of $Cp*Al_2H^-$ are 1.04 eV, 0.85 eV, and 1.20 eV, respectively. Note that all these electron detachment energies correspond to transition from anionic doublet to neutral singlet state. The first low energy band in the photoelectron spectrum of $Cp*Al_2H^-$ (ranging from 0.8 eV to 1.3 eV) seems to be a result of an overlap of three peaks centered at 0.85, 1.04, and 1.20 eV. Thus, the first broad peak in the photoelectron spectrum of $Cp*Al_2H^-$ is due to the electron detachment from all three isomers (Figure 2.2.3(c) – (e)). In addition, the calculated electron detachment energies corresponding to transition from anionic doublet to neutral triplet state for the first isomer (2.54 eV), second isomer (1.78 eV), and the third isomer (1.95 eV) together are contributing towards the higher energy peak/band in the photoelectron spectrum (Figure 2.2.2) between 1.9 and 3.0 eV. Since all three isomers are contributing towards various features/bands of the photoelectron spectrum, it appears that all three isomers (Figure 2.2.3(c), (d), and (e)) are present in the anion cluster beam of $Cp*Al_2H$ system.

In the case of neutral Cp*Al$_2$H, our calculations revealed two distinct structures, which are shown in Figure 2.2.3(f) and 3(g). The lowest energy structure of neutral Cp*Al$_2$H (Figure 2.2.3(f)) consists of the aluminum dimer, with only one of the aluminum atoms directly interacting with the Cp* ring in η^5 coordination, while the hydrogen atom is bound to the terminal aluminum atom. This isomer is similar to that of the second lowest energy isomer (Figure 2.2.3(d)) of the anion. On the other hand, in the higher energy isomer ($\Delta E = 0.25$ eV), both aluminum atoms of the Al-dimer are interacting with the Cp* ring (Figure 2.2.3(g)), with the hydrogen atom bound to one of the aluminum atoms. Interestingly, the lowest energy isomer of the anion (Figure 2.2.3(c)) is not a minimum on the potential energy surface of the neutral system. The calculated EA of Cp*Al$_2$H is 0.73 eV, which is in good agreement with the measured value of 0.8 ± 0.1 eV.

The PES of Cp*Al$_3$H$^-$ begins with a small peak around 1.4 eV and followed by two major EBE bands, the first between 1.7 eV and 2.4 eV, with the next higher EBE band between 2.6 eV and 3.5 eV. (Figure 2.2.2(c)). The two lowest energy isomers of Cp*Al$_3$H$^-$ obtained from our calculations are shown in Figure 2.2.4(a) and 2.2.4(b). In both these isoenergetic structural isomers, aluminum atoms form an Al$_3$ triangular moiety with only one of the aluminum atoms interacting with the Cp* ring (η^5 coordination). Similar to the Cp*Al$_2$H$^-$ case, here the two isomers differ only in the way the hydrogen atom is bound to the Al$_3$ moiety. In the case of the lowest energy isomer (Figure 2.2.4(a)), the hydrogen atom is bound terminally to one of the aluminum atoms, while in the second isomer (Figure 2.2.4(b)), the hydrogen atom is bridging between two aluminum atoms. The calculated VDE values of the first isomer is 1.40 eV, while the VDE of second isomer is 1.20 eV. These values are in good agreement with the measured value of 1.4 ± 0.1 eV. In addition, the calculated higher transition energies of 2.40 eV and 3.22 eV for the first isomer; 2.71 and 3.72 eV for the second isomer seem to be contributing towards the higher EBE bands of the photoelectron

spectrum. Thus, we cannot rule out the possibility of the presence of both these isomers in the anion cluster beam. Interestingly, the lowest energy isomer of the neutral Cp*Al$_3$H system (Figure 2.2.4(c)] is similar to the second (slightly higher energy) isomer of its anionic counterpart, while the isomer similar to that of the lowest energy structure of the anion is 0.20 eV higher in energy (Figure 2.2.4(d)). Since the lowest energy structures of anion and neutral systems are not identical, the threshold of the lowest EBE in the spectrum corresponds to adiabatic detachment energy (ADE) of the anion, but not the EA of the neutral system. The calculated adiabatic detachment energies (ADE) of Cp*Al$_3$H$^-$ are 1.20 eV for the lowest energy isomer (Figure 2.2.4(a)) and 1.0 eV for the second (slightly higher energy) isomer (Figure 2.2.4(b)). These ADE values are in decent agreement with the measured ADE value of 1.1 ± 0.1 eV.

References

1. H. W. Roesky and S. S. Kumar, *Chem. Commun*. **2005**, 4027 (2005).

2. H. W. Roesky, *Inorg. Chem.* **43**, 7284 (2004).

3. H. Schnöckel, *Z. Nafurforsch. B* **31**, 1291 (1976).

4. M. Tacke and H. Schnöckel, *Inorg. Chem.* **28**, 2896 (1989).

5. A. Purath, R. Köppe and H. Schnöckel, *Angew. Chem.* **111**, 3114 (1999); *Angew. Chem., Int. Ed. Engl.* **38**, 2926 (1999).

6. A. Purath, R. Köppe and H. Schnöckel, *Chem. Commun.* **1999**, 1933 (1999).

7. H. Köhnlein, A. Purath, C. Klemp, E. Baum, I. Krossing, G. Stösser and H. Schnöckel, *Inorg. Chem.* **40**, 4830 (2001).

8. C. Dohmeier, M. Mocker, H. Schnöckel, A. Lötz, U. Schneider and R. Ahlrichs, *Angew. Chem.* **105**, 1491 (1993); *Angew.Chem., Int. Ed. Engl.* **32**, 1428 (1993).

9. A. Schnepf and H. Schnöckel, *Adv. Organomet. Chem.* **47**, 235 (2001).

10. C. Üffing, A. Ecker, R. Köppe, K. Merzweiler and H. Schnöckel, *Chem. Eur. J.* **4**, 2142 (1998).

11. C. Dohmeier, C. Roble, M. Tacke and H. Schnöckel, *Angew. Chem.* **103**, 594 (1991).

12. C. Dohmeier, D. Loos and H. Schnöckel, *Angew. Chem.* **108**, 141 (1996).

13. J. Gauss, U. Schneider, R. Ahlrichs, C. Dohmeier and H. Schnöckel, *J. Am. Chem. Soc.* **115**, 2402 (1993).

14. A. Haaland, K.-G. Martinsen, S. A. Shlykov, H. V. Volden, C. Dohmeier and H. Schnöckel, *Organometallics* **14**, 3116 (1995).

15. J. D. Gorden, A. Voigt, C. L. B. Macdonald, J. S. Silverman and A. H. Cowley, *J. Am. Chem. Soc.* **122**, 950 (2000).

16. C. Dohmeier, H. Krautscheid and H. Schnöckel, *Angew. Chem.* **106**, 2570 (1994).

17. C. Üffing, A. Ecker, R. Köppe and H. Schnöckel, *Organometallic* **35**, 2373 (1998).

18. Q. Yu, A. Purat, A. Douchev and H. Schnöckel, *J. Organomet. Chem.* **584**, 94 (1999).

19. J. Weiß, D. Stetzkamp, B. Nuber, R. A. Fischer, C. Boehme and G. Frenking, *Angew. Chem., Int. Ed. Engl.* **36**, 70 (1997).

20. D. Weiß, T. Steinke, M. Winter, R. A. Fischer, N. Fröhlich, J. Uddin and G. Frenking, *Organometallics* **19**, 4583 (2000).

21. S. Schulz, T. Schoop, H. W. Roesky, L. Häming, A. Steiner and R. Herbst-Irmer, *Angew. Chem., Int. Ed. Engl.* **34**, 919 (1995).

22. C. K. F. von Haenish, C. Üffing, M. A. Junker, A. Ecker, B. O. Kneisel and H. Schnöckel, *Angew. Chem., Int. Ed. Engl.* **35**, 2875 (1996).

23. C. Dohmeier, H. Schnöckel, C. Robl, U. Schneider and R. Ahlrichs, *Angew. Chem., Int. Ed. Engl.* **33**, 199 (1994).

24. J. Vollet, J. R. Hartig, and H. Schnöckel, *Angew. Chem. Int. Ed.* **43**, 3186 (2004).

25. K. S. Williams, and J. P. Hooper, *J. Phys. Chem. A* **115**, 14100 (2011).

26. K. Weiß, and H. SchnPckel, *Anal. Bioanal. Chem.* **377**, 1098 (2003).

27. C. Ganesamoorthy, S. Loerke, C. Gemel, P. Jerabek, M. Winter, G. Frenking, and R. A. Fischer, *Chem. Commun.* **49**, 28580 (2013).

28. X. Zhang,Y.Wang, H. Wang,A. Lim,G. Gantefoer, K.H. Bowen,J. U. Reveles, and S. N. Khanna, *J. Am. Chem. Soc.,* **135**, 4856 (2013).

29. M. Gerhards, O. C. Thomas, J. M. Nilles, W.J. Zheng, and K. H. Bowen, *J. Chem. Phys.* **116**, 10247 (2002).

30. J. Ho, K. M. Ervin, and W. C. Lineberger, *J. Chem. Phys.* **93**, 6987 (1990).

31. A. D. Becke, *Phys. Rev. A* **38**, 3098 (1988).

32. J. P. Perdew and Y. Wang, *Phys. Rev. B* **45,** 13244 (1992).

33. M. J. Frisch, G. W. Trucks, H. B. Schlegel, et al., GAUSSIAN 09, Revision B.01, Gaussian, Inc., Wallingford, CT, 2004.

34. A. K. Kandalam, B. K. Rao, and P. Jena, *J. Chem. Phys.* **120**, 10414 (2004).

35. A. K. Kandalam, B. K. Rao, and P. Jena, *J. Phys. Chem. A* **109 (41)**, 9220 (2005).

36. A. K. Kandalam, B. Kiran, P. Jena, X. Li, A. Grubisic, and K. H. Bowen, *J. Chem. Phys.* **126**, 084306 (2007).

37. A. K. Kandalam, P. Jena, X. Li, S. N. Eustis, and K. H. Bowen, *J. Chem. Phys.* **129**, 134308 (2008).

38. X. Li, S. Eustis, K. H. Bowen, A. K. Kandalam, and P. Jena, *J. Chem. Phys.* **129**, 074313 (2008).

Table 2.2.1. Experimental EA and VDE, theoretical ADE and VDE values. Results from different calculated isomers are separated by a slash. All the numbers are in eV, and the experimental values are uncertain by ±0.1 eV.

Species	ADE/EA		VDE	
	Theo.	Expt.	Theo.	Expt.
Cp*AlH/Cp*AlH⁻	0.85	1.0	1.60	1.6
Cp*Al₂H/Cp*Al₂H⁻	0.73	0.8	1.04/0.85/1.20	1.2
Cp*Al₃H/Cp*Al₃H⁻	1.20/1.00	1.1	1.40/1.20	1.4

Figure Captions

Figure 2.2.1. The mass spectra of aluminum hydride cluster anions before reaction (a) and $Cp*Al_{1-3}H^-$ cluster anions after reaction (b).

Figure 2.2.2. Photoelectron spectra of $Cp*Al_{1-3}H^-$ taken with 3.49 eV laser.

Figure 2.2.3. Calculated structures of $Cp*Al_{1,2}H^{-/0}$.

Figure 2.2.4. Calculated structures of $Cp*Al_3H^{-/0}$.
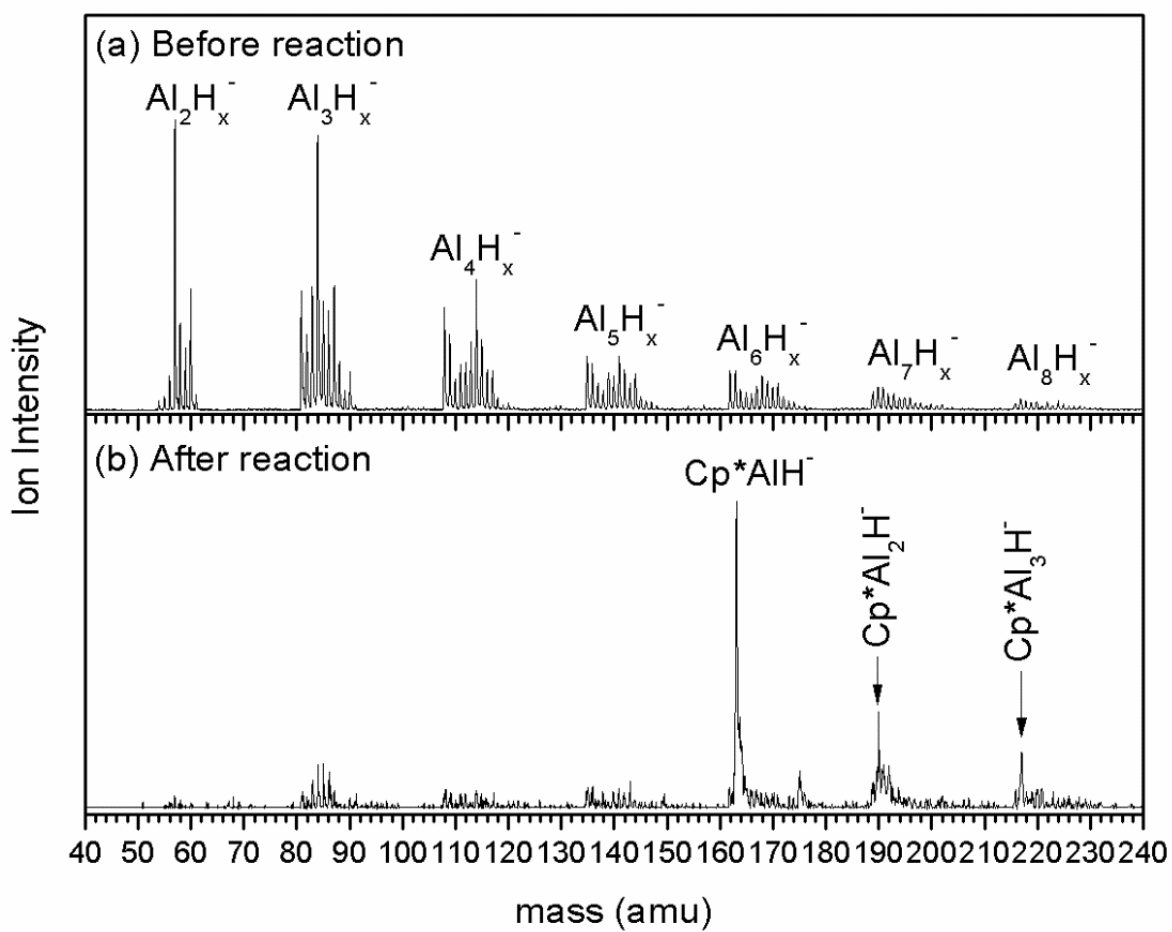
Figure 2.2.1
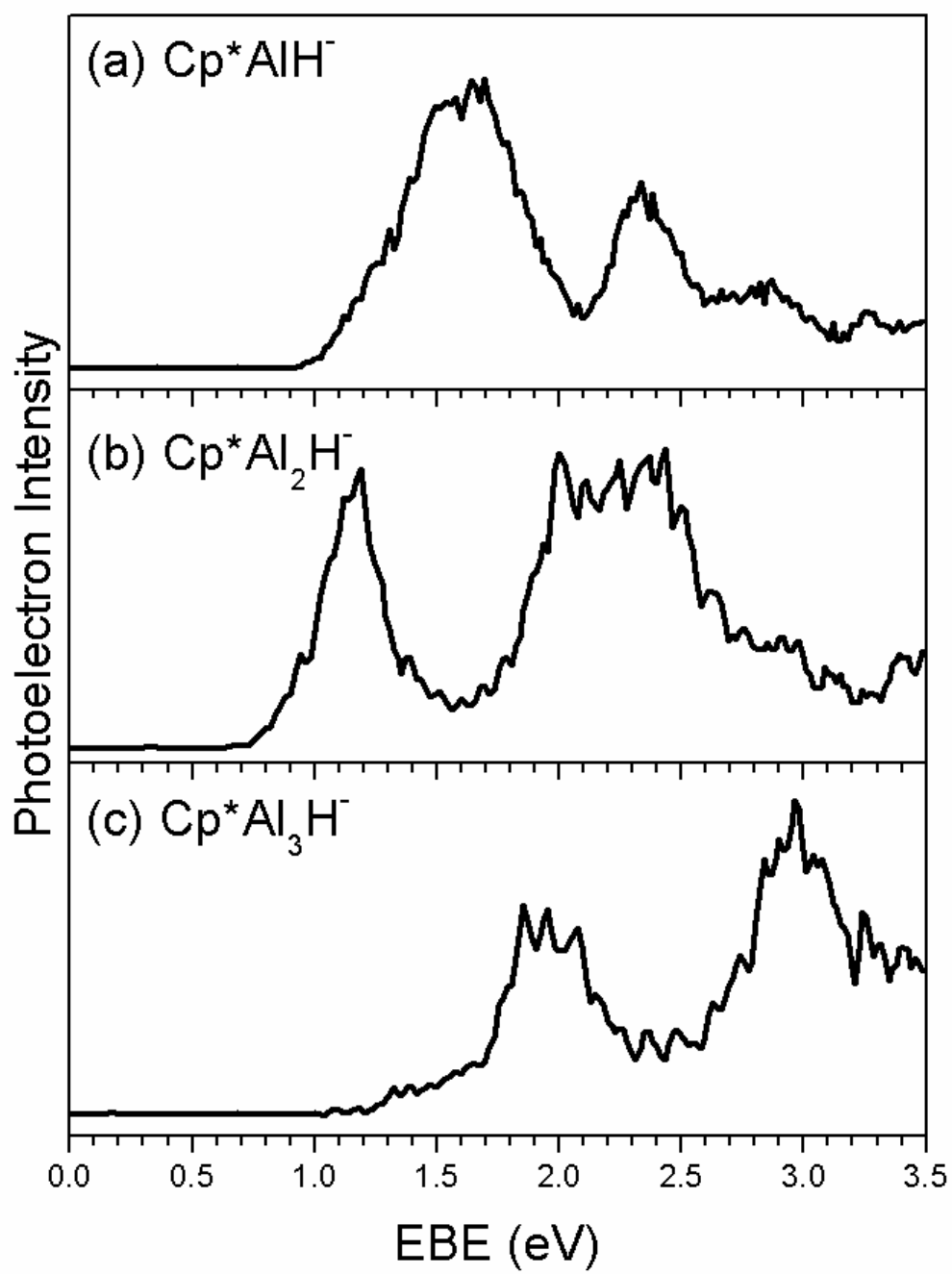
Figure 2.2.2
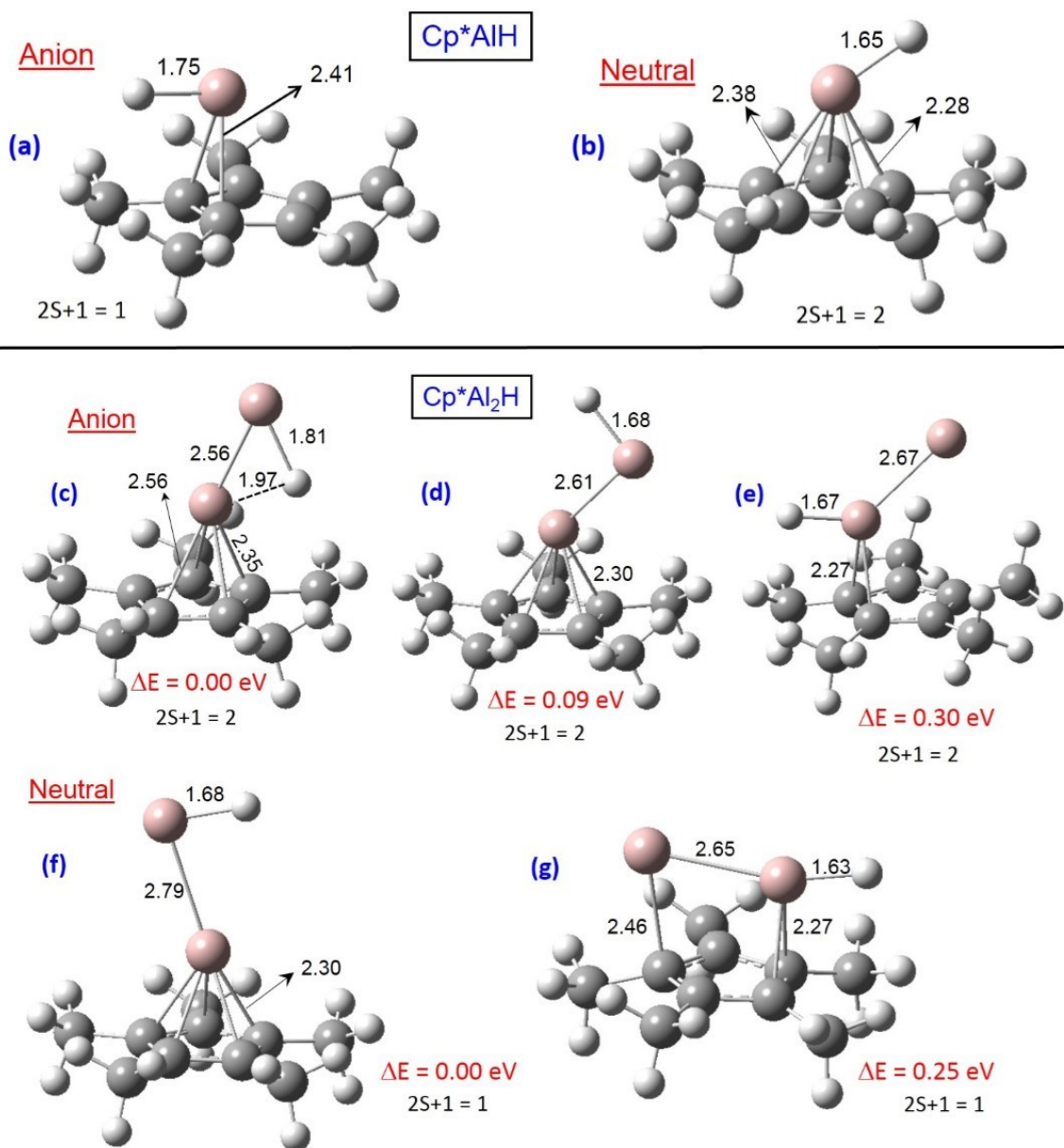
Figure 2.2.3
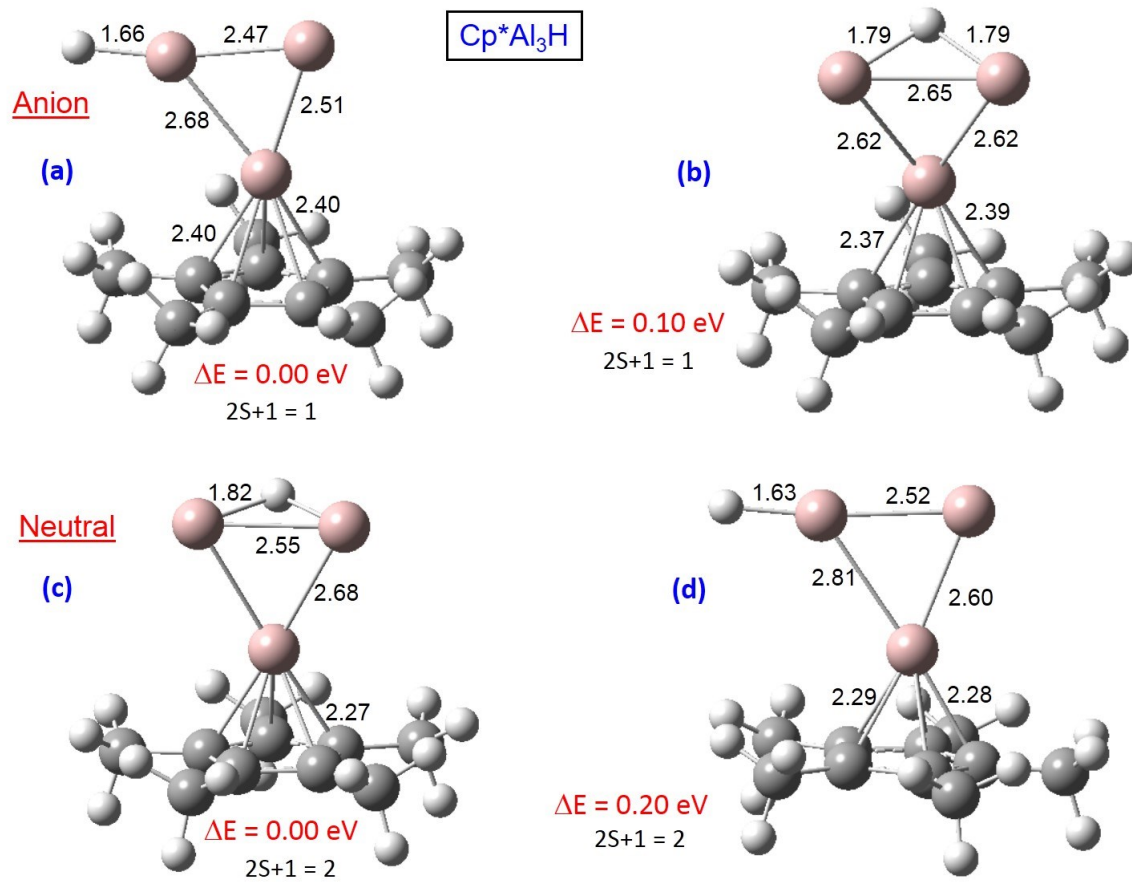
Figure 2.2.4

2.3 The Reactions between Aluminum Hydride Cluster Anions and Several Other Ligands

Xinxing Zhang and Kit Bowen

Introduction

In this section, experimental results of reactions between aluminum hydride cluster anions and several other ligands are presented. These ligands, having an acidic H atom in common, include bis(trimethylsilyl)amine (HMDS), triisopropylsilane ((i-pr)$_3$SiH), and tris(trimethylsilyl)silane (TTMSS). The deprotonated ligand is denoted as "L". For HMDS, the final products include LAlH$^-$, LAl$_2$H$_2^-$ and LAl$_{2,3,4}^-$. The average OS of aluminum in these five products are +1, +1, 0, 0, 0. For (i-pr)$_3$SiH, the products are LAl$_{1,2,3,4}^-$, and the average OS of aluminum in these 4 products are all 0. For TTMSS, the products are LAl$_{1,2,3}$H$_2^-$, and the average OS of aluminum in these 4 clusters are +2, +1 and +2/3.

For Al, any oxidation states other than +3 are considered to be "low oxidation state" and energetic. This gas phase reaction is a novel way of enriching the low oxidation state aluminum cluster family.

Figure Captions

Figure 2.3.1. The mass spectrum and photoelectron spectra of the products from the reaction between aluminum hydride cluster anions and HMDS.
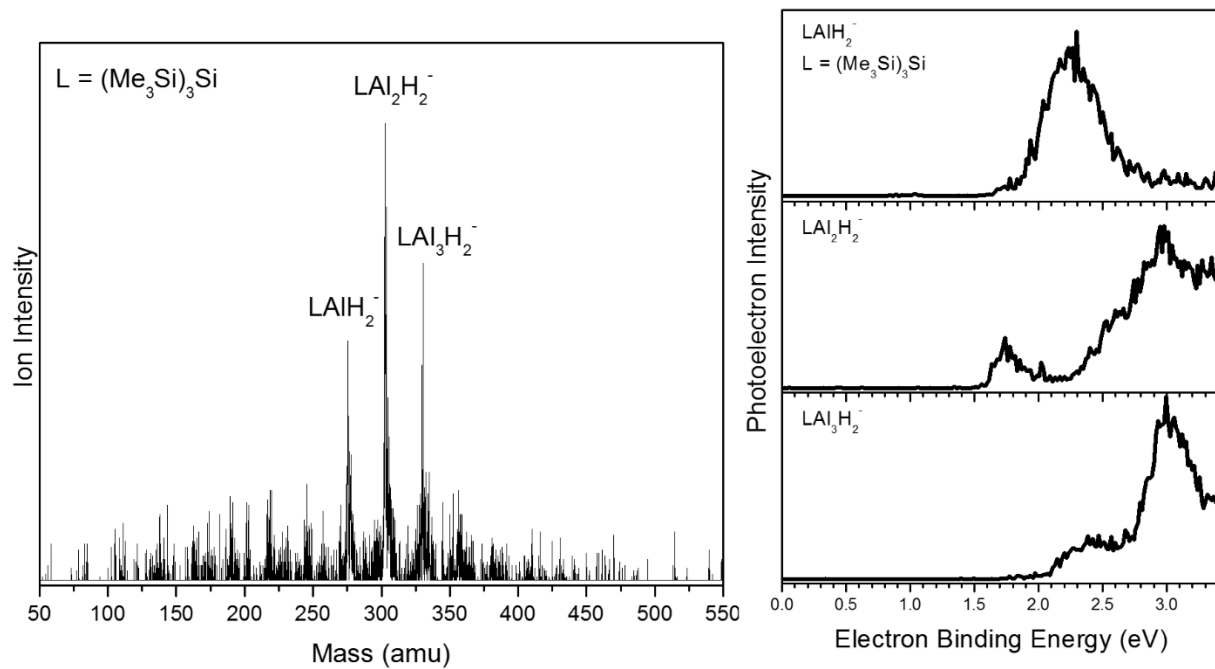
Figure 2.3.2. The mass spectrum and photoelectron spectra of the products from the reaction between aluminum hydride cluster anions and (i-pr)$_3$SiH.

Figure 2.3.3. The mass spectrum and photoelectron spectra of the products from the reaction between aluminum hydride cluster anions and TTMSS.
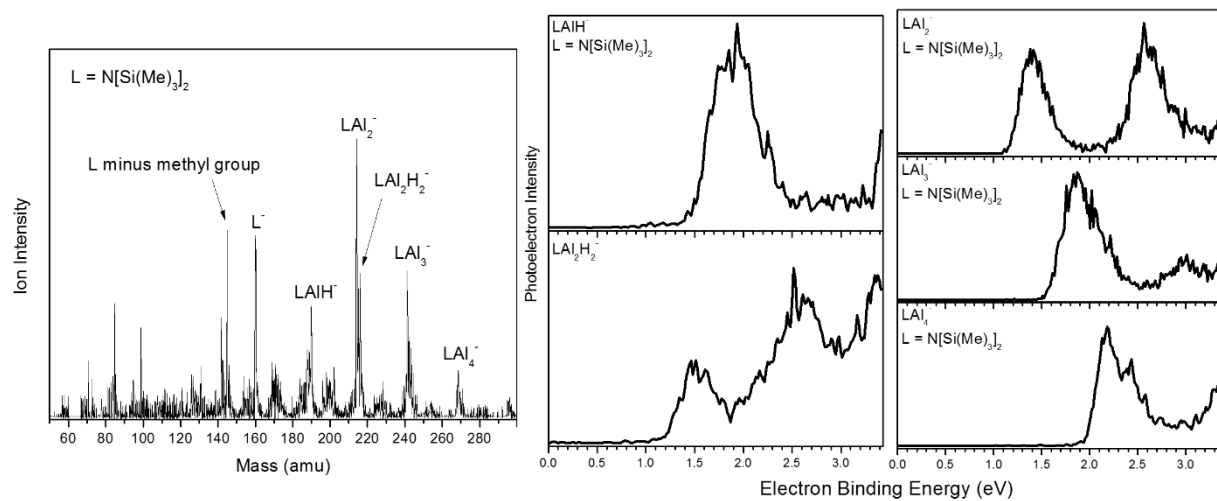
Figure 2.3.1
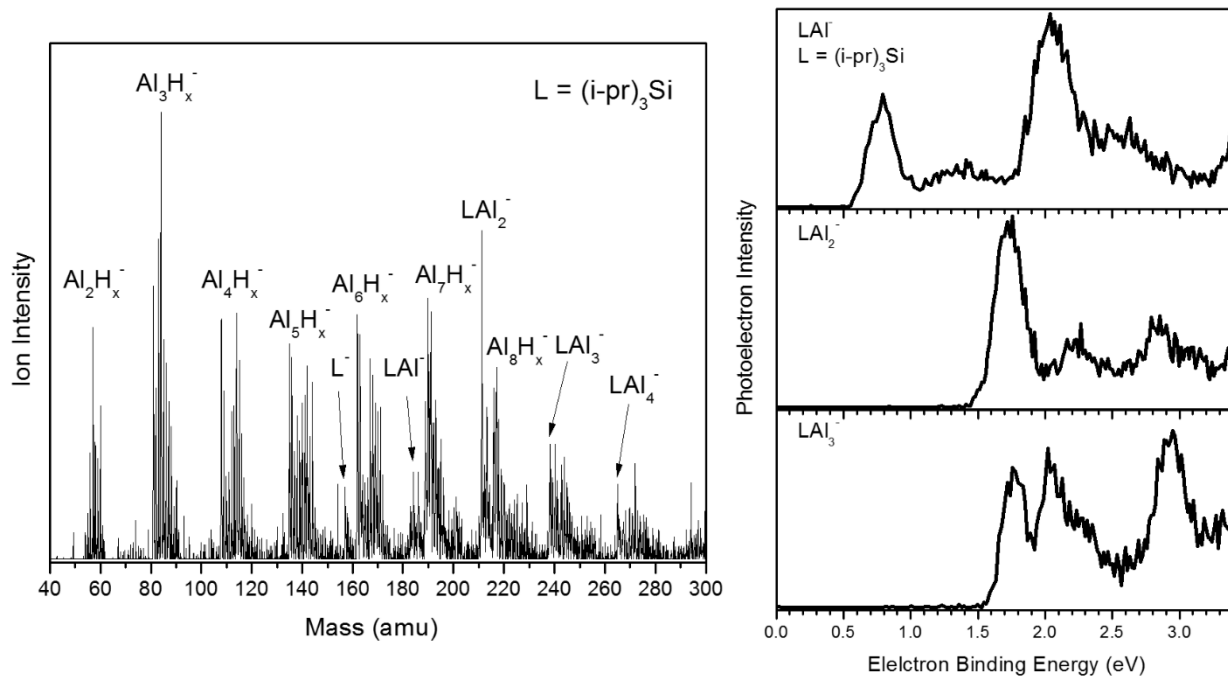
Figure 2.3.2

Figure 2.3.3

CHAPTER 3. Sustainability: CO$_2$ Activation and Fixation

Due to environmental considerations, recycling CO$_2$ has been a hot topic for years. However, the high stability of CO$_2$ molecule makes its reduction very difficult and energetically expensive. Therefore, pre-activation before fixation becomes the key. After activation, fixating CO$_2$ into other carbon form becomes easier.

In this chapter, the activation of CO$_2$ by coinage metal anions is presented in section 3.1. In section 3.2, fixation of CO$_2$ into formate by platinum hydride cluster anions into is presented, where the mechanism of CO$_2$ inserting into Pt-H bond is discussed in detail.

3.1 Photoelectron Spectroscopic and Computational Study of (M-CO$_2$)$^-$ Anions, M = Cu, Ag, Au

Xinxing Zhang,[1] Seong K. Kim,[2] and Kit H. Bowen[1, a)]

^{1} Department of Chemistry, Johns Hopkins University, Baltimore, Maryland 21218, USA

^{2}Department of Chemistry, Seoul National University, Seoul, 151-747, Korea

$^{a)}$ Electronic mail: kbowen@jhu.edu

Abstract

In a combined photoelectron spectroscopic and computational study of (M-CO$_2$)$^-$, M= Au, Ag, Cu, anionic complexes, we show that (Au-CO$_2$)$^-$ forms both the chemisorbed and physisorbed isomers, AuCO$_2^-$ and Au$^-$(CO$_2$), respectively; that (Ag-CO$_2$)$^-$ forms only the physisorbed isomer, Ag$^-$(CO$_2$); and that (Cu-CO$_2$)$^-$ forms only the chemisorbed isomer, CuCO$_2^-$. The two chemisorbed complexes, AuCO$_2^-$ and CuCO$_2^-$ are covalently-bound, formate-like anions, in which their CO$_2$ moieties are significantly reduced. These two species are examples of electron-induced CO$_2$ activation. The two physisorbed complexes, Au$^-$(CO$_2$) and Ag$^-$(CO$_2$) are electrostatically and thus weakly bound.

Introduction

Interest in carbon dioxide fixation derives both from environmental concerns and the prospect of converting CO_2 into fuels. Since the carbon in CO_2 is already in its highest oxidation state, any attempt to activate CO_2 must involve its reduction, and that implies adding negative charge to it. This, however, is challenging, because CO_2 must deform in order to accept an electron and the resulting bent CO_2^- anion is metastable, i.e., the electron affinity of CO_2 is -0.6 eV.[1-3] While some studies have dealt with free CO_2^- anions, most have focused on gas-phase, anionic complexes made up of CO_2 and various atoms and molecules.[4-33] Of particular interest are studies that found significant covalent character in the intermolecular bond between CO_2 and pyridine within the gas-phase (pyridine-CO_2)$^-$ anionic complex.[6,7] The CO_2 moiety in that case exhibited a negative charge of -0.5. Other (N-heterocyclic molecule-CO_2)$^-$ anionic complexes were also found to be analogously bonded.[8,9] In all these cases, the carbon dioxide moiety was found to be partially bent and to possess significant negative charge, i.e., to be partially reduced. At the macroscopic level, analogous reduction processes involving CO_2 and pyridine have been explored electrochemically.[34,35]

More recently, Weber and co-workers have reported gas-phase, infrared photodissociation studies of transition metal-CO_2 anionic complexes, $[M(CO_2)_n]^-$, where M = Cu, Ag, Au, Co, and Ni. Both electrostatically-bound, atomic metal anion-CO_2 complexes (physisorption) and covalently-bound anionic complexes (chemisorption) were found, where in the latter cases the CO_2 moieties were partially bent and had accepted some significant portion of the negative charge.[22-29] The coinage metal-CO_2 anionic complexes, (Au-CO_2)$^-$, (Ag-CO_2)$^-$, and (Cu-CO_2)$^-$, are particularly interesting, since among those that are covalently-bound, they are formate anion analogs. In those cases, their s^1 coinage metal atoms substitute for the formate anion's hydrogen atom.

Here, we study the anionic complexes, $(Au\text{-}CO_2)^-$, $(Ag\text{-}CO_2)^-$, and $(Cu\text{-}CO_2)^-$, using anion photoelectron spectroscopy and theoretical calculations. Among these, we found differences in their physisorption and chemisorption behaviors. While $(Cu\text{-}CO_2)^-$ exhibited only chemisorption, and $(Ag\text{-}CO_2)^-$ showed only physisorption, $(Au\text{-}CO_2)^-$ displayed both chemisorption and physisorption isomers. These studies provide an additional context in which to view these fascinating species.

Methods

Experimental

Anion photoelectron spectroscopy is conducted by crossing a mass-selected, negative ion beam with a fixed-energy photon beam and analyzing the energies of the resultant photodetached electrons. This technique is governed by the well-known energy-conserving relationship, $h\nu = EBE + EKE$, where $h\nu$, EBE, and EKE are the photon energy, electron binding energy (photodetachment transition energy), and the electron kinetic energy, respectively. Our photoelectron instrument, which has been described elsewhere,[36] consists of an ion source, a linear time-of-flight mass spectrometer, a mass gate, a momentum decelerator, a neodymium-doped, yttrium aluminum garnet (Nd:YAG) laser, operated in either the third harmonic (355 nm) or the fourth harmonic (266 nm) for photodetachment, and a magnetic bottle, electron energy analyzer with a resolution of 35 meV at EKE=1 eV. The photoelectron spectra were calibrated against the well-known photoelectron spectrum of Cu^-.[37] The $(M\text{-}CO_2)^-$ (M = Au, Ag, Cu) anion complexes were generated in a laser vaporization ion source. It consisted of either a rotating, translating gold, silver or copper rod, which was being ablated with second harmonic (532 nm) photon pulses from a

Nd:YAG laser, while a 50%/50% He/CO_2 gas mixture at 100 psi was being expanded from a pulsed valve over the rods.

Theoretical

The lowest energy structures of $(M-CO_2)^{-1/0}$ systems were obtained by density functional theory (DFT)-based electronic structure calculations with the Becke's three-parameter hybrid functional (B3LYP).[38-40] The 6-311G+(3df) basis set[41] was used for C and O, while the LANL2DZ[42-44] and Stuttgart/Dresden (SDD)[45,46] effective core potentials were used for Au, Ag and Cu. All of the calculations were carried out using the Gaussian 09 software package.[47]

The vertical detachment energy (VDE) is the energy difference between the ground state anion and its corresponding neutral at the geometry of the anion, i.e., these are vertical photodetachment transitions. The adiabatic detachment energy (ADE) is the energy difference between the lowest energy, relaxed geometry of the anionic cluster and the relaxed geometry of a structurally similar isomer (nearest minimum) of its neutral counterpart. The adiabatic electron affinity (EA) is the energy difference between the lowest energy, relaxed geometry of the anionic cluster and the relaxed geometry of the lowest energy isomer (the global minimum) of its neutral counterpart. When the nearest local minimum and the global minimum are one and the same, ADE = EA. The EBE value of the photoelectron spectral onset (threshold), E_T, can be compared with both the calculated ADE and EA values.

The potential energy surfaces along the M-C coordinate were computed by scanning the M-C bond length with a step width of 0.1 Å, while relaxing the rest of the cluster. Several different levels of theory, e.g., B3LYP/SDD, CCSD/SDD, and B3LYP/def2-TZVPP were used and compared to one another. In the cases of the first two examples, the 6-311G+(3df) basis set[41] was used for C and O, while the SDD effective core potential was used for the noble metal atoms.

However, in the case of B3LYP/def2-TZVPP, its basis set was applied to all the atoms. Natural population analysis (NPA), as implemented in the Gaussian09 code, was also carried out to determine the charge distributions in these clusters. NPA has been found to be satisfactory in predicting charge distributions.[48,49]

Results

Experimental

The photoelectron spectra of $(M-CO_2)^-$ (M = Au, Ag, Cu) are shown in Figure 3.1.1. For comparison, the spectra of Au^-, Ag^- and Cu^- are also presented below each respective spectrum. Consider the photoelectron spectrum of $(Au-CO_2)^-$. The lowest EBE peak is relatively narrow and is shifted to only slightly higher EBE compared to that of the lowest EBE peak in the photoelectron spectrum of Au^-. This gold-carbon dioxide anion peak is due to the anion-molecule complex, $Au^-(CO_2)$, where the interaction between Au^- and CO_2 is weak. $Au^-(CO_2)$ can be considered to be a solvated Au^- anion or alternatively an example of physisorption in the gas phase. In anion-molecule complexes such as these, the core anion, i.e., Au^- in this case, acts as the chromophore for photodetachment, and the resulting photoelectron spectrum looks like a slightly broadened version of the core anion's photoelectron spectrum, just shifted to slightly higher EBE.

The higher EBE feature in the photoelectron spectrum of $(Au-CO_2)^-$ is relatively broad, suggesting a significant structural difference between the anionic complex and its neutral counterpart. While this broad band overlaps with a sharp peak that is due to the solvation-induced shift of the higher EBE peak in the photoelectron spectrum of Au^- to slightly higher EBE, both the width and the center of the broad band are slightly lower in EBE than that of the higher EBE Au^- peak, showing that this band is not primarily due to the solvation of the higher EBE Au^- peak. Also,

if this band had been due to the solvation of the lowest EBE peak in the Au$^-$ spectrum, it would have involved a solvation shift (stabilization energy) of an eV or more, this being an unrealistically strong physisorption interaction between the Au$^-$ atomic anion and a CO_2 molecule. Thus, the higher EBE feature in the photoelectron spectrum of (Au-CO_2)$^-$ is due to a strong, chemical bond-like interaction between the moieties; it is due to chemisorption. The photoelectron spectrum of (Au-CO_2)$^-$ provides evidence for the presence of two isomers, one physisorbed, Au$^-$(CO_2) and the other chemisorbed, AuCO_2^-, both of which are labeled as such in Figure 3.1.1.

Next, consider the photoelectron spectrum of (Ag-CO_2)$^-$. Its single peak is shifted to only slightly higher EBE and is slightly broadened compared to the single narrow peak observed in the photoelectron spectrum of Ag$^-$. The amount of shift is comparable to that seen for Au$^-$(CO_2), the lowest EBE peak in the spectrum of (Au-CO_2)$^-$. Thus, this silver-carbon dioxide anion peak is due to the anion-molecule complex, Ag$^-$(CO_2). Since the interaction between Ag$^-$ and CO_2 is weak, it can be viewed as a solvated anion and as another example of physisorption in the gas phase. Unlike the photoelectron spectrum of (Au-CO_2)$^-$, the photoelectron spectrum of (Ag-CO_2)$^-$ shows no evidence of a chemically-bound (chemisorption) isomer. See Figure 3.1.1.

Finally, consider the photoelectron spectrum of (Cu-CO_2)$^-$. There is no similarity between the single broadened band in its photoelectron spectrum and the photoelectron spectrum of Cu$^-$. This band in the photoelectron spectrum of (Cu-CO_2)$^-$ is due to the chemically-bound (chemisorption) isomer, CuCO_2^-. There is no evidence of a physisorbed/solvated anion Cu$^-$(CO_2) isomer in the photoelectron spectrum of (Cu-CO_2)$^-$. See Figure 3.1.1.

Energetic parameters can also be determined from the spectra in Figure 3.1.1. The threshold energy (EBE) for each peak/band in the photoelectron spectra of (M-CO_2)$^-$ (M = Au, Ag, Cu) is denoted as E_T. If there is sufficient Franck-Condon overlap between the ground state of the

anion and the ground state of the neutral and if there is not significant hot band signal, then E_T is an estimate of the value of ADE and perhaps of EA. However, if the structural difference is too great between the anion and the neutral, one will not be able to observe the origin transition, and the EBE of E_T will be significantly greater than that of the true EA. The EBE of the intensity maximum for each peak is its VDE value. The E_T and VDE values of all four of the above species are listed in Table 3.1.1 and are compared there to our computed values of EA and VDE.

Theoretical

Four anionic species were observed experimentally in this work. The structures of both their anionic and their neutral forms were determined using the B3LYP/SDD computational method and are presented in Figure 3.1.2. There, the M-C bond length (Å), the C-O bond length (Å) and the O-C-O bond angle (in degrees) are shown for each case. For the physisorption species, $Au^-(CO_2)$ and $Ag^-(CO_2)$, their M-C bond lengths are both significantly longer than for typical chemical (single) bonds, indicating weak interactions between Au^-/Ag^- and CO_2. Also, the C-O bond length is 1.16 Å, which is the same as in isolated CO_2. The O-C-O moiety, however, is slightly bent, indicating that the metal atom does have some influence, albeit weak, on it.

For the chemisorption species, $AuCO_2^-$ and $CuCO_2^-$, the M-C bond length is 2.30 Å and 2.04 Å, respectively, implying the formation of a single bond between M and C in both cases. A natural population analysis showed that in $AuCO_2^-$, the CO_2 moiety has a negative charge of -0.45 e, whereas in $CuCO_2^-$, its charge is -0.64 e. Therefore, the CO_2 moiety has been significantly reduced in both these complexes. The CO_2 moiety in $CuCO_2^-$ has been activated more than it has been in $AuCO_2^-$, this being consistent with their relative M-C bond lengths. It is also consistent with the difference in their C-O bond lengths, i.e., in $CuCO_2^-$, the C-O bond (1.22 Å) is longer than that in $AuCO_2^-$ (1.20 Å), both being longer than the C-O bond length in isolated CO_2 (1.16 Å).

This implies that the more negative charge is on the CO_2 moiety, the more the C-O bond is weakened. The difference in negative charges is also consistent with the O-C-O bond angles. This angle is bent more in $CuCO_2^-$ (139.7º) than in $AuCO_2^-$ (145.0º), and in $CuCO_2^-$, it is close to that of the isolated CO_2^- anion (134º). The difference in the amount of negative charge on the CO_2 moiety in $CuCO_2^-$ versus in $AuCO_2^-$ is likely due to the electronegativity difference between the metal atoms, i.e., Au > Cu. Since, like the hydrogen atom, gold and copper atoms each have only one valence electron, both $AuCO_2^-$ and $CuCO_2^-$ are isostructural and isoelectronic to the formate anion; they are metalloformates.[22] The highest occupied molecular orbitals (HOMO) of $AuCO_2^-$ and $CuCO_2^-$ accommodate the excess electron, and these are also shown in Figure 3.1.2. Note the charge transfer from the metal atoms to the CO_2 moieties.

In all three neutral $M(CO_2)$ species, the metal atom is far away from CO_2. Also, both the O-C-O bond angle and the C-O bond length are the same in these neutral species as in an isolated CO_2 molecule. Together, these structural parameters show that there is very little interaction between M and CO_2. Also, notice that the structures of the physisorbed anionic complexes, Au^- (CO_2) and $Ag^-(CO_2)$, are similar to those of the neutral species. The structures of the chemisorbed species, $AuCO_2^-$ and $CuCO_2^-$, on the other hand, are quite different from those of the neutral species.

The calculated EA and VDE values obtained from B3LYP/SDD and B3LYP/LANL2DZ computational methods are listed in Table 3.1.1. These two methods gave similar results. The theoretical EA and VDE values for the physisorption species, $Au^-(CO_2)$ and $Ag^-(CO_2)$ are in very good agreement with the experimental E_T and VDE results. Thus, the observed E_T values are also EA values in those cases. While the theoretical VDE values for the chemisorption species, $AuCO_2^-$ and $CuCO_2^-$ are in very good agreement with the experimental VDE values, the theoretical EA values for these species are smaller than the spectral E_T values; see Table 3.1.1. This is likely due

to structural differences between $AuCO_2^-$ and $CuCO_2^-$ and their neutral counterparts, these leading in turn to less Franck-Condon overlap during photodetachment.

Figure 3.1.3 plots the potential energy (Hartrees), the O-C-O bond angle (°), and the negative charge on the CO_2 moiety (*e*) for all three $(M\text{-}CO_2)^-$ systems as a function of the M-C bond length with the remainder of the complex relaxed. All of these computations were performed at the B3LYP/SDD level of theory. Along the potential energy surface of $(Au\text{-}CO_2)^-$, there are two wells, these corresponding to $AuCO_2^-$ and $Au^-(CO_2)$, the chemisorbed and physisorbed isomers, respectively. Note that their energies are very similar to each other, with a calculated barrier between of only 0.03 eV. This very low barrier is probably why they co-exist in our experiment. Along the potential energy surfaces of $(Ag\text{-}CO_2)^-$ and $(Cu\text{-}CO_2)^-$, there is only one well in each, these corresponding to physisorped $Ag^-(CO_2)$ and to chemisorped $CuCO_2^-$. The feature at ~2.4 Å on the potential energy surface of $(Ag\text{-}CO_2)^-$ is an inflection point and not a well. In all three $(M\text{-}CO_2)^-$ systems, the O-C-O bond angle exhibits an asymptote that leads to 180°, while the negative charge on the CO_2 moiety has an asymptote that trends to zero.

Discussion

There are a couple of differences between our findings (ultraviolet photoelectron spectroscopy and theory) and those of Weber and coworkers (infrared photodissociation spectroscopy and theory).[24,26] In the photoelectron spectrum of $(Ag\text{-}CO_2)^-$, evidence for only the physisorbed $Ag^-(CO_2)$ isomer was seen. By contrast, in the infrared photodissociation work[26], neither isomer was observed. Nevertheless, calculations at the B3LYP/def2-TZVPP level of theory in that study predicted the viability the chemisorbed $AgCO_2^-$ isomer. As noted above, our calculations at the B3LYP/SDD level of theory, found only the physisorbed $Ag^-(CO_2)$ isomer. To

further investigate this situation, we conducted calculations at both the B3LYP/def2-TZVPP and the CCSD/SDD levels of theory. The results are shown in Figure 3.1.4. Using B3LYP/def2-TZVPP, we saw two potential wells, i.e., one for $AgCO_2^-$ and the other for $Ag^-(CO_2)$. At the CCSD/SDD level of theory, however, we observed only one well, it corresponding to physisorbed $Ag^-(CO_2)$. Thus, CCSD/SDD and B3LYP/SDD gave the same qualitative result. To summarize, both the anion photoelectron spectrum of $(Ag-CO_2)^-$ and these two levels of theory imply that physisorbed $Ag^-(CO_2)$ is the only isomer of $(Ag-CO_2)^-$ that is stable.

In the case of $(Au-CO_2)^-$, calculations both by Weber et al. and by us found nearly iso-energetic chemisorbed and physisorbed isomers. Yet, while the photoelectron spectrum of $(Au-CO_2)^-$ showed strong evidence for both physisorbed and chemisorped isomers, only the chemisorped $AuCO_2^-$ isomer was observed in the IR photodissociation work.[24] Different source conditions likely account for these differing observations.

Interestingly, there are partial parallels between the physisorbed and chemisorbed isomers of $(M-CO_2)^-$ and those of $(M-O_2)^-$, M = Au, Ag, Cu. For gold and copper, both chemisorbed, MO_2^- and physisorped, $M^-(O_2)$ isomers are known to coexist.[50,51] In the case of silver, on the other hand, only physisorped $Ag^-(O_2)$ is known, it having been reported in neon matrices[52] and in RF-octopole ion trap reactions[53] as well as having been revealed through calculations.[54] No chemisorped AgO_2^- has been reported. As in $(M-CO_2)^-$ complexes, silver stands apart in $(M-O_2)^-$ complexes as well.

Acknowledgements

References

1. R. N. Compton, P. W. Reinhardt, and C. D. Cooper, *J. Chem. Phys.* **63**, 3821 (1975).

2. M. Knapp, O. Echt, D. Kreisle, T. D. Mark, and E. Recknagel, *Chem. Phys. Lett.* **126**, 225 (1986).

3. S. T. Arnold, J. V. Coe, J. G. Eaton, C. B. Freidhoff, L. H. Kidder, G. H. Lee, M. R. Manaa, K. M. McHugh, D. Patel-Misra, H. W. Sarkas, J. T. Snodgrass, and K. H. Bowen, *in Proceedings of the Enrico Fermi International School of Physics, CVII Course,* Varenna, edited by G. Scoles (North-Holland, Amsterdam, 1989), pp. 467-490.

4. C. E. Klots, *J. Chem. Phys.* **71**, 4172 (1979).

5. T. Tsukuda and T. Nagata, *J. Phys, Chem. A* **107**, 8476 (2003).

6. S. Y. Han, I. Chu, J. H. Kim, J. K. Song, and S. K. Kim, *J. Chem. Phys*. **113**, 596 (2000).

7. M. Z. Kamrath, R. A. Relph, and M. A. Johnson, *J. Am. Chem. Soc.* **132**, 15508 (2010).

8. S. H. Lee, N. Kim, D. G. Ha, and S. K. Kim, *J. Am. Chem. Soc*. **130**, 16241 (2008).

9. N. Kim, *Bull. Korean Chem. Soc*. **34**, 2247 (2013).

10. M. J. DeLuca, B. Niu, and M. A. Johnson, *J. Chem. Phys*. **88**, 5857 (1988).

11. S. H. Fleischman and K. D. Jordan, *J. Phys. Chem.* **91**, 1300 (1987).

12. T. Tsukuda, M. A. Johnson, and T. Nagata, *Chem. Phys. Lett*. **268**, 429 (1997).

13. J. W. Shin, N. I. Hammer, M. A. Johnson, H. Schneider, A. Glöβ, and J. M. Weber, *J. Phys. Chem. A* **109**, 3146 (2005).

14. D. W. Arnold, S. E. Bradforth, E. H. Kim, and D. M. Neumark, *J. Chem. Phys.* **102**, 3493 (1995).

15. G. Markovich, R. Giniger, M. Levin, and O. Cheshnovsky, *Z. Phys. D* **20**, 69 (1991).

16. D. W. Arnold, S. E. Bradforth, E. H. Kim, and D. M. Neumark, *J. Chem. Phys.* **97**, 9468 (1992).

17. D. W. Arnold, S. E. Bradforth, E. H. Kim, and D. M. Neumark, *J. Chem. Phys.* **102**, 3510 (1995).

18. A. Muraoka, Y. Inokuchi, N. I. Hammer, J. W. Shin, M. A. Johnson, and T. Nagata, *J. Phys. Chem. A* **113**, 8942 (2009).

19. K. Hiraoka and S. Yamabe, *J. Chem. Phys.* **97**, 643 (1992).

20. K. Sudoh, Y. Matsuyama, A. Muraoka, R. Nakanishi, and T. Nagata, *Chem. Phys. Lett.* **433**, 10 (2006).

21. T. Sanford, S. Y. Han, M. A. Thompson, R. Parson, and W.C. Lineberger, *J. Chem. Phys.* **122**, 054307 (2005).

22. J. M. Weber, *Int. Rev. Phys. Chem.* **33**, 489 (2014).

23. H. Schneider, A. D. Boese, and J. M. Weber*, J. Chem. Phys.* **123**, 074316 (2005).

24. A. D. Boese, H. Schneider, A. N. Glöß, and J. M. Weber, *J. Chem. Phys.* **122**, 154301 (2005).

25. B. J. Knurr and J. M. Weber, *J. Am. Chem. Soc.* **134**, 18804 (2012).

26. B. J. Knurr and J. M. Weber, *J. Phys. Chem. A* **117**, 10764 (2013).

27. B. J. Knurr and J. M. Weber, *J. Phys. Chem. A* **118**, 4056 (2014).

28. B. J. Knurr and J. M. Weber, *J. Phys. Chem. A* **118,** 10246 (2014).

29. B. J. Knurr and J. M. Weber, *J. Phys. Chem. A* **118**, 8753 (2014).

30. R. F. Höckendorf, K. Fischmann, Q. Hao, C. v.d. Linde, O. P, Balaj, C. K. Siu, and M. K. Beyer, *Intern. J. Mass Spectro.* **354**, 175 (2013).

31. A. Akhgarnusch, R. F. Hoeckebdorf, Q. Hao, K. P. Jaeger, C-K. Siu, and M. K. Beyer, *Angew, Chem. Int. Ed.* **53**, 9327 (2013).

32. A. Akhgarnusch and M. K. Beyer, *Intern. J. Mass Spectro*. **365**, 295 (2014).

33. A. M. Buytendyk, Y. Wang, J. D. Graham, A. K. Kandalam, B. Kiran, and K. H. Bowen, *Molecular Physics*. (2015) [DOI: 10.1080/00268976.2014.1003261].

34. E. E. Barton, D. M. Rampulla, and A. B. Bocarsly, *J. Am. Chem. Soc.* **130**, 6342 (2008).

35. E. Barton Cole, P. S. Lakkaraju, D. M. Rampulla, A. J. Morris, E. Abelev, and A. B. Bocarsly, *J. Am. Chem. Soc.* **132**, 11539 (2010).

36. X. Zhang, Y.Wang, H. Wang, A. Lim, G. Gantefoer, K. H. Bowen, J. U. Reveles, and S. N. Khanna, *J. Am. Chem. Soc.* **135**, 4856 (2013).

37. J. Ho, K. M. Ervin, and W. C. Lineberger, *J. Chem. Phys.* **93**, 6987 (1990).

38. A. D. Becke, *Phys. Rev. A* **38**, 3098 (1988).

39. A. D. Becke, *J. Chem. Phys.* **98**, 5648 (1993).

40. C. Lee, W. Yang, and R. G. Parr, *Phys. Rev. B* **37**, 785 (1988).

41. R. Krishnan, J. S.Binkley, R. Seeger, and J. A. Pople, *J. Chem. Phys.* **72**, 650 (1980).

42. P. J. Hay and W. R. Wadt, *J. Chem. Phys.* **82**, 270 (1985).

43. P. J. Hay and W. R. Wadt, *J. Chem. Phys.* **82**, 284 (1985).

44. P. J. Hay and W. R. Wadt, *J. Chem. Phys.* **82**, 299 (1985).

45. M. Dolg, U. Wedig, H. Stoll, and H. Preuss, *J. Chem. Phys.* **86**, 866 (1987).

46. P. Schwerdtfeger, M. Dolg, W. H. E. Schwarz, G. A. Bowmaker, and P. D. W. Boyd, *J. Chem. Phys.* **91**, 1762 (1989).

47. Gaussian 09, Revision D.01, M. J. Frisch, G. W. Trucks, H. B. Schlegel, G. E. Scuseria, M. A. Robb, J. R. Cheeseman, G. Scalmani, V. Barone, B. Mennucci, G. A. Petersson, H. Nakatsuji, M. Caricato, X. Li, H. P. Hratchian, A. F. Izmaylov, J. Bloino, G. Zheng, J. L. Sonnenberg, M. Hada, M. Ehara, K. Toyota, R. Fukuda, J. Hasegawa, M. Ishida, T. Nakajima, Y. Honda, O. Kitao, H.

Nakai, T. Vreven, J. A. Montgomery, Jr., J. E. Peralta, F. Ogliaro, M. Bearpark, J. J. Heyd, E. Brothers, K. N. Kudin, V. N. Staroverov, R. Kobayashi, J. Normand, K. Raghavachari, A. Rendell, J. C. Burant, S. S. Iyengar, J. Tomasi, M. Cossi, N. Rega, J. M. Millam, M. Klene, J. E. Knox, J. B. Cross, V. Bakken, C. Adamo, J. Jaramillo, R. Gomperts, R. E. Stratmann, O. Yazyev, A. J. Austin, R. Cammi, C. Pomelli, J. W. Ochterski, R. L. Martin, K. Morokuma, V. G. Zakrzewski, G. A. Voth, P. Salvador, J. J. Dannenberg, S. Dapprich, A. D. Daniels, Ö. Farkas, J. B. Foresman, J. V. Ortiz, J. Cioslowski, and D. J. Fox, Gaussian, Inc., Wallingford CT, 2009.

48. H. Wang, X. Zhang, J. Ko, A. Grubisic, X. Li, G. Ganteför, H. Schnöckel, B. Eichhorn, M. Lee, P. Jena, A. Kandalam, B. Kiran, and K. H. Bowen, *J. Chem. Phys.* **140,** 054301 (2014).

49. H. Wang, Y. Ko, X. Zhang, G. Gantefoer, H. Schnoeckel, B. W. Eichhorn, P. Jena, B. Kiran, A. K. Kandalam, and K. H. Bowen, *J. Chem. Phys*. **140**, 124309 (2014).

50. W. Huang, H. Zhai, and L. -S. Wang, *J. Am. Chem. Soc.* **132**, 4344 (2010).

51. H. Wu, S. R. Desai, and L. –S. Wang, *J. Chem. Phys*. **103**, 4363 (1995).

52. X. Wang and L. Andrews, *J. Phys. Chem. A* **105**, 5812 (2001).

53. T. M. Bernhardt, J. Hagen, S. M. Lang, D. M. Popolan, L. D. Socaciu-Siebert, and L. Wöste, *J. Phys. Chem. A* **113**, 2724 (2009).

54. V. Bonačić-Koutecký, R. Mitrić, C. Bürgel, H. Noack, M. Hartmann, and J. Pittner, *Eur. Phys. J. D* **34**, 113 (2005).

Table 3.1.1. E_T, EA and VDE values obtained from both experiment and theory.[a]

Species	Expt. E_T	Theo. EA	Expt. VDE	Theo. VDE
$Au^-(CO_2)$	2.3	2.44/2.39	2.45	2.51/2.47
$AuCO_2^-$	3.0	2.51/2.41	3.31	3.28/3.18
$Ag^-(CO_2)$	1.25	1.38/1.53	1.40	1.42/1.57
$CuCO_2^-$	2.1	1.67/1.73	2.37	2.26/2.43

[a]The theoretical calculations of both EA and VDE values used the 6-311G+(3df) basis set for the C and O atoms and the LANL2DZ/SDD basis sets for the noble metal atoms at the B3LYP level of theory.

Figure Captions

Figure 3.1.1. Photoelectron spectra of $(Au-CO_2)^-$ and Au^- (266 nm), $(Ag-CO_2)^-$ and Ag^- (355 nm), and $(Cu-CO_2)^-$ and Cu^- (355 nm)

Figure 3.1.2. Calculated structures of $Au^-(CO_2)$, $AuCO_2^-$, $Ag^-(CO_2)$, $CuCO_2^-$, $AuCO_2$, $AgCO_2$ and $CuCO_2$. HOMOs of $AuCO_2^-$ and $CuCO_2^-$ are also presented.

Figure 3.1.3. The curves of potential energy (Hartree), O-C-O bond angle (°) and negative charge on CO_2 (e) versus the M-C bond length (Å) obtained from B3LYP/SDD level of theory.

Figure 3.1.4. The potential energy surfaces of $(Ag-CO_2)^-$ obtained from B3LYP/def2-TZVPP and CCSD/SDD levels of theory.
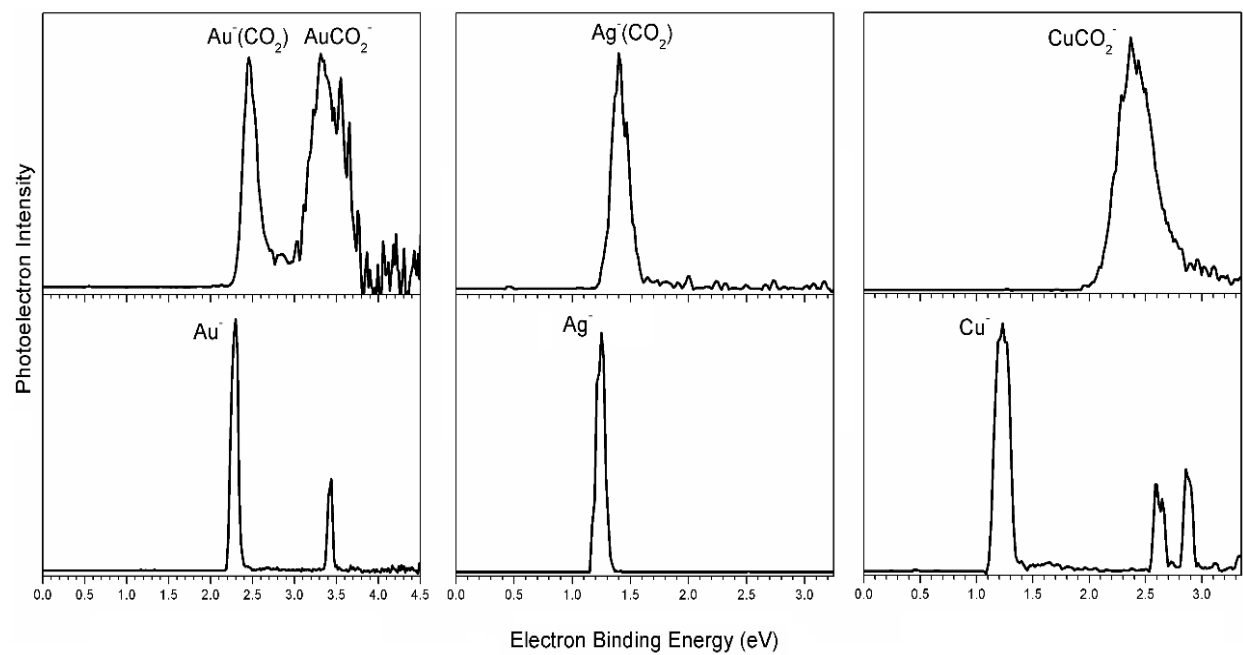
Figure 3.1.1
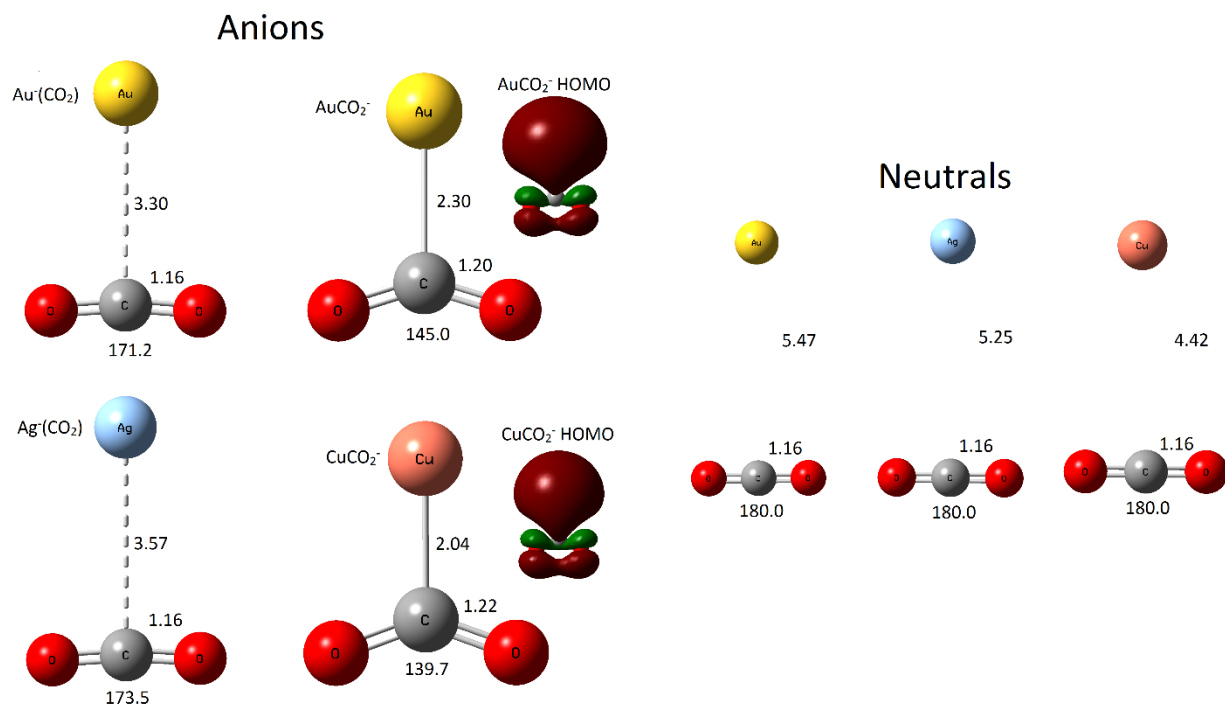
Figure 3.1.2
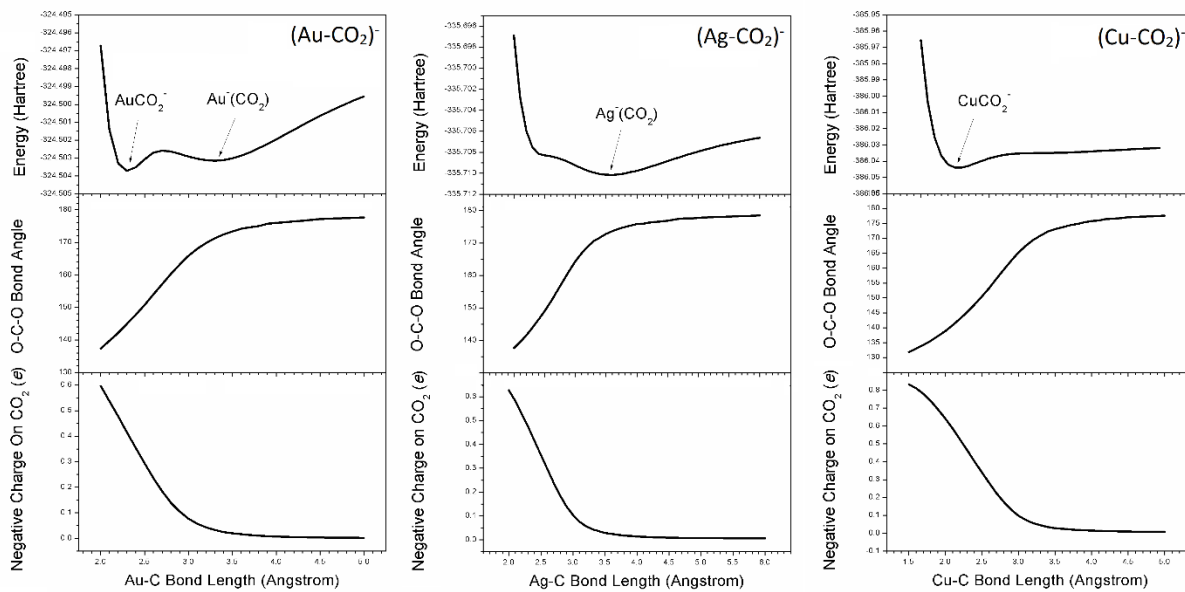
Figure 3.1.3
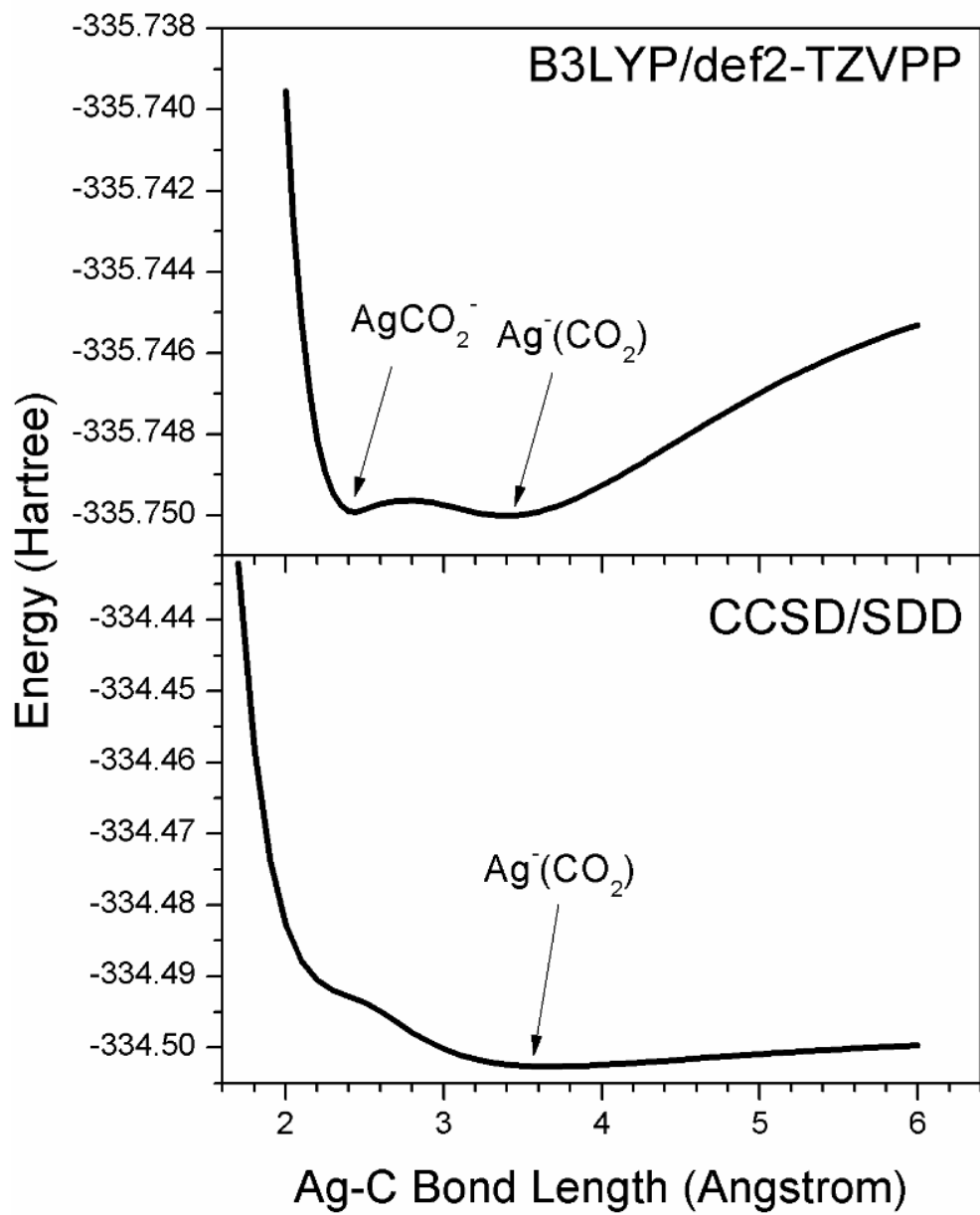
Figure 3.1.4

3.2 CO_2 Hydrogenation by PtH_n^- Cluster Anions in the Gas Phase

Xinxing Zhang, Gaoxiang Liu, Kit Bowen*

Department of Chemistry, Johns Hopkins University, Baltimore, Maryland 21218, USA

[a] Electronic mail: kbowen@jhu.edu

Abstract

Gas phase reactions between PtH_n^- cluster anions and CO_2 are investigated by mass spectrometry, anion photoelectron spectroscopy and theoretical calculations. Two major products, $PtCO_2H_{1,3}^-$, are identified. For $PtCO_2H^-$, its molecular structure can be written as $HPtCO_2^-$ where CO_2 is bonded to the Pt atom in the form of being bent and activated. For $PtCO_2H_3^-$, its structure can be written as $H_2Pt(formate)^-$ where CO_2 has been hydrogenated to formate. Detailed mechanistic studies reveal the reaction pathways and the energy levels, which give evidences that the hydrogenation of CO_2 by PtH_3^- is highly energetically favorable. This study can be appreciated in potential catalytic applications.

Introduction

Transformation of carbon dioxide into reduced, high value molecules, such as methanol and formic acid, is of great interest due to environmental and economic considerations. Ligand protected transition metal hydride complexes, written as L_nMH, play important roles in these processes.[1-18] The critical step of the reduction involves the insertion of C=O into the M-H bond to produce a formate-metal adduct, L_nM-OC(O)H, which can then generate the reduction product formate in the solution, or be further reduced to other final products by additional metal hydrides. All of these transition metal hydrides, however, are in the form of complexes protected by various ligands. Pure metal hydrides, on the other hand, are scarcely reported in CO_2 reduction. Andreas Züttel et al peformed the methanation of CO_2 on the surface of Mg_2NiH_4.[19] Similar reactions were also achieved by the catalysis of the hydrogen storage materials $LaNi_5$ and $LaNi_4Cr$ where the hydrides played critical roles.[20] In the gas phase, reactions between cluster cations, FeD^+, CoD^+, NiD^+, and hydrocarbons were reported.[21] To the best of our knowledge, there has been no study on the hydrogenation of CO_2 with gas phase metal hydride clusters yet.

The lack of CO_2 reduction with gas phase metal hydride clusters is partially due to the difficulty in synthesizing them. If accessible, study of this kind, usually with the help of modern characterization methods such mass spectrometry and laser spectroscopy as well as theoretical calculations, helps to understand the reaction mechanism at the atomic and molecular level. The mentioned CO_2 hydrogenation reactions,[1-18] on the contrary, were mostly performed in much more complicated environments such as solutions, which makes the fine control of each molecule and thus the investigation of reaction mechanism difficult. Very recently, with our unique pulsed arc cluster ionization source, we were able to produce various transition metal hydride cluster anions in the gas phase. For example, a recently discovered $PtZnH_5^-$ cluster possessed an unprecedented

planar pentagonal coordination between the H_5^- moiety and Pt, and exhibited special σ-aromatic character.[22] Afterwards, we extended this work to the isoelectronic and isostructural cluster $PtMgH_5^-$ in which similar bondings were also found. We also have synthesized a lot of other Pd-containing hydride cluster anions. Given this ability of ours and the conventional wisdom that these transition metals have been widely used as hydrogenation catalyst, we envision that these hydride cluster anions can be utilized as excellent hydrogen source for hydrogenation of unsaturated molecules such as CO_2.

In the current paper, we present the experimental results of the reactions between CO_2 and platinum hydride cluster anions PtH_n^-. Two products, $PtCO_2H_{1,3}^-$ were identified by mass spectrometry and characterized by anion photoelectron spectroscopy. For $PtCO_2H^-$, its molecular structure can be written as $HPtCO_2^-$ where CO_2 is bonded to the Pt atom in the form of being bent and activated. For $PtCO_2H_3^-$, its structure can be written as $H_2Pt(formate)^-$ where CO_2 has been hydrogenated to formate. *Ab initio* calculations were performed to reveal the reaction mechanism. How CO_2 was activated and hydrogenated in the current case has been explained in details at the atomic level.

Experimental Method

Anion photoelectron spectroscopy is conducted by crossing a mass-selected beam of negative ions with a fixed-energy photon beam and energy analyzing the resulting photodetached electrons. This technique is governed by the energy-conservation relationship, $hν = EBE + EKE$, where $hν$, EBE, and EKE are the photon energy, electron binding (transition) energy, and the electron kinetic energy, respectively. Our photoelectron spectrometer, which has been described

previously,[23] consists of one of several ion sources, a linear time-of-flight mass spectrometer, a mass gate, a momentum decelerator, a neodymium-doped yttrium aluminum garnet (Nd:YAG) laser for photodetachment, and a magnetic bottle electron energy analyzer. Photoelectron spectra were calibrated against the well-known photoelectron spectrum of Cu^-.[24] The PtH_n^- anions were generated using a pulsed arc cluster ionization source (PACIS), which has been described in detail elsewhere.[25] In brief, a ~30 μs long 150 V electrical pulse applied across anode and sample cathode in the discharging chamber vaporizes the Pt atoms. The sample cathode was prepared in a nitrogen protected glove box, where fresh Pt powder was firmly pressed onto a copper rod. Almost simultaneously, 220 psi of ultrahigh purity hydrogen gas was injected into the discharge region, where it was dissociated into hydrogen atoms. The resulting mixture of atoms, ions, and electrons then reacted and cooled as it flowed along a 15 cm tube before exiting into high vacuum. To perform the reaction between CO_2 and PtH_n^-, pure CO_2 was injected into the downstream of the 15 cm tube using a second pulsed valve. The resultant anions were then extracted and mass-selected prior to photodetachment. Due to the isotopes of Pt, photoelectron spectra were taken from all of the isotopic peaks for analysis and to avoid mutual contamination of the photoelectron spectra.

Computational Method

Theoretical studies on the reaction between carbon dioxide and platinum hydrides and the resultant product were performed using the Orca program package.[26] Geometry optimizations and frequency calculations were carried out using the hybrid density functional theory (DFT) PBE0.[27,28] The electron affinity (EA) and vertical detachment energy (VDE) of the optimized structures were calculated using PBE0 and B3LYP[29] DFT functionals with the unrestricted Kohn-

Sham solution, and then improved by single point energy calculations at the CCSD and CCSD(T) level of theory.[30] Natural Population Analysis (NPA) was conducted to examine the charge distribution at the PBE0 level. [31] NPA has been found to be satisfactory in predicting charge distributions within a cluster.[32,33] The initial estimated structures of transition states were obtained by selecting appropriate coordinates from relaxed potential energy surface scans. Vibrational frequencies were calculated to verify if the stationary points are local minima or transition states. The Stuttgart effective core potential SDD (for Pt) and aug-def2-tzvpp basis sets (for C, H, O) were used throughout our computations.[34]

Results and discussion

Experimental results

The mass spectra with or without CO_2 pulsed into the PACIS reactor tube are shown in Figure 3.2.1. When CO_2 was not added, only PtH_n^- were observed in the mass spectrum (Figure 3.2.1A). The species of PtH_n^- were characterized by taking the photoelectron spectra (PES) of every mass peak that was observed in this PtH_n^- series. By comparing the obtained spectra, PtH_n^- where n = 0, 1, 2, 3 and 5 are identified. $PtCO_2H_m^-$ cluster series showed up in the mass spectrum when CO_2 was added (Figure 3.2.1B). The lowest mass peak for $PtCO_2H^-$ is 239 while the highest mass peak for $PtCO_2H_3^-$ is 245, hence, $PtCO_2H^-$ and $PtCO_2H_3^-$ exist. $PtH_2CO_2^-$ is not formed because of the absence of ion intensity at mass = 244. Noteworthy, $PtCO_2H_{1,3}^-$ both have close-shell electron configuration.

Figure 3.2.2 presents the photoelectron spectrum of $PtCO_2H_3^-$ with 3rd harmonic Nd:YAG laser (355nm, 3.496 eV). It was taken at mass = 245 to make sure that the photoelectron signal

was mostly from $PtCO_2H_3^-$ and there was the least $PtCO_2H^-$ contribution to it. A major electron binding energy (EBE) band ranging from 3.1 to 3.3 eV and peaking at 3.24 eV is observed. The intensity maximum in the EBE band is its vertical detachment energy (VDE), the transition energy where the Franck-Condon overlap is maximal between the anion wave functions and its neutral counterpart. The adiabatic electron affinity (EA) is the energy difference between the ground state of the anion and the ground state of its neutral counterpart. The EA of $PtCO_2H_3^-$ is estimated to be ~3.1 eV by extrapolating of the lower EBE side. Please note that the small peak at EBE = 3.08 eV and other very weak features at low EBE side are from the much less abundant isotope of $PtCO_2H^-$ at mass = 245.

The photoelectron spectrum of $PtCO_2H^-$ is much more complicated than that of $PtCO_2H_3^-$, with at least four EBE bands identified (Figure 3.2.3C). Such a complexity can be accounted by the process of photodissociation of $PtCO_2H^-$ into PtH^- and CO_2 followed by photodetachment of the resultant anion PtH^- as well as the parent anion $PtCO_2H^-$. In order to confirm this idea, it is necessary to compare the spectrum with that of PtH^-. Taking a pure photoelectron spectrum of PtH^- is impossible because every isotopic mass peak of PtH^- is at least overlapped with one of three other anions: Pt^-, PtH_2^- and PtH_3^-. However one can still acquire its photodetachment features by comparing the photoelectron spectra at mass 194, which is pure Pt^-, and mass 195, which is a mix of Pt^- and PtH^- (Figure 3.2.3A and 3B). For mass at 195, in addition to the Pt^- peaks at 2.1, 2.9 and 3.4 eV (marked by green dots), three new peaks appear at 1.60, 1.85 and 3.08 eV (marked by red dots) and thus these three peaks are attributed to PtH^-. Noticeably, these three peaks reappear in the photoelectron spectrum of $PtCO_2H^-$ not only at the same positions but also with almost identical relative intensities. Therefore it is reasonable to conclude that the peaks denoted by red dots in the spectrum of $PtCO_2H^-$ are from PtH^-, which is a photodissociation product of $PtHCO_2^-$. The peak at

high EBE side (blue dots) should be the EBE bands of the parent $PtHCO_2^-$ cluster anion. It has a step at 3.3 eV and peaks at around 3.5 eV. Therefore its VDE is determined to be 3.5 eV and its EA is determined to be 3.2 eV by extrapolating the step. A computational study will be presented to further illustrate the photoelectron spectroscopic results.

Theoretical study

Figure 3.2.4 presents the optimized structures of $PtCO_2H_{1,3}^-$. For $PtH_3CO_2^-$, the global minimum is found to be a C_{2v} structure. It is in the form of a formate adduct of Pt hydride, namely $H_2Pt(formate)^-$, with the Pt atom planar tetracoordinated (PTC) by two H atoms and the two O atoms of the formate moiety. A PTC structure is commonly seen for Pt. We assume that the reaction starts with PtH_3^- anion and neutral CO_2, and the formation of such a formate-type product is the result of the CO_2 molecule insertion into the Pt-H bond. Natural Population Analysis (NPA) shows that, along with the CO_2 insertion and H atom migration, charge is also transferred from Pt hydride anion to CO_2, making the formate moiety negatively charged by -0.77 e. Unlike $PtCO_2H_3^-$, in the optimized structure of $PtCO_2H^-$, the H atom is still bonded to Pt. The Pt atom also bounds to the C atom of the CO_2 moiety, which is bent from its original linear structure, indicating that CO_2 is activated by PtH^-. NPA shows that the negative charge is also partially transferred from PtH^- to CO_2, with a total charge of -0.66 e on the CO_2 part. The angle of the O-C-O bond is determined to be 139.5°, very close to the bond angle of free CO_2^- at its global minimum (134°).[35-37] This indicates that even though hydrogenation is not occurred, CO_2 still gets highly activated through the interaction with PtH^-. This behavior is similar to Au^-, which is shown to be able to activate CO_2 through charge transfer.[38] Since PtH^- and Au^- are isoelectronic, it is reasonable that they have similar behavior in CO_2 activation.

Table 3.2.1 presents the electron affinity (EA) values and vertical detachment energy (VDE) values of $PtHCO_2^-$ and $PtH_3CO_2^-$ calculated at different theory levels. The agreement across different theory levels obvious. The calculated values are in good agreement with experimental results as well.

DFT calculations were carried out to investigate the mechanism of CO_2 activation and hydrogenation. The reaction pathways were calculated for the reactions of PtH^- and PtH_3^- with CO_2, respectively. The pathway of CO_2 hydrogenation by PtH_3^- is presented in Figure 3.2.5. Before reaction PtH_3^- has a C_{2v} symmetry. The first step of the reaction is the CO_2 activation through charge transfer from PtH_3^-. CO_2 activation is completed by its interaction with the Pt atom, since the Pt atom possesses almost all the negative charge of PtH_3^- according to the NPA result. After being activated, CO_2 is ready to accept an H atom from PtH_3^-. The insertion of CO_2 into the Pt-H bond needs to overcome an energy barrier of 0.42 eV. After the hydrogen transfer the CO_2 the hydrogenation process is completed, and this local minima has a structure as formic acid. However, this structure has a VDE of 3.88 eV and was not observed in the photoelectron spectrum. In order to reach the global minimum structure as shown in Figure 3.2.4A, this formic acid type structure needs to overcome a small rotational barrier (0.09 eV) so that the other O atom can coordinate with the Pt atom, and this bonding further stabilizes the whole cluster.

Figure 3.2.6 presents the reaction between CO_2 and PtH^-. Similar to the first step of the reaction between PtH_3^- and CO_2, here CO_2 is also activated through charge transfer from Pt atom and a bond between Pt atom and C atom is formed. The reaction stops at the stage of activation, however, rather than move on to CO_2 hydrogenation. Also, the CO_2 activation provides a stabilization energy as large as 1.70 eV for $PtCO_2H^-$, which is much larger than that of $PtCO_2H_3^-$. Though not seen in experiment, further calculation is still performed to explore the possibility of

CO_2 hydrogenation by PtH^-. The energy barrier for H atom transfer is calculated to be as high as 2.84 eV, which is much higher than the 0.42 eV when PtH_3^- reacts with CO_2. Such a high activation energy is almost impossible to acquire in gas phase reactions where collisions between molecules and clusters dominate the whole process. Therefore, the high energy barrier for H transfer is accounted as the reason why PtH^- is unable to hydrogenate CO_2.

CO_2 activation and hydrogenation occur when it interacts with $PtH_{1,3}^-$, and calculation shows for both cases it is achieved by firstly interacting with the Pt atom. For PtH_5^-, it has a D_{5h} structure, and the Pt atom is surrounded by H atoms making CO_2 difficult to access the Pt (Supporting Information). PtH_5^- is a very stable cluster which processes σ-aromaticity. This may be the reason why $PtCO_2H_5^-$ was not observed in the mass spectrum.

Conclusion

In summary, CO_2 activation and hydrogenation by PtH_n^- cluster anions were achieved using our unique PACIS source and the reactor tube attached to it. With a combined study of photoelectron spectroscopy and theoretical investigation, the mechanisms of these reactions were revealed. While PtH^- could remarkably activate CO_2, PtH_3^- went further to hydrogenate it into formate. The low energy barrier for H atom transfer from PtH_3^- to CO_2 made PtH_3^- a good H source for CO_2 hydrogenation. All of the calculated results have great agreement with experiment. We believe these results can shed light designing proper materials for efficient CO_2 hydrogenation.

Reference

1. P. G. Jessop, T. Ikariya and R. Noyori, *Chem. Rev*. **95**, 259 (1995).

2. M. S. Jeletic, M. L. Helm, E. B. Hulley, M. T. Mock, A. M. Appel and J. C. Linehan, *ACS Catal*. **4**, 3755 (2014).

3. M. A. Rankin and C. C. Cummins, *J. Am. Chem. Soc.* **132**, 10021 (2010).

4. A. J. M. Miller, J. A. Labinger and J. E. Bercaw, *Organometallics* **30**, 4308 (2011).

5. B. P. Sullivan and T. J. Meyer, J. Chem. Soc. *Chem. Commun*. 1244 (1984).

6. M. K. Whittlesey, R. N. Perutz and M. H. Moore, *Organometallics* **15**, 5166 (1996).

7. P. Kang, C. Cheng, Z. Chen, C. K. Schauer, T. J. Meyer and M. Brookhart, *J. Am. Chem. Soc.* **134**, 5500 (2012).

8. D. J. Darensbourg, A. Rokicki and M. Y. Darensbourg, *J. Am, Chem.* Soc. **103**, 3223 (1991).

9. D. L. DuBois and D. E. Berning, *Appl. Organometal. Chem.* **14**, 860 (2000).

10. **J.** R. Pugh, M. R. M. Bruce, B. P. Sullivan and T. J. Meyer, *Inorg. Chem.* **30**, 86 (1991).

11. S. E. Clapham, A. Hadzovic, R. H. Morris, *Coord. Chem. Rev*. **248**, 2201 (2004).

12. W. Leitner, *Angew. Chem., Int. Ed. Engl.* **34**, 2207 (1995).

13. P. G. Jessop, T. Ikariya and R. Noyori, *Chem. Re*v. **96**, 259 (1996).

14. T. J. Marks and et al. *Chem. Re*v. **101**, 953 (2001).

15. M. Aresta and A. Dibenedetto. *Dalton Trans.* **28**, 2975 (2007).

16. G. Fachinetti, C. Floriani, A. Roselli and S. Pucci, *J. Chem. Soc., Chem. Commun.* **6**, 269 (1978).

17 S. Gambarotta, S. Strologo, C. Floriani, A. Chiesi-Villa and C. Guastini, *J. Am. Chem. Soc.* **107**, 6278 (1985).

18 A. Cutler, M. Raja, and A. Todaro, *Inorg. Chem.* **26**, 2877 (1987).

19 S. Kato, J. C. Crivello, P. Rossbach, A. Borgschulte, D. Wiedenmann, Y. Lu, A. Remhof, D. Ferri, M. Bielmann, M. Parlinska-Wojtan and A. Züttel, *Phys. Chem. Chem. Phys.* **14**, 5518 (2012).

20 K. Soga, K. Otsuka, M. Sato, T. Sano and S. Ikede, *Journal of the Less-Common Metals*, **71**, 259 (1980).

21 T. J. Carlin, L. Sallans, C. J. Cassady, D. B. Jacobson and B. **S.** Freiser, *J. Am. Chem. Soc.* **105**, 6320 (1983).

22 X. Zhang, G. Liu, G. Gantefoer, K. H. Bowen and A. N. Alexandrova, *J. Phys. Chem. Lett.* **5,** 1596 (2014).

23. M. Gerhards, O. C. Thomas, J. M. Nilles, W.-J. Zheng, and K. H. Bowen, *J. Chem. Phys.* **116**, 10247 (2002).

24. J. Ho, K. M. Ervin, and W. C. Lineberger, *J. Chem. Phys.* **93**, 6987 (1990).

25. X. Zhang, Y. Wang, H. Wang, A. Lim, G. Ganteför, K. H. Bowen, J. U. Reveles and S. N. Khanna, *J. Am. Chem. Soc.* **135,** 4856 (2013).

26. F. Neese, *Wiley Interdiscip. Rev.: Comput. Mol. Sci.* **2**, 73 (2012).

27. J. P. Perdew, M. Ernzerhof; K. Burke, *J. Chem. Phys*, **105**, 9982 (1996).

28. C. Adamo, B. Vincenzo Barone, *J. Chem. Phys.* **110**, 6158 (1999).

29. R. G. Parr and W. Yang, *Density-Functional Theory of Atoms and Molecules* (Oxford University Press, Oxford, 1989); A. D. Becke, *J. Chem. Phys*. **98**, 5648 (1993); J. P. Perdew, J. A. Chevary, S. H. Vosko, K. A. Jackson, M. R. Pederson, D. J. Singh, and C. Fiolhais, *Phys. Rev. B* **46**, 6671 17 (1992).

30. J. Cizek, *Adv. Chem. Phys*. **14**, 35 (1969); G. D. Purvis III and R. J. Bartlett, *J. Chem. Phys*. **76**, 1910 (1982); G. E. Scuseria, C. L. Janssen, and H. F. Schaefer III, *ibid*. **89**, 7382 (1988); G. E. Scuseria and H. F. Schaefer III, *ibid*. **90**, 3700 (1989).

31. E. Carpenter and F. Weinhold, *J. Mol. Struct.: THEOCHEM* 169, 41 (1988); J. E. Carpenter, Ph.D. thesis, University of Wisconsin, 1987; J. P. Foster and F. Weinhold, *J. Am. Chem. Soc*. **102**, 7211 (1980); A. E. Reed and F. Weinhold, *J. Chem. Phys*. **78**, 4066 (1983); A. E. Reed, L. A. Curtiss, and F. Weinhold, *Chem. Rev*. **88**, 899 (1988).

32. H. Wang, X. Zhang, J. Ko, A. Grubisic, X. Li, G. Ganteför, H. Schnöckel, B. Eichhorn, M. Lee, P. Jena, A. Kandalam, B. Kiran, and K. H. Bowen, *J. Chem. Phys.* **140,** 054301 (2014).

33. H. Wang, Y. Ko, X. Zhang, G. Gantefoer, H. Schnoeckel, B. W. Eichhorn, P. Jena, B. Kiran, A. K. Kandalam, and K. H. Bowen, *J. Chem. Phys*. **140**, 124309 (2014).

34. D. Andrae, U. Haeussermann, M. Dolg, H. Stoll and H. Preuss, *Theor. Chim. Acta* **77**, 123 (1990); J. M. L. Martin and A. Sundermann, J. Chem. Phys. **114**, 3408 (2001); F. Weigend, R. Ahlrichs, *Phys. Chem. Chem. Phys*. **7**, 3297 (2005); T. H. Dunning, Jr. *J. Chem. Phys*. **90**, 1007 (1989).

35. R. N. Compton, P. W. Reinhardt, and C. D. Cooper, *J. Chem. Phys*. **63**, 3821 (1975).

36. M. Knapp, O. Echt, D. Kreisle, T. D. Mark, and E. Recknagel, *Chem. Phys. Lett.* **126**, 225 (1986).

37. S. T. Arnold, J. V. Coe, J. G. Eaton, C. B. Freidhoff, L. H. Kidder, G. H. Lee, M. R. Manaa, K. M. McHugh, D. Patel-Misra, H. W. Sarkas, J. T. Snodgrass, and K. H. Bowen, *in Proceedings of the Enrico Fermi International School of Physics, CVII Course,* Varenna, edited by G. Scoles (North-Holland, Amsterdam, 1989), pp. 467-490.

38. X. Zhang, S. K. Kim, and K. H. Bowen, *J. Chem. Phys.* Submitted (2015).

Table 3.2.1. Experimental and calculated VDE/EA values for $PtCO_2H_{1,3}^-$. All numbers are in eV.

Anion	Expt.	UPBE0	CCSD	CCSD(T)
$PtCO_2H_3^-$	3.24/3.1	3.37/3.21	3.10/2.94	3.19/2.94
$PtCO_2H^-$	3.48/3.25	3.55/3.23	3.38/3.28	3.46/3.44

Figure Captions

Figure 3.2.1. The mass spectra of PtH_n^- cluster anions without (A) and with (B) CO_2 injected into the reactor.

Figure 3.2.2. Photoelectron spectrum of $PtCO_2H_3^-$ taken at mass 245 with 355 nm (3.496 eV) photons.

Figure 3.2.3. Photoelectron spectra of Pt^- (taken at mass = 194, A), Pt^- and PtH^- (taken at mass = 195, B) and $PtCO_2H^-$ (taken at mass = 239, C). Peaks from Pt^-, PtH^- and $PtCO_2H^-$ are denoted by green, red and blue dots, respectively.

Figure 3.2.4. Optimized structures of $PtCO_2H_3^-$ (A) and $PtCO_2H^-$ (B).

Figure 3.2.5. Calculated reaction pathway for the CO_2 hydrogenation by PtH_3^-.

Figure 3.2.6. Calculated reaction pathway for the CO_2 activation and possible hydrogenation by PtH^-. The photodisscociation process of $PtCO_2H^-$ is also presented.
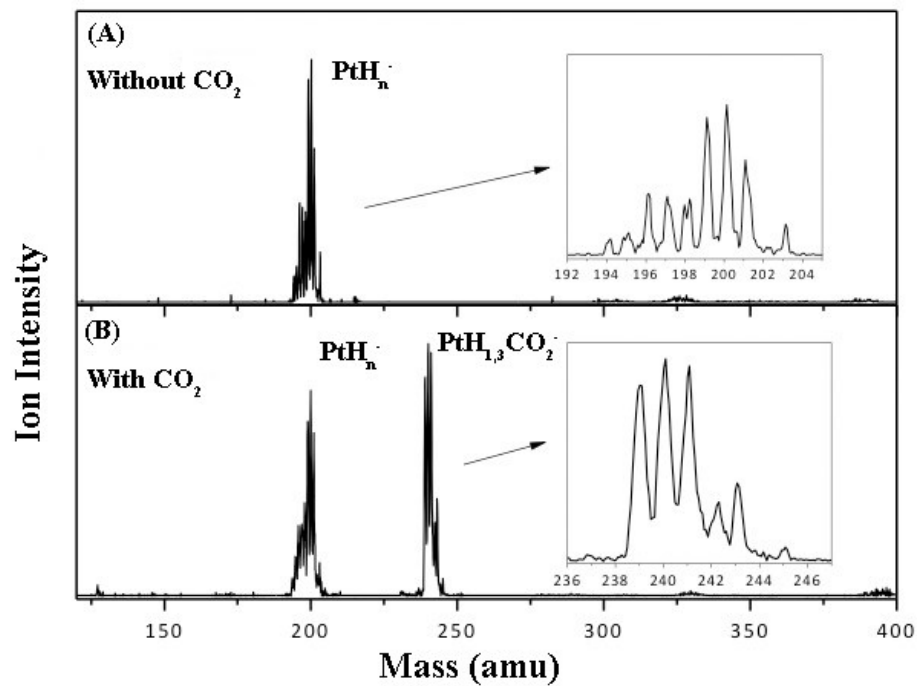
Figure 3.2.1
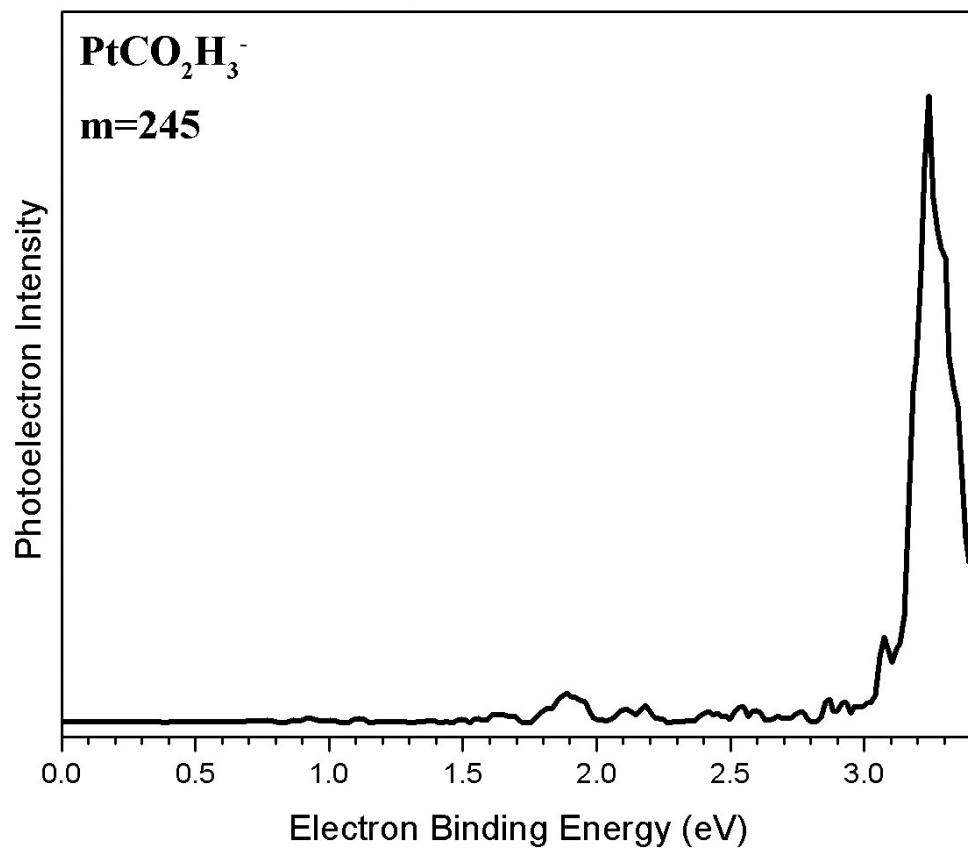
Figure 3.2.2
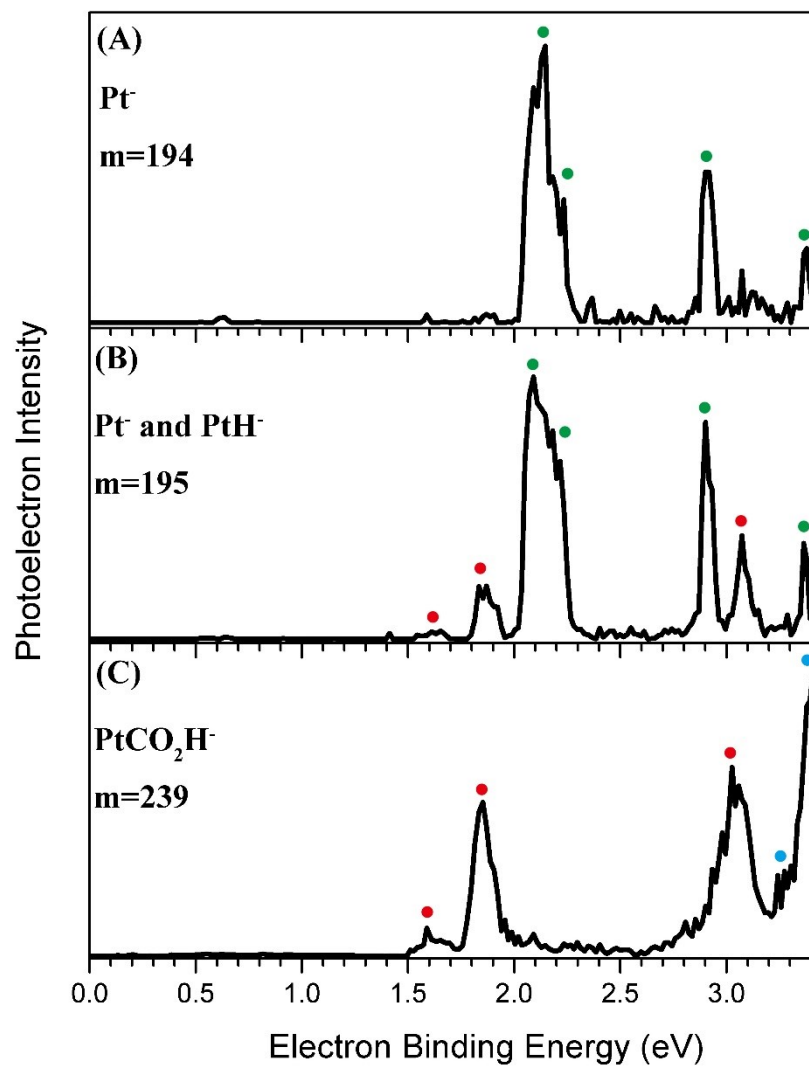
Figure 3.2.3

Figure 3.2.4

$$PtH_3^- + CO_2 \longrightarrow H_2Pt(HCO_2)^-$$
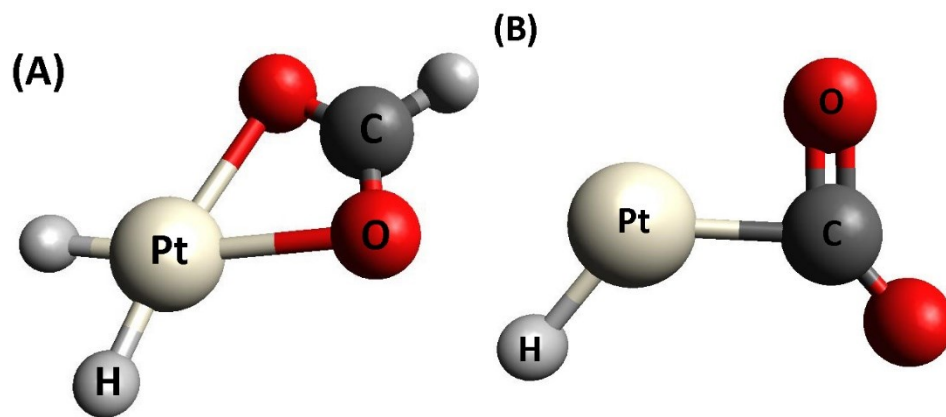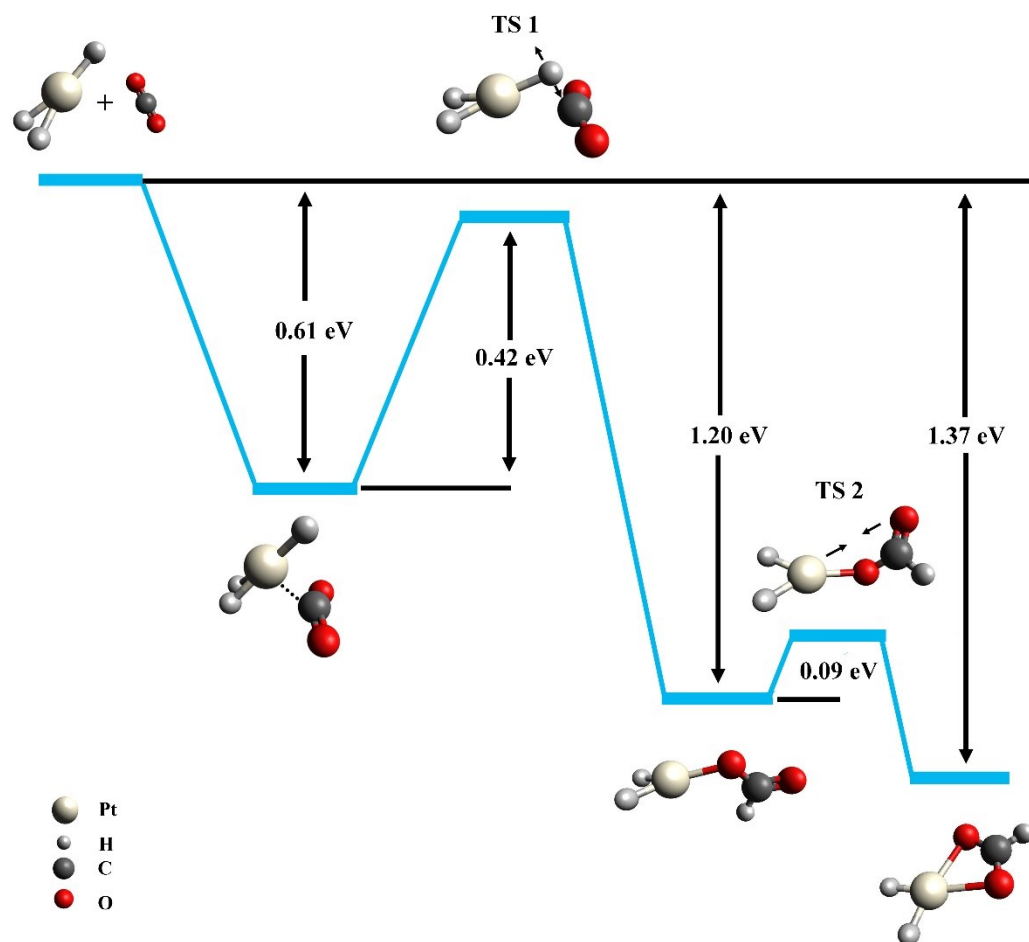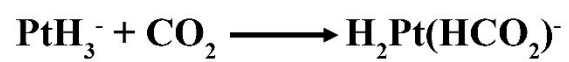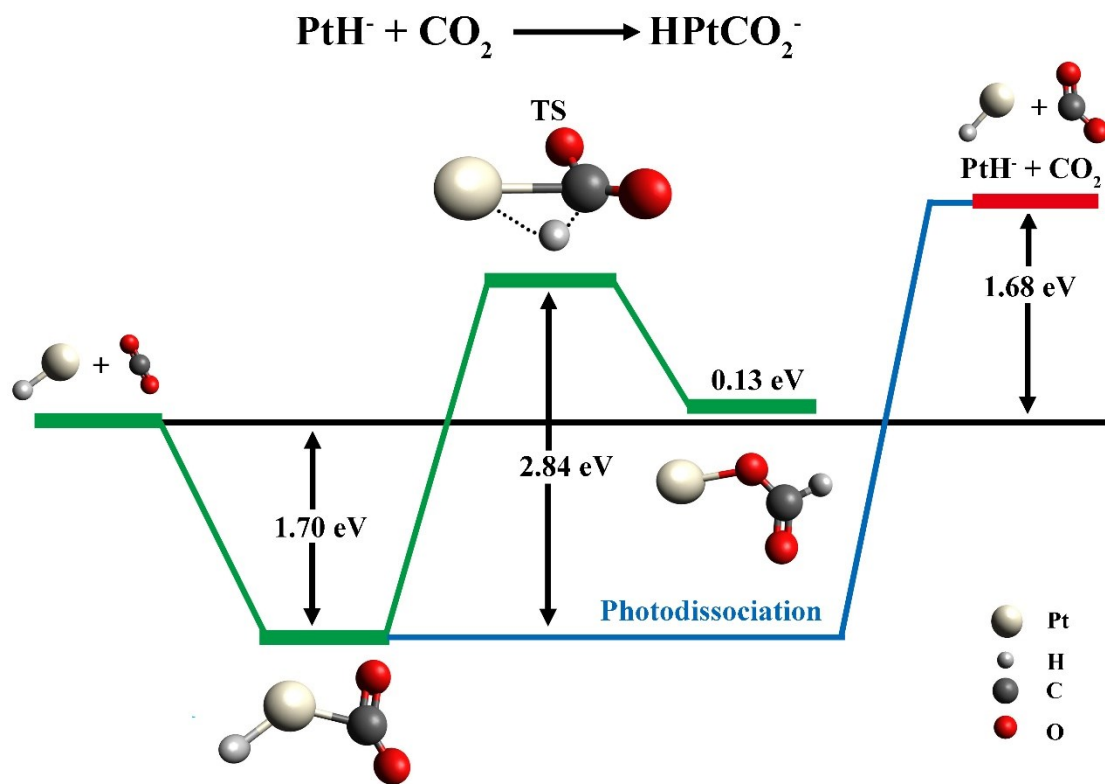
Figure 3.2.5

Figure 3.2.6

CHAPTER 4. The Revelry of Aluminum Hydride Related Clusters

Our group discovered more than 200 new aluminum hydride cluster anions, $Al_xH_y^-$, afterwards, my work focused on the discovery of new clusters that are related to them. All of them are mutually linked in different manners.

In Section 4.1, a mass spectrometric study of aluminum hydride cluster cations are presented, where the stability of several stable clusters are interpreted by theory. All of the stable clusters, as revealed by mass spectrum, can be viewed as the assembly of smaller stable units.

In Section 4.2, the derivative of AlH_4^-, $AlH_2Cp^*Cl^-$, is discussed. Its special structure and stability are pointing towards the direction of being used as a building block for ionic liquid or salt.

In Section 4.3, a novel cluster anion $Li_2Al_3H_8^-$ shows an unprecedented homocatenated chain, Al-Al-Al. By obtaining electron from Li, Al transmutates into C, and the $Al_3H_8^{3-}$ kernel mimics propane, C_3H_8. This discovery sheds light on the synthesis of a new salt, $Li_3Al_3H_8$, an extension of an existing salt, $LiAlH_4$.

In Section 4.4, I designed a new precursor, $Al^+Ph_2CO^-$, for synthesizing low oxidation state Al containing compounds. $Al^+Ph_2CO^-$ is similar to the famous monovalent AlCl, but the synthesis should be much simpler. Our inorganic chemistry collaborator will start the synthesis shortly.

In Section 4.5, the photoelectron spectroscopy of o-carborane, $C_2B_{10}H_{12}^-$, is presented. Different from published work in which people thought this molecule had a negative EA, our experiment gave evidences of its very high electrophilicity.

In Section 4.6, series data of carbon aluminum hydride cluster anions, $C_xAl_yH_z^-$, is displayed. These clusters, viewed as derivatives of $Al_xH_y^-$, promise potential energetic materials.

4.1 Aluminum Hydride Cluster Cations: A Mass Spectrometric and Theoretical Study

Xinxing Zhang, [1] Haopeng Wang, [1] Boggavarapu Kiran, [2] and Kit Bowen[1]

[1] *Department of Chemistry, Johns Hopkins University, Baltimore, Maryland 21218, USA*

[2] *Department of Chemistry, McNeese State University, Lake Charles, Louisiana 70609, USA*

Abstract

A combined study using mass spectrometry and density functional theory (DFT) was conducted to investigate aluminum hydride cluster cations, $Al_nH_m^+$ ($1 \leqslant n \leqslant 5$, $0 \leqslant m \leqslant 12$). The mass spectra revealed about 20 undiscovered aluminum hydride cluster cations. Among these new species, several of them showed unusual stability. Density Functional Theory calculation was conducted to investigate the structures of these clusters. All of these stable clusters can be viewed as assemblies of smaller, stable units, such as Al^+, AlH_3, $Al_2^{+/0}$, H^+ and H_2.

Introduction

Though boron can form many hydrides, known as boranes, its sister element, aluminum, only has a few. The chemistry of aluminum hydrides had long been limited to AlH_3 and Al_2H_6 seen in cryogenic matrices and perhaps the gas phase;[1] alane, $(AlH_3)_n$, a polymeric solid; and AlH_4^- along with its alkali metal salts.[2] Such aluminum hydride species are thought to be stable. Ever since the groundbreaking work of Li et al. on the unusual stability of gas-phase Al_4H_6 cluster anions, [3] the chemistry of aluminum hydride has been largely expanded. Over the past few years, many aluminum hydride cluster anions were discovered in gas-phase molecular beams. [3-12] Most of these were prepared in a unique ion beam source, identified by mass spectrometry, and in some cases studied by a combination of photoelectron spectroscopy and theoretical computations.

Despite the fast growing family of aluminum hydride cluster anions, the research on its cations has been surprisingly scarce. The first report on the cations of probably the most well-known aluminum hydrides, AlH_3^+ and $Al_2H_6^+$, appeared half a century ago, in which the cations were prepared by slow evaporation of aluminum into hydrogen gas.[13] Ever since then there hasn't been much breakthrough in finding aluminum hydride cations. Only limited species, such as $AlH_{1,2,4}^+$ and AlH_2^+, were discovered.[14, 15] In a theoretical study of the analogues of aromatic cyclopropenyl cation ($C_3H_3^+$), Sirnivas. G. et al. indicated the presence of $Al_3H_6^+$. Unlike $C_3H_3^+$, they pointed out that the π-delocalization stabilizing effect was largely diminished for $Al_3H_6^+$, thus rather than the planar Al_3 ring geometry, $Al_3H_6^+$ preferred to form other stable nonplanar isomers.[16]

Aluminum is electron deficient in nature, which may be the reason why aluminum hydride clusters tend to capture an electron and form such a large variety of anions in gas phase. Its cation chemistry, however, is not well understood. With this interest, we investigated aluminum hydride cluster cations using a combined study of mass spectrometry and theoretical computation. Around

20 previously unobserved $Al_nH_m^+$ clusters were revealed in the mass spectrum. A density functional theory (DFT) study was carried out to investigate the species with relatively higher intensities in the mass spectrum, such as $Al_3H_4^+$, $Al_3H_6^+$, $Al_4H_3^+$, $Al_4H_6^+$, $Al_4H_9^+$, $Al_5H_6^+$, $Al_5H_{12}^+$.

Experimental

In the present work, the aluminum hydride cations were generated using a pulsed arc cluster ionization source (PACIS), which has been described in detail elsewhere.[17] In brief, a ~30 μs long 150 V electrical pulse applied across anode and sample cathode of the discharging chamber vaporizes the Al atoms. The sample cathode was an aluminum rod. Almost simultaneously, 200 psi of ultra-high purity hydrogen gas was injected into the discharge region, where it was dissociated into hydrogen atoms. The resulting mixture of atoms, ions, and electrons then reacted and cooled as it flowed along a 20 cm tube before exiting into high vacuum. The resulting canions were then extracted and analyzed by mass spectrometer.

Computational method

Electronic structure calculations based on density functional theory (DFT) were carried out on positively charged $Al_3H_4^+$, $Al_3H_6^+$, $Al_4H_3^+$, $Al_4H_6^+$, $Al_4H_9^+$, $Al_5H_6^+$ and $Al_5H_{12}^+$ clusters using the Gaussian 09 program.[18] The Becke's three parameter hybrid exchange functional with Lee, Yang, and Parr correlation functional36 (B3LYP)[19-21] form, along with 6-311+G** basis set[22] was used for all calculations. In the geometry optimization, the convergence criterion for energy was set to 10^{-9} hartree, while the gradient was converged to 10^{-4} hartree/Å.

Results and discussion

The whole mass spectrum showing $Al_nH_m^+$ species observed in this study is presented in Figure 4.1.1. Figure 4.1.2(a)-(e) present the magnified, separated versions of these mass spectra for n=1-5. The mass spectra revealed around 20 new aluminum hydride cluster cations, and a very distinct hydride formation trend for different Al atom number per cluster. For n=1, no hydride was formed; only Al atom cation was observed in the mass spectra. The peak was intense, indicating Al^+ was relatively stable in gas phase. Aluminum hydride cations started to come into existence when n = 2. However, the peak of Al_2H^+ was rather weak comparing to $Al2^+$ (Figure 4.1.2(b)). The tendency of the formation of aluminum hydrides changed dramatically when n went from 2 to 3, 4 and 5. For $Al_3H_m^+$ species, the number of bonded hydrogen atom increased stepwise from 1 to 7, though some of them have relatively weak signals (Figure 4.1.2(c)). $Al_4H_m^+$ and $Al_5H_m^+$ clusters followed the same pattern as $Al_3H_m^+$, with the hydrogen atom number as high as 9 for $Al_4H_m^+$ and 12 for $Al_5H_m^+$ (Figure 4.1.2(d, e)).

Among all these newly discovered aluminum hydride cluster cations, $Al_3H_6^+$ showed the highest intensity in the whole mass spectrum (Figure 4.1.1), which demonstrates that this cluster cation is unusually stable. The DFT study was performed in order to gain an understanding of its special stability. Figure 4.1.3 presents the lowest-energy structure of $Al_3H_6^+$. This global minima is a four H-bridged C_{2v} structure with a lone pair and can be interpreted as stable Al_2H_6 interacting with stable Al^+. This structure is different from that of its borane cation analog, in which every borane atom is bonded to three hydrogen atoms.[16] Our calculation on the structure of $Al_3H_6^+$ is in consistency with the work of Sirnivas. G. et al.,[16] in which they pointed out that the π delocalization stabilizing effect was weak for $Al_3H_6^+$ cluster, and this would result in the co-existence of several nonplanar isomers as stable species.

Also, we observed that $Al_3H_4^+$ is also relatively strong in n = 3 series, the peaks of $Al_4H_3^+$, $Al_4H_6^+$ and $Al_4H_9^+$ clusters were strongest in $Al_4H_m^+$ species, while $Al_5H_{6,12}^+$ clusters were local maxima among $Al_5H_m^+$ species, indicating that they were stable as well. The structure of the global minimum of $Al_3H_4^+$ has three bridge H atoms connecting two of the Al atoms, and the other H and Al connect with the Al atoms from both ends. In all it makes a C_{3v} structure. The global minimum structure of $Al_4H_3^+$ can be viewed as one of the H atom in $Al_3H_4^+$ is replaced by an Al atom, and the symmetry becomes D_{3h} in this case. The strucuture of $Al_4H_6^+$ cluster forms a cage, where two Al atoms are tetra-coordinated. The phenomenon of the stability of $Al_4H_9^+$ and $Al_5H_{12}^+$ is very interesting. They have the formula of $Al(AlH_3)_{3,4}^+$, and their calculated structures showed that all the Al atoms were tetrahedral bonded to either H atoms or its neighboring Al atoms. For $Al_4H_9^+$, the four Al atoms and five bridged H atoms form a C_{2v} cage structure, while the rest four H atoms are radially bonded to each Al atom. For $Al_5H_{12}^+$, the five Al atoms and seven bridged H atoms form a bigger Cs cage, while the rest five H atoms are radially bonded to each Al atom. Al atoms in tetrahedral environment fulfills the octet rule and thus are stable. This is in agreement with our previous research on AlH_4^- anion, in which we showed the unusual stability and very high vertical detachment energy of the tetrahedral AlH_4^-.[23] $Al_5H_6^+$ on the other hand, has a C_{2v} cage structure in which four Al atoms are connected by four bridge H atoms, and the rest two H atoms radially bond to the cage.

Figure 4.1.4 presents the structural evolution diagram of the cluster cations. All of these stale cations as described above, can be viewed as the assemblies of smaller and much more stable units, such as Al^+, $Al_2^{+/0}$, AlH_3, H^+ and H_2.

Conclusion

In summary, this report extends our knowledge about the chemistry of aluminum hydride cluster. Around 20 previously undiscovered aluminum hydride cluster cations were generated in the PACIS source and identified by mass spectrometer. Stable $Al_nH_m^+$ clusters, $Al_3H_4^+$, $Al_3H_6^+$, $Al_4H_3^+$, $Al_4H_6^+$, $Al_4H_9^+$, $Al_5H_6^+$ and $Al_5H_{12}^+$ revealed by mass spectrum were calculated by DFT, and they can be viewed as the assemblies of Al^+, $Al_2^{+/0}$, AlH_3, H^+ and H_2.

References

1. L. Andrews and X. Wang, *Science* **299**, 2049 (2003); F. A. Kurth, R. A. Eberlein, H. Schnöckel, A. J. Downs and C. R. Pulham, *J. Chem. Soc.* **16**, 1302 (1993).

2. F. A. Cotton and G. Wilkinson, Advanced Inorganic Chemistry (Interscience, New York, ed. 2, 1966).

3. X. Li, A. Grubisic, S. T. Stokes, J. Cordes, G. F. Ganteför, K. H. Bowen, B. Kiran, M. Willis, P. Jena, R. Burgert, and H. Schnöckel, *Science* **315**, 356 (2007).

4. B. Kiran, P. Jena, X. Li, A. Grubisic, S. T. Stokes, G. F. Ganteför, K. H. Bowen, R. Burgert, and H. Schnöckel, *Phys. Rev. Lett*. **98**, 256802 (2007).

5. A. Grubisic, X. Li, G. F. Ganteför, K. H. Bowen, B. Kiran, P. Jena, R. Burgert, and H. Schnöckel, *J. Am. Chem. Soc*. **129**, 5969 (2007).

6. A. Grubisic, X. Li, S. T. Stokes, K. Vetter, G. F. Ganteför, K. H. Bowen, P. Jena, B. Kiran, R. Burgert, and H. Schnöckel, *J. Chem. Phys.* **131**, 121103 (2009).

7. X. Li, A. Grubisic, K. H. Bowen, A. K. Kandalam, B. Kiran, G. F. Ganteför and P. Jena. *J. Chem. Phys.* **131**, 121103 (2009).

8. B. Kiran, A. K. Kandalam, J. Xu, Y. H. Ding, M. Sierka, K. H. Bowen, and H. Schnöckel, *J. Chem. Phys.* **137**, 134303 (2012).

9. P. J. Roach, A. C. Reber, W. H. Woodward, S. N. Kjanna, and A. W. Castleman, Jr., *Proc. Natl. Acad. Sci. U.S.A.* **104**, 14565 (2007).

10. L. F. Cui, X. Li, and L.-S. Wang, *J. Chem. Phys.* **124**, 054308 (2006).

11. A. C. Reber, S. N. Khanna, P. J. Roach, W. H. Woodward, and A. W. Castleman, Jr., *J. Am. Chem. Soc.* **129**, 16098 (2007).

12. X. Zhang, H. Wang, E. Collins, A. Lim, G. Ganteför, B. Kiran, H.Schnöckel, B. Eichhorn, and K.H. Bowen, *J. Chem. Phys.* **138**, 124303 (2013).

13. P. Breisacher and B. Siegel, *J. Am. Chem. Soc.* **86**, 5053 (1964).

14. M. Hara, K. Domen, T. Onishi, and H. Nozoye, *J. Chem. Phys.* **65**, 6 (1991).

15. K. Franzreb, R. C. Sobers Jr., J. Lorincik and P. Williams, *Appl. Surf. Sci.* **82**, 231 (2004).

16. G. N. Srinivas, A. Anoop, E. D. Jemmis, T. P. Hamilton, K. Lammertsma, J. Leszczynski, and H. F. Schaefer III, *J. Am. Chem. Soc.* **125**, 16397 (2003).

17. X. Zhang, Y. Wang, H. Wang, A. Lim, G. Gantefoer, K. H. Bowen, J. U. Reveles, and S. N. Khanna, *J. Am. Chem. Soc.,* **135**, 4856 (2013).

18. Gaussian 09, Revision D.01, M. J. Frisch, G. W. Trucks, H. B. Schlegel, G. E. Scuseria, M. A. Robb, J. R. Cheeseman, G. Scalmani, V. Barone, B. Mennucci, G. A. Petersson, H. Nakatsuji, M. Caricato, X. Li, H. P. Hratchian, A. F. Izmaylov, J. Bloino, G. Zheng, J. L. Sonnenberg, M. Hada, M. Ehara, K. Toyota, R. Fukuda, J. Hasegawa, M. Ishida, T. Nakajima, Y. Honda, O. Kitao, H. Nakai, T. Vreven, J. A. Montgomery, Jr., J. E. Peralta, F. Ogliaro, M. Bearpark, J. J. Heyd, E. Brothers, K. N. Kudin, V. N. Staroverov, R. Kobayashi, J. Normand, K. Raghavachari, A. Rendell, J. C. Burant, S. S. Iyengar, J. Tomasi, M. Cossi, N. Rega, J. M. Millam, M. Klene, J. E. Knox, J. B. Cross, V. Bakken, C. Adamo, J. Jaramillo, R. Gomperts, R. E. Stratmann, O. Yazyev, A. J. Austin, R. Cammi, C. Pomelli, J. W. Ochterski, R. L. Martin, K. Morokuma, V. G. Zakrzewski,

G. A. Voth, P. Salvador, J. J. Dannenberg, S. Dapprich, A. D. Daniels, Ö. Farkas, J. B. Foresman, J. V. Ortiz, J. Cioslowski, and D. J. Fox, Gaussian, Inc., Wallingford CT, 2009.

19. A. D. Becke, *Phys. Rev. A* **38**, 3098 (1988).

20. A. D. Becke, *J. Chem. Phys.* **98**, 5648 (1993).

21. C. Lee, W. Yang, and R. G. Parr, *Phys. Rev. B* **37**, 785 (1988).

22. R. Krishnan, J. S.Binkley, R. Seeger, and J. A. Pople, *J. Chem. Phys.* **72**, 650 (1980).

23. J. D. Graham , A. M. Buytendyk , X. Zhang , E. L. Collins , K. Boggavarapu , G. Gantefoer , B. W. Eichhorn , G. L. Gutsev , S. Behera , P. Jena , and K. H. Bowen, *J. Phys. Chem. A,* **118**, 8158 (2014).

Figure Captions

Figure 4.1.1. The whole mass spectrum of AlnHm+ clusters.

Figure 4.1.2. The separated mass spectra of AlnHm+ clusters, where n ranges from 1 to 5. The ion intensities are not normalized.

Figure 4.1.3. Calculated structures of $Al_3H_4^+$, $Al_3H_6^+$, $Al_4H_3^+$, $Al_4H_6^+$, $Al_4H_9^+$, $Al_5H_6^+$ and $Al_5H_{12}^+$. Al atoms are presented by pink balls while H atoms are in white.

Figure 4.1.4. Structural evolution of $Al_nH_m^+$.
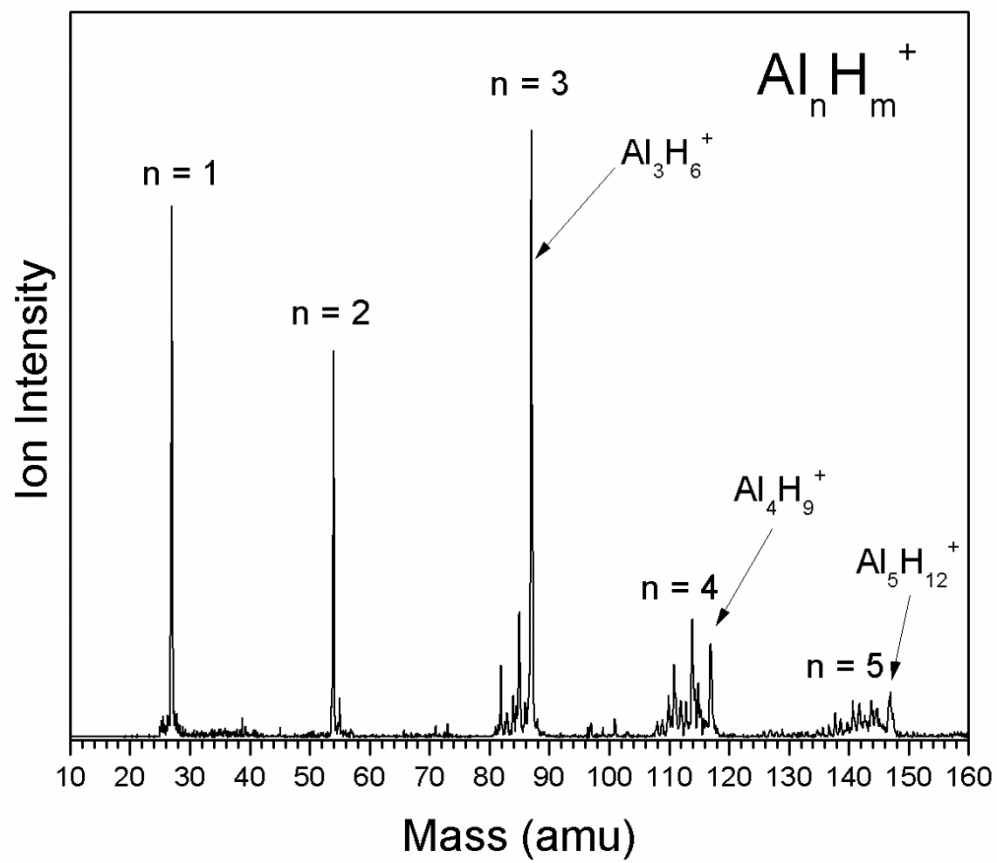
Figure 4.1.1
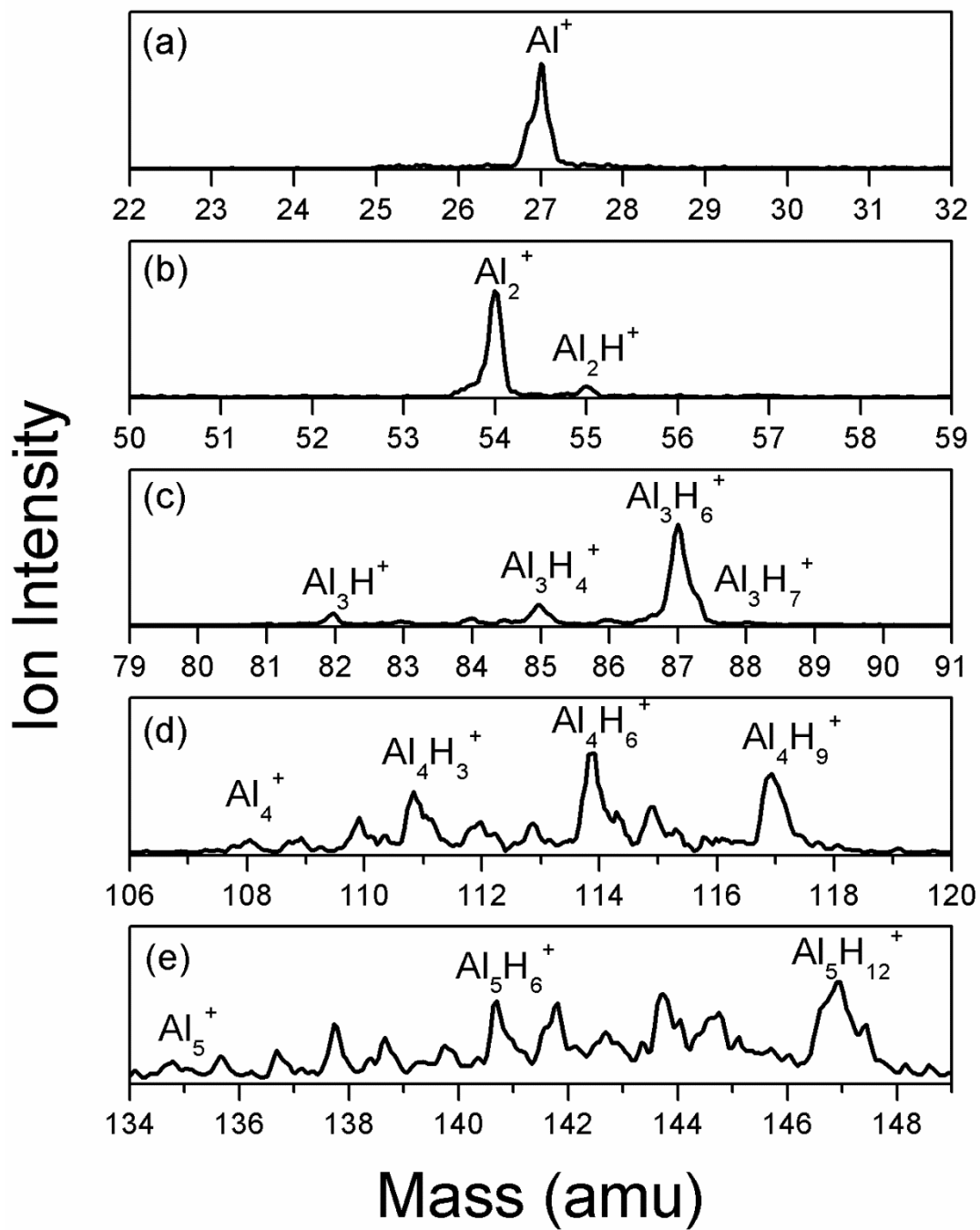
Figure 4.1.2
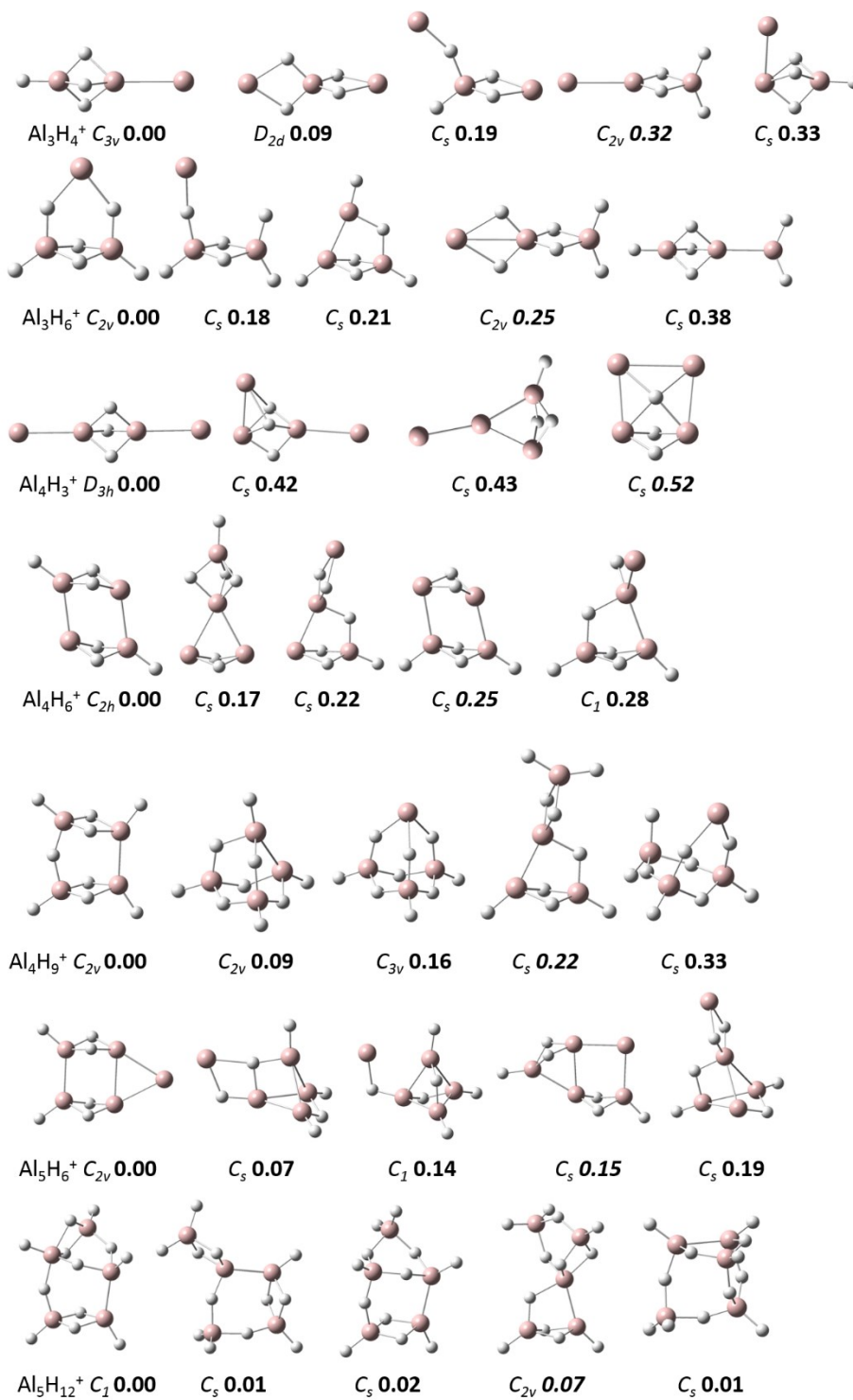
Figure 4.1.3
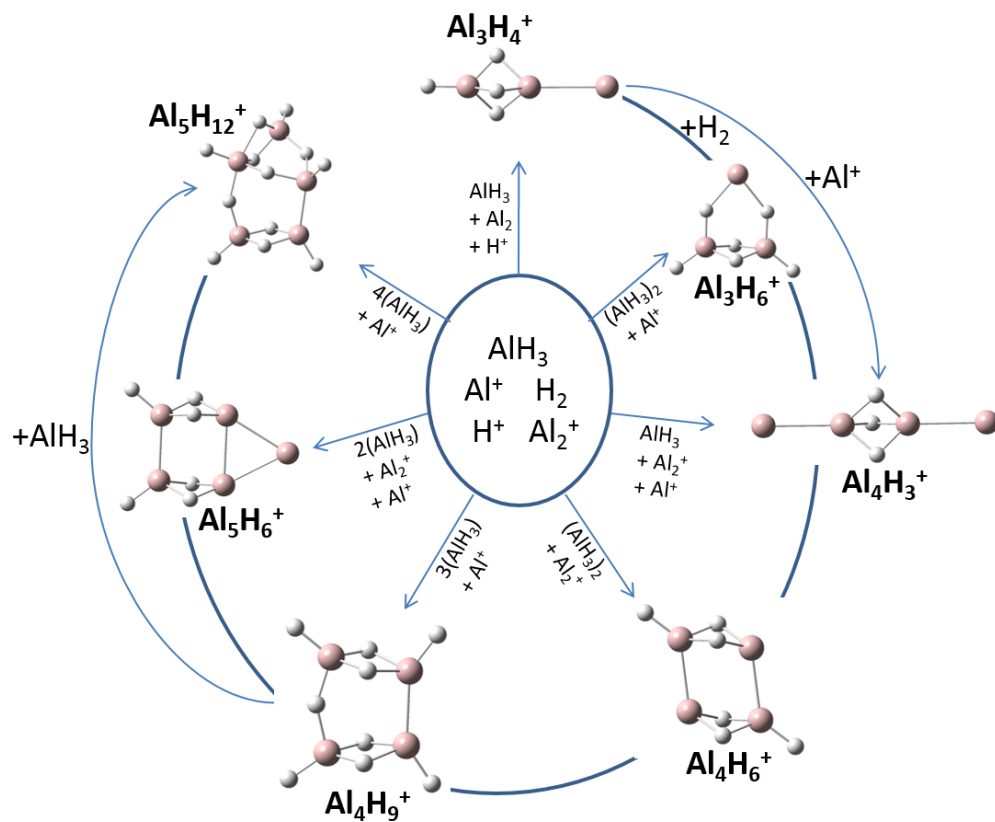
Figure 4.1.4

4.2 Photoelectron Spectroscopic Study of AlCp*H₂Cl⁻ Cluster Anion

Xinxing Zhang, [1] and Kit Bowen[1*]

[1] *Department of Chemistry, Johns Hopkins University, Baltimore, MD 21218*

Corresponding author: kbowen@jhu.edu

Phone: 001-410-516-8425

Abstract

A combined photoelectron spectroscopy and density functional theory study has been performed for a newly found cluster, AlCp*H$_2$Cl⁻. The experimental electron affinity (EA) and vertical detachment energy (VDE) are 2.7 eV and 3.13 eV, respectively, both of which are in good agreement with theoretical values. In this cluster, Al is tetra-coordinated and located at the tetrahedron center. The excess electron of the anion is mainly delocalized in the ligand, Cp*, resulting a lower EA comparing to other tetrahedral clusters such as AlH$_4$⁻ and AlCl$_4$⁻.

Introduction

Tetracoordinated aluminum anions, such as AlH_4^-, have been widely used due to their high stability. The formal valence of an aluminum atom with the electronic configuration of $[Ne]3s^23p^1$ is three, and an excess electron serves as the fourth valence electron of aluminum, together with the four coordinations makes Al fulfill the octet rule. Owing to the high stability, tetracoordinated aluminum anions have been used as anionic building blocks of salts and ionic liquids. The famous reducing agents, such as $LiAlH_4$ and $NaAlH_4$, have AlH_4^- anion as the anionic moiety.[1] $AlCl_4^-$ is the anionic moiety of many kinds of ionic liquids [2-5], and so is $AlBr_4^-$.[6] $AlCl_3Et^-$ and $AlCl_2Et_2^-$ were also found in molten salts,[7, 8] which implies that in order to make tetracoordinated aluminum a good building block, the ligand, such as ethyl, does not necessarily to be inorganic.

The study of tetracoordinated aluminum anions as isolated and intact clusters is relatively scarce. Experimentally, gas phase photoelectron spectroscopy[9] and cryogenic matrices[10] studies were performed for AlH_4^- and revealed a very high vertical detachment energy (VDE) and relatively low reactivity. Theoretically, ab inito study[11] and Green's function method[12] were also employed to study the stability of AlH_4^-. Density functional theory study[13] was performed for $AlCl_4^-$ and $Al(CN)_4^-$, and DVM Xα calculation method[14] was performed for $AlCl_4^-$.

In the current paper, we utilize photoelectron spectroscopy and density functional theory to study a newly found cluster anion, $AlCp^*H_2Cl^-$. The electrophilicity of this tetracoordinated Al cluster is remarkable even though not as high as those of AlH_4^- or $AlCl_4^-$. Comparing to AlH_4^- and $AlCl_4^-$, this cluster anion is bigger in size, and could be a potential building block of new ionic compounds.

Methods

Experimental Methods

Anion photoelectron spectroscopy is conducted by crossing a mass-selected, negative ion beam with a fixed-energy photon beam and analyzing the energies of the resultant photo-detached electrons. This technique is governed by the well-known energy-conserving relationship, hν = EBE+EKE, where hν, EBE, and EKE are the photon energy, electron binding energy (transition energy), and the electron kinetic energy, respectively.

Our photoelectron instruments, which have been described elsewhere, [15] consist of an ion source, a linear time-of-flight mass spectrometer, a mass gate, a momentum decelerator, a neodymium-doped yttrium aluminum garnet (Nd:YAG) laser operated in the third harmonic (355 nm) for photodetachment, and a magnetic bottle electron energy analyzer with a resolution of 35 meV at EKE=1 eV. The photoelectron spectra were calibrated against the well-known photoelectron spectrum of Cu−. [16]

AlCp*H_2Cl$^-$ cluster anions were generated by a pulsed arc cluster ionization source (PACIS), which has been described in detail elsewhere.[17] In brief, a ~30 μs long 150 V electrical pulse was applied between the anode and the sample cathode of the discharging chamber vaporizing the aluminum atoms and forming plasma. In this case, the sample cathode was a 0.5" diameter pure aluminum rod. About 200 psi of ultrahigh purity He gas was then injected into the arc region by the first pulsed valve, in which a drop of Cp*H was added. He diluted HCl gas was injected by a second pulsed valve. The flowing gases, dissociated in the plasma, flushed the plasma mix into a 10 cm flow tube, where it reacted, formed clusters and cooled.

Theoretical Methods

The lowest energy structures of neutral and negatively charged AlCp*H_2Cl$^-$ clusters were obtained by density functional theory (DFT) based electronic structure calculations. The Becke's

three-parameter hybrid functional (B3LYP)[18-20], along with 6-311++G(d,p)[21] basis set was used for all the calculations. All of the calculations were carried out using the Gaussian 09 software package[22]. Structures were optimized without any symmetry constraints. Natural population analysis (NPA), as implemented in the Gaussian09 code, was also carried out to determine the charge distribution of the anion. The NPA method has been found to be satisfactory in calculating the charge distribution within a cluster. [23, 24]

The vertical detachment energy (VDE) obtained from the theoretical calculations was compared with the corresponding measured values. The vertical detachment energy (VDE) is the energy between the ground state anion and its corresponding neutral at the geometry of the anion. The calculated adiabatic detachment energy (ADE) of the lowest energy isomers of anion were also compared to the onset (threshold) region of the lowest electron binding energy of the PES spectrum. The ADE is calculated as the energy difference between the lowest energy geometry of the anionic cluster and the structurally similar/identical isomer (nearest local minimum) of its neutral counterpart.

Results

Experimental results

The resulted photoelectron spectrum of $AlCp*H_2Cl^-$ taken from 355 nm laser is presented in Figure 4.2.1. An EBE band starts from around 2.7 eV and peaks at 3.13 eV. If there is sufficient Franck-Condon overlap between the ground state of the anion and the ground state of the neutral and there is not much hot band signal, the threshold of the first EBE peak, ~2.7 eV, should be the electron affinity (EA). The experimental vertical detachment energy (VDE), corresponding to the peak position, is 3.13 eV. Besides the information of electronic structures, some vibrational

features are also observed. As shown in Figure 4.2.1, the spacings between the three vibrational-resolved peaks are both 0.10 eV, and they are assigned to be the H-Al-H bending mode. The 0.10 eV number is very close to the calculated values 748 cm^{-1} (0.093 eV) in this work and also in consistency with the H-Al-H bending frequency in the calculated and experimental photoelectron spectrum of AlH_2^-. [25, 26]

Theoretical results

The optimized structures of $AlCp*H_2Cl^-$ and $AlCp*H_2Cl$ are shown in Figure 4.2.2. H atoms are in white, C in gray, Al in pink and Cl in green. The lengths of the four bonds that connect to tetrahedral Al center are marked in Å. In the anion, Al is located at the distorted tetrahedron center. Only one C atom of the five in the Cp* ring coordinates to Al. Due to the coordination, this Cp* ring is no longer planar. The neutral structure is similar to the anion in general, however, the Al-C bond is longer than that in the anion, while Al-H and Al-Cl bonds are shorter. The AlH_2Cl moiety is more planar in the neutral than in the anion, which is due to the weaker interaction between the AlH_2Cl moiety and Cp* (longer Al-C bond). The highest occupied molecular orbital (HOMO) of $AlCp*H_2Cl^-$ is presented in Figure 4.2.3. One can observe that the excess electron is delocalized and occupies the π^* anti-bonding orbital of the Cp* ring. The charge distributions of each atom of the AlH_2Cl moiety and the whole Cp* ring obtained from NPA analysis are also shown in Figure 4.2.2. For the anion, the Cp* ring moiety is highly negatively charged (-0.73 e), indicating that the ring has strong trend to maintain its aromaticity. For the the neutral, the ring is almost neutral (0.05 e).

The calculated ADE and VDE values are tabulated in Table 4.2.1 and compared to those obtained from experiment. The zero point energy corrected ADE value, 2.83 eV, is in good agreement with the experimental EA value, 2.7 eV, indicating that the calculated ADE is actually

the EA in this case. The calculated VDE, 3.27 eV, also agrees well with the experimental value, 3.13 eV.

Discussion

The structures of anionic AlH_4^- [9] and $AlCp*H_2Cl^-$ are both tetrahedral, however, the structures of their neutral counterparts are very different. The neutral AlH_4 can be viewed as AlH_2-H_2, an H_2 molecule attaches to a V-shaped AlH_2 moiety. This is because Al atom cannot maintain its octet electronic structure without the excess electron, therefore, the molecule falls apart into two relatively stable fragments, AlH_2 and H_2. In neutral $AlCp*H_2Cl$, on the other hand, due to the electron-richness of the Cp* ring, Al atom can still form a bond with the ring and maintain its tetrahedral structure, even though the Al-C bond is weaker than that in the anion. Therefore, during the photodetachment process, the structural change from the anion to the neutral is not very large. Therefore, there is sufficient Frank-Condon overlap between the ground state of the anion and ground state of the neutral, and we were able to observe the origin transition (EA) in the experiments. On the contrary, for AlH_4^-, one was unable to observe the EA experimentally due to too large structural difference between the anion and the neutral.[9]

Next we will discuss the electrophilicity difference of several tetracoordinated Al systems. Previous studies reported that the VDE of $AlCl_4^-$ is 6.17 eV [10], AlH_4^- is 4.14 eV [9], $AlCp*H_2Cl^-$ in current study is 3.13 eV. The VDE values follow the trend: $AlCl_4^- > AlH_4^- > AlCp*H_2Cl^-$. Both $AlCl_4^-$ and AlH_4^- anions satisfy the superhalogen [27, 28] formula, MX_{k+1} for monovalent ligands, X, where k is the maximal formal valence of the central atom, M. In $AlCl_4^-$ and AlH_4^-, the excess electron occupies a bonding molecular orbital spread over each of its Al−X bond and helps Al atom fulfill the octet rule, making it isoelectronic to methane and very difficult to be photodetached.

The VDE of $AlCl_4^-$ is higher than AlH_4^-, owing to the large electronegativity difference between Cl and H. The molecular orbitals HOMO and HOMO-1 of AlH_4^- obtained from same level of theory as $AlCp^*H_2Cl^-$ are shown in Figure 4.2.4. One can clearly see that the excess electron participates in forming the Al-H single bonds, in good consistency with existing studies.[11,12] However, the scenario is different in the $AlCp^*H_2Cl^-$ case (Figure 4.2.3). The excess electron in HOMO is mainly delocalized within the Cp* ring and does not participate in forming any Al-X bond, which is in consistency with the NPA analysis. In the anion, the Cp* ring is heavily negatively charged, but after photodetachment, the ring is almost neutral, indicating that it is indeed the electron delocalized in the ring that is photodetached. Thus, the HOMO where the excess electron resides is not part of Al's octet, and the excess electron is easier to be photodetached in $AlCp^*H_2Cl^-$ than in $AlCl_4^-$ and AlH_4^-, which makes $AlCp^*H_2Cl^-$ non-superhalogen. However, its EA, 2.7 eV, still indicates a very high electrophilicity and makes it a potential building block of new ionic compounds, such as ionic liquid.

Conclusion

A new tetra-coordinated Al cluster, $AlCp^*H_2Cl^-$, is produced via a PACIS source and characterized by photoelectron spectroscopy. Its electron affinity is reported to be 2.7 eV and VDE 3.13 eV. The experimental values agree well with theoretical predictions. The anion has a tetrahedral structure, and only one C atom out of five from the Cp* ring participates in coordinating with the Al center. Unlike AlH_4 (AlH_2-H_2), neutral $AlCp^*H_2Cl$ still maintains a tetrahedral structure, owing to the electron-richness of the Cp* ring. The excess electron of $AlCp^*H_2Cl^-$ is delocalized in the Cp* ring and is not part of Al atom's octet electronic structure, which is different

from other tetracoordinated Al clusters, such as AlH_4^- and $AlCl_4^-$, making it easier to be photodetached and non-superhalogen.

References

1. F. A. Cotton and G. Wilkinson, Advanced Inorganic Chemistry; Interscience: New York, 1996.

2, F. H. Hurley and T. P. Weir, *J. Electrochem. Soc.* **98**, 203 (1951).

3. J. Robinson and R. A. Osteryoung, *J. Am. Chem. Soc.* **101**, 323 (1979).

4. J. S. Wilkes, L. A. Levisky, R. A. Wilson, and C. L. Hussey, *Inorg. Chem.* **21**, 1263 (1982).

5. A. A. Fannin, D. A. Floreani, L. A. King, J. S. Landers, B. J. Piersma, D. J. Stech, R. L. Vaughn, J. S. Wilkes, and J. L. Williams, *J. Phys. Chem.* **88**, 2614 (1984).

6. J. R. Sanders, E. H. Ward, and C. L. Hussey, *J. Electrochem. Soc.* **133**, 325 (1986).

7. C. E. Keller, W. R. Carper, and W. B. J. Piersma, *Inorg. Chim. Acta.* **209**, 239 (1993).

8. Y. Chauvin, F. D. M.-V. Tiggelen, and H. Olivier, *J. Chem. Soc., Dalton Trans.* **1993**, 1009 (1993).

9. J. D. Graham, A. M. Buytendyk, X. Zhang, E. L. Collins, B. Kiran, G. Gantefoer, B. W. Eichhorn, G. L. Gutsev, S. Behera, P. Jena, and K. H. Bowen, *J. Phys. Chem. A* **37**, 118 (2014).

10. P. Pullumbi, Y. Bouteiller, and L. Manceron, *J. Chem. Phys.* **101**, 3610 (1994).

11. A. I. Boldyrev and J. Simons, *J. Chem. Phys.* **99**, 4628 (1993).

12. A. I. Boldyrev and W. von Niessen, *Chem. Phys.* **155**, 71 (1991).

13. S. Behera and P. Jena, *J. Phys. Chem. A* **116**, 5604 (2012).

14. G. L. Gutsev and A. I. Boldyrev. *Chem. Phys. Lett.* **84**, 352, (1981).

15. M. Gerhards, O. C. Thomas, J. M. Nilles, W.J. Zheng, and K. H. Bowen, *J. Chem. Phys.* **116**, 10247 (2002).

16. J. Ho, K. M. Ervin, and W. C. Lineberger, *J. Chem. Phys.* **93**, 6987 (1990).

17. X. Zhang, Y. Wang, H. Wang, A. Lim, G. Gantefӧr, K. H. Bowen, J. U. Reveles and S. N. Khanna, *J. Am. Chem. Soc.* **135,** 4856 (2013).

18. A. D. Becke, *Phys. Rev. A* **38,** 3098 (1988).

19. A. D. Becke, *J. Chem. Phys.* **98,** 5648 (1993).

20. C. Lee, W. Yang and R. G. Parr, *Phys. Rev. B* **37,** 785 (1988).

21. R. Krishnan, J. S. Binkley, R. Seeger, and J. A. Pople, *J. Chem. Phys.* **72**, 650 (1980).

22. M. J. Frisch, G. W. Trucks, H. B. Schlegel, et al., GAUSSIAN 09, Revision B.01, Gaussian, Inc., Wallingford, CT, 2004.

23. H. Wang, X. Zhang, J. Ko, A. Grubisic, X. Li, G. Gantefӧr, H. Schnӧckel, B. Eichhorn, M. Lee, P. Jena, A. Kandalam, B. Kiran, and K. H. Bowen, *J. Chem. Phys.* **140,** 054301 (2014).

24. H. Wang, Y. Ko, X. Zhang, G. Gantefoer, H. Schnoeckel, B. W. Eichhorn, P. Jena, B. Kiran, A. K. Kandalam, and K. H. Bowen, *J. Chem. Phys.* **140,** 124309 (2014).

25. X. Zhang, H. Wang, E. Collins, A. Lim, G. Gantefӧr, B. Kiran, H.Schnӧckel, B. Eichhorn, and K.H. Bowen , *J. Chem. Phys.* **138**, 124303 (2013).

26. D. K. W. Mok, E. P. F. Lee, F. Chau, and J. M. Dyke, *J. Chem. Phys.* **139**, 014301 (2013).

27. G. L. Gustev, and A. I. Boldyrev, *Chem. Phys.* **56**, 277 (1981).

28. G. L. Gustev, A. I. Boldyrev, *Adv. Chem. Phys.* **61**, 169 (1985).

Table 4.2.1. Theoretical and experimental ADE/EA values for AlCp*H$_2$Cl and VDE values for AlCp*H$_2$Cl$^-$. All numbers are in eV.

Species	ADE/EA		VDE	
	Theo.	Expt.	Theo.	Expt.
AlCp*H$_2$Cl/AlCp*H$_2$Cl$^-$	2.83	2.7	3.27	3.13

Figure Captions

Figure 4.2.1. Photoelectron spectroscopy of AlCp*H$_2$Cl$^-$.

Figure 4.2.2. Calculated structures of anionic and neutral AlCp*H$_2$Cl. The bond lengths are in Å.

Figure 4.2.3. The highest occupied molecular orbital (HOMO) of AlCp*H$_2$Cl$^-$.

Figure 4.2.4. The molecular orbitrals of AlH$_4$$^-$.
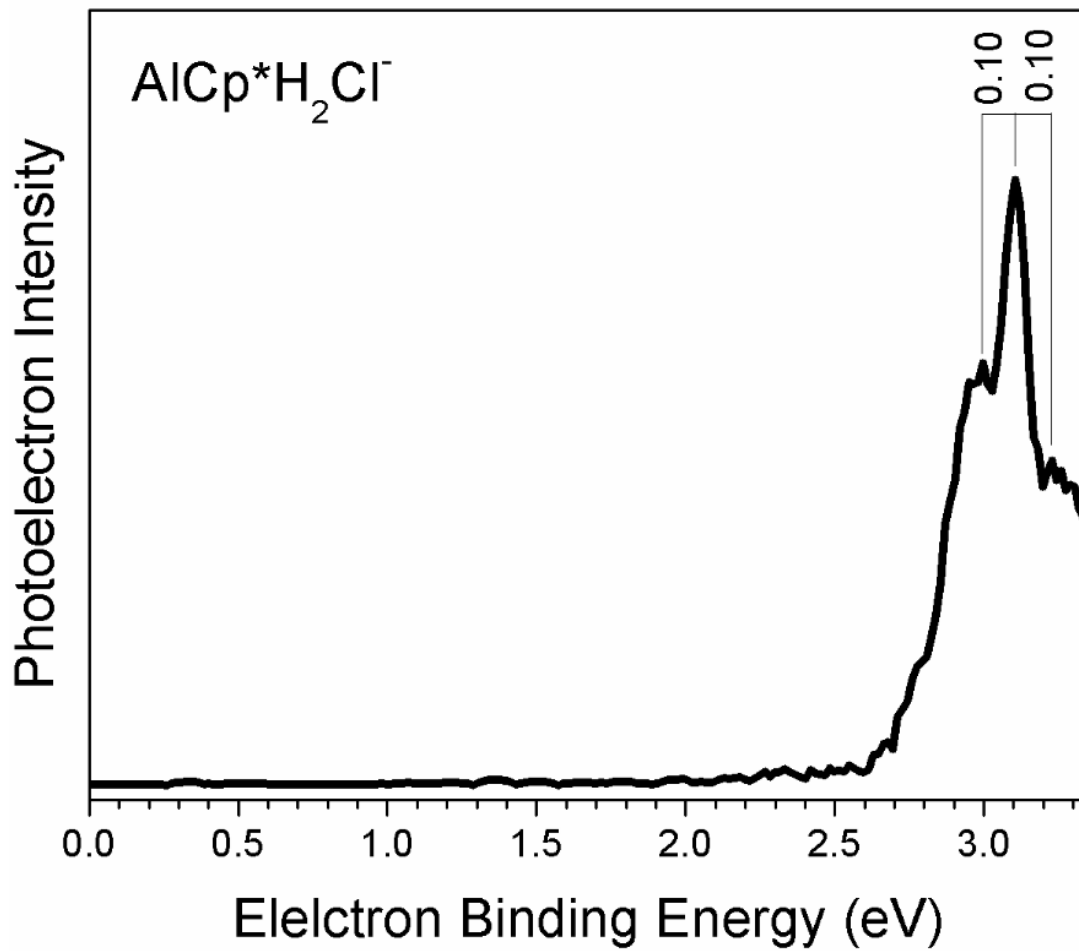
Figure 4.2.1
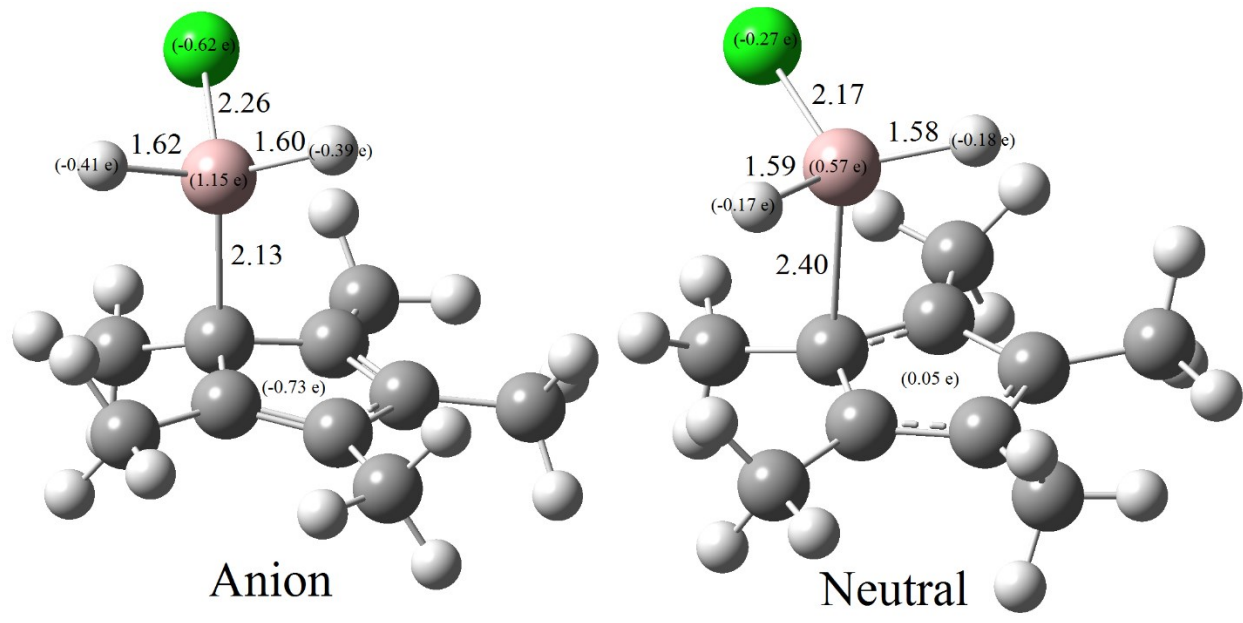
Figure 4.2.2
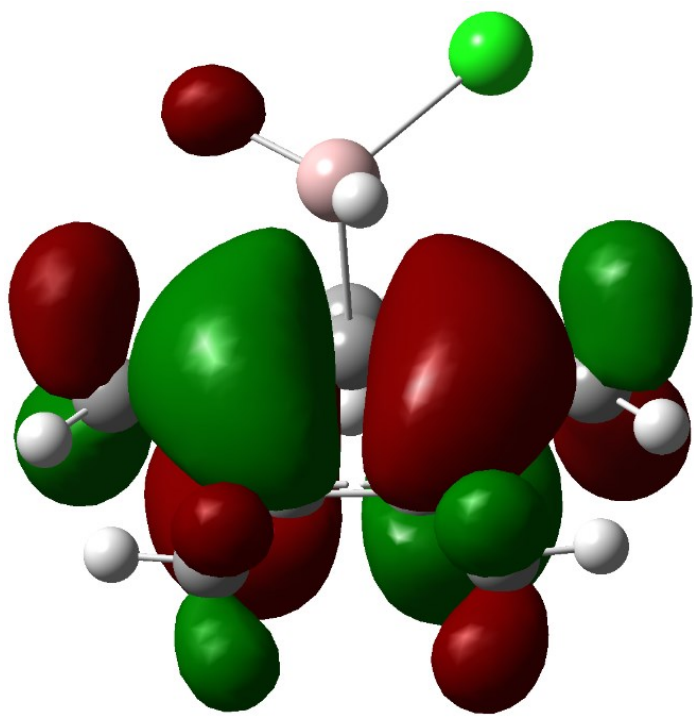
Figure 4.2.3
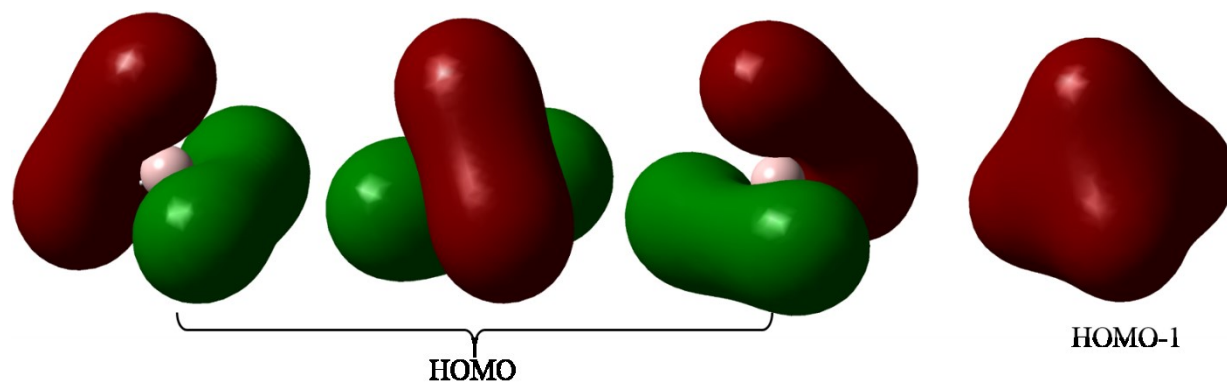
Figure 4.2.4

4.3 Experimental Observation of Aluminum Chain in $Li_2Al_3H_8^-$

Ivan A. Popov,‡[1] Xinxing Zhang,‡[2] Bryan W. Eichhorn,[3] Alexander I. Boldyrev,[1] and Kit H. Bowen[2]

[1] *Department of Chemistry and Biochemistry, Utah State University, Logan, UT 84322, USA, E-mail: a.i.boldyrev@usu.edu*

[2] *Departments of Chemistry and Materials Science, Johns Hopkins University, Baltimore, MD 21218, USA, E-mail: kbowen@jhu.edu*

[3] *Department of Chemistry and Biochemistry, University of Maryland at College Park, College Park, MD 20742, USA*

‡These authors contributed equally

Abstract

Group 13 elements are very rarely observed to catenate into linear chains and experimental observation of such species is challenging. Herein we report unique results obtained via combined photoelectron spectroscopy and ab initio studies of the $Li_2Al_3H_8^-$ cluster that confirm the formation of Al chain surrounded by hydrogen atoms in a very particular manner. Comprehensive searches for the most stable structure of the $Li_2Al_3H_8^-$ cluster have shown that the global minimum isomer I possesses a geometric structure, which resembles the structure of propane, similar to the experimentally known Zintl-phase $Cs_{10}H[Ga_3H_8]_3$ compound featuring the propane-like $[Ga_3H_8]^{3-}$ polyanions. Theoretical simulations of the photoelectron spectrum have demonstrated the presence of only one isomer (isomer I) in the molecular beam. Chemical bonding analysis of the $Li_2Al_3H_8^-$ cluster has revealed two classical Al-Al σ bonds constituting the propane-like kernel.

Introduction

Scarce examples of compounds featuring Group 13 metal–metal (M-M) single bonds represent unique cases deserving much attention. The chance for the experimental verification of the extended species featuring M-M bonding in a chain-like fashion is even smaller and hence fundamentally important. In contrast to Group 14 elements, which are quite frequently observed to form long and stable homonuclear chains,[1] Group 13 elements tend to form cluster-like species instead.[2] Homocatenated boron chains and rings of up to only eight boron atoms are known up to date.[3] Catenation of boron by a metal and catenation of borylene subunits without the use of strong alkali metals as reducing agents has been recently made by Braunschweig et al. thus representing a unique example known for boron.[4] Recent efforts to provide new, mild, functional-group-tolerant, and convenient synthetic methods for the formation of electron-precise B-B single bonds have been summarized elsewhere.[5] The use of the electronic transmutation principle[6] and similar Zintl-Klemm concept[7] have enabled designing novel materials, which are isoelectronic and isostructural to existing compounds. Wörle and Nesper demonstrated the existence of pure-phase LiB_x samples (with the approximate range $0.82 < x < 1.0$) possessing chains of boron atoms surrounded by a lithium shell that illustrate the structural analogy between borynide chains in LiB_x and isoelectronic polyyne and polycumulene chains.[8] Fahlquist et al. have shown the viability of this concept for gallium containing species: a hydrogenous Zintl-phase $Cs_{10}H[Ga_3H_8]_3$ featuring the propane-like polyanions[9] $[Ga_3H_8]^{3-}$ and $(K_xRb_{1-x})_n[GaH_2]_n$ ($0 \leqslant x \leqslant 1$) composed of $[GaH_2]_n^{n-}$ anionic chains with a polyethylene structure.[10] Remarkably, six indium atoms were previously found to arrange into one line upon the treatment of indium(I) iodide with a protonated N-xylyl β-diketiminate and a strong potassium base in tetrahydrofuran.[11] Examples of the main-group homocatenated compounds are reported elsewhere.[12] Noteworthy, thus far there have been no

experimental reports on the Al homocatenated compounds. The first remarkable example of a stable molecule with an Al-Al bond to be structurally characterized was R_2AlAlR_2 (R=CH(SiMe$_3$)$_2$).[13] Later, a cyclic structure of the Al$_3$Cl$_3$ featuring direct Al–Al bonds was reported by matrix isolation tech technique using IR and Raman spectroscopies.[14] The first "dialuminyne" (Na$_2$[Ar'AlAlAr']) synthesized has been shown to have Al-Al bond with the bond order of 1.13.[15] It was also found that "cycloaluminene" (Na$_2$[(AlAr'')$_3$]) features somewhat weakened Al-Al σ bonding, which is due the lone-pair character at the metal centers.[15] Very recently, Gish et al.[16] have theoretically predicted the existence of a new "Al homocatenated alkane" family $Li_nAl_nH^{2n+2}$, featuring striking similarities of the Al_nH_{2n+2} kernel with their respective alkanes based on the electronic transmutation concept. In this communication we report a first experimental example of "Al homocatenated propane" $Li_2Al_3H_8^-$ species possessing direct Al-Al bonds arranged in a chain-like fashion.

Conceptually,[6] a donation of one electron to Al atom might "transmute" it into Group 14 atoms. Thus, the theoretically proposed $Li_3Al_3H_8$ molecule was recently shown to be isostructural analogue of propane.[16] Here we utilized anion photoelectron spectroscopy (PES) to test the viability of this hypothesis using the $Li_2Al_3H_8^-$ anion species, which is isoelectronic to the neutral $Li_3Al_3H_8$ cluster.

Experimental and Computational Methods

Anion photoelectron spectroscopy is conducted by crossing a mass-selected beam of negative ions with a fixed-frequency photon beam and energy-analyzing the resultant photodetached electrons. It is governed by the energy-conserving relationship, $h\nu = EBE + EKE$, where $h\nu$ is the photon energy, EBE is the electron binding (transition) energy, and EKE is the electron kinetic energy. Our anion photoelectron spectrometer, which has been described

previously,[17] consists of one of many kinds of ion sources, a linear time-of-flight mass spectrometer, a mass gate, a momentum decelerator, a pulsed Nd:YAG photodetachment laser, and a magnetic bottle electron energy analyzer. Photoelectron spectra were taken with both 355 nm (3.49 eV) and 266 nm (4.66 eV) photon energies and calibrated against the well-known photoelectron spectrum of Cu^-.[18] $Li_2Al_3H_8^-$ cluster anions were generated in a laser vaporization source. Briefly, an aluminum rod was coated by a very thin layer of $LiAlH_4$ powder, and then ablated by a pulsed Nd:YAG laser beam operating at a wavelength of 532 nm. The resulting plasma was cooled by supersonically expanding a plume of helium gas from a pulsed gas valve (backing pressure of ~100 psi). Negatively charged anions were then extracted into the spectrometer prior to mass selection and photodetachment.

In order to find the most energetically favorable arrangement of atoms for the $Li_2Al_3H_8^-$ stoichiometry, we have utilized an unbiased search for the global minimum (GM) and low-energy isomers using the Coalescence Kick (CK) program[19] to follow the geometry optimization procedure with the Gaussian 09 program.[20] Exhaustive searches (30 thousand trial structures) for each multiplicity (singlet and triplet) were performed at the PBE0[21]/LanL2DZ[22] to initially explore the potential energy surface of $Li_2Al_3H_8^-$. Afterwards, the low-lying isomers (Δ=20 kcal/mol) were recalculated using the more expansive 6-311++G(d, p) basis set[23] (geometry optimization and follow-up frequency analyses to ensure that each structure is a minimum on the potential energy surface). Single-point coupled cluster calculations (CCSD(T)[24]/aug-cc-pVTZ[25]) at the DFT-optimized geometry were subsequently performed to give more precise relative energy ordering. VDEs of isomer I of $Li_2Al_3H_8^-$ were calculated at three different levels of theory: TD-DFT,[26] OVGF,[27] and CCSD(T)[24] (Table S3) and compared with experimental results. The chemical bonding analysis of the isomer I via Natural Bond Orbital (NBO)[28] method at the PBE0/6-

311++G(d, p) level of theory are also presented. Molekel 5.4.0.8[29] program was used for structural

and molecular orbitals visualization.

Results and discussion

The photoelectron spectra of $Li_2Al_3H_8^-$ taken with 3.49 eV and 4.66 eV photon energies

are presented in Figure 4.3.1. Both spectra have an electron binding energy (EBE) band (X) starting

from ~2.20 eV and peaking at 2.70 eV. In case of a sufficient Franck-Condon overlap between the

ground state of the anion and the ground state of the neutral, and given there is not much hot band

signal, the threshold of the first EBE band (~2.20 eV) should be the electron affinity (EA). The

first experimental vertical detachment energy (VDE), corresponding to the peak position, is 2.70

eV. The width of the band X suggests an appreciable geometry change between the ground state

of $Li_2Al_3H_8^-$ and that of its neutral. In Figure 4.3.1b, one can observe a second band (A) at the

higher EBE end, which peaks at 4.32 eV that corresponds to the transition from the ground state

of the anion to the first excited state of the neutral molecule.

Theoretically, twenty eight isomers were found within 20 kcal/mol range at PBE0/6-

311++G(d, p) (Figure S1). One can see that all of them are in singlet state; the lowest energy

isomer in triplet state appears to be 28.4 kcal/mol higher in energy than GM at CCSD(T).

Interestingly, several low-lying isomers were found to have chiral enantiomers. As we expected,

the GM isomer I (*Cs*, 1A') was found to possess a propane-like geometry with the R(Al-Al)=2.68

Å, similar to the corresponding bond length (2.67 Å)[16] in its neutral isoelectronic analogue

$Li_3Al_3H_8$. Noteworthy, two closest in energy isomers (II and III in Figure 4.3.2) adopt similar

Al_nH_{2n+2} kernels with somewhat different arrangement of Li atoms. Akin to the neutral $Li_3Al_3H_8$

molecule,[16] the GM structure of $Li_2Al_3H_8^-$ maintains the structural features of propane better than

any other isomers (Table S1). Apparently, higher Al-H perturbation caused by Li cations (the weaker the lithium–hydrogen interaction, the shorter the Al-H σ bond) evokes some deviation from the propane-like framework, and, probably, overall system destabilization. Thus, isomers II and III are 7.2 kcal/mol and 12.2 kcal/mol higher in energy than isomer I at CCSD(T). It should be noted that the valence Al-Al-Al angle in $Li_2Al_3H_8^-$ (100.0°) is almost the same as in propane molecule (112.8°). Relative to the experimentally synthesized $(Cs_{10}H[Ga_3H_8]_3)$[9] and theoretically predicted $(Li_3B_3H_8)$[6] X-homocatenated (X=B, Ga) propane-like species, $Li_2Al_3H_8^-$ cluster shows the smallest deviation in the valence angle from that of C_3H_8 molecule (Table S2).

To facilitate comparisons between the experimental and theoretical results, we calculated VDEs of isomer I of $Li_2Al_3H_8^-$ at three different levels of theory: TD-DFT,[26] OVGF,[27] and CCSD(T)[24] (Table S3). We found that the VDEs computed using all these methodologies are in excellent agreement with the first two detachment channels observed in the experiment (Figure 4.3.1). The electron detachment from 4a''-HOMO of the anion leads to a doublet final state for the neutral, thus giving rise to the first VDE of 2.78 eV (at CCSD(T)), compared with the experimental VDE of 2.70 eV (peak X). The next electron detachment from the 6a'-HOMO-1 produces the second theoretically calculated VDE of 4.21 eV, in excellent agreement with the experimental value of 4.32 eV corresponding to the peak A. Furthermore, the calculated adiabatic detachment energy (ADE) of isomer I (2.28 eV at CCSD(T)/aug-cc-pVTZ//PBE0/6-311++G(d, p)) is also in excellent agreement with the experimentally measured ADE value of 2.20 eV. As expected, appreciable geometry changes upon the electron detachment from $Li_2Al_3H_8^-$ were observed for the neutral $Li_2Al_3H_8$ cluster (Table S4), consistent with the broad X band observed in the PES spectra (Figure 4.3.1). We have also checked the VDEs of the second in energy isomer II (Table S3). However, the high relative energy of isomer II (Figure 4.3.2), as well as its somewhat higher

theoretical first VDE of 2.94 eV, makes this isomer unlikely to be populated in the molecular beam in any appreciable amount. Thus, we believe that the propane-like structure I is the only one contributing to the PES.

Results of the chemical bonding analysis of the isomer I via Natural Bond Orbital (NBO)[28] method at the PBE0/6-311++G(d, p) level of theory are summarized in Figure 4.3.3. According to the NBO results, the Li2Al3H8– cluster has two direct two-center two-electron (2c-2e) Al-Al σ bonds with ON=1.79 |e| and eight 2c-2e Al-H σ bonds with ON=1.85-1.99 |e|. Li atoms are involved into the bonding primarily ionically, bearing charges of +0.49 and +0.56 (Table S5). These numbers are comparable to the existing studies on charge transfer from alkali metals to Al.30 Al-H σ bonding is highly polarized towards hydrogen. On average, 70% of the electron density comes from hydrogen to form Al-H σ bonds. It should be pointed out that the obtained chemical bonding picture for $Li_2Al_3H_8^-$ confirms the fact of Al homocatenation and is in perfect agreement with the NBO pattern revealed for propane molecule (Figure S2). Although the positive charges on Li atoms are smaller than the ideal value of +1 according to the electronic transmutation principle,[6] Al atoms gain enough electron density from lithium atoms to be able to transmute into Group 14 atoms and mimic the structural features of Group 14 hydrides.

Conclusions

In conclusion, thorough ab initio and PES studies of the $Li_2Al_3H_8^-$ cluster have reliably established the structure as well as deciphered the chemical bonding pattern of this unique species, thus introducing the first experimental example of Al homocatenation, yet unknown in chemistry. We hope that the current work will be of broad interest to scientists who are involved in synthesis

of homocatenated chemical species across the Periodic Table as well as that our work will extend the view of chemical community on Al chemistry in particular.

Acknowledgements

References

1. (a) N. R. Pace, *Proc. Natl. Acad. Sci. USA* 2001, **98**, 805-808; (b) W. W. Porterfield, Inorganic Chemistry: A Unified Approach, Academic Press, San Diego (USA), 1993; (c) J. E. Huheey, E. A. Keiter and R. L. Keiter Inorganic Chemistry, 4th ed., Harper, New York, 1995.

2. (a) Z. A. Piazza, I. A. Popov, W.-L. Li, R. Pal, X. C. Zeng, A. I. Boldyrev and L.-S. Wang, *J. Chem. Phys.* 2014, **141**, 034303; (b) A. P. Sergeeva, I. A. Popov, Z. A. Piazza, W.-L. Li, C. Romanescu, L.-S. Wang and A. I. Boldyrev, *Acc. Chem. Res.* 2014, **47**, 1349-1358; (c) A. Grubisic, X. Li., S. T. Stokes, J. Cordes, G. F. Ganteför, K. H. Bowen, B. Kiran, P. Jena, R. Burgert and H. Schnöckel, *J. Am. Chem. Soc.* 2007, **129**, 5969-5975; (d) X. Li, A. Grubisic, S. T. Stokes, J. Cordes, G. F. Ganteför, K. H. Bowen, B. Kiran, M. Willis, P. Jena and R. Burgert, H. Schnöckel, *Science* 2007, **315**, 356-358; (e) X. Li, A. Grubisic, K. H. Bowen, A. K. Kandalam, B. Kiran, G. F. Ganteför and P. Jena, *J. Chem. Phys.* 2010, **132**, 241103-1–241103-415; (f) B. Kiran, A. K. Kandalam, J. Xu, Y. H. Ding, M. Sierka, K. H. Bowen and H. Schnöckel, *J. Chem. Phys.* 2012, **137**, 134303-1–

134303-5; (g) B. Kiran, P. Jena, X. Li, A. Grubisic, S. T. Stokes, G. F. Gantefӧr, K. H. Bowen, R. Burgert and H. Schnӧckel, *Phys. Rev. Lett.* 2007, **98**, 256802-1–256802-4.

3. (a) K. H. Hermannsdӧrfer, E. Matejcikova and H. Nӧth, *Chem. Ber. Recl.* 1970, **103**, 516-527; (b) H. Nӧth and H. Pommerening, *Angew. Chem., Int. Ed. Engl.* 1980, **19**, 482-483; *Angew. Chem.* 1980, **92**, 481-482; (c) M. Baudler, K. Rockstein and W. Oehlert, *Chem. Ber.* 1991, **124**, 1149-1152.

4. H. Braunschweig, Q. Ye, A. Vargas, R. D. Dewhurst, K. Radacki and A. Damme, *Nat. Chem.* 2012, **4**, 563-567.

5. H. Braunschweig, R. D. Dewhurst and S. Mozo, ChemCatChem, doi: 10.1002/cctc.201500219.

6. J. K. Olson and A. I. Boldyrev, *Chem. Phys. Lett.* 2012, **523**, 83-86.

7. R. Nesper, *Z. Anorg. Allg. Chem.* 2014, **640**, 2639–2648.

8. M. Wӧrle and R. Nesper, *Angew., Chem. Int. Ed.* 2000, **39**, 2349-2353; *Angew. Chem.* 2000, **112**, 2439-2443.

9. H. Fahlquist and D. Noréus, *Inorg. Chem.* 2013, **52**, 7125-7129.

10. (a) H. Fahlquist, D. Noréus and M. H. Sørby, *Inorg. Chem.* 2013, **52**, 4771-4773; (b) H. Fahlquist, D. Noréus, S. Caller, W. I. F. David and B. C. Hauback, *J. Am. Chem. Soc.* 2011, **133**, 14574-14577.

11. M. S. Hill, P. B. Hitchcock and R. Pongtavornpinyo, *Science* 2006, **311**, 1904-1907.

12. (a) J. Sun, M. Martinez-Canales, D. D. Klug, C. J. Pickard and R. Needs, *Phys. Rev. Lett.* 2012, **108**, 045503; (b) A. S. Ivanov, A. J. Morris, K. V. Bozhenko, C. J. Pickard and A. I. Boldyrev, *Angew. Chem., Int. Ed.* 2012, **51**, 8330-8333; *Angew. Chem.* 2012, **124**, 8455-8458; (c) I. A. Popov, B. B. Averkiev, A. A. Starikova, A. I. Boldyrev, R. M. Minyaev and V. I. Minkin, *Angew. Chem., Int. Ed.* 2015, **54**, 1476-1480; *Angew. Chem.* 2015, **127**, 1496-1500; (d) I. A. Popov and A. I.

Boldyrev, *Comp. Theor. Chem.* 2013, **1004**, 5-11; (e) A. Poater, S. Moradell, E. Pinilla, J. Poater, M. Solà, M. A. MartÍnez and A. Llobet, *Dalton Trans.* 2006, 1188-1196; (f) P. L. Timms, *J. Am. Chem. Soc.* 1967, **89**, 1629-1632; (g) A. Schnepf, C. Doriat, E. Möllhausen and H. Schnöckel, *Chem. Commun.* 1997, 2111-2112.

13. W. Z. Uhl, *Naturforsch. B* 1988, **43**, 1113-1118.

14. H.-J. Himmel, *Eur. J. Inorg. Chem.* 2005, 1886–1894.

15. R. J. Wright, M. Brynda and P. P. Power, *Angew. Chem., Int. Ed.* 2006, **45**, 5953-5956.

16. T. J. Gish, I. A. Popov and A. I. Boldyrev, *Chem. Eur. J.* 2015, **21**, 5307-5310.

17. X. Zhang, Y. Wang, H. Wang, A. Lim, G. Ganteför, K. H. Bowen, J. U. Reveles and S. N. Khanna, *J. Am. Chem. Soc.* 2013, **135**, 4856-4861.

18. J. Ho, K. M. Ervin and W. C. Lineberger, *J. Chem. Phys.* 1990, **93**, 6987-7002.

19. A. P. Sergeeva, B. B. Averkiev, H. J. Zhai, A. I. Boldyrev and L. S. Wang, *J. Chem. Phys.* 2011, **134**, 224304.

20. M. J. Frisch, et al. Gaussian 09, Revision D.01; Gaussian, Inc.: Wallingford, CT, 2013.

21. C. Adamo and V. Barone, *J. Chem. Phys.* 1999, **110**, 6158-6170.

22. P. J. Hay and W. R. Wadt, *J. Chem. Phys.* 1985, **82**, 270-283.

23. R. Krishnan, J. S. Binkley, R. Seeger and J. A. Pople, *J. Chem. Phys.* 1980, **72**, 650-654.

24. (a) G. D. Purvis and R. J. Bartlett, *J. Chem. Phys.* 1982, **76**, 1910-1918; (b) K. Raghavachari, G. W. Trucks, J. A. Pople and M. Head-Gordon, *Chem. Phys. Lett.* 1989, **157**, 479-483.

25. T. H. Dunning, *J. Chem. Phys.* 1989, **90**, 1007-1023.

26. E. Runge and E. Gross, *Phys. Rev. Lett.* 1984, **52**, 997-1000.

27. (a) L. S. Cederbaum, *J. Phys. B* 1975, **8**, 290; (b) J. V. Ortiz, *Int. J. Quantum Chem., Chem. Symp.* 1989, **36**, 321; (c) J. S. Lin and J. V. Ortiz, *Chem. Phys. Lett.* 1990, **171**, 197.

28. (a) A. E. Reed, L. A. Curtiss and F. Weinhold, *Chem. Rev.* 1988, **88**, 899-926; (b) J. P. Foster and F. Weinhold, *J. Am. Chem. Soc.* 1980, **102**, 7211-7218; (c) F. Weinhold and C. R. Landis, Valency and Bonding, A Natural Bond Orbital Donor—Acceptor Perspective, Cambridge University Press, Cambridge (UK), 2005.

29. U. Varetto and Molekel 5.4.0.8, Swiss National Supercomputing Centre, Manno, Switzerland, 2009.

30. H. Wang, X. Zhang, J. Ko, A. Grubisic, X. Li, G. Ganteför, H. Schnöckel, B. Eichhorn, M. Lee, P. Jena, A. Kandalam, B. Kiran and K. H. Bowen, *J. Chem. Phys.* 2014, **140**, 054301.

Figure Captions

Figure 4.3.1. Photoelectron spectra of $Li_2Al_3H_8^-$. a) at 355 nm (3.496 eV) and b) at 266 nm (4.661 eV).

Figure 4.3.2. Lowest energy isomers of $Li_2Al_3H_8^-$, their point group symmetries, ground electronic states, and ZPE corrected relative energies (in kcal/mol) at the PBE0/6-311++G(d, p) and CCSD(T)/aug-cc-pVTZ//PBE0/6-311++G(d, p) (in square brackets) levels of theory. The solid rods between atoms help visualization and do not necessarily represent 2c-2e σ bonds here and elsewhere. H is blue, Al is yellow, and Li is magenta.

Figure 4.3.3. Visualization of the NBO results for the $Li_2Al_3H_8^-$ cluster. a) Two aluminum-aluminum 2c-2e σ bonds (shown superimposed, left) b) Eight aluminum-hydrogen 2c-2e σ bonds (shown superimposed, right). ON denotes occupation number.

Figure 4.3.1

Figure 4.3.2

I
C_s, $^1A'$
0.0
[0.0]

II
C_1, ^1A
7.2
[7.2]

III
C_1, ^1A
11.6
[12.2]

IV
C_{2v}, $^1A_1$
12.3
[13.0]

V
C_1, ^1A
12.6
[12.5]

VI
C_1, ^1A
12.9
[11.0]

VII
C_s, $^1A'$
13.9
[13.0]

VIII
C_1, ^1A
14.0
[12.5]

IX
C_1, ^1A
16.5
[16.7]

X
C_1, ^1A
17.0
[15.6]
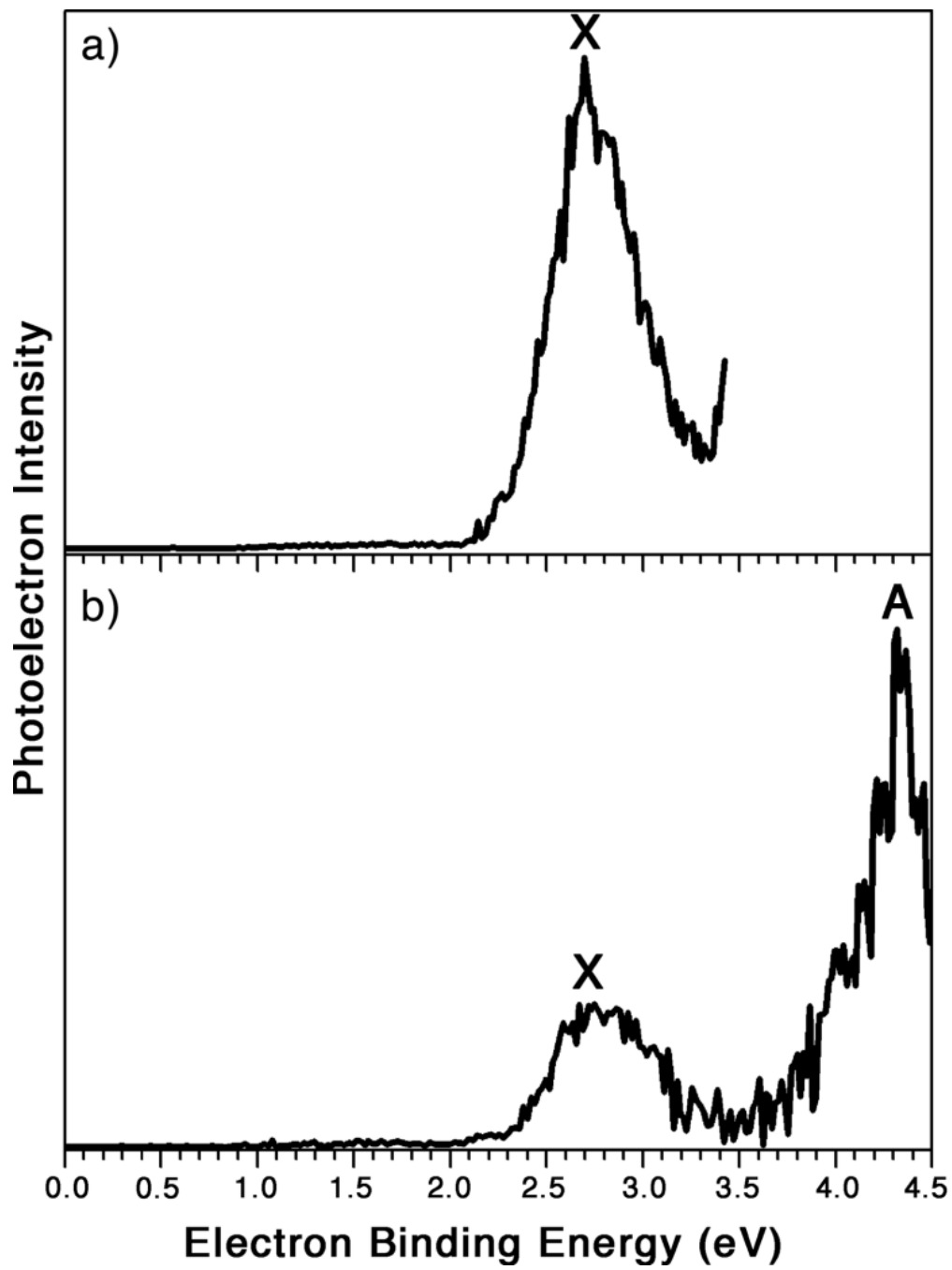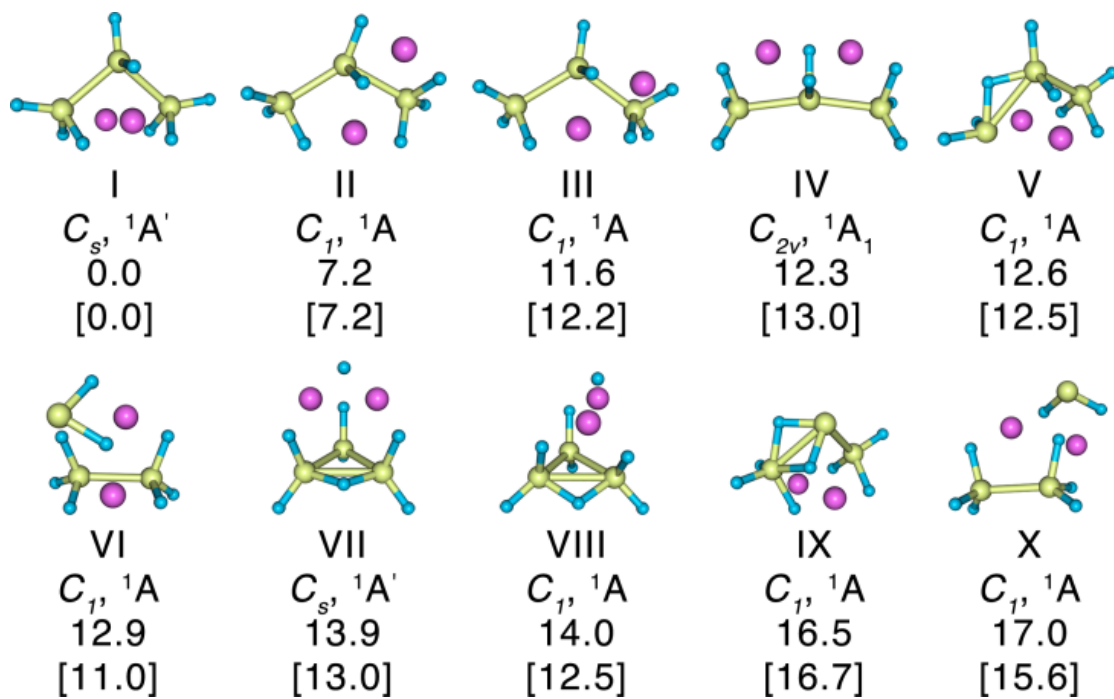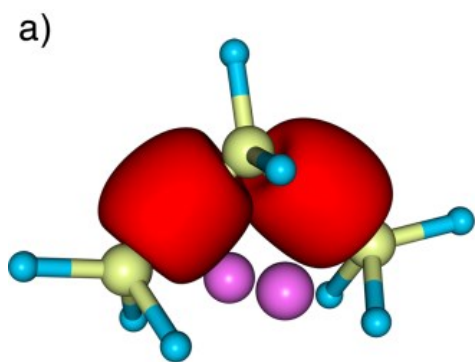
a) two 2c-2e Al-Al σ bonds
ON=1.79 |e|
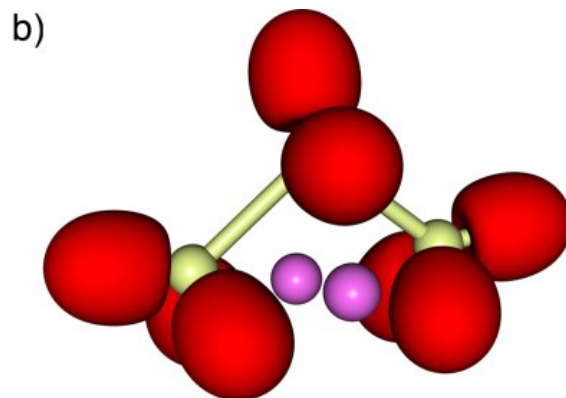
b) eight 2c-2e Al-H σ bonds
ON=1.85-1.99 |e|

Figure 4.3.3

4.4 On the Design of a New Precursor towards Low Oxidation State Al Chemistry

Xinxing Zhang, [1] Bryan Eichhorn, [2] Hansgeorg Schnöckel [3] and Kit Bowen[1]*

[1] *Department of Chemistry, Johns Hopkins University, Baltimore, MD 21218*

[2] *Department of Chemistry, University of Maryland at College Park, College Park, MD 20742*

[3] *Institute of Inorganic Chemistry, Karlsruhe Institute of Technology, 76128 Karlsruhe, Germany*

* Corresponding author: kbowen@jhu.edu

Phone: 001-410-516-8425

Abstract

A combined study of anion photoelectron spectroscopy (PES) and density functional theory (DFT) has been utilized to study neutral and anionic $Ph_2CO^-Al^+$. The comparisons between the experimental and theoretical vertical detachment energies (VDE) of both the anion isomers are made, and excellent agreement is found. Natural population analysis (NPA) show that in $Ph_2CO^-Al^+$, Al is positively charged by +0.81 e, indicating a highly ionic bond between Al and Ph_2CO, which is comparable to the case of AlCl. This Al(I) containing molecule $Ph_2CO^-Al^+$ could further be utilized as precursor of low oxidation state Al chemistry.

Introduction

Aluminum chemistry has drawn much attention these years as a result of increased interests in the reactivity of its low oxidation state.[1, 2] Since Schnöckel synthesized monovalent aluminum halides AlX (X = Cl, Br, I), [3-5] they have become the precursors from which a large variety of low oxidation state aluminum compounds were synthesized.[1-2, 6-15] Particularly, from the reaction between AlCl solution and Cp*$_2$Mg (Cp* = pentamethylcyclopentadienyl), [12-14] another interesting molecule, (Cp*Al)$_4$ was obtained, which itself is also an excellent precursor to a lot of other Al compounds. [15-25] The plentiful chemistry of low oxidation state Al is owing to its lower stability comparing to Al(III) compounds, therefore, designing new Al(I) compounds and utilizing them as reaction precursors could largely enrich Al chemistry. Undoubtedly, the first step of designing such a compound is to find the electron acceptor, a counterpart of the X in AlX, and the Cp* in (Cp*Al)$_4$.

In solution, benzophenone (Ph$_2$CO) can readily react with alkali metals to form a stable dark-colored Ph$_2$CO$^-$M$^+$ (M = Li, Na, and K) solution. [26] The anion photoelectron spectroscopy study of intact (Ph$_2$CO)$^-$ radical anion in the gas phase revealed that its electrophilicity was rather high and its vertical detachment energy (eV) was measured to be 1.11 eV. [27] The stability of the anion largely comes from the delocalization of the excess electron in the π* anti-bonding orbital. Therefore, as a reactive metal, Al might also react with Ph$_2$CO and give up one electron to form a monovalent Al compound, Ph$_2$CO$^-$Al$^+$, which might further be utilized as a precursor towards other low oxidation state Al compounds. To the best of our knowledge, none of this kind of studies exist yet.

In the present work, we explore the viability of producing monovalent Al compound Ph$_2$COAl via gas phase anion photoelectron spectroscopy and density functional theory (DFT)

calculations. We produced the parent anion of Ph_2COAl, measured its electronic structure both experimentally and theoretically. More importantly, we also calculated the charge distribution within this compound and confirmed that Al is indeed in its +1 oxidation state in this compound.

Experimental and Theoretical Methods

Anion photoelectron spectroscopy is conducted by crossing a mass-selected beam of negative ions with a fixed-frequency photon beam and energy-analyzing the resultant photodetached electrons. It is governed by the energy-conserving relationship, $h\nu = EBE + EKE$, where $h\nu$ is the photon energy, EBE is the electron binding (transition) energy, and EKE is the electron kinetic energy. Our anion photoelectron spectrometer, which has been described previously,[28] consists of a laser vaporization anion source, a linear time-of-flight mass analyzer/selector, a pulsed Nd:YAG photodetachment laser operating at 355 nm (3.49 eV), and a magnetic bottle electron energy analyzer. Photoelectron spectra were calibrated against the well-known photoelectron spectrum of Cu^-.[29] Parent anions of Ph_2COAl were generated in a laser vaporization source. Briefly, an aluminum rod was coated by a thin layer of Ph_2CO powder and then ablated by a pulsed Nd:YAG laser beam operating at a wavelength of 532 nm. The resulting plasma was cooled by supersonically expanding a plume of helium gas from a pulsed gas valve (backing pressure of ~60 psi). Negatively charged anions were then extracted into the spectrometer prior to mass selection and photodetachment.

Density functional theory calculations were conducted by applying Becke's three-parameter hybrid functional (B3LYP)[30-32] using the Gaussian09 software package[33] to determine the geometries of both neutral and anionic Ph_2COAl, the vertical detachment energy (VDE) values,

the neutral excited states, the charge distribution and the potential energy surface. All geometries, including that of the anion and its corresponding neutral molecule, were fully optimized without any geometrical constraints. The VDE is the energy difference between the ground state of the anion and the neutral with the same structure as the anion. The energies for the excited states of the neutral molecule were calculated with time-dependent DFT (TDDFT) methods. [34-36] Natural population analysis (NPA), as implemented in the Gaussian09 code, was also carried out to determine the charge distributions. As a comparison, the NPA charge distribution of AlCl was also calculated. The NPA method has been found to be satisfactory in calculating the charge distribution within a cluster. [37, 38] The potential energy surface was scanned along the Al-O coordinate with a step width of 0.05 Å. All the above calculations were performed with the the 6-311++G (3df, 3pd) basis set

Results

Before confirming the charge distribution, we write the molecule of interest in the form of "Ph_2COAl" other than "$Ph_2CO^-Al^+$". The resultant photoelectron spectrum of $(Ph_2COAl)^-$ is presented in Figure 4.4.1. Two broad EBE bands can be observed. The first EBE band, which peaks at 1.43 eV, corresponds to the photodetachment of the first isomer of the anion (Iso 1). The second EBE band, which peaks at 2.14 eV, corresponds to the second isomer of the anion (Iso 2). The relative intensity of these two EBE bands varied during different days' experiments, confirming that they belonged to different isomers. The calculated VDE values of these two isoerms are 1.39 eV and 2.00 eV, respectively. Experimental and theoretical VDEs are tabulated in Table 4.4.1, and very good agreement can be found there. Our TDDFT calculations reveal that the vertical transition energies from the ground state of the anion Iso 1 to the excited states of the

neutral are at least 3.8 eV, which is beyond the laser energy used in the experiments. Therefore, this information further confirms that the two EBE bands belong to the two different isomers but not different transitions of the same isomer.

The calculated structures of the anion isomers and the neutral are presented in Figure 4.4.2. Both of the anion isomers relaxed to the same neutral during the optimization, therefore, we use green arrows to connect the anions and the neutral. In Figure 4.4.2, the characteristic bond lengths are marked in black numbers (Å), bond angles are marked in red numbers (°) and the charge of Al are marked in blue numbers (e). The energy difference between the two anion isomers is only 0.05 eV, which explains their coexistence in the ion beam. In anion Iso 1, the Al atom bonds with O from the end and the Al-O-C moiety forms a linear structure. In anion Iso 2, the Al-O-C moiety shows an angle of 83.7°. Both the Al-O bond and the C-O bond are longer in Iso 2 than in Iso 1. The neutral molecule keeps the linear Al-O-C structure as in anion Iso 1, but the Al-O and C-O bond lengths are slightly longer. The Al-O bond length in the neutral, 1.72 Å, is similar to a normal Al-O single bond, indicating that there might be only single charge transfer from Al to Ph_2CO. Due to steric hindrance, the two benzene rings are slightly off the plane in all of these structures.

The NPA charge distributions of both anionic and neutral Ph_2COAl are tabulated in Table 4.4.2. In both of the anion isomers, the Al atom has a positive charge of around +0.6 e, and Ph_2CO is negatively charged by around -1.6 e. But in neutral Ph_2COAl, the Al atom has a positive charge of +0.81 e, which means that the bond between Al and Ph_2CO is highly ionic. Therefore, we formally write Ph_2COAl as $Ph_2CO^-Al^+$ at this stage. Even though Ph_2CO could very slowly form dianion, $Ph_2CO^{2-}M_2$, when reacting with excess alkali metals, [26] Al^{2+} and Ph_2CO^{2-} are not observed in the present study. From the comparison of the anion and the neutral, we can observe that the excess electron is partially delocalized on Al (-0.2 e) and partially delocalized on Ph_2CO (-0.8 e),

this is due to the high electron accommodating ability of the π conjugate system of Ph_2CO. As a comparison, the charge of Al in the widely used precursor AlCl was calculated to be +0.69 e at the same level of theory, which is also very ionic, but lower than that of $Ph_2CO^-Al^+$, hence, the electron transfer from Al to the anion part is more thorough in $Ph_2CO^-Al^+$ than in AlCl.

Discussion

Now we discuss the viability of synthesizing $Ph_2CO^-Al^+$. The potential energy surface along the Al-O bond in neutral $Ph_2CO^-Al^+$ is shown in Figure 4.4.3. It is obvious that when Al is approaching Ph_2CO, the Al-O bond can readily form without an energy barrier. More than 2 eV (190 kJ/mol) heat can be released during this gas phase reaction. Therefore, this reaction is thermodynamically favorable. However, in solution, one would expect more complications, such as solvent effect, reaction temperature, etc. More importantly, it is critical to keep Al at its +1 oxidation state and prevent it from being further oxidized to +3. To achieve this, two precautions need to be taken. The first one is keeping a low temperature environment. For example, AlCl can only be kept for a long time under 77K. [3] The second one is stoichiometrically starving Al, i.e. adding excess Al and limited Ph_2CO to the reaction system, so that there are not enough oxidants to drag Al down to the +3 state. Other conditions such as rigorous absence of oxygen and water also need to be taken care of. We look forward to the work from the experts in synthetic chemistry.

Conclusion

The parent anion of $Ph_2CO^-Al^+$ was produced in the gas phase. The combination of photoelectron spectroscopy and DFT calculations found two isomers for the parent anion but only one isomer for the neutral. The experimental VDE values of these two anion isomers, 1.43 eV and

2.13 eV had very good agreement with the calculated ones. The NPA analysis revealed that the bond between Al and Ph_2CO was quite ionic, and Al was indeed in its +1 oxidation state. The comparison between $Ph_2CO^-Al^+$ and AlCl indicated that their charge distributions were comparable, which gave us confidence in this designer precursor. The gas phase potential energy surface along the Al-O bond showed no barrier, therefore, this reaction could readily occur in an energetically favorable way. However, in solution, more precautions should be taken in order to achieve this reaction, such as the reaction temperature and the reactant ratio.

References

1. H. W. Roesky and S. S. Kumar, *Chem. Commun.* **2005** (2005) 4027.

2. H. W. Roesky, *Inorg. Chem.* **43** (2004) 7284.

3. M. Tacke and H. Schnöckel, *Inorg. Chem.* **28** (1989) 2896.

4. M. Mocker, C. Rob and H. Schnöckel, *Angew. Chem.* **106** (1994) 1860.

5. A. Ecker and H. Schnöckel, *Z. Anorg. Allg. Chem.* **622** (1996) 149.

6. A. Purath, R. Köppe and H. Schnöckel, *Angew. Chem.* **111**, 3114 (1999); *Angew. Chem. Int. Ed. Engl.* **38**, 2926 (1999).

7. A. Purath, R. Köppe and H. Schnöckel, *Chem. Commun.* **1999**, 1933 (1999).

8. H. Köhnlein, A. Purath, C. Klemp, E. Baum, I. Krossing, G. Stösser and H. Schnöckel, *Inorg. Chem.* **40**, 4830 (2001).

9. C. Dohmeier, M. Mocker, H. Schnöckel, A. Lötz, U. Schneider and R. Ahlrichs, *Angew. Chem.* **105**, 1491 (1993); *Angew.Chem. Int. Ed.* Engl. **32**, 1428 (1993).

10. A. Schnepf and H. Schnöckel, *Adv. Organomet. Chem.* **47**, 235 (2001).

11. C. Üffing, A. Ecker, R. Köppe, K. Merzweiler and H. Schnöckel, *Chem. Eur. J.* **4**, 2142 (1998).

12. C. Dohmeier, C. Roble, M. Tacke and H. Schnöckel, *Angew. Chem.* **103**, 594 (1991); *Angew. Chem., Int. Ed. Engl.* **30**, 564 (1991).

13. C. Dohmeier, D. Loos and H. Schnöckel, *Angew. Chem.* **108**, 141(1996); *Angew. Chem., Int. Ed. Engl.* **35**, 129 (1996).

14. J. Gauss, U. Schneider, R. Ahlrichs, C. Dohmeier and H. Schnöckel, *J. Am. Chem. Soc.* **115**, 2402 (1993).

15. A. Ecker, E. Weckert and H. Schnöckel, *Nature*, **387**, 379 (1997).

16. A. Haaland, K.-G. Martinsen, S.A. Shlykov, H.V. Volden, C. Dohmeier and H. Schnöckel, *Organometallics*, **14**, 3116 (1995).

17. J. D. Gorden, A. Voigt, C. L. B. Macdonald, J. S. Silverman, and A. H. Cowley, *J. Am. Chem. Soc.* **122**, 950 (2000).

18. C. Dohmeier, H. Krautscheid and H. Schnöckel, *Angew. Chem.* 106 (1994) 2570; *Angew. Chem., Int. Ed. Engl.* **33**, 2482 (1994).

19. C. Üffing, A. Ecker, R. Köppe and H. Schnöckel, *Organometallics,* **35**, 2373 (1998).

20. Q. Yu, A. Purat, A. Douchev and H. Schnöckel, *J. Organomet. Chem.* **584**, 94 (1999).

21. J. Weiß, D. Stetzkamp, B. Nuber, R.A. Fischer, C. Boehme and G. Frenking, *Angew. Chem.* **109**, 95 (1997); *Angew. Chem., Int. Ed. Engl.* **36**, 70 (1997).

22. D. Weiß, T. Steinke, M. Winter, R.A. Fischer, N. Fröhlich, J. Uddin and G. Frenking, *Organometallics,* **19**, 4583 (2000).

23. S. Schulz, T. Schoop, H. W. Roesky, L. Häming, A. Steiner and R. Herbst-Irmer, *Angew. Chem.* **107**, 1015 (1995); *Angew. Chem., Int. Ed. Engl.* **34**, 919 (1995).

24. C. K. F. von Haenish, C. Üffing, M. A. Junker, A. Ecker, B. O. Kneisel and H. Schnöckel, *Angew. Chem.* **108**, 3003 (1996); *Angew. Chem., Int. Ed. Engl.* **35**, 2875 (1996).

25. C. Dohmeier, H. Schnöckel, C. Robl, U. Schneider and R. Ahlrichs, *Angew. Chem.* **106**, 225 (1994); *Angew. Chem., Int. Ed. Engl.* **33**, 199 (1994).

26. N. G. Connelly and W. E. Geiger, *Chem. Rev.* **96**, 877 (1996).

27. T. Maeyama, I. Yagi, A. Fujii, and N. Mikami, *Chem. Phys. Lett.* **457**, 18 (2008).

28. X. Zhang, Y. Wang, H. Wang, A. Lim, G. Gantefÿr, K.H. Bowen, J.U. Reveles and S.N. Khanna, *J. Am. Chem. Soc.* **135,** 4856 (2013).

29. J. Ho, K.M. Ervin, and W.C. Lineberger. *J. Chem. Phys.* **93,** 6987 (1990).

30. A.D. Becke, *Phys. Rev. A* **38,** 3098 (1988).

31. A.D. Becke, *J. Chem. Phys.* **98,** 5648 (1993).

32. C.Lee, W. Yang and R.G. Parr, *Phys. Rev. B* **37,** 785 (1988).

33. M.J. Risch, G.W. Trucks, H.B. Schlegel, G.E. Scuseria, M.A. Robb, J.R. Cheeseman, G. Scalmani, V. Barone, B. Mennucci, G.A. Petersson, et al. Gaussian 09, revision A.1; Gaussian, Inc.:Wallingford, CT, 2009

34. M.A.L. Marques, E.K.U. Gross, *Annu. Rev. Phys. Chem.* **55**, 427 (2004).

35. K. Burke, J. Werschnik, E.K.U. Gross, *J. Chem. Phys.* **123**, 062206 (2005).

36. M.E. Casida, M. Huix-Rotllant, *Annu. Rev. Phys. Chem.* **63**, 287 (2012).

37. H. Wang, X. Zhang, J. Ko, A. Grubisic, X. Li, G. Gantefÿr, H. Schnöckel, B. Eichhorn, M. Lee, P. Jena, A. Kandalam, B. Kiran, and K.H. Bowen, *J. Chem. Phys.* **140**, 054301 (2014).

38. H. Wang, Y. Ko, X. Zhang, G. Gantefoer, H. Schnoeckel, B.W. Eichhorn, P. Jena, B. Kiran, A. K. Kandalam, and K.H. Bowen, *J. Chem. Phys.* **140**, 124309 (2014).

Table 4.4.1. Experimental and theoretical VDE values of the two anion isomers.

	Expt. VDE (eV)	Theo. VDE (eV)
Iso 1	1.43	1.39
Iso 2	2.13	2.00

Table 4.4.2. The charge distribution on Al and on the rest of the molecule.

	Charge on Al (e)	Charge on the rest of the molecule (e)
Ph_2COAl anion Iso 1	+0.60	-1.60
Ph_2COAl anion Iso 2	+0.61	-1.61
Ph_2COAl neutral	+0.81	-0.81
AlCl	+0.69	-0.69

Figure Captions

Figure 4.4.1. Photoelectron spectrum of $(Ph_2CO^-Al^+)^-$ taken with 3.49 eV laser.

Figure 4.4.2. Calculated structures of the anion isomers and the neutral.

Figure 4.4.3. Potential energy surface of neutral $Ph_2CO^-Al^+$ when Al atom is approaching Ph_2CO.

Figure 4.4.1

+0.60

1.68

180.0

1.37

1.43 1.43

Anion Iso 1
E = 0 eV

+0.81

1.72

180.0

1.34

1.45 1.45

Neutral

1.78 +0.61

83.7

1.43

1.45 1.45

Anion Iso 2
E = 0.05 eV
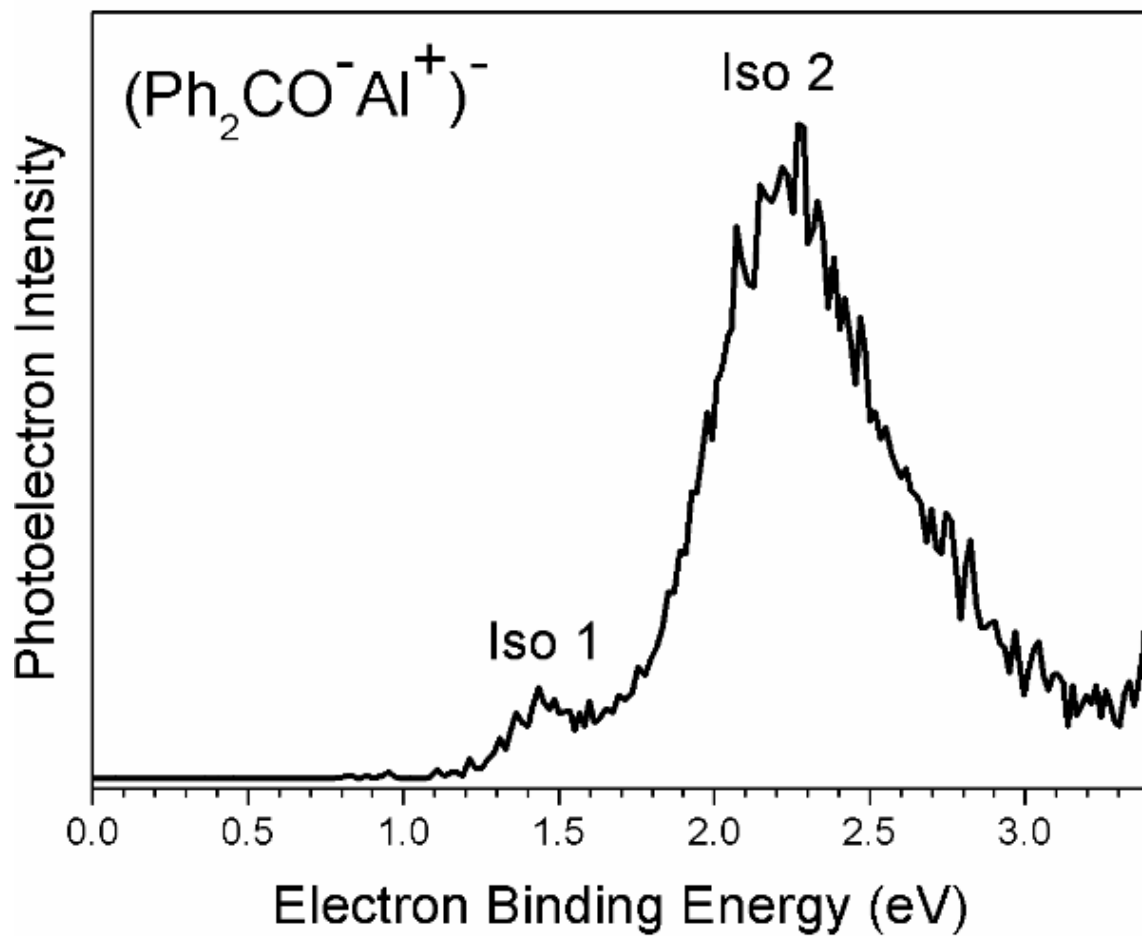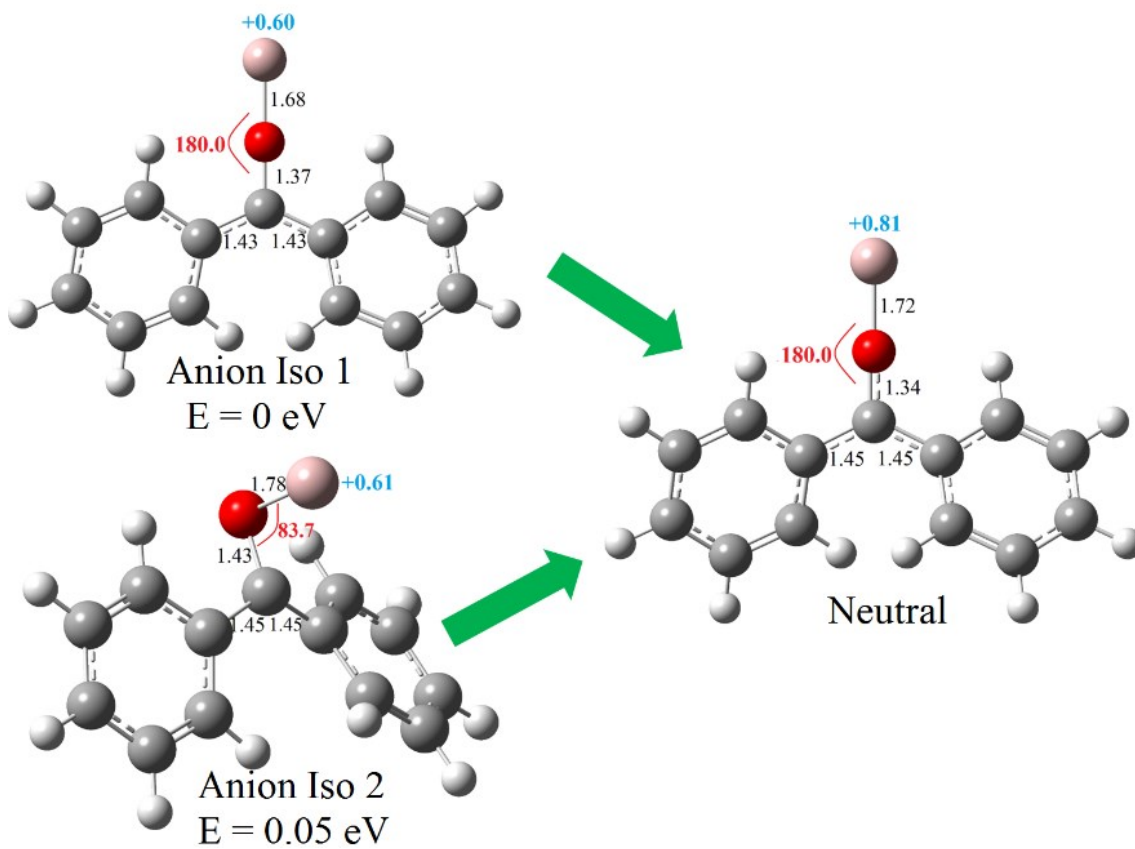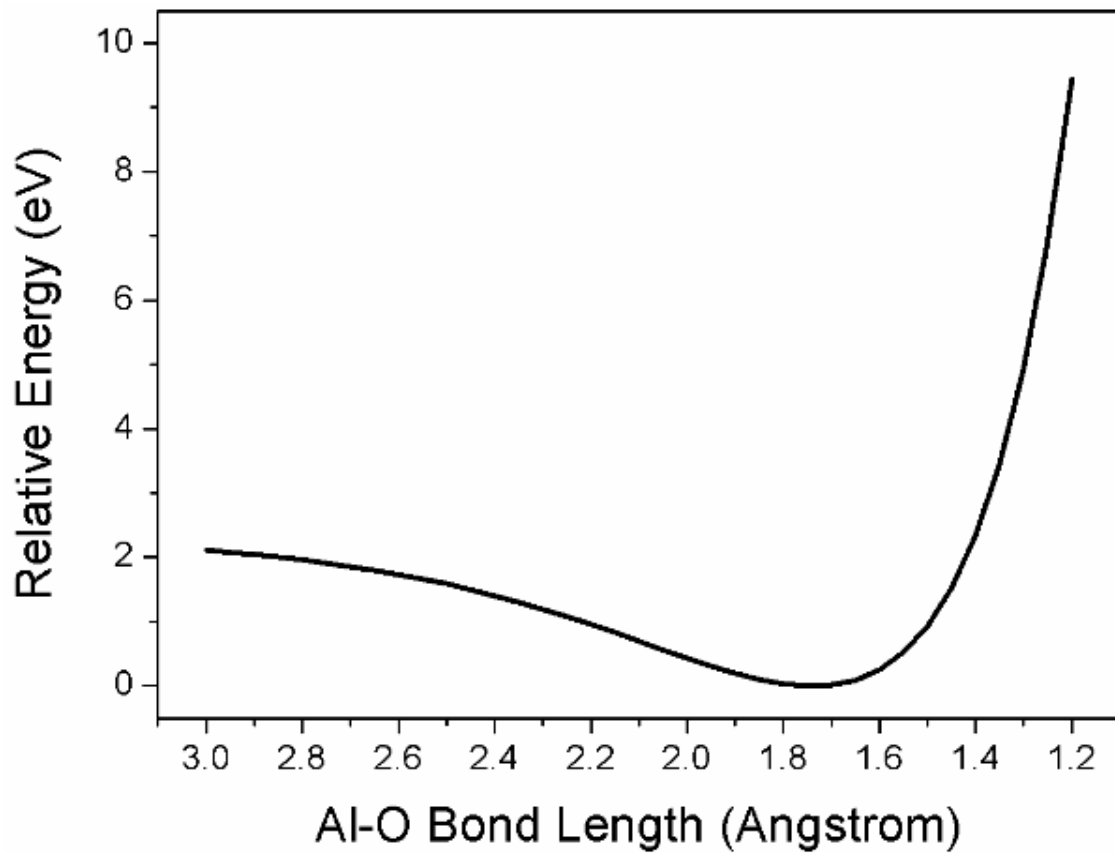
Figure 4.4.2

Figure 4.4.3

4.5 A Photoelectron Spectroscopic and Theoretical Study of o-Dicarbadodecaborane Parent Anion

Xinxing Zhang, [1] and Kit Bowen[1, a)]

[1] *Department of Chemistry, Johns Hopkins University, Baltimore, Maryland 21218, USA*

[a)] Electronic mail: kbowen@jhu.edu

Abstract

A combined study of anion photoelectron spectroscopy (PES) and density functional theory (DFT) has been utilized to study the o-dicarbadodecaborane (o-carborane) parent anion. Different from some published work in which o-carborane shows a negative electron affinity, in the present work, we report a remarkable electrophilicity of o-carborane. Two isomers were found for o-carborane anion, and one of them, with the C-C bond broken, shows an unusual stability. According to its potential energy surface, we cannot observe the electron affinity experimentally due to the lack of Franck-Condon overlap, thus, we report a theoretical electron affinity value of 1.19 eV. The experimental vertical detachment value (2.33 eV) has satisfactory agreement with the theoretical value (2.26 eV).

Introduction

O-dicarbadodecaborane (o-$C_2B_{10}H_{12}$), or simply known as o-carborane, was firstly synthesized and reported in 1963. [1-9] Its slightly distorted icosahedral structure, unusual stability, chemical properties and isomerization among its o-, m-, p- isomers were recorded at the same time. [1-9] The hydrogen atoms attached the C atoms are found to be acidic. By reacting with n-butyllitium in tetrahydrofuran, the doubly-deprotonated dianion $C_2B_{10}H_{10}^{2-}$ was synthesized. [10-12] The $C_2B_{10}H_{12}$ cage itself can accommodate as many as two electrons. On the experimental front, the dianion $(C_2B_{10}H_{12})^{2-}$ can be obtained by mixing o-carborane and Na/K alloy in tetrahydrofuran. [13] On the theoretical front, ab initio calculations found that it has a *nido*-structure. [14,15] Despite the stability of the dianion, the study on the monoanion is relatively scarce. Experimentally, only [(15-crown-5)$_3$Na$_2$]$^{2+}$ [$(C_2B_{10}H_{11})_2$]$^{2-}$ and [(P(C_6H_5)$_3$CH$_3$]$_2$ $^{2+}$[$(C_2B_{10}H_{11})_2$]$^{2-}$ salts were synthesized,[16,17] in which the anion part, [$(C_2B_{10}H_{11})_2$]$^{2-}$, is a connected double cage with one negative charge on each cage. $(C_2B_{10}H_{12})^-$ was also observed in a chemical equilibrium, in which one electron transferred from $(C_2B_{10}H_{12})^{2-}$ to $C_2B_{10}H_{10}RR'$, resulting in $(C_2B_{10}H_{12})^-$ and $(C_2B_{10}H_{10}RR')^-$.[13] Theoretically, Hermansson *et al* [18] found that o-carborane has an electron affinity (EA) of -212 KJ/mol (-2.20 eV) with Hartree-Fock/6-31g* level of theory. To the best of our knowledge, there is no gas phase study of isolated $(C_2B_{10}H_{12})^-$ monoanion yet.

From the above knowledge, it seems that $(C_2B_{10}H_{12})^-$ can only exist in metastable state or stabilized by counter ions in salts. However, in this work, we present evidences of remarkable electrophilicity of o-carborane by synthesizing its intact, isolated parent anion in the gas phase, characterizing it with anion photoelectron spectroscopy (PES) and reporting positive electron affinity and vertical detachment energy values. Density functional theory (DFT) is also utilized to validate and interpret the experimental results.

Experimental and Theoretical Methods

Anion photoelectron spectroscopy is conducted by crossing a mass-selected beam of negative ions with a fixed-frequency photon beam and energy-analyzing the resultant photodetached electrons. It is governed by the energy-conserving relationship, $h\nu = EBE + EKE$, where $h\nu$ is the photon energy, EBE is the electron binding (transition) energy, and EKE is the electron kinetic energy. Our anion photoelectron spectrometer, which has been described previously,[19] consists of a laser vaporization anion source, a linear time-of-flight mass analyzer/selector, a pulsed Nd:YAG photodetachment laser, and a magnetic bottle electron energy analyzer. Photoelectron spectra were calibrated against the well-known photoelectron spectrum of Cu^-.[20] Parent anions of o-carborane were generated in a laser vaporization source. Briefly, a silver rod was coated by a layer of o-carborane powder (Alfa Aesar, 98%), and then ablated by a pulsed Nd:YAG laser beam operating at a wavelength of 532 nm. The resulting plasma was cooled by supersonically expanding a plume of helium gas from a pulsed gas valve (backing pressure of ~100 psi). Negatively charged anions were then extracted into the spectrometer prior to mass selection and photodetachment.

Density functional theory calculations were conducted by applying Becke's three-parameter hybrid functional (B3LYP)[21-23] using the Gaussian09 software package[24] to determine the geometries of both neutral and anionic o-carborane, the electron affinity (EA) and vertical detachment energy (VDE) values, the potential energy surface, and the charge distribution. All geometries, including that of the anion and its corresponding neutral molecule, were fully optimized without any geometrical constraints using the 6-311++G (d, p) basis set. The EA value is the energy difference between the ground state of the neutral and the ground state of the anion with zero point energy correction. The VDE is the energy difference between the ground state of the anion and the neutral with the same structure as the anion. The potential energy surface was

scanned along the C-C coordinate with a step width of 0.05 Å by relaxing the rest of the molecule to its ground state. Natural population analysis (NPA), as implemented in the Gaussian09 code, was also carried out to determine the charge distribution of the anion. The NPA method has been found to be satisfactory in calculating the charge distribution within a cluster. [25, 26]

Results and Discussion

Experimental results

The resulted mass spectrum is presented in Figure 4.5.1(a). One can observe mass peaks ranging from 135 to 146. Figure 4.5.1(b) is the simulated isotopic distribution of $C_2B_{10}H_{12}^-$. By comparing Figure 4.5.1(a) and 1(b), we conclude that the parent anion, $C_2B_{10}H_{12}^-$ was indeed the major component of the ion signal. However, there were other $C_2B_{10}H_n^-$ (n < 12) ions existing in the ion beam at the same time. Thus, we took photoelectron spectrum from the mass = 146 peak in order to avoid the contamination from those fragments. The photoelectron spectrum taken with 3.49 eV laser is presented in Figure 4.5.2. One observes that the first EBE band starts from ~1.8 eV and peaks at 2.33 eV. If there is sufficient Franck-Condon overlap between the ground state of the anion and the ground state of the neutral and there is not much hot band signal, the threshold of the first EBE peak, ~1.8 eV, should be the electron affinity (EA). However, it might not be this case if the structural displacement is too large between the anion and the neutral. Therefore, the potential energy surface discussed later in this article will be utilized to determine the EA value. The experimental vertical detachment energy (VDE), corresponding to the peak position, is 2.33 eV.

Theoretical Results and Discussion

The optimized structures of $C_2B_{10}H_{12}^{0/-}$ are embedded in Figure 4.5.3. The C atoms are in grey, H atoms in white, and B atoms in pink. The neutral cluster has a well-known C_{2v}, slightly distorted icosahedral structure. Two isomers were found for the anion: isomer 1, on the one hand, was found to have a very similar structure as the neutral. Isomer 2, on the other, showed that the C-C bond was broken, while the whole molecule maintains a C_{2V} structure. The coordinates of the neutral and anion isomers are provided in the supporting information. The energy of anion isomer 1 is 1.07 eV higher than that of anion isomer 2, and 0.06 eV higher than that of the neutral, which eliminates the possibility of anion isomer 1's existence in the ion beam. The calculated EA, obtained by subtracting the zero point energy corrected energies of the neutral and anion isomer 2, is 1.19 eV, which is very different from the experimental EBE threshold value, 1.8 eV, indicating that the Franck-Condon overlap might be too small to observe the origin transitions. The calculated VDE, 2.26 eV, has a very good agreement with the experimental value, 2.33 eV.

The NPA analysis shows that the charge on each of the carbon atom of anion isomer 2 is - 0.75 e, which means the excess electron of the anion mainly attaches to the carbon atoms. This is due to its higher electronegativity comparing to B and H atoms. Hence, the heavily charged C-C coordinate is essential in determining the Franck-Condon overlap of the electron detachment process. Figure 4.5.3 presents the potential energy surface of both the anion and the neutral along the C-C coordinate, in which red line is for the neutral and black for the anion. For the neutral, only one potential well is observed at 1.624 Å, in great consistency with reported C-C bond length, 1.622 Å.[11] For the anion, two wells are observed at 1.614 Å and 2.389 Å, corresponding to isomer 1 and isomer 2 respectively. Between the two wells, there is a barrier of 0.78 eV from isomer 1 to isomer 2. We suggest that it is the laser power used to vaporize the molecules that overcomes this barrier and break the C-C bond. The C-C bond displacement between anion isomer 2 and the

neutral is as large as 0.77 Å, and there is clearly no Franck-Condon overlap between anion isomer 2 and the neutral, which explains why we did not observe the origin transition experimentally, and confirms that the observed threshold, 1.8 eV, is not the electron affinity. From the great agreement between the experimental and theoretical VDE values, we gain confidence that the real electron affinity value should be the calculated value, 1.19 eV.

In Figure 4.5.3, next to the structures of anion isomer 1 and isomer 2, we present their highest occupied molecular orbitals (HOMO) where the excess electron dwells. For isomer 1, the electron cloud is mainly localized on the two C-H groups, while in isomer 2, it is delocalized within the whole molecule. Therefore, isomer 2 is able to better accommodate the excess electron and is much more stable.

References

1. T. L. Heying, J. W. Ager, S. L. Clark, D. J. Mangold, H. L. Goldstein, M. Hillman, R. J. Polak, and J. W. Szymanski,. *Inorg. Chem.* **2,** 1089 (1963).

2. H. Schroeder, T. L. Heying, and J. R. Reiner, *Inorg. Chem.* **2,** 1092 (1963).

3. T. L. Heying, J. W. Ager, S. L. Clark, R. P. Alexander, S. Papetti, J. A. Reid and S. I. Trotz, *Inorg. Chem.* **2,** 1097 (1963).

4. S. Papetti, and T. L. Heying, *Inorg. Chem.* **2** 1105 (1963).

5. M. M. Fein, J. Bobinski, N. Mayes, N. Schwartz and M. S. Cohen, *Inorg. Chem.* **2,** 1111 (1963).

6. M. M. Fein, D. Grafstein, J. E. Paustian, J. Bobinski, B. M. Lichstein, N. Mayes, N. Schwartz and M. S. Cohen, *Inorg. Chem.* **2,** 1115 (1963).

7. D. Grafstein, J. Bobinski, J. Dvorak, H. Smith, N. Schwartz, M. S. Cohen and M. M. Fein, *Inorg. Chem.* **2,** 1120 (1963).

8. D. Grafstein, J. Bobinski, J. Dvorak, J. E. Paustian, H. F. Smith, S. Karlan, C. Vogel and M. M. Fein, *Inorg. Chem.* **2,** 1125 (1963).

9. D. Grafstein and J. Dvorak, *Inorg. Chem.* **2,** 1128 (1963).

10. H. L. Gingrich, T. Ghosh, Q. Huang and M. Jones, *J. Am. Chem. Soc.* **112,** 4082 (1990).

11. E. D. Jemmis, and B. Kiran, *J. Am. Chem. Soc.* **119,** 4076 (1997).

12. B. Kiran, A. Anoop and E. D. Jemmis, *J. Am. Chem. Soc.* **124,** 4402 (2002).

13. L. I. Zakharkin and V. N. Kalinin, Bulletin of the Academy of Sciences of the USSR, Division of chemical science **19,** 2246 (1970).

14. M. L. McKee, M. Bühl and P. v. R. Schleyer, *Inorg. Chem.* **32,** 1712 (1993).

15. M. L. McKee, *J. Am. Chem. Soc.* **114,** 5856 (1992).

16. T. D. Getman, C. B. Knobler and M. F. Hawthorne, *J. Am. Chem. Soc.* **112,** 4593 (1990).

17. T. D. Getman, C. B. Knobler and M. F. Hawthorne, *Inorg. Chem.* **31,** 101 (1992).

18. K. Hermansson, M. Wòjcik and S. Sjöberg, *Inorg. Chem.* **38,** 6039 (1999).

19. X. Zhang, Y. Wang, H. Wang, A. Lim, G. Ganteför, K. H. Bowen, J. U. Reveles and S. N. Khanna, *J. Am. Chem. Soc.* **135,** 4856 (2013).

20. J. Ho, K. M. Ervin, and W. C. Lineberger. *J. Chem. Phys.* **93,** 6987 (1990).

21. A. D. Becke, *Phys. Rev. A* **38,** 3098 (1988).

22. A. D. Becke, *J. Chem. Phys.* **98,** 5648 (1993).

23. C. Lee, W. Yang and R. G. Parr, *Phys. Rev. B* **37,** 785 (1988).

24. M. J. Risch, G. W. Trucks, H. B. Schlegel, G. E. Scuseria, M. A. Robb, J. R. Cheeseman, G. Scalmani, V. Barone, B. Mennucci, G. A. Petersson, et al. Gaussian 09, revision A.1; Gaussian, Inc.:Wallingford, CT, 2009

25. H. Wang, X. Zhang, J. Ko, A. Grubisic, X. Li, G. Gantefér, H. Schnöckel, B. Eichhorn, M. Lee, P. Jena, A. Kandalam, B. Kiran, and K. H. Bowen, *J. Chem. Phys*. **140,** 054301 (2014).

26. H. Wang, Y. Ko, X. Zhang, G. Gantefoer, H. Schnoeckel, B. W. Eichhorn, P. Jena, B. Kiran, A. K. Kandalam, and K. H. Bowen, *J. Chem. Phys*. **140,** 124309 (2014).

Figure Captions

Figure 4.5.1. Experimental mass spectrum and simulated isotopic distribution of $C_2B_{10}H_{12}^-$.

Figure 4.5.2. The photoelectron spectrum of $C_2B_{10}H_{12}^-$ taken with 3.49 eV laser.

Figure 4.5.3. Potential energy surfaces of neutral (red) and anionic (black) o-carborane along the

C-C coordinate. Their structures and HOMOs are embedded as well.
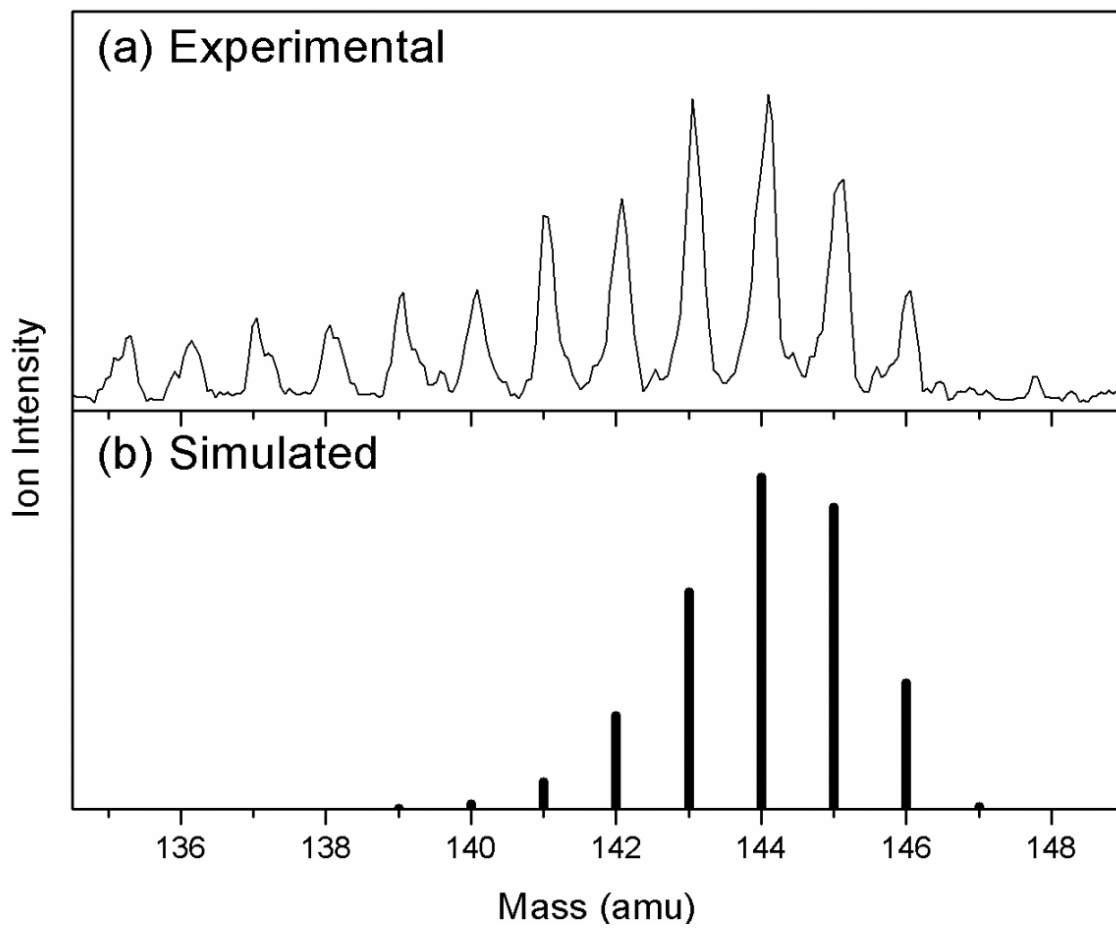
Figure 4.5.1
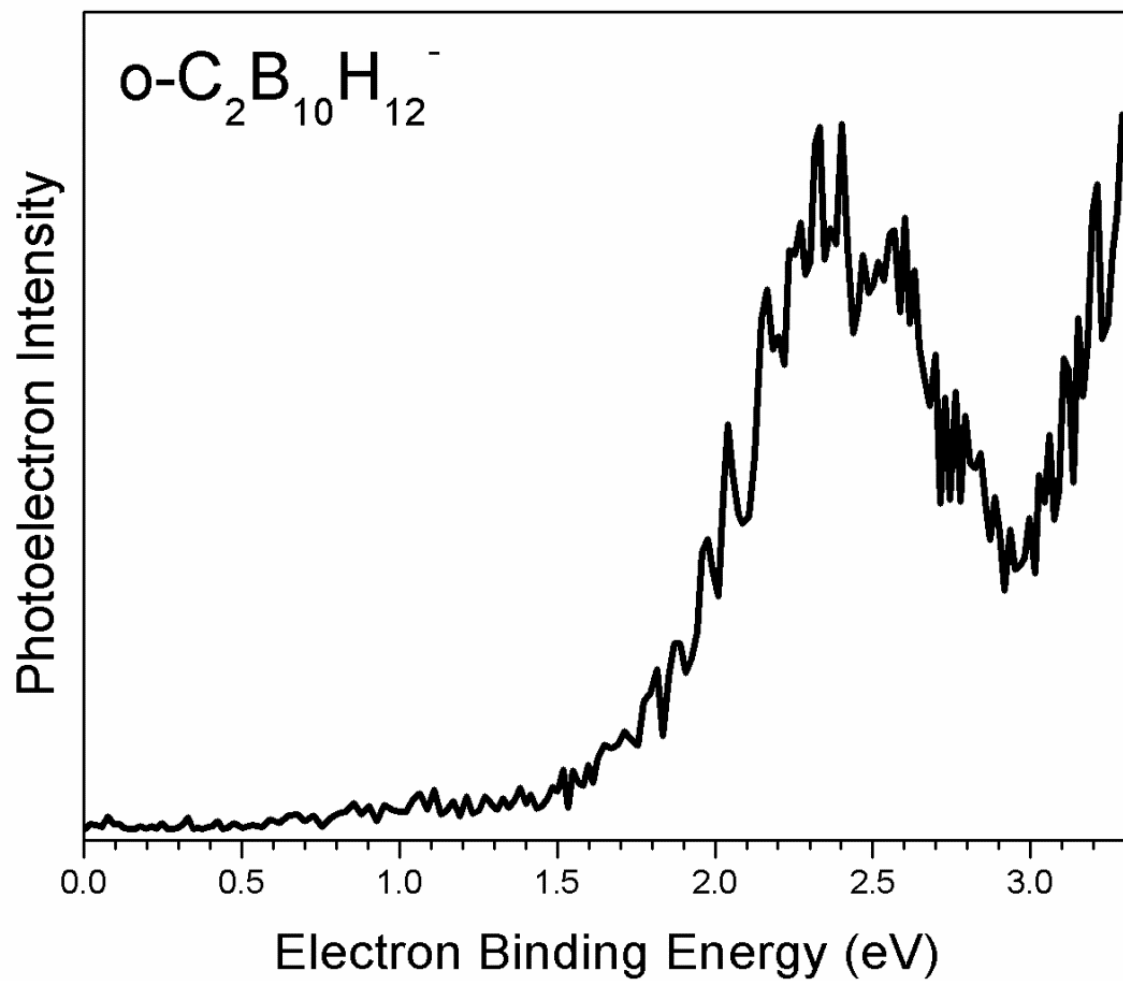
Figure 4.5.2
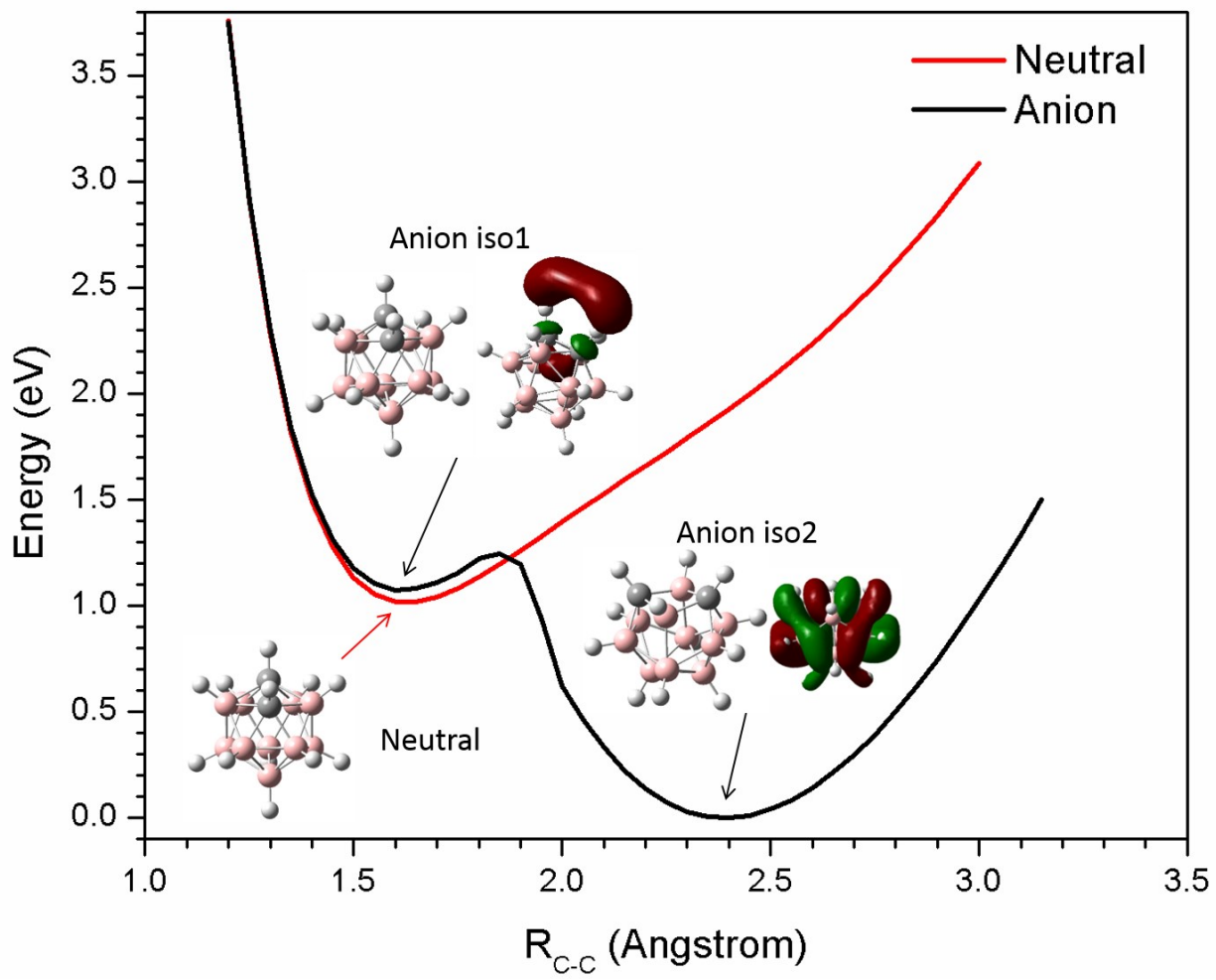
Figure 4.5.3

4.6 Photoelectron Spectroscopy of Carbon Aluminum Hydride Cluster Anions, $C_xAl_yH_z^-$

Introduction

In this section, I report the experimental discovery of a series of carbon aluminum hydride cluster anions, $C_xAl_yH_z^-$ (x = 1-3; y = 1-8; z = 0-3), generated by a pulsed arc cluster ionization source (PACIS), identified by time-of-flight mass spectrometer, and characterized by photoelectron spectroscopy. Some of the structures were also calculated and presented. Ultra-high coordination numbers for carbon were observed. The study of carbon aluminum hydride is an extension of aluminum hydride cluster and boron aluminum hydride cluster studies.

Further interpretations are needed.

Figure Captions

Figure 4.6.1. Mass spectrum of $C_xAl_yH_z^-$

Figure 4.6.2. Photoelectron spectra of $C_xAl_yH_z^-$

Figure 4.6.3. Some calculated structures.

Figure 4.6.1

Figure 4.6.2

CAl₅H⁻ CAl₆H⁻ CAl₇H⁻

CAl₈H⁻ CAl₉H⁻
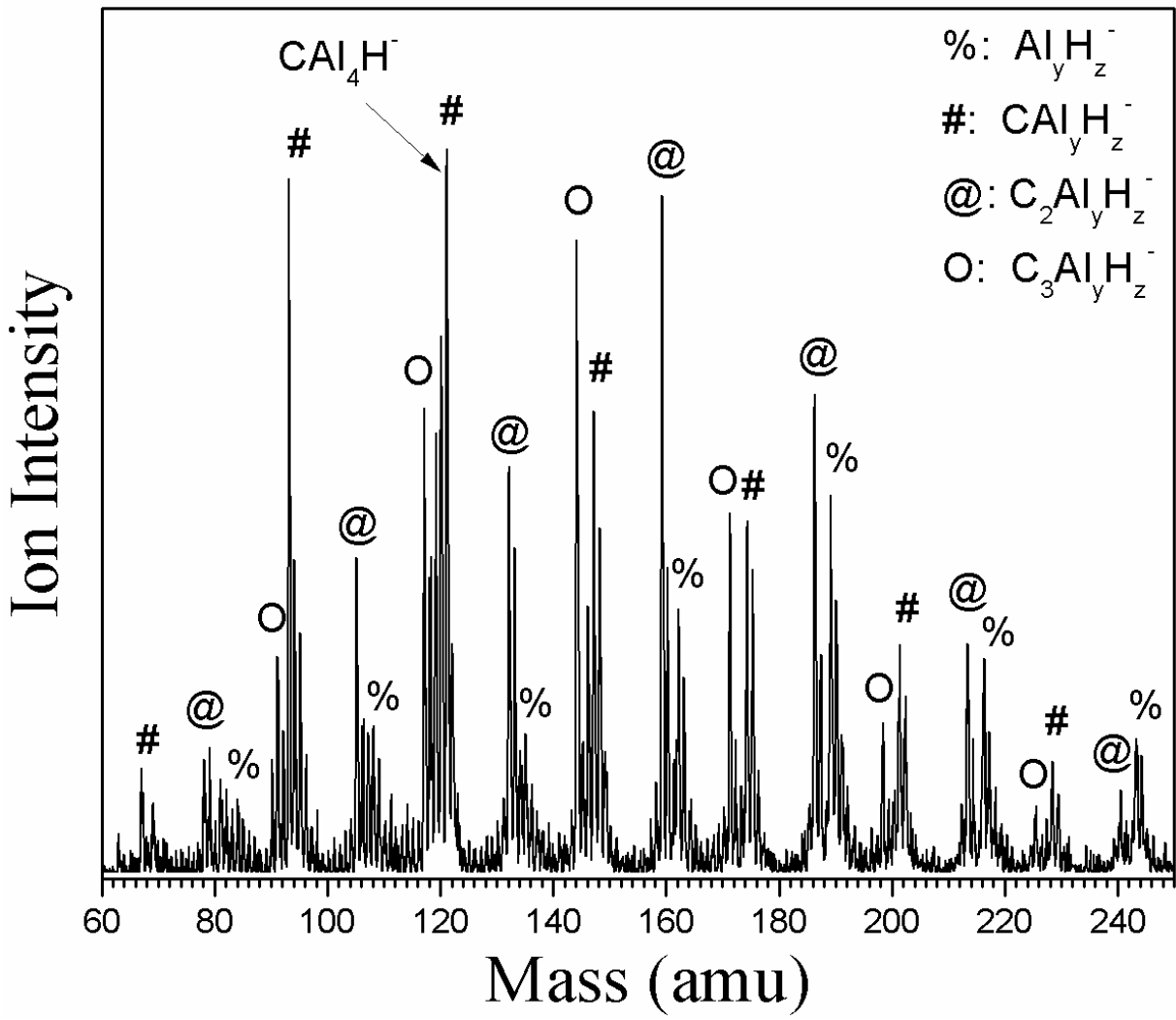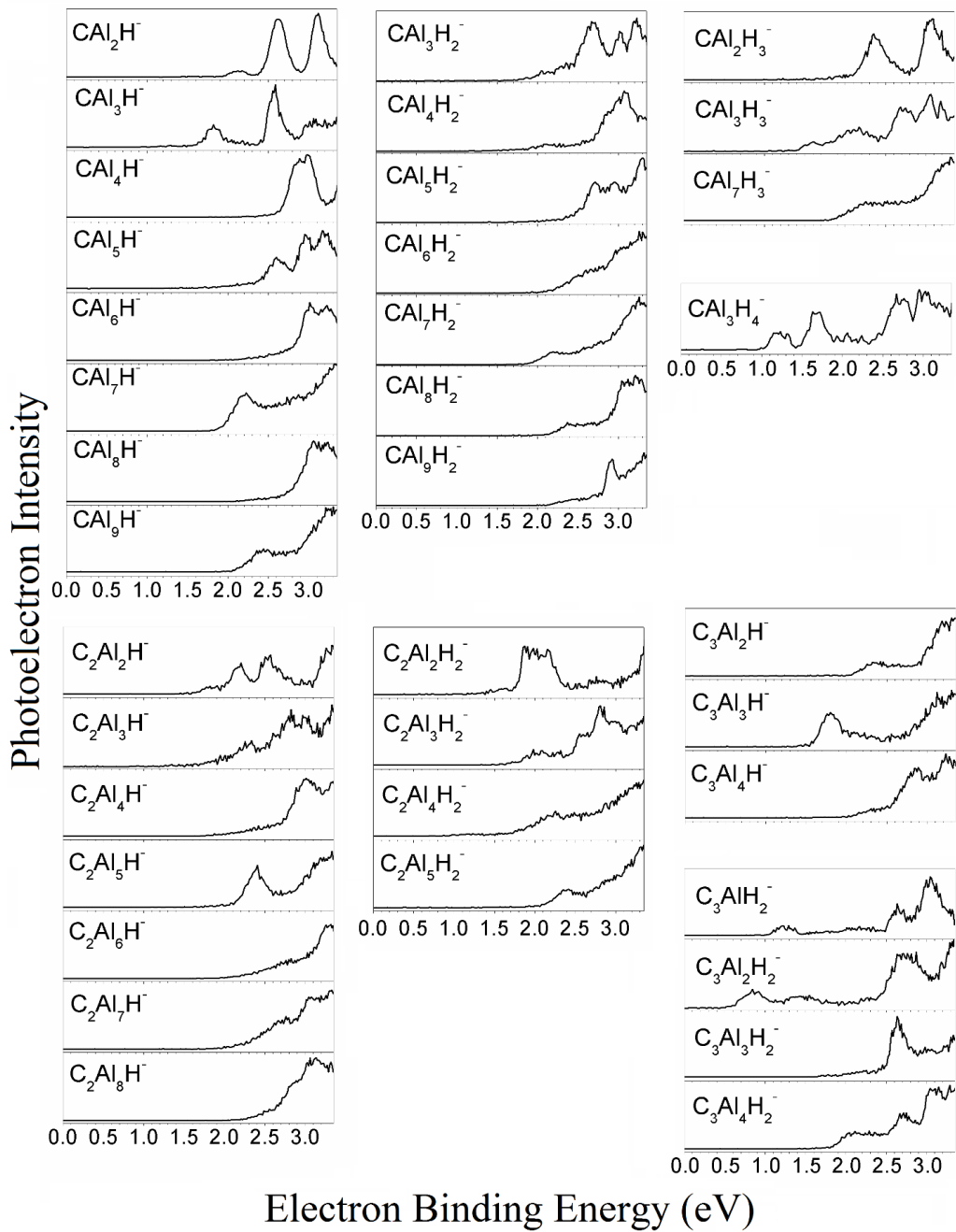
CAl₅H₂⁻ CAl₆H₂⁻ CAl₇H₂⁻
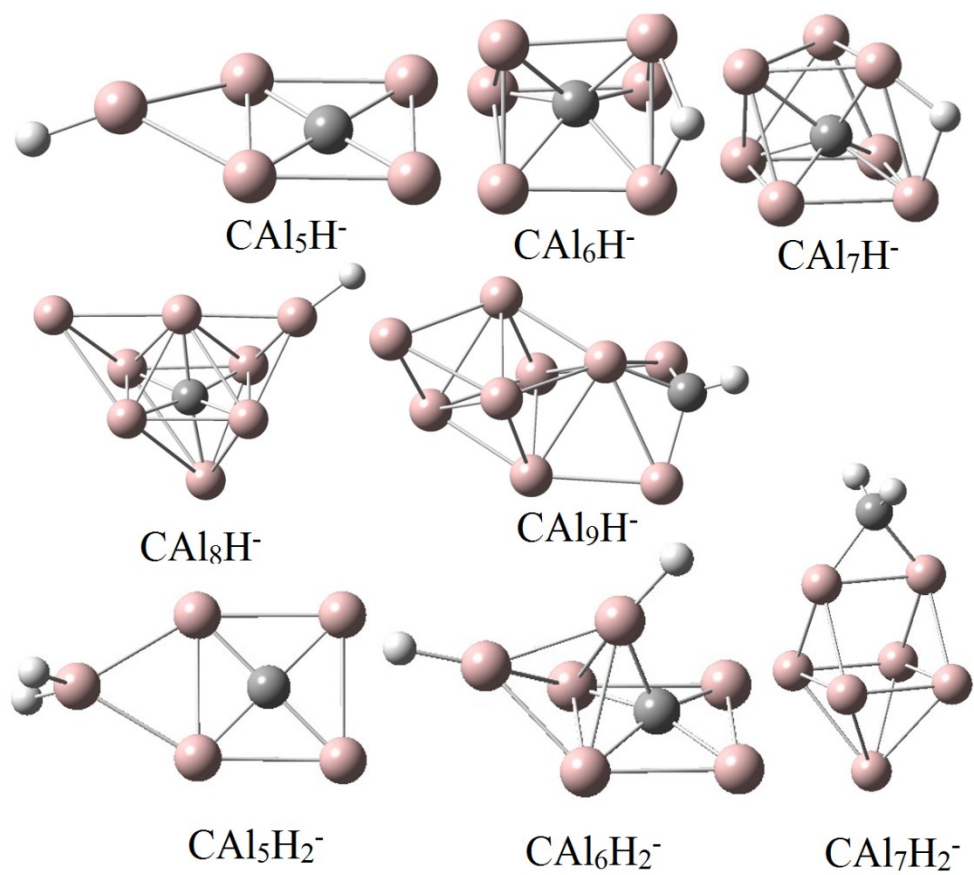
Figure 4.6.3

CHAPTER 5. LiOH$_2^-$, a Double-Rydberg Anion

Xinxing Zhang,[†,1] Zhen Zeng,[†,2] Weijun Zheng,[2] Kit Bowen[1,a]

[1] Department of Chemistry, Johns Hopkins University, Baltimore, Maryland 21218, USA

[2] Beijing National Laboratory for Molecular Sciences, State Key Laboratory of Molecular Reaction Dynamics, Institute of Chemistry, Chinese Academy of Sciences, Beijing 100190, China

[a] Electronic mail: kbowen@jhu.edu

[†] These authors contributed equally

Abstract

For years researchers have been exploring the double Rydberg anion (DRA), H$_3$O$^-$, however, no positive results have been reported other than theoretical predictions. By substituting one H atom in H$_3$O$^-$ with Li atom, we successfully designed and obtained a DRA LiOH$_2^-$ via anion photoelectron spectroscopy and theoretical calculations. The photoelectron spectrum of LiOH$_2^-$ strikingly showed a red shift comparing to that of Li$^-$, which is different from a lot of other cases where an anion interacts with water molecule and solvation occurs. Our calculations have a great agreement with measured values, confirming that the DRA is the only isomer existed in the experiments. NBO analysis also exhibits a doubly occupied, very diffuse, Rydberg type highest occupied molecular orbital.

Introduction

The nature of Double-Rydberg Anions (DRA) is a stable, closed-shell cation core around which there are a pair of electrons delocalized in a very diffuse orbital.[1] Such cation cores can be H_3^+, H_3O^+, NH_4^+, Na^+, etc. In 1988, Bowen announced the first experimental observation of the DRA NH_4^- and reported its vertical detachment energy (VDE) to be 0.472 eV.[2] Afterwards, Oritz[3] and Gutowski[4] carried out geometry and energy calculations of DRA NH_4^- and reported the VDE to be 0.42 eV and 0.45 eV, respectively, both of which are in excellent agreement with experiments. Later on, anion photoelectron spectroscopy and interpretations of DRAs $N_nH_{3n+1}^-$ (n = 2-7) were reported.[5, 6] Ortiz's calculation[7] on $N_2H_7^-$ was consistent with the experiment. Another intriguing DRA, H_3O^-, was also predicted by theory,[4,8] and the VDE of DRA H_3O^- was calculated to be 0.46 eV, geometry to be pyramidal C_{3v}.[4] However, to the best of our knowledge, there has been no experimental evidence of the existence of DRA H_3O^-, and only its isomer, $H^-(H_2O)$, was reported.[9] $H^-(H_2O)$ can be viewed as an H^- anion solvated by one water molecule via hydrogen bond. In our group, numerous experimental efforts have been made to discover DRA H_3O^- but no success has been achieved yet. On the other hand, the metastable Rydberg neutral molecule, D_3O, was discovered by neutralized ion beam spectroscopy,[10] but the experimental observation of H_3O via neutralization-reionization spectroscopy has met controversy.[11,12] Therefore, neither the Rydberg molecule H_3O nor the DRA H_3O^- has solid experimental evidences yet.

To design a DRA that is similar to H_3O^-, we draw our attention to lithium. Lithium is in the same group as H, and $LiOH_2^-$ is isoelectronic to H_3O^-, therefore, $LiOH_2^-$ has a chance to be a DRA, a sister cluster of H_3O^-. However, when Li forms anion and interacts with water molecule, one would expect a water solvated cluster anion, $Li^-(H_2O)$, which is similar to $H^-(H_2O)$. Therefore, identifying the right isomer is one of the major tasks of the current paper. Noteworthy, the ground

state of Li_3O^-, which is also isoelectronic to H_3O^-, has been reported to be a triplet state with a C_{2v} structure, which is not a DRA.[13,14] In this work, we utilized anion photoelectron spectroscopy and theoretical calculations to explore the existence of designer DRA $LiOH_2^-$ and its corresponding neutral. We have found that the DRA isomer $LiOH_2^-$ has lower energy than the solvation isomer $Li^-(H_2O)$, and the agreement between theory and experiment confirmed that $LiOH_2^-$ was the only isomer present in experiment. The molecular orbital analysis revealed that $LiOH_2^-$ was indeed a DRA. Its VDE and geometry are also similar to those of H_3O^-. Its neutral counterpart, $LiOH_2$, was confirmed to be a Rydberg molecule.

Experimental and theoretical methods

Anion photoelectron spectroscopy is conducted by crossing a mass-selected beam of negative ions with a fixed-frequency photon beam and energy-analyzing the resultant photodetached electrons. It is governed by the energy-conserving relationship, $h\nu = EBE + EKE$, where $h\nu$ is the photon energy, EBE is the electron binding (transition) energy, and EKE is the electron kinetic energy. The anion photoelectron spectrometer, which has been described previously,[15] consists of an ion source, a linear time-of-flight mass spectrometer, a mass gate, a momentum decelerator, a pulsed Nd:YAG photodetachment laser, and a magnetic bottle electron energy analyzer. Photoelectron spectra were taken with 1064 nm photon energy. Li^- and $Li(H_2O)^-$ cluster anions were generated in a laser vaporization source. Briefly, a rotating and translating pressed LiI disk is ablated by a pulsed Nd:YAG laser beam operating at a wavelength of 532 nm. The resulting plasma was cooled by supersonically expanding a plume of helium gas from a pulsed gas valve (backing pressure of ~60 psi). Negatively charged anions were then extracted into the spectrometer prior to mass selection and photodetachment.

All of the calculations were carried out using the Gaussian 09 software package.[16] The structures of neutral and anionic $Li(H_2O)^-$ were obtained by density functional theory (DFT) based electronic structure calculations. The M06-2X functional[17] along with 6-311++G (3df, 3pd) basis set[18] was used for all the calculations. Structures were optimized without any symmetry constraints. The chemical bonding analysis via Natural Bond Orbital (NBO)[19,20] method is also presented.

The vertical detachment energy (VDE) obtained from the theoretical calculations was compared with the corresponding measured values. VDE is the energy between the ground state anion and its corresponding neutral at the geometry of the anion. The calculated adiabatic detachment energy (ADE) of the lowest energy isomers of anion were also compared to the onset (threshold) region of the lowest electron binding energy of the PES spectrum. The ADE is calculated as the energy difference between the lowest energy geometry of the anionic cluster and the structurally similar/identical isomer (nearest local minimum) of its neutral counterpart. If the local minimum is also the global minimum, then the ADE is also the electron affinity (EA), defined to be the energy difference between the ground state of the anion and the ground state of the neutral.

Results and discussion

Two $Li(H_2O)^-$ isomers might co-exist, the DRA isomer is written as $LiOH_2^-$, and the solvation isomer is written as $Li^-(H_2O)$. Before confirming the structure, we generally write it in the form of $Li(H_2O)^-$. The resultant photoelectron spectra of Li^- and $Li(H_2O)^-$ are presented in Figure 5.1.1. The spectrum of Li^- peaks at EBE = 0.62 eV, which is corresponding to the EA, perfectly reproduces the published work.[21] Comparing to Li^-, the spectrum of $Li(H_2O)^-$ red shifts to the low EBE side, starts from EBE = 0.52 eV (EA) and peaks at EBE = 0.56 eV (VDE). This

red shift itself is striking enough because when an anion interacts with water molecule, solvation effect takes place and the spectrum always shifts to the high EBE side.[22-31, Appendix A. XIII]

Calculated information obtained from M06-2X/6-311++G (3df, 3pd) level of theory is presented in Figure 5.1.2. Two anionic isomers, $LiOH_2^-$ and $Li^-(H_2O)$ and the neutral $LiOH_2$, together with the relative energies (eV), VDE of the anions (eV), bond lengths (Å, in black) and bond angles (°, in red) are displayed. $LiOH_2^-$ and $LiOH_2$ both have *Cs* symmetry, their structures are very similar, and only the bond lengths in the anion are slightly shorter than in the neutral, indicating the bond order is higher in the anion. If they are indeed Rydberg anion and neutral, the very diffuse HOMO will have two electrons in the anion and one electron in the neutral, respectively, therefore, the bond order of the anion should be higher than the neutral by 0.5, which is consistent with the calculated bond lengths. Such a small structural difference also promises very high Frank-Condon overlap, very close ADE and VDE values and sharp experimental EBE peak. The calculated ADE (0.54 eV) and VDE (0.55 eV) have excellent agreement with the experimental results (0.52 eV and 0.56 eV), hence, we are confident that the calculated ADE is actually the measured EA in this case. The solvation anion isomer, $Li^-(H_2O)$ has a C_{2v} structure, and is 0.27 eV higher in energy comparing to $LiOH_2^-$. The calculated VDE of $Li^-(H_2O)$ is 0.85 eV, much higher than the experimental value. Therefore, we conclude that $Li^-(H_2O)$ does not exist in our experiment, and at this stage, we can formally write the cluster anion as $LiOH_2^-$ as it appears in the title. Please note that the calculated VDE of $Li^-(H_2O)$ is higher than the EA of Li, which makes sense when solvation occurs.

As a matter of fact, a few experimental and theoretical investigations on $LiOH_2^-$ have been reported previously,[32-35] and those results are consistent with the current paper, but none of them realized the DRA nature of $LiOH_2^-$. As the major goal of the present study, next we discuss the

chemical bonding within this cluster. Figure 5.1.3 exhibits all the molecular orbitals (MOs) of LiOH$_2^-$ obtained from the NBO analysis. Figure 5.1.4 is the correlation diagram describing how these MOs in Figure 5.1.3 are formed from the combinations of the atomic orbitals of each atom. HOMO – 6 is the nonbonding *1s* orbital of O, HOMO – 5 is the nonbonding *1s* orbital of Li, and HOMO – 4 is the nonbonding *2s* orbital of O. HOMO – 3, HOMO – 2 and HOMO – 1 are the three MOs that describe the three single bonds between O-H and O-Li, and they are obtained from the combinations of the *s* orbitals of H and Li and the three *2p* orbitals of O. HOMO, highlighted by a red box, is the Rydberg MO. It is the combination of the *s* orbitals of H and Li and the *2s* orbital of O. From Figure 5.1.3, one can clearly observe that the HOMO is highly delocalized around the whole cluster, which is very similar to the calculated HOMO of DRA H$_3$O$^-$,[8] confirming that LiOH$_2^-$ is indeed a DRA. The observed VDE (0.56 eV) is similar to the calculated VDE of DRA H$_3$O$^-$ (0.46 eV)[4], which further confirms that our design is feasible. Please note that the MOs of neutral LiOH$_2$ are very similar to those of LiOH$_2^-$, and the singly occupied HOMO is also a very diffuse molecular orbital, confirming that the neutral is a Rydberg molecule.

Concluding Remarks

The DRA nature of LiOH$_2^-$ is an excellent example of the electron counting rule. By substituting the H atom with Li in DRA H$_3$O$^-$, we successfully designed and obtained DRA LiOH$_2^-$ via anion photoelectron spectroscopy and calculations. To extend the current results, we noticed that the published works[36,37] on LiNH$_3^-$ have already proved its DRA nature which is similar to NH$_4^-$ [2] even though the authors did not claim it was. The existence of DRA LiOH$_2^-$ in turn gives us courage continuing to explore DRA H$_3$O$^-$.

References

1. J. Simons and M. Gutowski, *Chem. Rev.* **91**, 669 (1991).

2. J. T. Snodgrass, J. V. Coe, C. B. Freidhoff, K. M. McHugh, and K. H. Bowen, *Faraday Discuss. Chem. Soc.* **86**, 241 (1988).

3. J. V. Ortiz, *J. Chem. Phys.* **87**, 3557 (1987).

4. M. Gutowski and J. Simons, *J. Chem. Phys.* **93**, 3874 (1990).

5. S. -J. Xu, J. M. Nilles, J. H. Hendricks, S. A. Lyapustina, and K. H. Bowen, *J. Chem. Phys.* **117**, 5742 (2002).

6. D. Radisic, S. T. Stokes, and K. H. Bowen, *J. Chem. Phys.* **123**, 011101 (2005).

7. J. V. Ortiz, *J. Chem. Phys.* **117**, 5748 (2002).

8. J. Melin and J. V. Ortiz, *J. Chem. Phys.* **127**, 014307 (2007).

9. E. de Beer, E. H. Kim, D. M. Neumark, R. F. Gunion and W. C. Lineberger *J. Phys. Chem.* **99**, 13627 (1995).

10. G. I. Gellene and R. F. Porter, *J. Chem. Phys.* **81**, 5570 (1984).

11. W. J. Griffiths, F. M. Harris, and J. H. Beynon, *Inter. J. Mass Spec. Ion Proc.* **77**, 233 (1987).

12. R. E. March and A. B. Young, *Inter. J. Mass Spec. Ion Proc.* **85**, 237, (1988).

13. D. Wang, J. D. Graham, A. M. Buytendyk, and K. H. Bowen *J. Chem. Phys.* **135**, 164308 (2011).

14. S. Zein and J. V. Ortiz, *J. Chem. Phys.* **135**, 164307 (2011).

15. H. –G. Xu, Z. –G. Zhang, Y. Feng, J. Yuan, Y. Zhao, and W. Zheng, *Chem. Phys. Lett.* **487**, 204 (2010).

16. 20. M. J. Risch, G. W. Trucks, H. B. Schlegel, G. E. Scuseria, M. A. Robb, J. R. Cheeseman, G. Scalmani, V. Barone, B. Mennucci, G. A. Petersson, et al. Gaussian 09, revision A.1; Gaussian, Inc.:Wallingford, CT, 2009

17. Y. Zhao and D. G. Truhlar, *J. Phys. Chem. A* **110**, 51215129 (2006).

18. R. Krishnan, J. S. Binkley, R. Seeger, and J. A. Pople, *J. Chem. Phys.* **72**, 650 (1980).

19. A. E. Reed, L. A. Curtiss and F. Weinhold, *Chem. Rev.* **88**, 899 (1988).

20. J. P. Foster and F. Weinhold, *J. Am. Chem. Soc.* **102**, 7211 (1980).

21. A. N. Alexandrova, A. I. Boldyrev, X. Li, H. W. Sarkas, J. H. Hendricks, S. T. Arnold, and K. H. Bowen, *J. Chem. Phys.*, **134**, 044322 (2011).

22. W. Zheng, X. Li, S. Eustis, A. Grubisic, O. Thomas, H. deClercq, and K. Bowen, *Chem. Phys. Lett.*, **444**, 232 (2007).

23. C. Chi, H. Xie, Y. Li, R. Cong, M. Zhou, and Z. Tang, *J. Phys. Chem. A* **115**, 5380 (2011).

24. G. J. Rathbone, T. Sanford, D. Andrews and W. Carl Lineberger, *Chem. Phys. Lett.* **401**, 570 (2005).

25. T. Nagata, H. Yoshida and T. Kondow, *Z. Phys. D: At., Mol. Clusters* **26**, 367 (1993).

26. G. Markovich, S. Pollack, R. Giniger, and O. Cheshnovsky, *J. Chem. Phys.* **101**, 9344 (1994).

27. G. Markovitch, R. Giniger, M. Levin, and O. Cheshnovsky, *Z. Phys. D: At., Mol. Clusters* **20**, 69 (1991).

28. G. Markovich, O. Cheshnovsky, and U. Kaldor, *J. Chem. Phys.* **99**, 6201(1993).

29. D. W. Arnold, S. E. Bradforth, E. H. Kim, and D. M. Neumark, *J. Chem. Phys.* **102**, 3510 (1995).

30. D. W. Arnold, S. E. Bradforth, E. H. Kim, and D. M. Neumark, *J. Chem. Phys.* **97**, 9468 (1992).

31. D. W. Arnold, S. E. Bradforth, E. H. Kim, and D. M. Neumark, *J. Chem. Phys.* **102**, 3493 (1995).

32. K. Hashimoto, T. Kamimoto, and K. Fuke, *Chem. Phys. Lett.* **266**, 7 (1997).

33. R. Takasu, T. Taguchi, K. Hashimoto, and K. Fuke, *Chem. Phys. Lett.* **290**, 481 (1998).

34. Z. Zeng, C. Liu, G. Hou, G. Feng, H. Xu, Y. Gao, and W. Zheng, *J. Phys. Chem. A* **119**, 2845 (2015).

35. K. Hashimoto, K. Daigoku, T. Kamimoto, and T. Shimosato, *Internet Electron. J. Mol. Des.* **1**, 503 (2002).

36. H. Zhang and Z. Liu, *J. Chem. Phys.* **136**, 124314 (2012).

37. R. Takasu, F. Misaizu, K. Hashimoto, and K. Fuke, *J. Phys. Chem. A* **101**, 3078 (1997).

Figure Captions

Figure 5.1.1. Photoelectron spectra of Li$^-$ and Li(H$_2$O)$^-$.

Figure 5.1.2. Calculated structures of LiOH$_2^{-/0}$ and Li$^-$(H$_2$O). The bond lengths, bond angles, relative energies, VDEs are also presented.

Figure 5.1.3. MOs of LiOH$_2^-$. The Rydberg orbital is highlighted with red box.

Figure 5.1.4. Correlation diagram depicting the MOs of LiOH$_2^-$.

Figure 5.1.1

LiOH$_2^-$

0.976
1.859
109.5
105.2

LiOH$_2$

0.969
1.872
113.2
106.3

Li$^-$(H$_2$O)

3.253
101.8
0.964
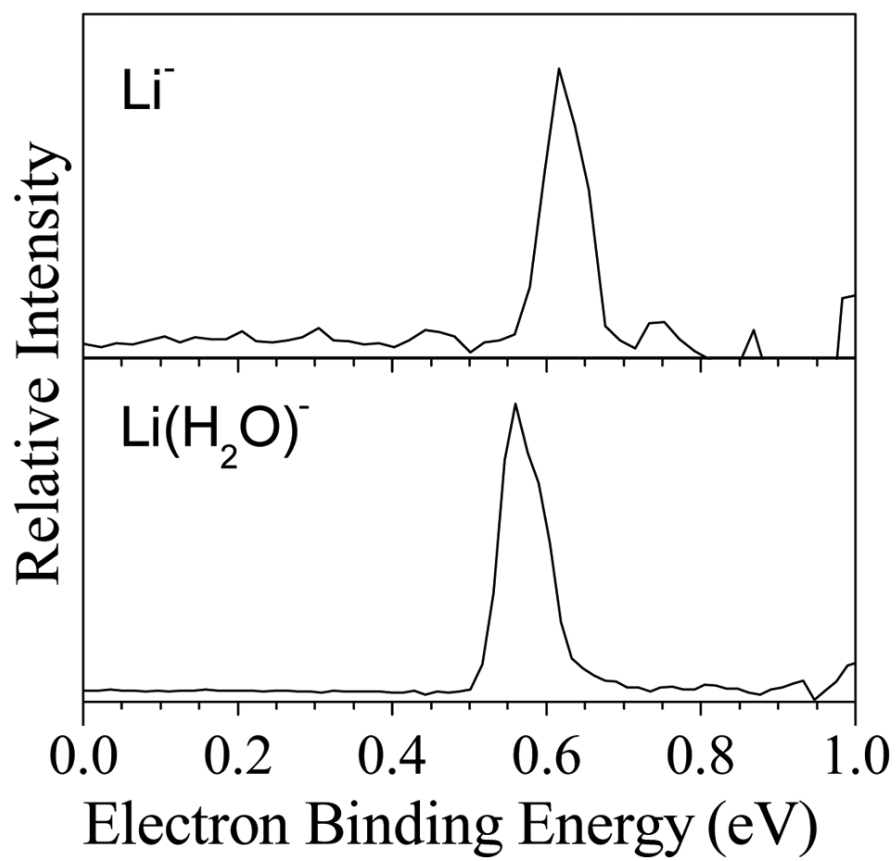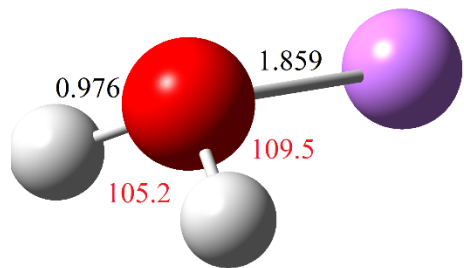
E = 0
VDE = 0.55
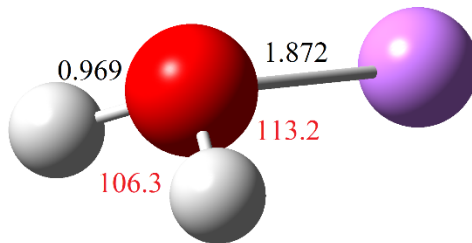
E = 0.54 (ADE)
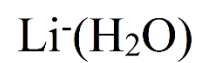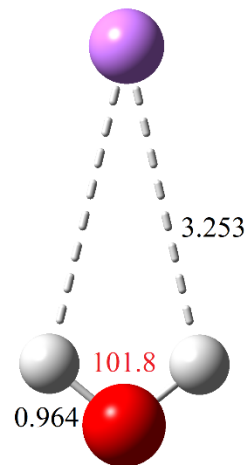
E = 0.27
VDE = 0.85

Figure 5.1.2

238
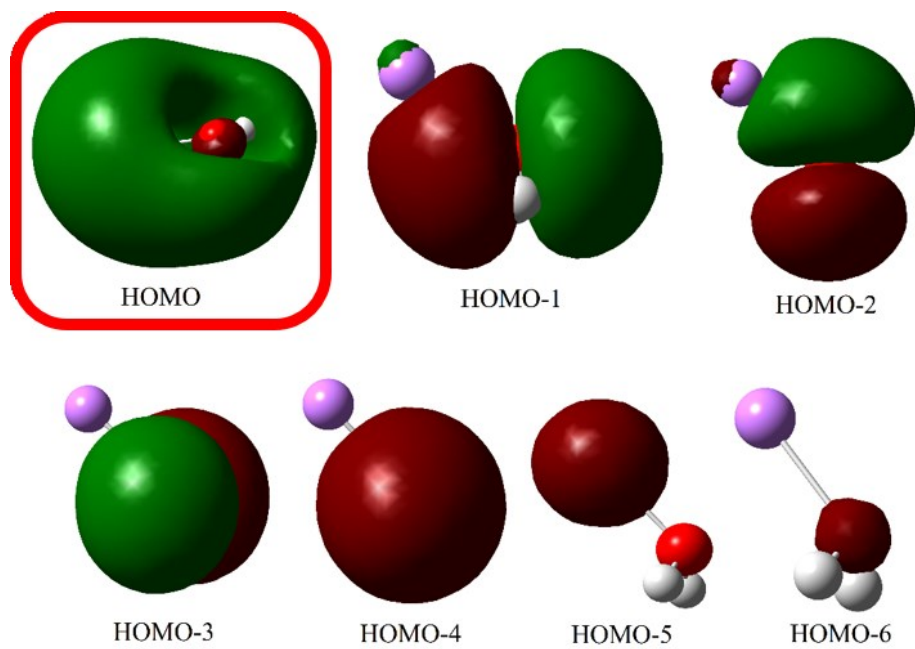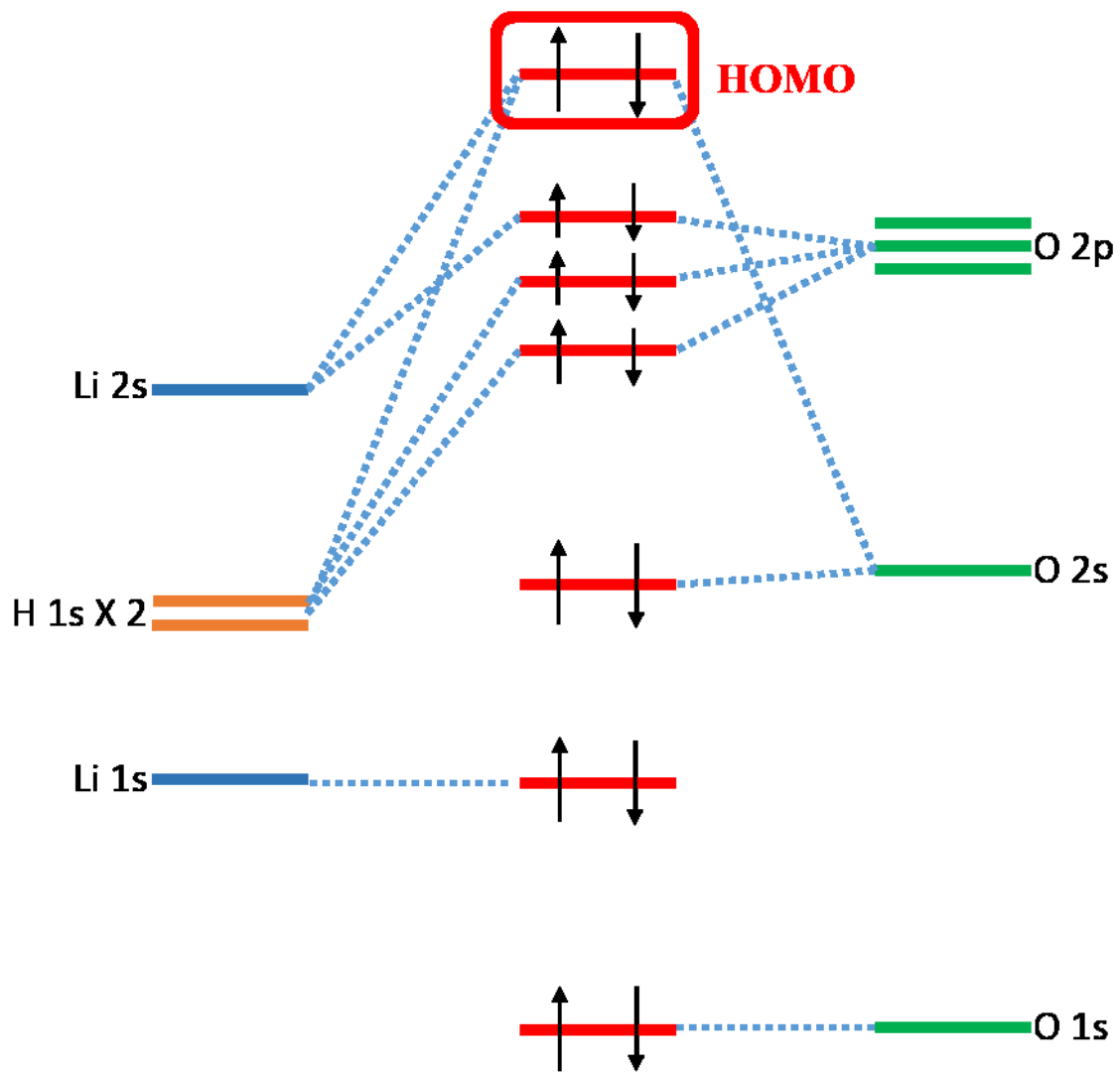
Figure 5.1.3

Figure 5.1.4

Appendix A. Photoelectron Spectroscopy of Various Systems: A Database

I. Photoelectron spectra of several neurotransmitters: laser induced tautomerization and low barrier hydrogen bond model

II. When anion PES meets solid state physics

III. Rare earth elements related systems

IV. Ligated cluster anions (for MURI)

V. PES of bimetallic $Al_xM_y^-$ cluster anions

VI. The concept of sub-nano thermite clusters

VII. Water solvation of unstable molecular radical anions

VIII. Clusters mimic precious elements

IX. Bimetallic transition metal cluster anions

X. Transition metal hydrides

XI. Electron induced proton transfer in formic acid trimer

XII. Anionic resonance of azobenzene parent anion

XIII. Transition metal anions solvated by water

XIV. Microsolvation of HCl

XV. PES of organic anions

XVI. Water activation by a single atom

XVII. Miscellaneous

In this section, all the spectra that were taken by me and have not been published during my PhD career will be presented in figures. Details of experiments and interpretations will be briefly discussed. This section is the most important one in Appendix.

I. Photoelectron spectra of several neurotransmitters: laser induced tautomerization and low barrier hydrogen bond model

The parent anion of five different neurotransmitters, including dopamine, adrenaline, tyrosine, phenylalanine and DOPA were made by coating the sample powders onto a Cu or Ag rod and then ablating the rod with 532 nm laser. The anions of intact neutrals have negative EA. What we have observed here are actually laser induced tautomer, in which active H atoms migrate to benzene rings and open up the C=C double bond. Different tautomers may coexist because there are several C=C double bonds in the benzene ring and there are several active H atoms in a certain neurotransmitter molecule. Different H atoms may migrate to different C=C bonds. One or more H atoms may migrate. The energy of the laser compensates the energy needed for the H atom migration. Due to unavoidable isotopic contamination, the spectra of the parent anion will always have some feature from the deprotonated anion. These features are identified and marked by X. The spectra of deprotonated anions and the deprotonated dimer anions are also compared and show a low barrier hydrogen bond (LBHB) pattern. Some preliminary theoretical calculations for tyrosine have been done by our collaborator M. Gutowski, and I did some calculations on dopamine.
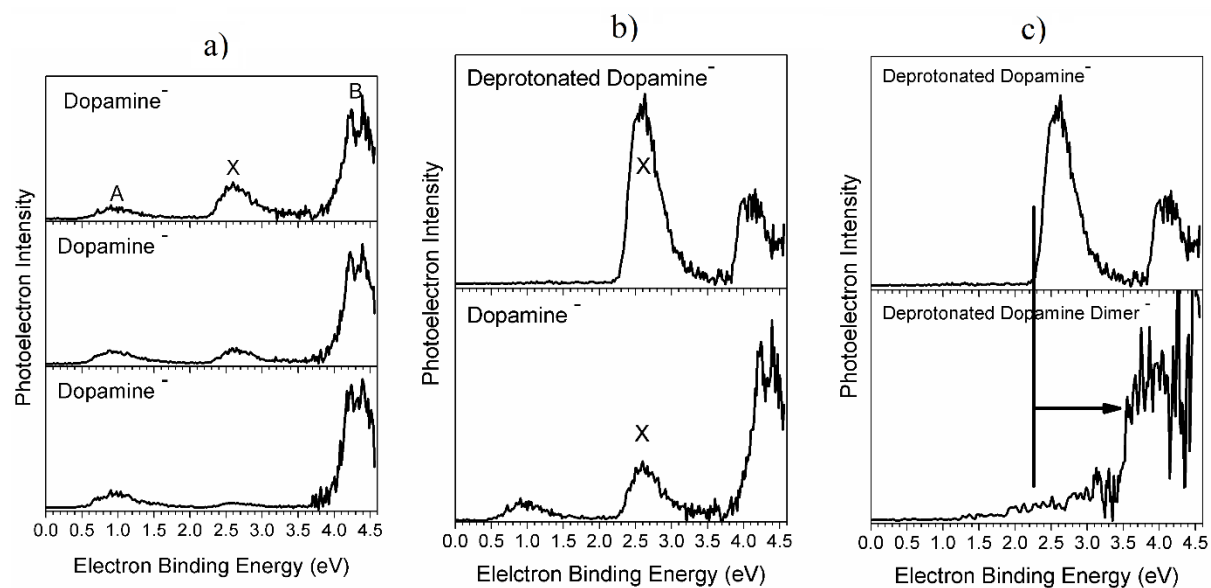
Figure A.1. The photoelectron spectra of dopamine parent anion taken on different days, the relative intensities of peak marked by X change day by day, which is from the deprotonated anion (a). The comparison between deprotonated dopamine anion and the parent anion confirms that peak X is from deprotonated anion (b). The comparison between deprotonated dopamine anion and deprotonated dopamine dimer anion shows an EA shift of ~1.2 eV, which is definitely a LBHB pattern.
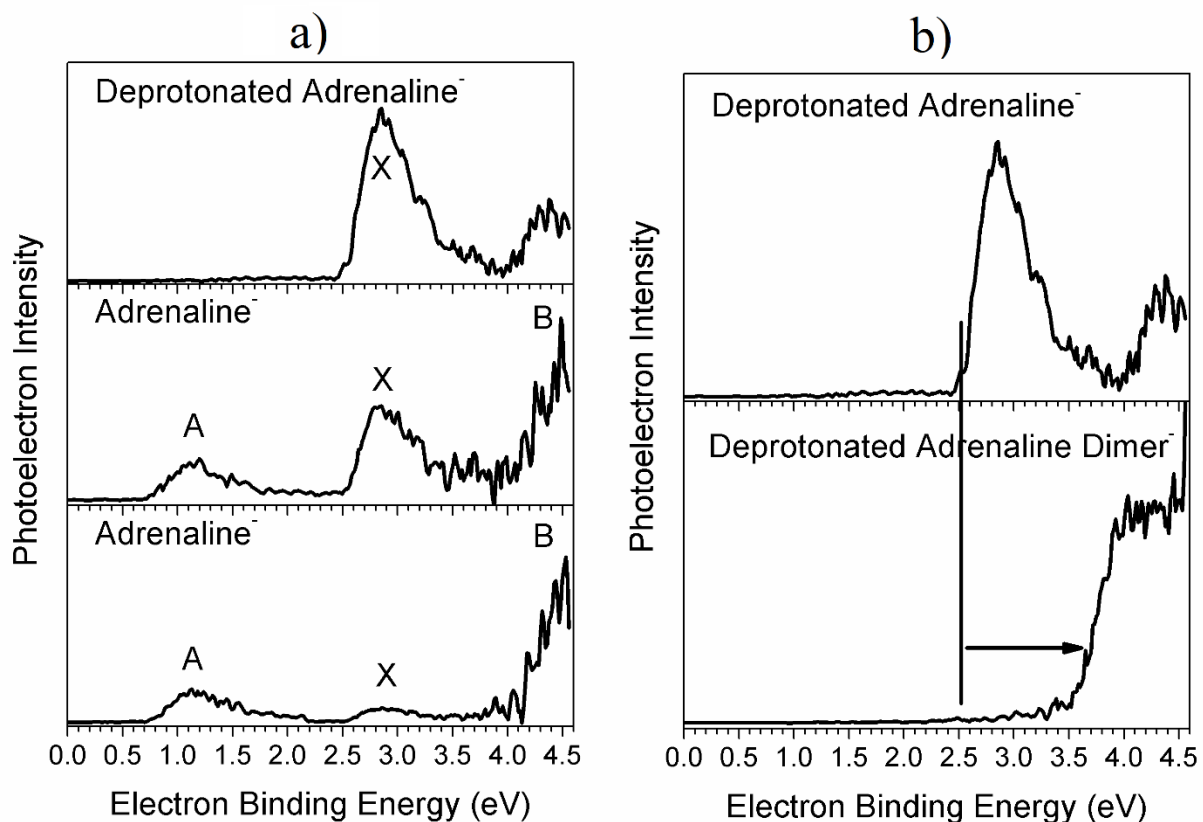
Figure A.2. The photoelectron spectra of deprotonated adrenaline anion and adrenaline parent anion taken on different days, the relative intensities of peak marked by X change day by day, which is from the deprotonated anion (a). The comparison between deprotonated adrenaline and deprotonated adrenaline dimer shows an EA shift of ~1.1 eV, which is definitely a LBHB pattern (b). Please note that due to similar structures, the spectra of dopamine and adrenaline are similar.
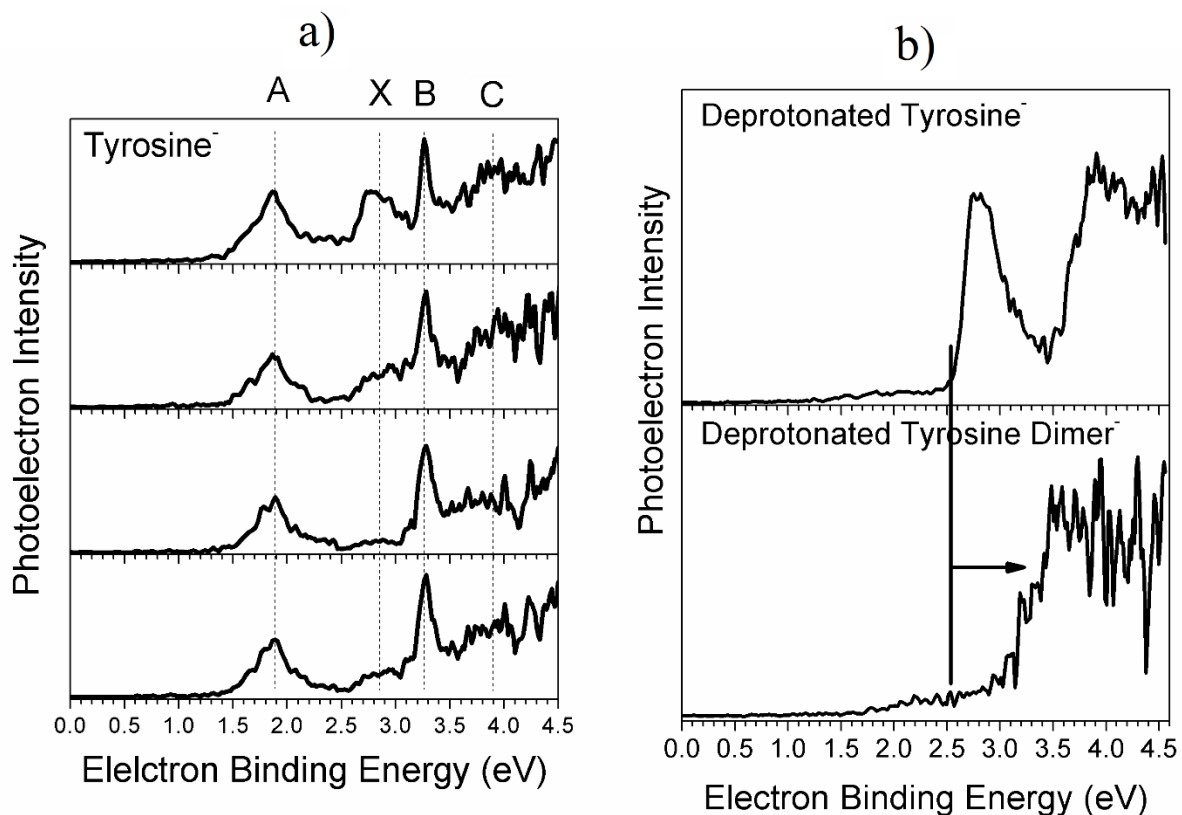
Figure A.3. Again, peak X belongs to deprotonated tyrosine anion, and peaks A, B and C may belong to different tautomers of tyrosine anion (a). The comparison between deprotonated tyrosine anion and deprotonated tyrosine dimer anion shows an EA shift of ~0.7 eV, which is also a LBHB pattern (b).
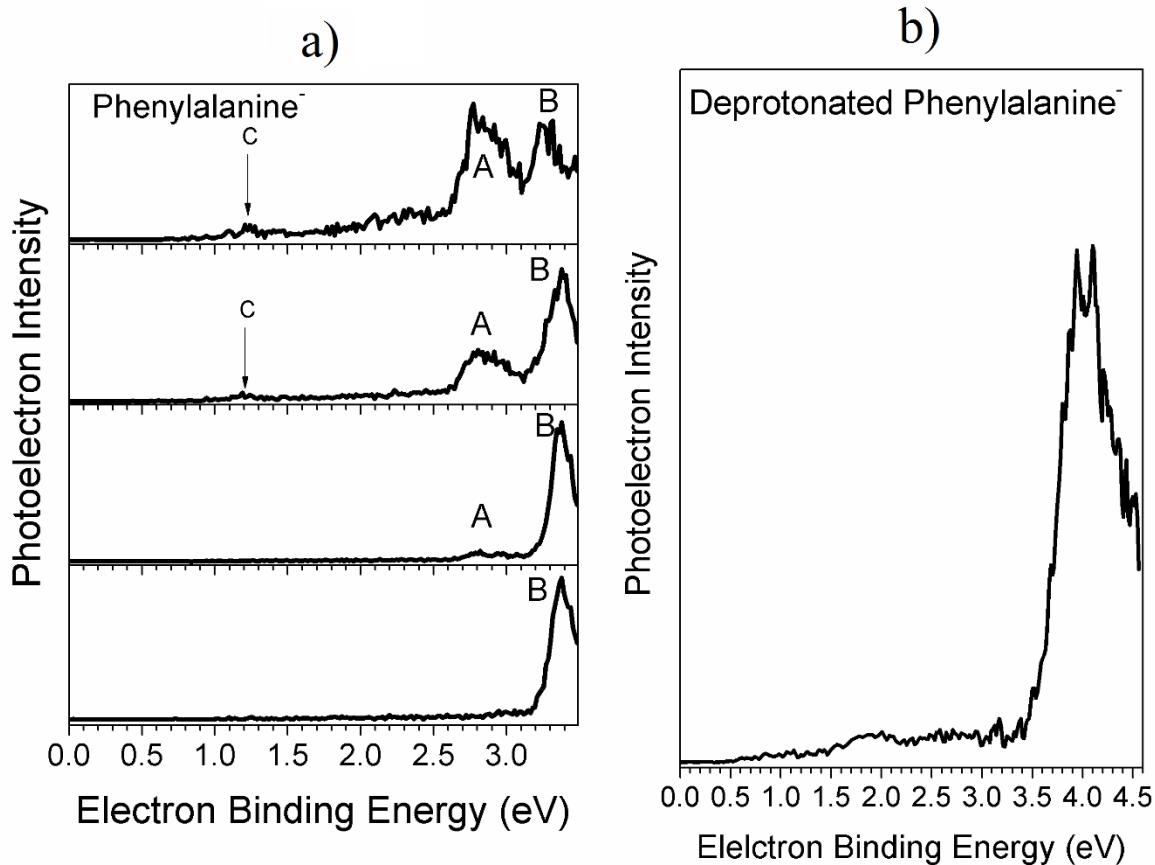
Figure A.4. The relative intensities of peaks A and B vary due to different laser powder, they may belong to different tautomers of phenylalanine anion (a). Please note that there is another small feature labeled by C. The PES of the deprotonated phenylalanine is shown in (b).
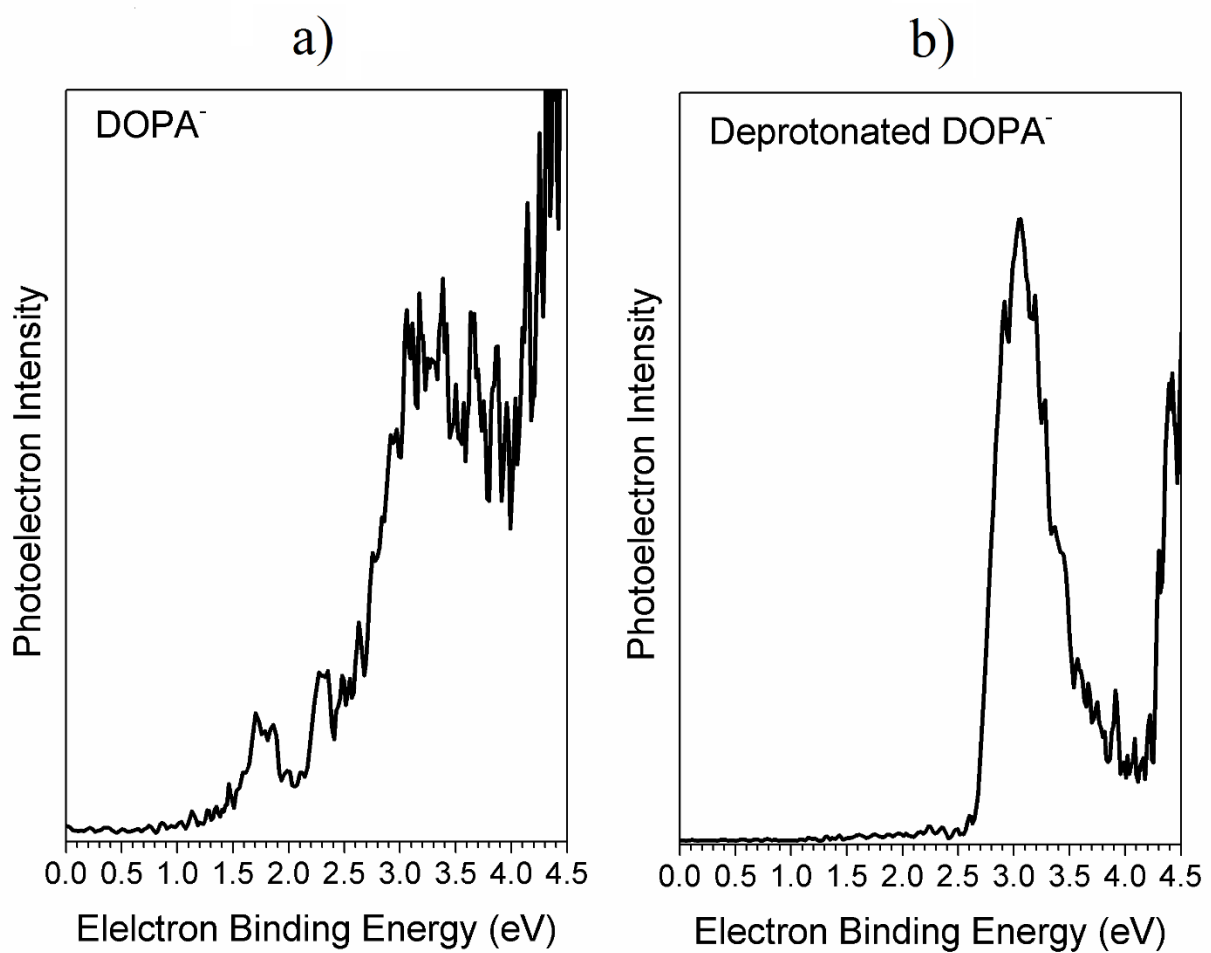
Figure A.5. PES of DOPA parent anion (a) and the deprotonated DOPA anion (b).

II. When anion PES meets solid state physics

Solid state physics has intriguing research areas such as semiconductor, superconductor, topological Kondo insulator etc. These properties of the materials can only appear when the size of the clusters/particles reaches certain regime. For example, when cluster gets big enough, it begins to show some macroscopic properties, and then this cluster can be called "baby crystal".[1,2] However, the embarrassing dilemma that PES study has encountered is that we can hardly make clusters as big as baby crystal. Therefore, what is the meaning of making very small clusters that are the single unit of systems that are of solid state physics' interest?

Next I will present two of these examples. SmB_6 as bulk material has amazing property called topological Kondo insulation.[3] The Sm element also has mixed valence in the material, i.e. it could have +2 and +3 oxidation state.[4] What occurs in a single SmB_6^- cluster? The photoelectron spectra of $SmB_{5,6}^-$ are presented in Figure A.6. Further calculations might help to solve the +2/+3 mixed valence enigma out of this single unit of the bulk material.

Bi_3Co as bulk material shows superconductivity at $Tc = 0.48$ K,[5,6] and it is the first binary superconductor. Figure A.7 shows the PES of $Bi_{2-4}Co^-$.
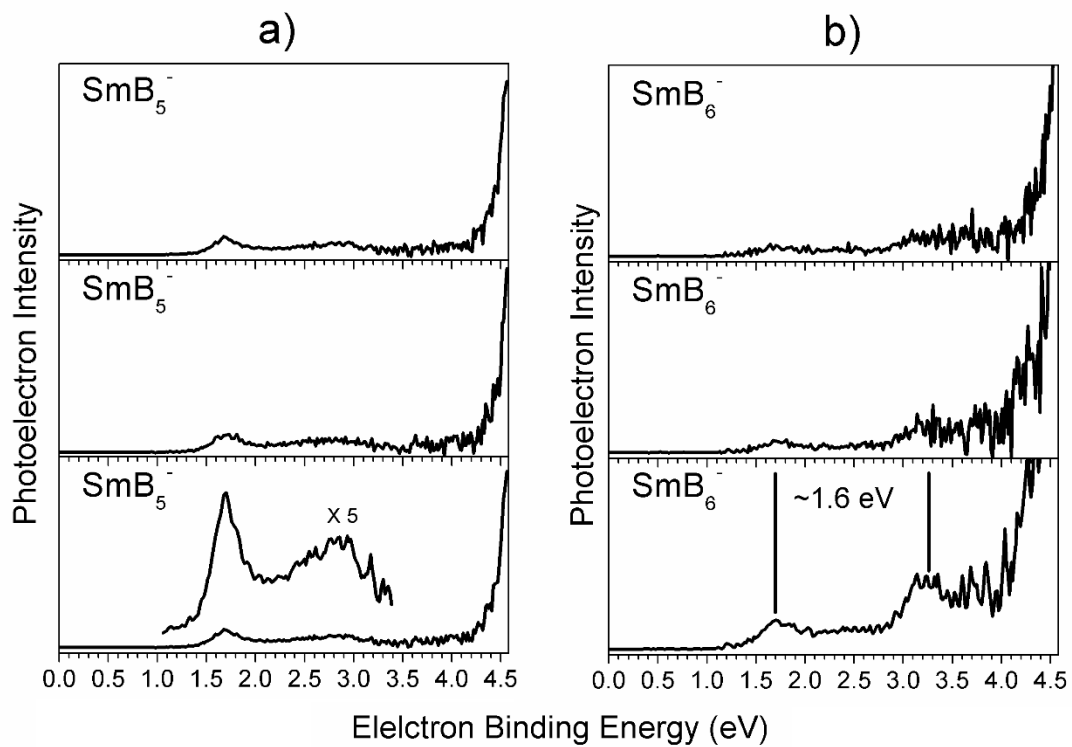
Figure A.6. PES of SmB$_5^-$ (a) and SmB$_6^-$ (b) taken on different days' experiments. Please note that SmB$_6$ has a HOMO-LUMO gap as high as C$_{60}$.
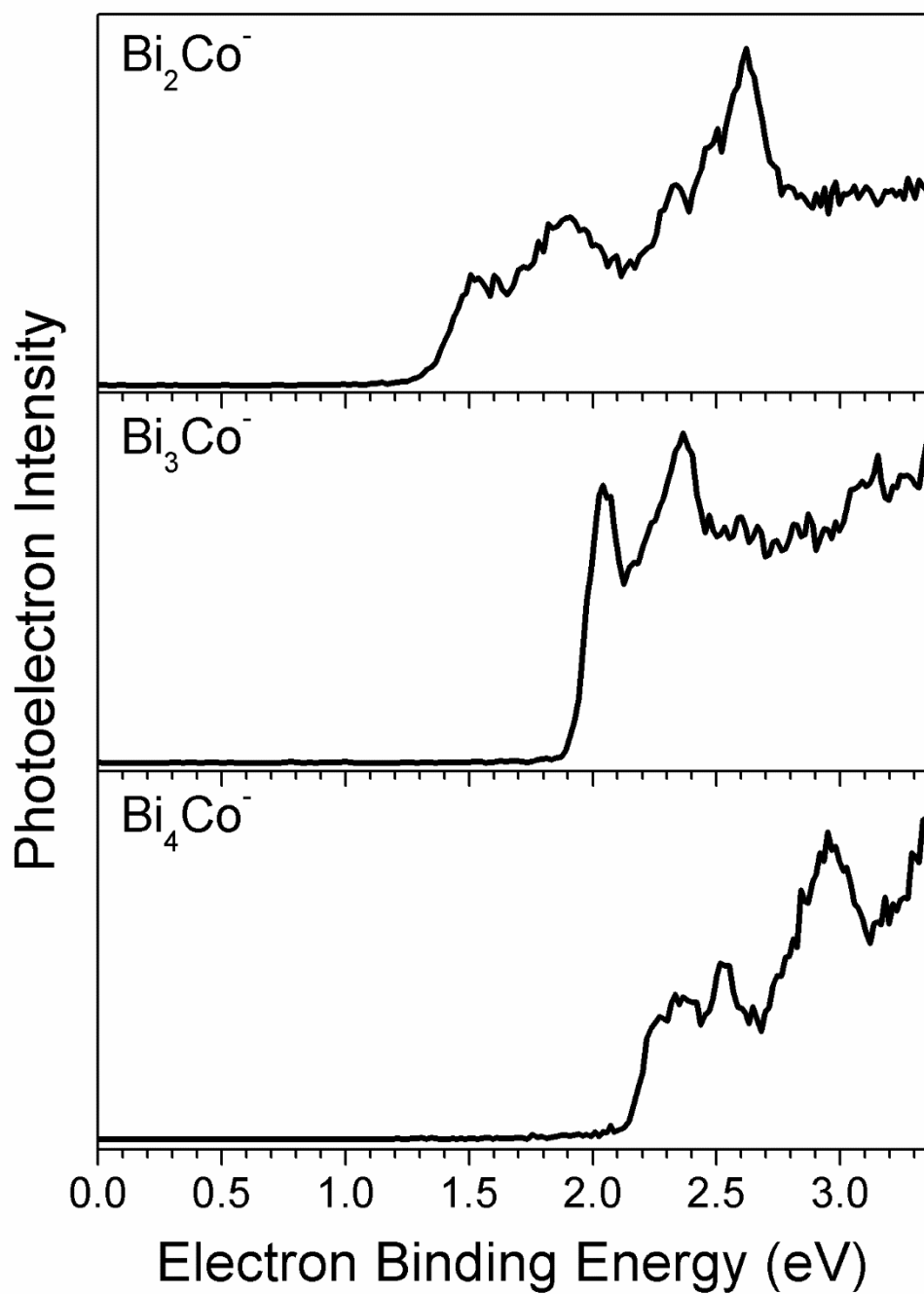
Figure A.7. PES of $Bi_{2-4}Co^-$.

III. Rare earth elements related sytems

In this section, I will present all the PES spectra that involve rare earth elements. There are PES of pure rare earth clusters as well as their oxides. Study on rare earth clusters is always interesting, however, the existence of f-electrons makes theoretical calculations very difficult. Further studies, especially theory collaborations are needed to study these systems.

Four systems, including La, Ce, Ho and Gd, will be shown in this section.
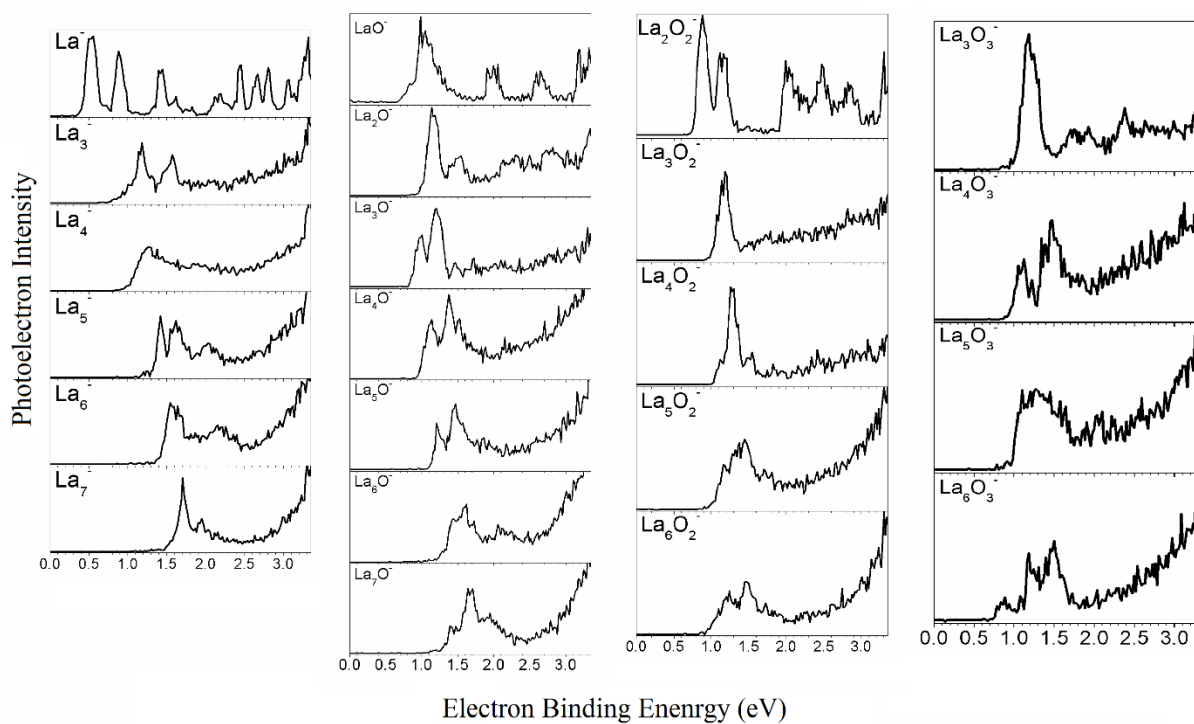
Figure A.8 PES of $La_xO_y^-$ (x = 1-7, y = 1-3).
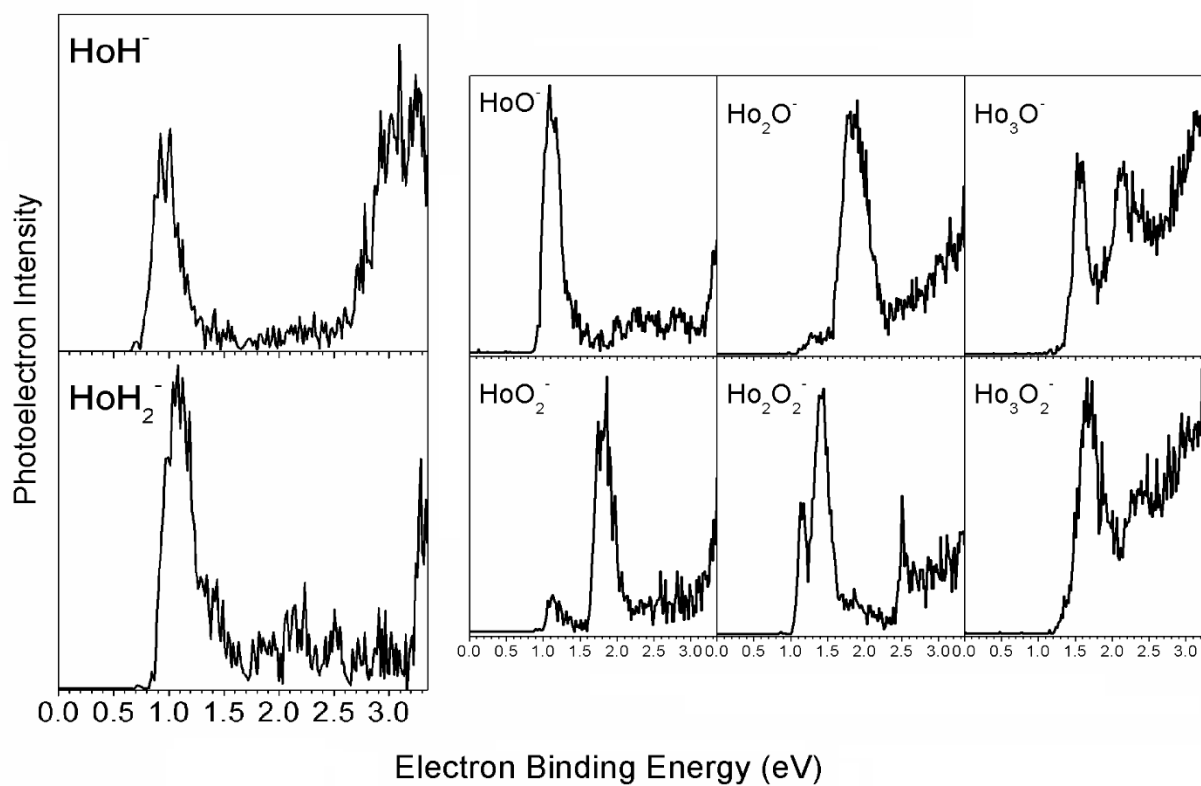
Figure A.9 PES of $HoH_{1,2}^-$ and $Ho_xO_y^-$ (x = 1-3, y = 1,2).
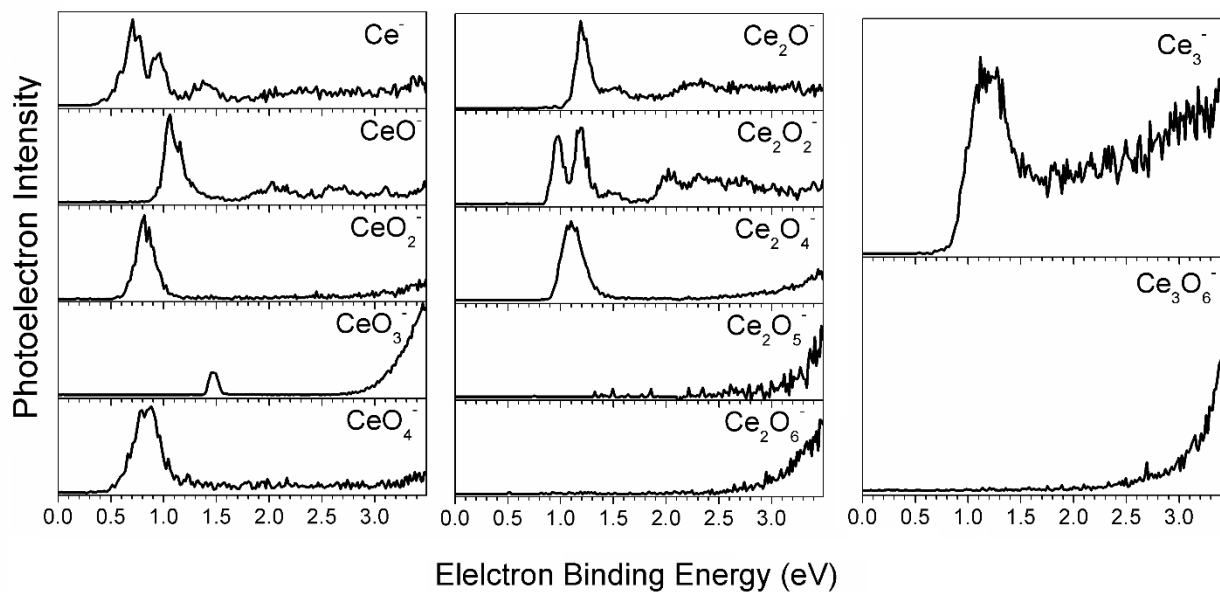
Figure A.10. PES of $Ce_xO_y^-$ (x = 1-3, y = 0-6). Please note that Ce^- and Ce_3^- might be interesting to a lot of theorists. $(CeO_2)_{1-3}^-$ might be interesting to experts in catalysis since CeO_2 as bulk material is widely used as redox catalyst. $CeO_2^{0/-}$ have oxidation state of +3 and +4, which are the two oxidation states involved in CeO_2 catalysis.
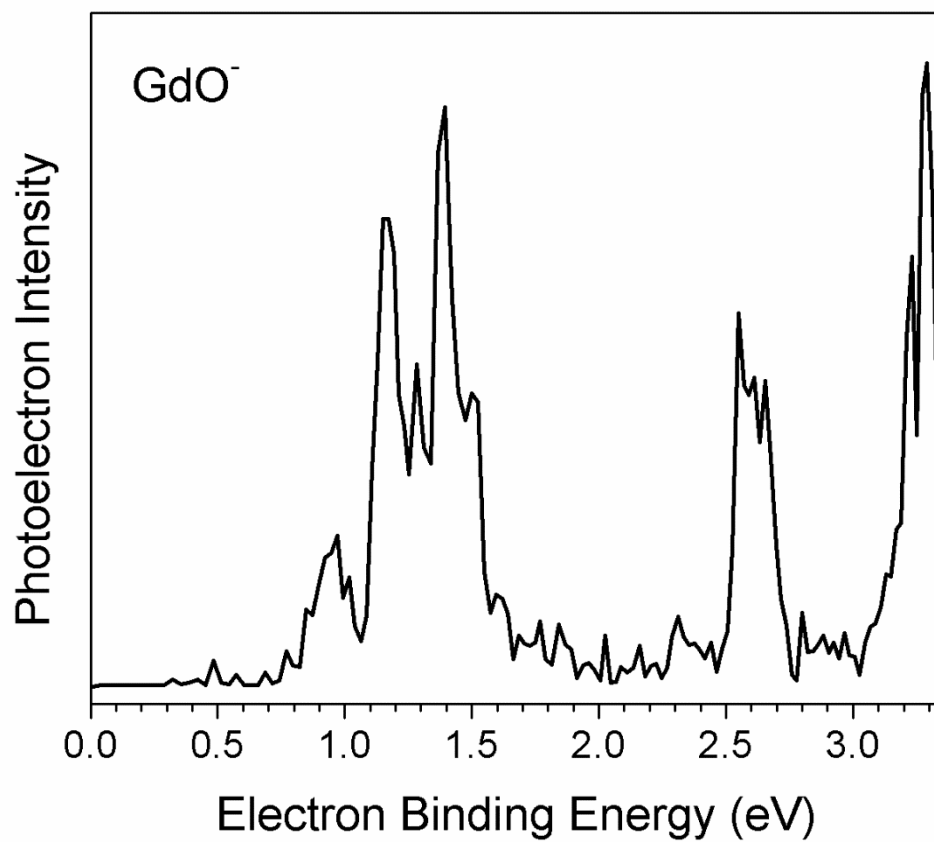
Figure A.11. PES of GdO⁻

IV. Ligated cluster anions (for MURI)

Metal/semimetal clusters can be widely utilized as energetic materials and catalysts, however, due to the high activity, these clusters sometimes need to be protected by certain ligands. In this section, I will present the PES of the metal, mixed metal, semimetal clusters protected by different ligands.

The works in this section are sponsored by the MURI funding.
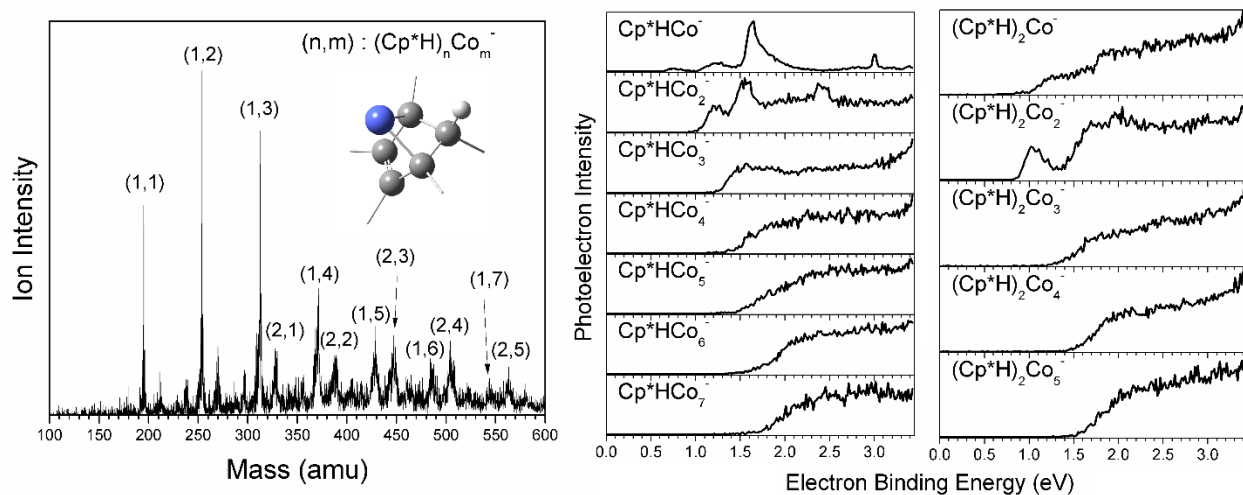
Figure A.12. Mass spectrum of $(Cp*H)_n Co_m^-$ (n = 1,2, m = 1-7) and corresponding photoelectron spectra. The structure of $Cp*HCo^-$ is embedded in the mass spectrum, please note that all the methyl groups are omitted for concision. The calculations were performed at B3LYP/6-31+ G (d, p) (C, H) and SDD (Co) level of theory. All calculated values match experiment very well.
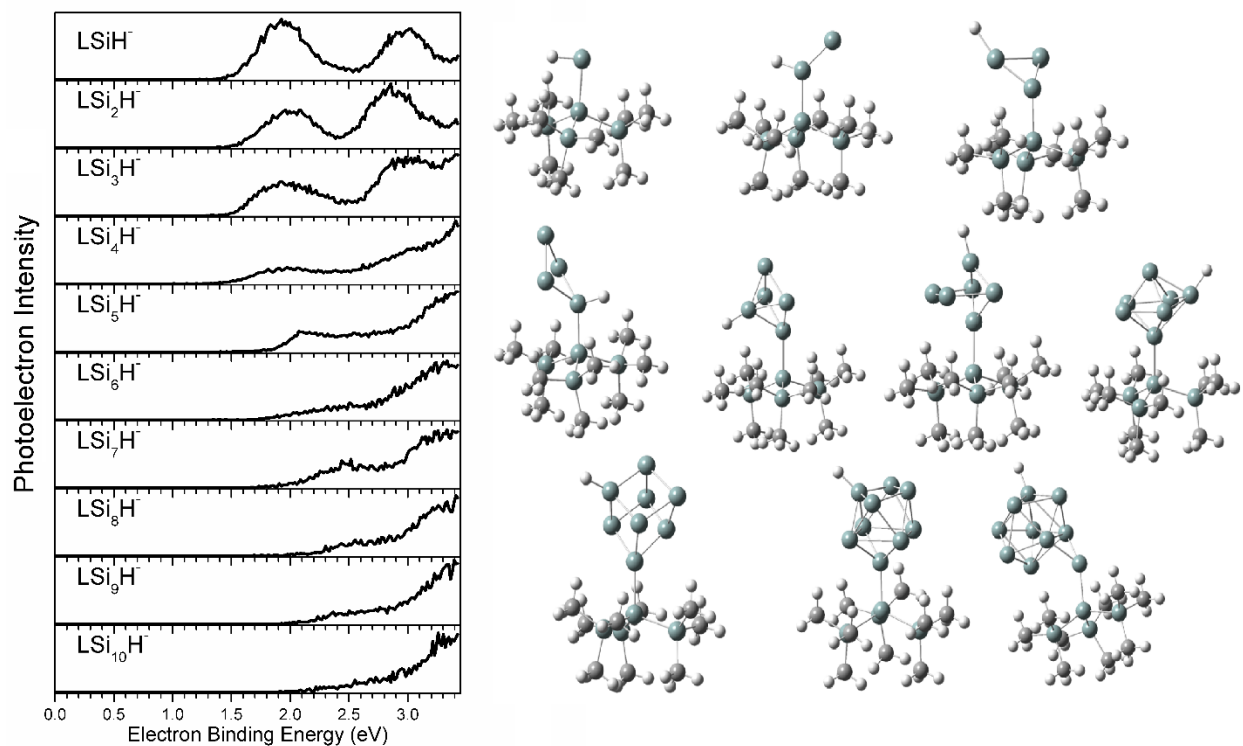
Figure A.13. PES of LSi_nH^- (L = ttmss, n = 1-10) and their calculated structures. All the calculations were performed at B3LYP/6-31+ G (d, p) level of theory. Only the lowest energy isomers are shown here. All the calculated VDEs matches the experiment very well.
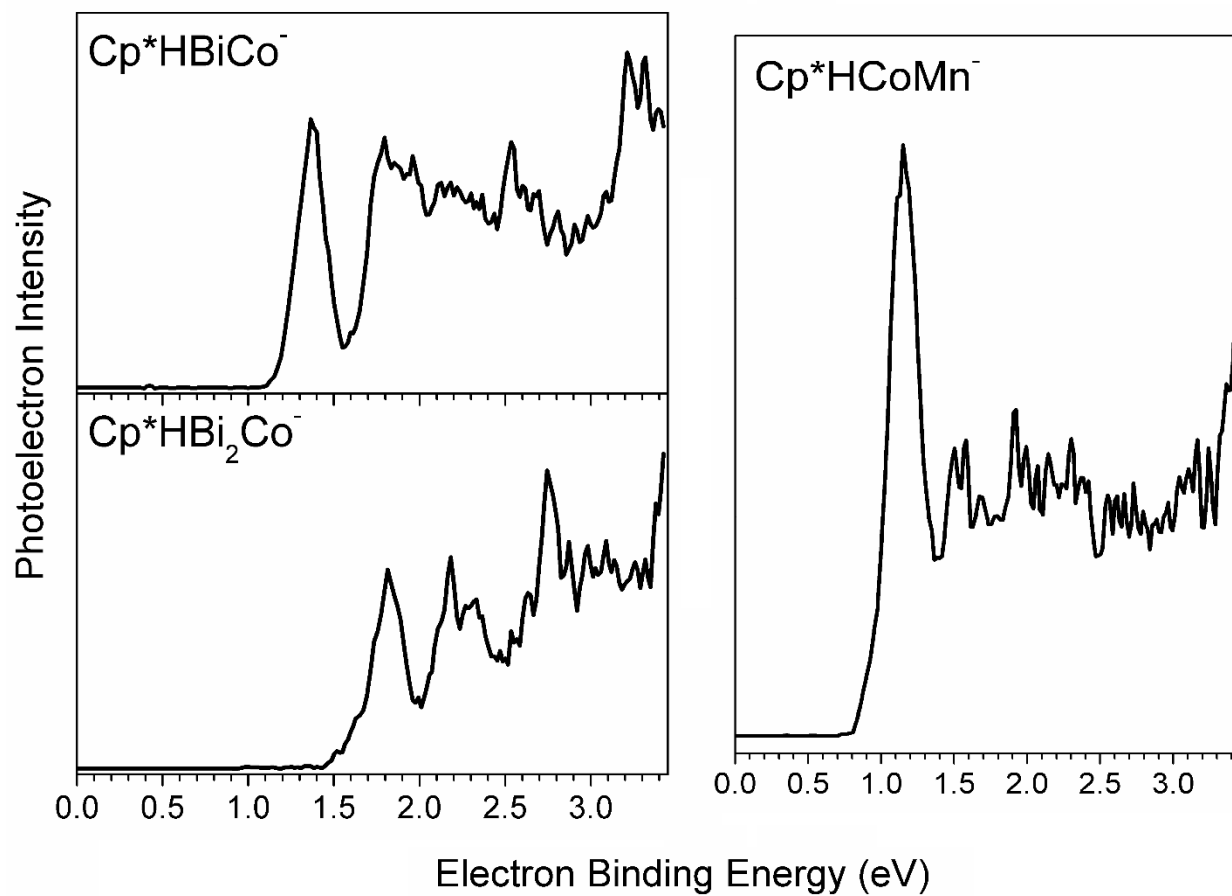
Figure A.14 PES of ligated mixed metal cluster anions.

V. PES of bimetallic $Al_xM_y^-$ cluster anions

In our group we have collected numerous spectra that contain aluminum. In Figure A.15, I summarized all the bi-elemental, Al-containing cluster anions that have been recorded by our group. The spectra of Al-Mo, Al-Pt, Al-Ni, Al-Sn and Al-Au systems that were collected by me are presented next. Please note that a lot of other Al-containing, bi-elemental system can be done with our unique PACIS source. Understanding the electronic structure of bimetallic clusters helps designing new catalysts.
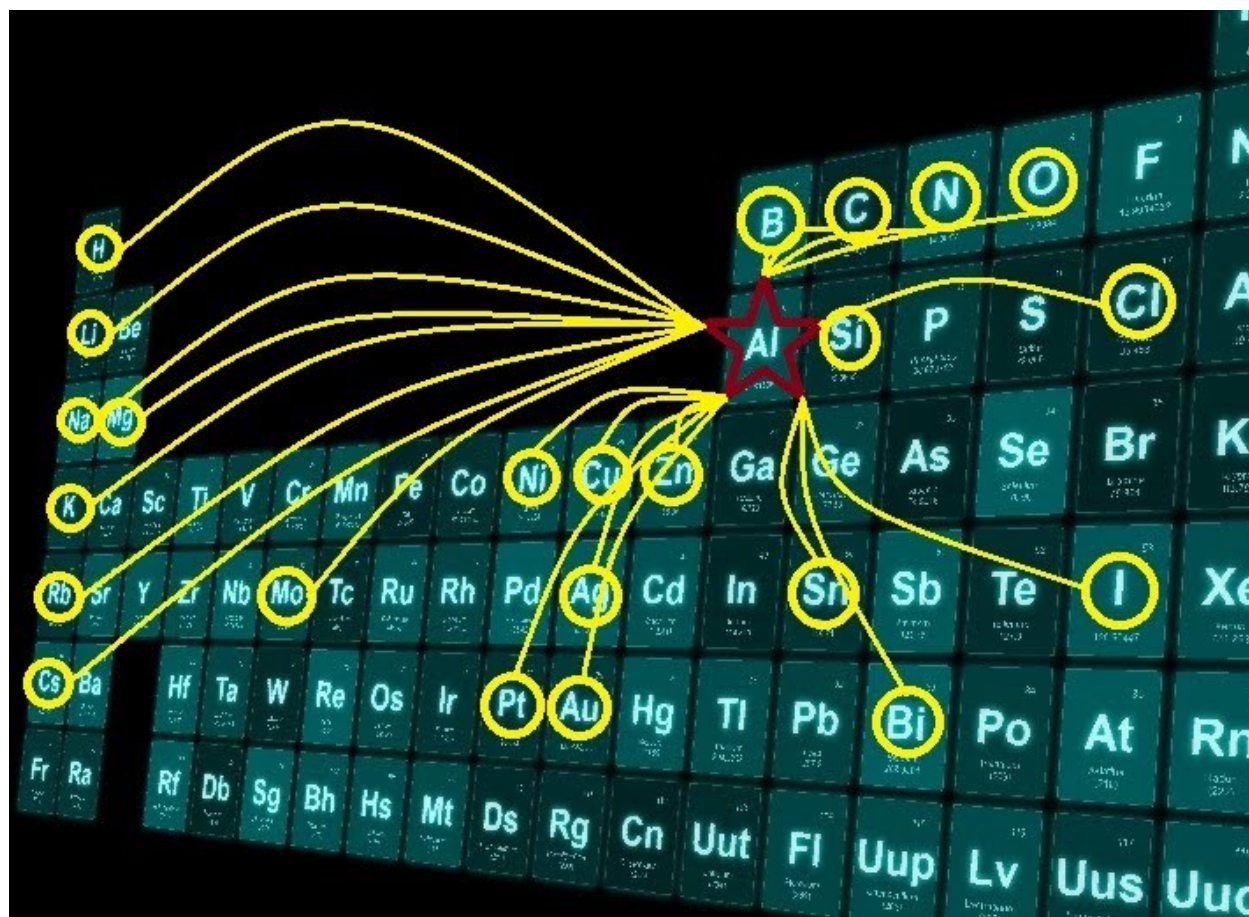
Figure A.15. All the Al-containing, bi-elemental systems that have been recorded by our group.
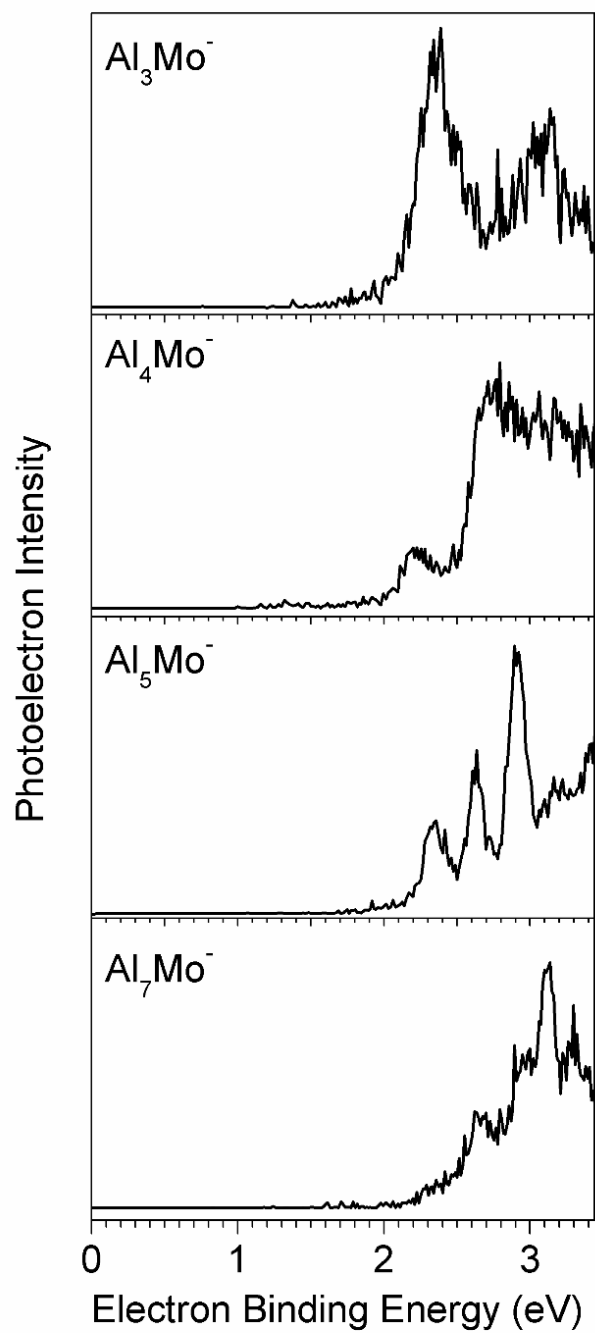
Figure A.16. PES of Al_xMo^- (x = 3-7).
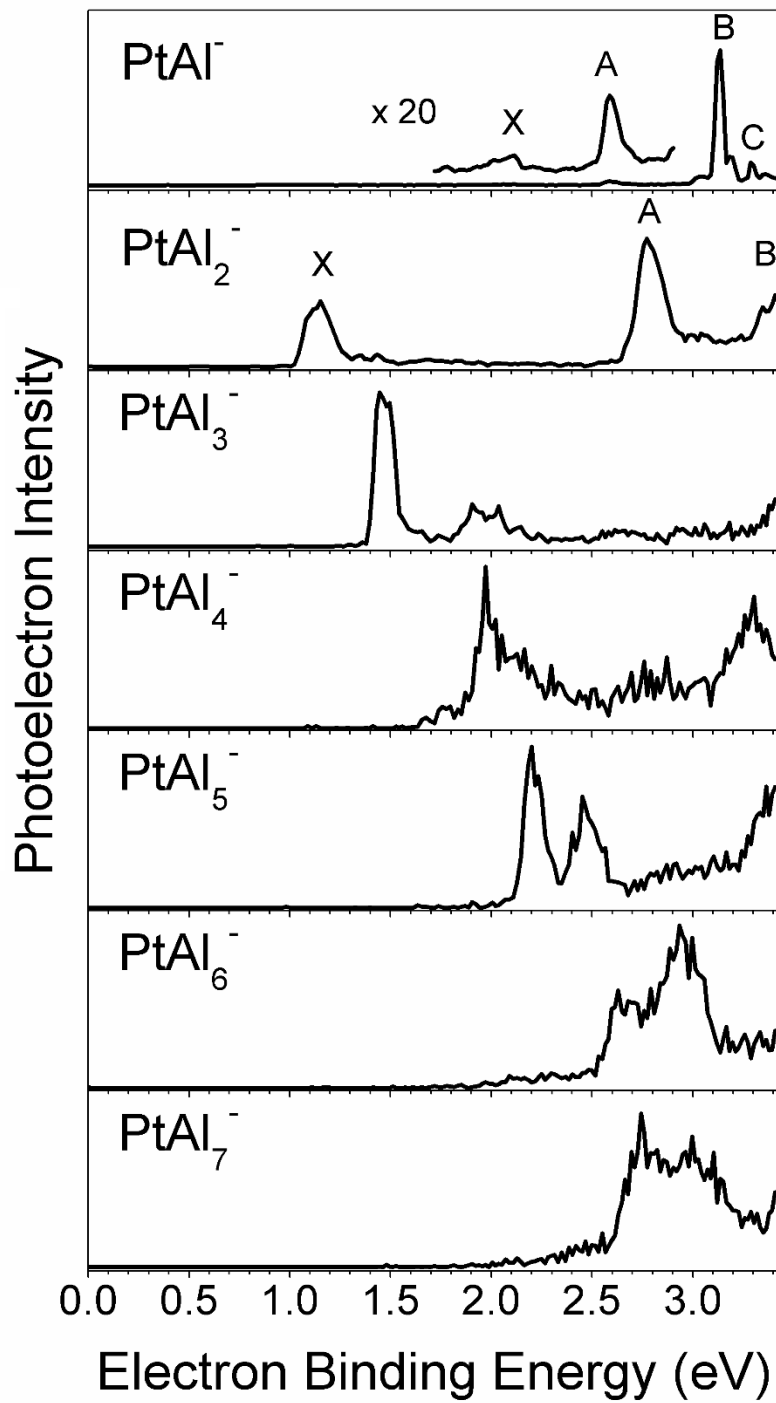
Figure A.17. PES of Al_xPt^- (x = 1-7).
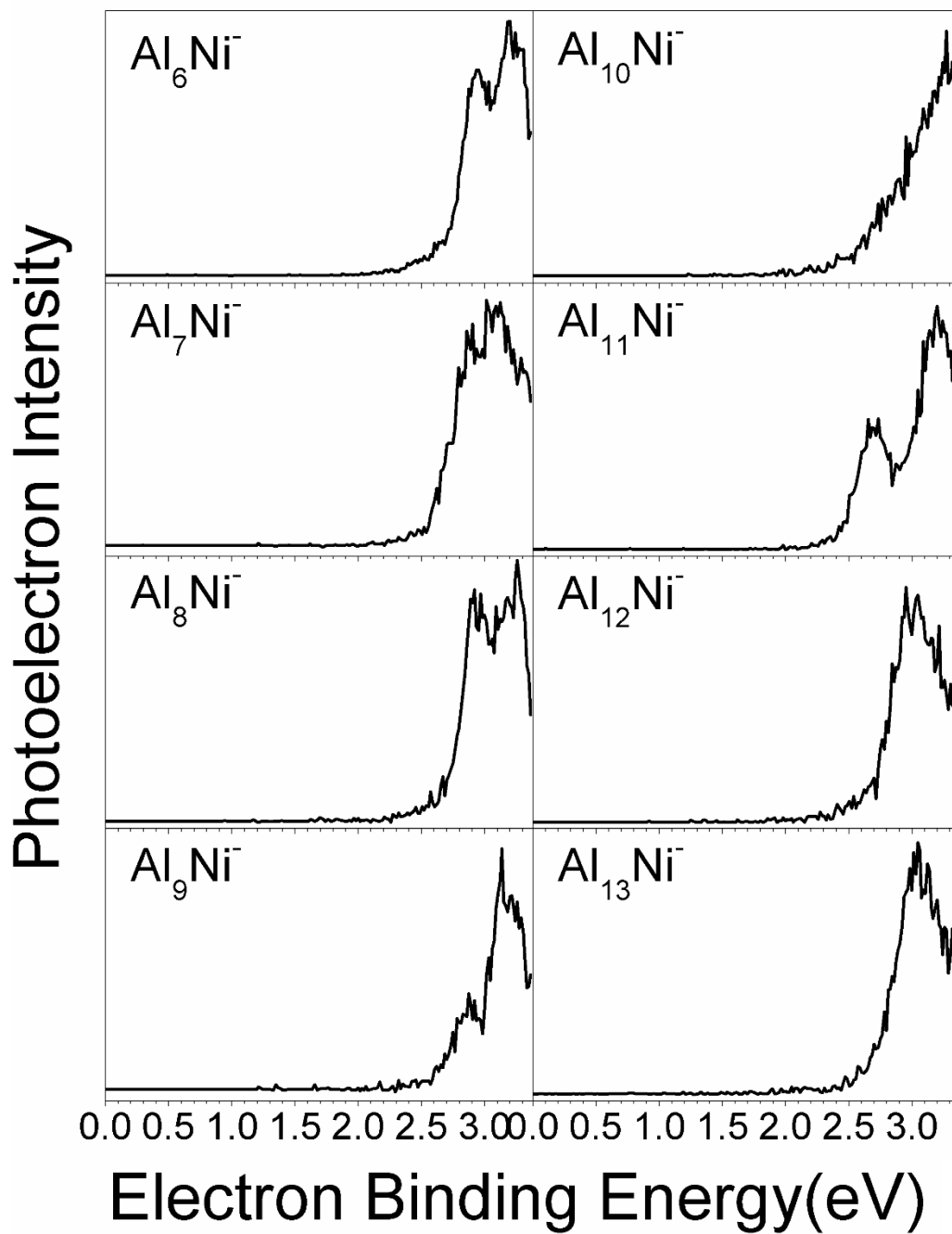
Figure A.18. PES of Al_xNi^- (x = 6-13).
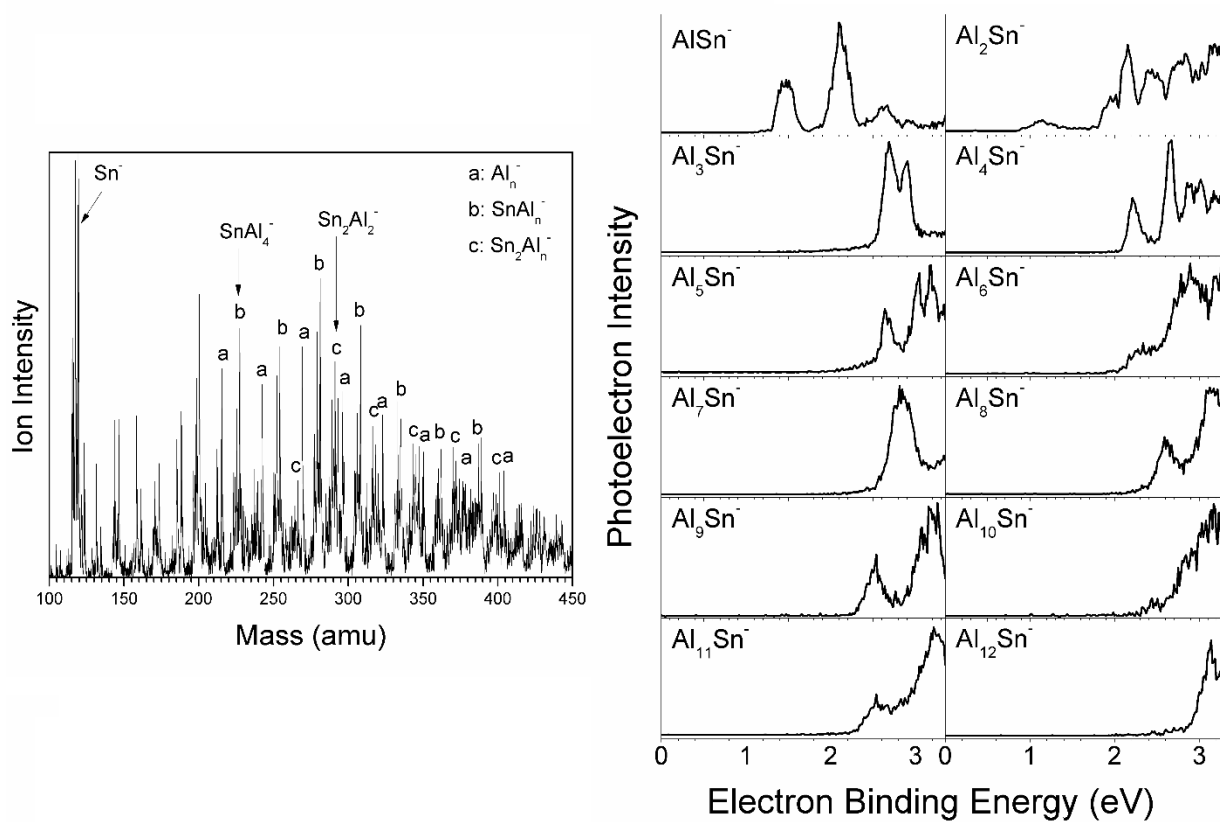
Figure A.19. Mass spectrum of Al-Sn system and PES of Al_xSn^- (x = 1-12).
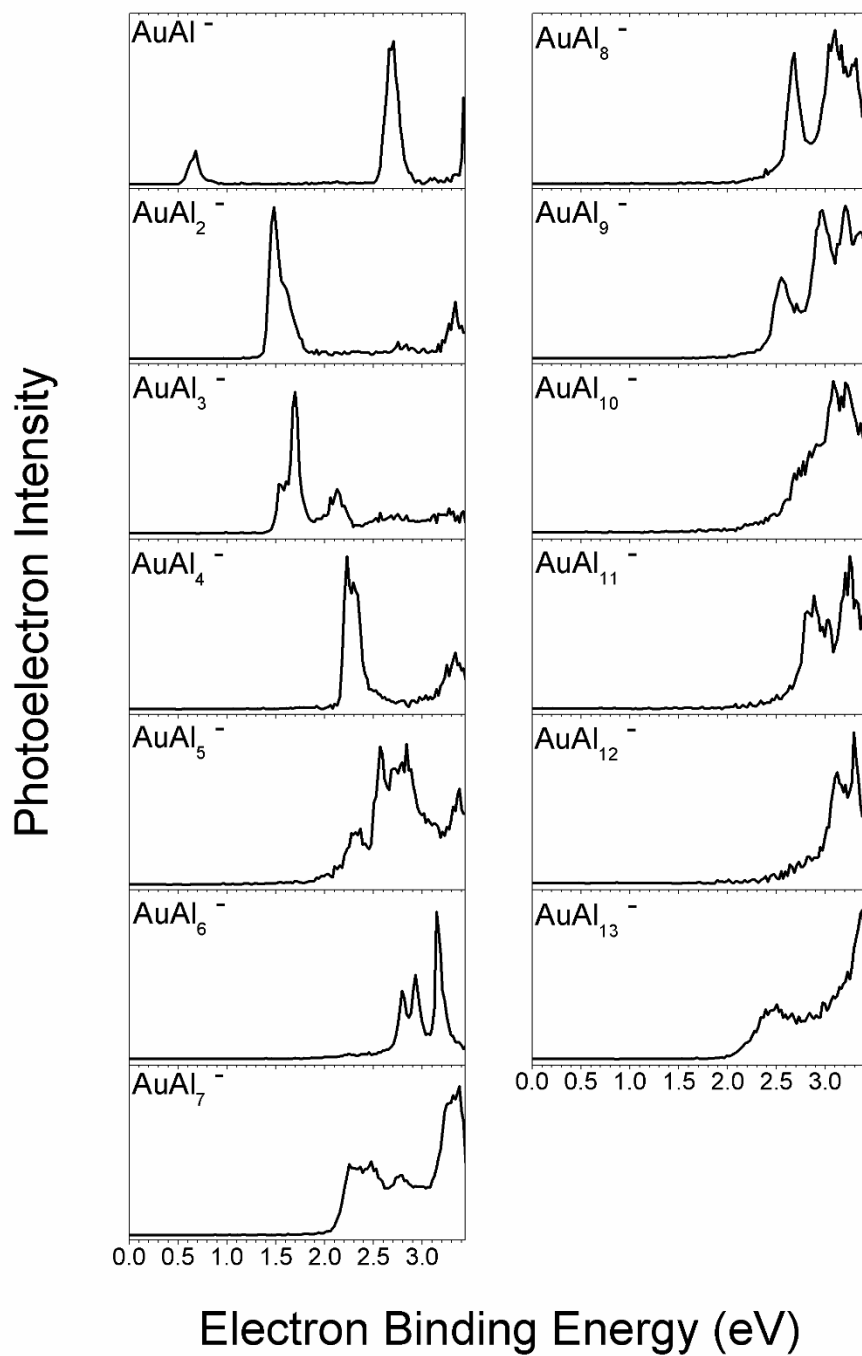
Figure A.20. PES of Al_xAu^- (x = 1-13).

VI. The concept of sub-nano thermite clusters

We are exploring the properties of sub-nano (cluster) thermites. The ingredients of these metastable species are not separate as is usually the case, but are intimately bound together within clusters. Since they are quasi-atomic, their eventual reaction to form bulk products, viz., lattice energy, should result in an energy release that is enhanced beyond the exothermicity of normal thermite. In all of the cases, Al element is not fully oxidized, indicating that it has potential to act as reductant. Figure A.21 presents the basic ideas behind this project. The PES and some calculation results of Al-Mn-O, Al-Cu-O and Al-Mo-O systems are presented next.
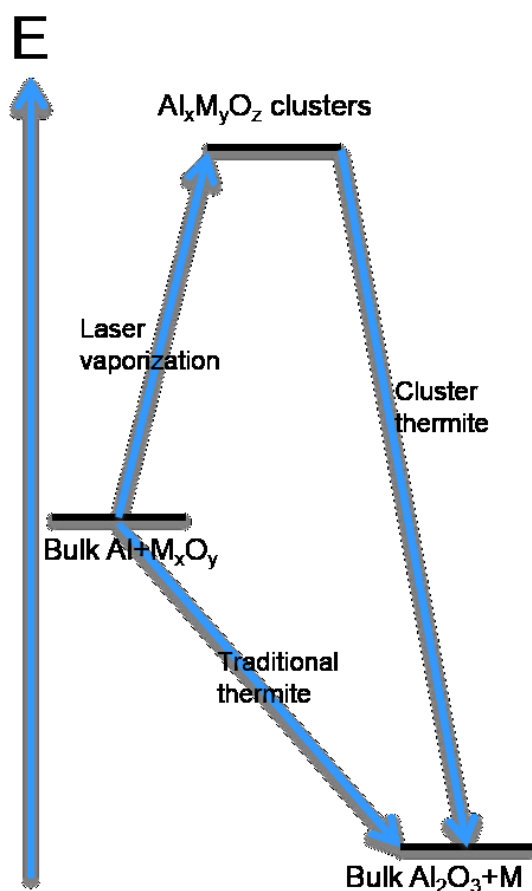
Figure A.21. The schematic relative energy diagram of the sub-nano thermite concept.
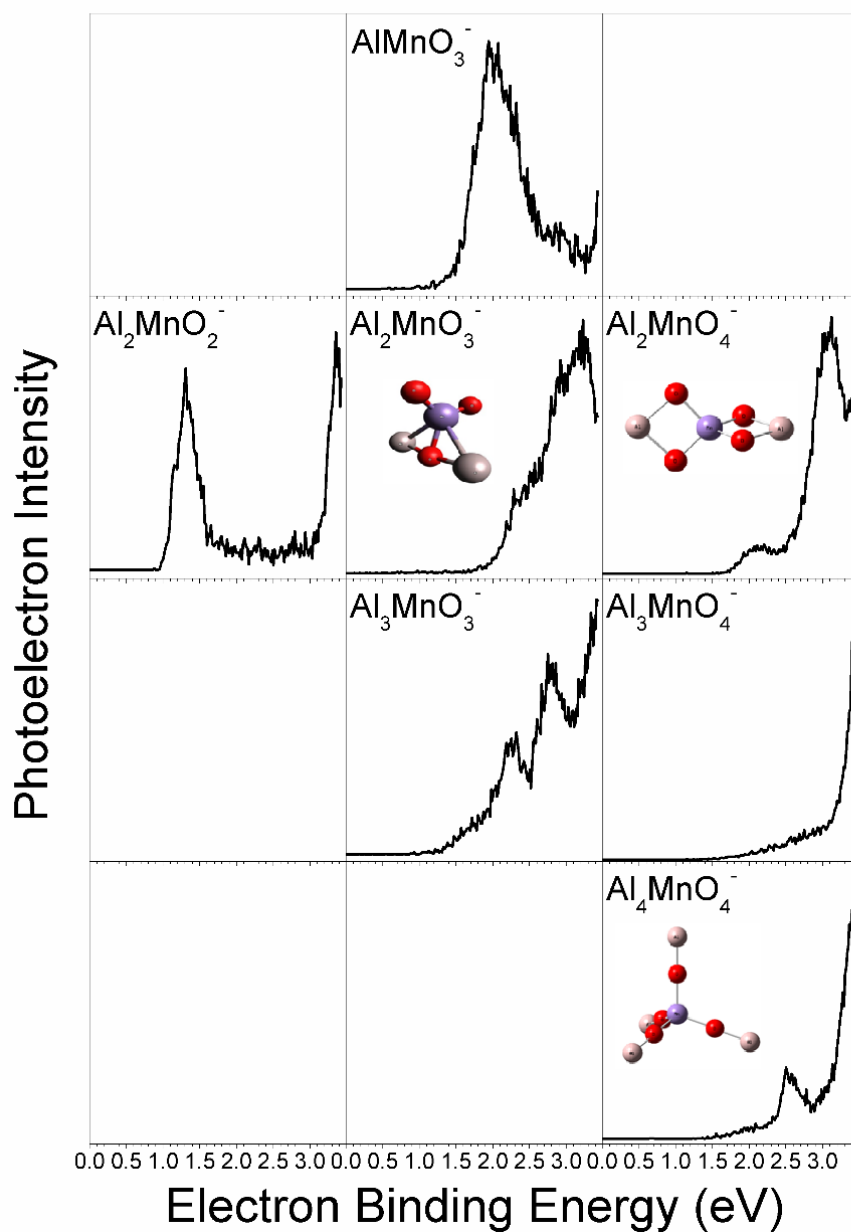
Figure A.22. PES of the Al-Mn-O system. Calculated structures are embedded in corresponding

spectra. One can observe that Al is not fully oxidized in all of these calculated structures.
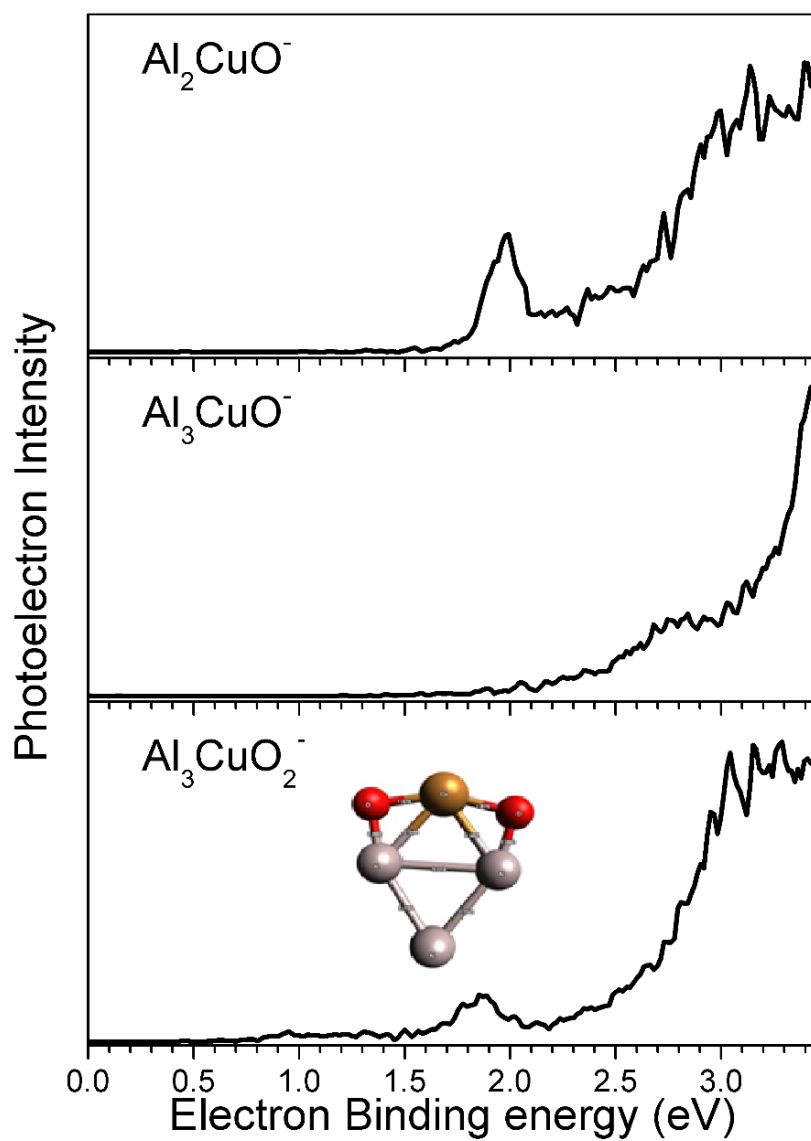
Figure A.23. PES of the Al-Cu-O system. Calculated structures are embedded in corresponding

spectra. One can observe that Al is not fully oxidized in the calculated structure.
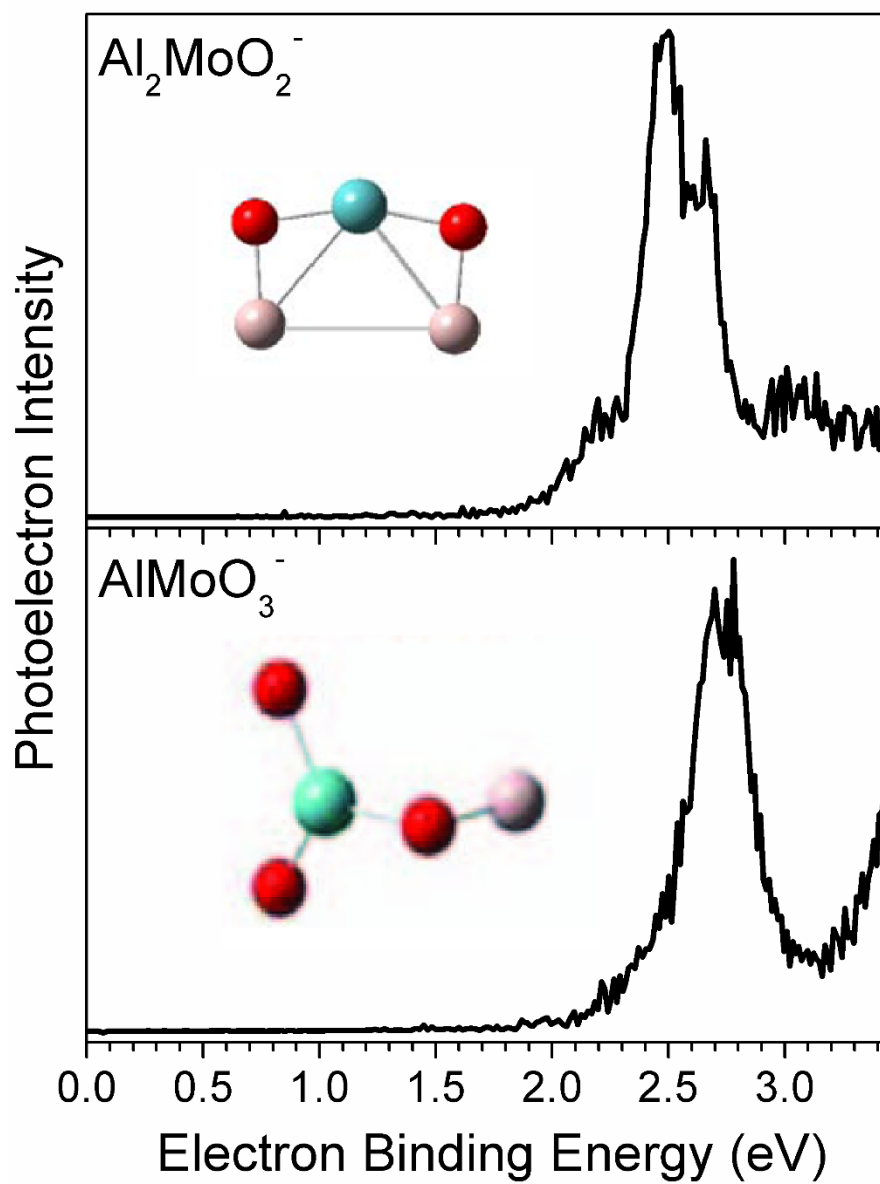
Figure A.24. PES of the Al-Mo-O system. Calculated structures extracted from references 7 and 8 are embedded in corresponding spectra. One can observe that Al is not fully oxidized in the calculated structures.

VII. Water solvation of unstable molecular radical anions

The parent anions of certain closed-shell molecules are not stable by itself. Their EAs are negative. However, by using water molecule, these radical anions can be stabilized by solvation. In this section, the solvation of formaldehyde, acetaldehyde, acetone, phenol and ethylene carbonate will be presented. Due to large structural difference of the neutral and the anion, it is very common that the EA cannot be observed experimentally for these systems, therefore, some extrapolation methods need to be utilized to estimate the negative EAs of these molecules.
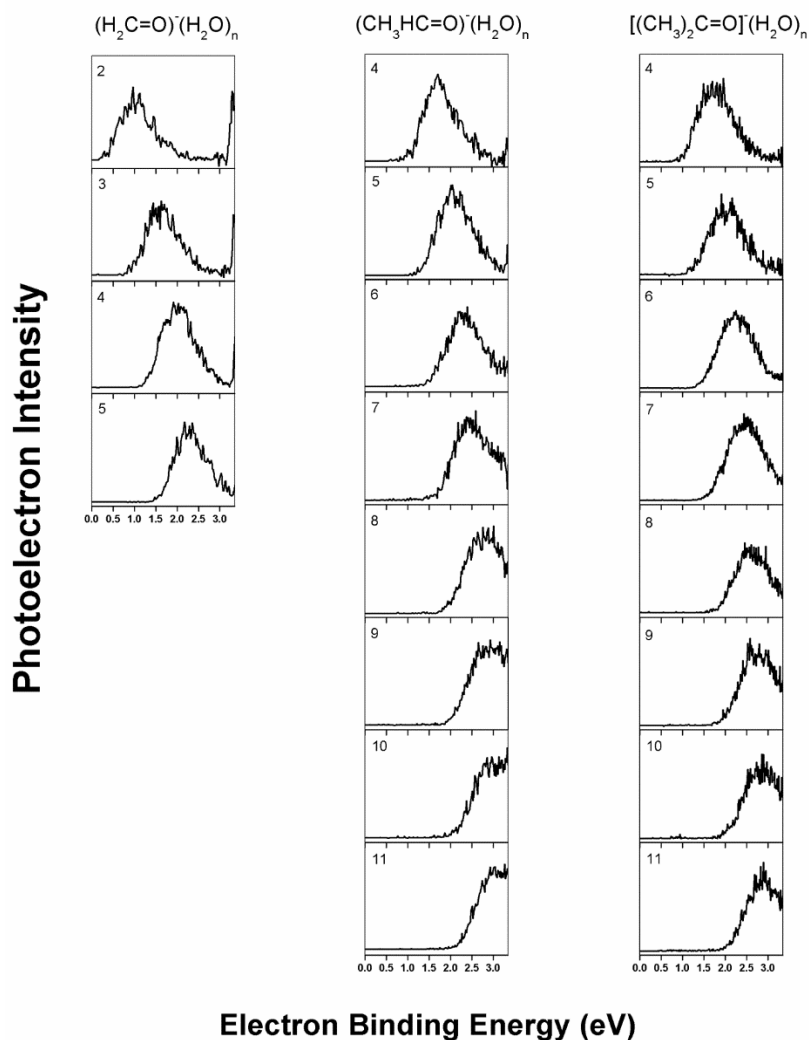
Figure A.25. PES of formaldehyde, acetaldehyde and acetone radical anions solvated by water.
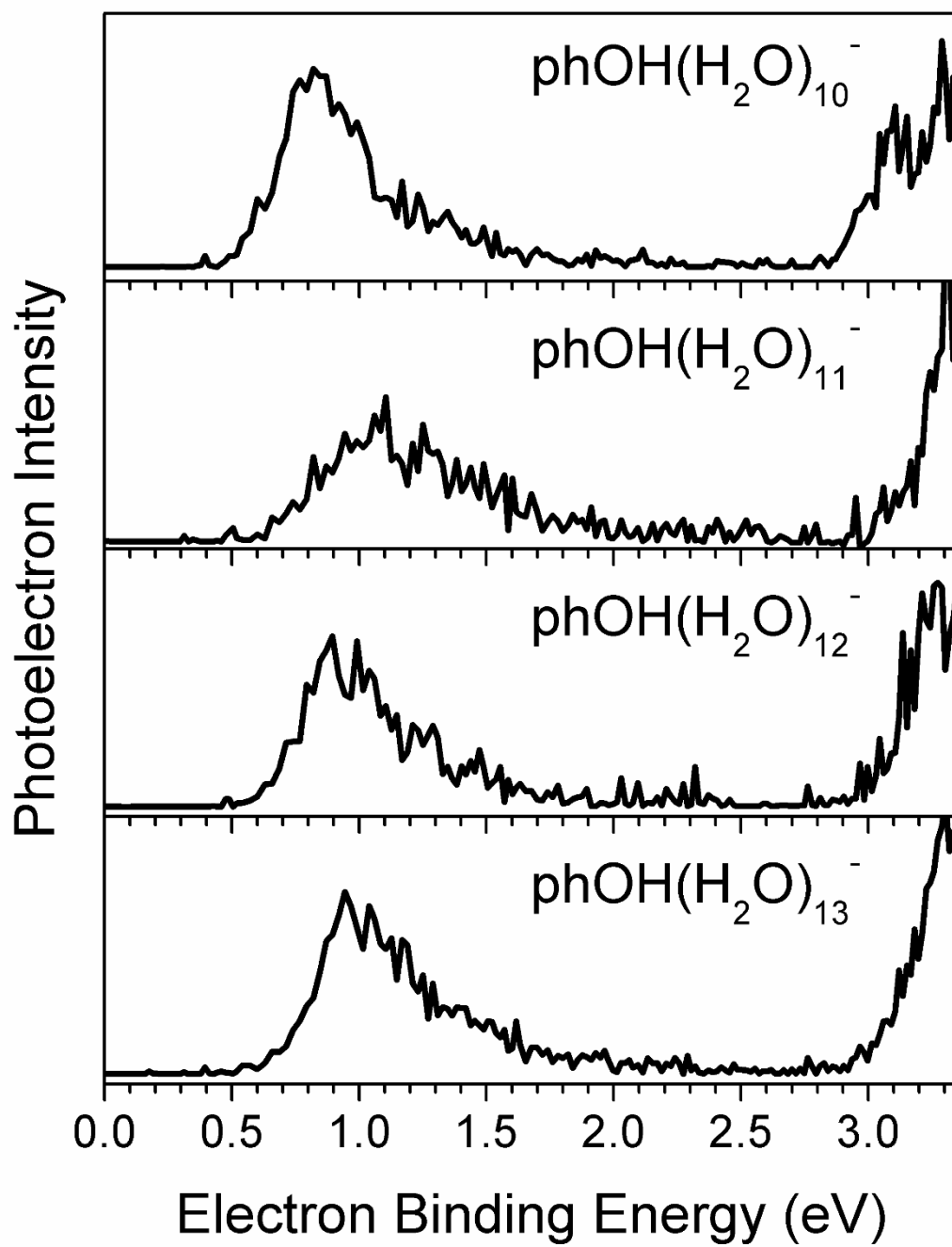
268

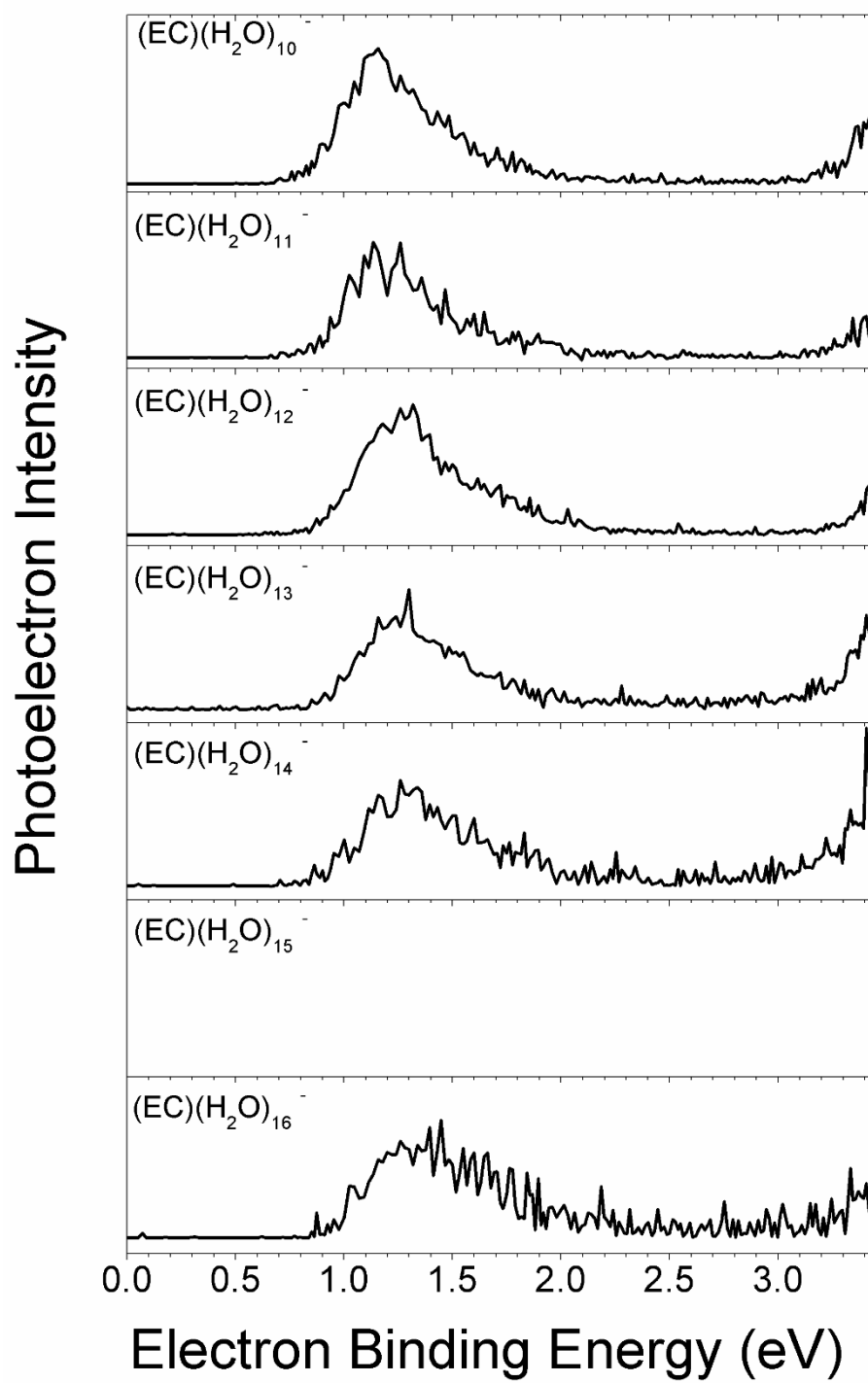Figure A.26. PES of phenol radical anion solvated by water.

Figure A.27. PES of ethylene carbonate radical anion solvated by water.

VIII. Clusters mimic precious elements

Some elements are very expensive such as noble metals and rare earth elements. There is great need for replacing these high-cost elements with other relative cheap materials. If a certain cluster is isoelectronic to an expensive element, and they share similar electronic structures (similar PES), this cluster might well be the replacement of this expensive element. In this section, I will present the comparison between $HMoO^-$ and Rh^-, $LaNa_2O^-$ and PrO^-. For HMoO-, my calculations confirms that its structure is $HMoO^-$ but not $MoOH^-$. O-Mo bond can be viewed as a covalent bond, hence O provides two electrons.
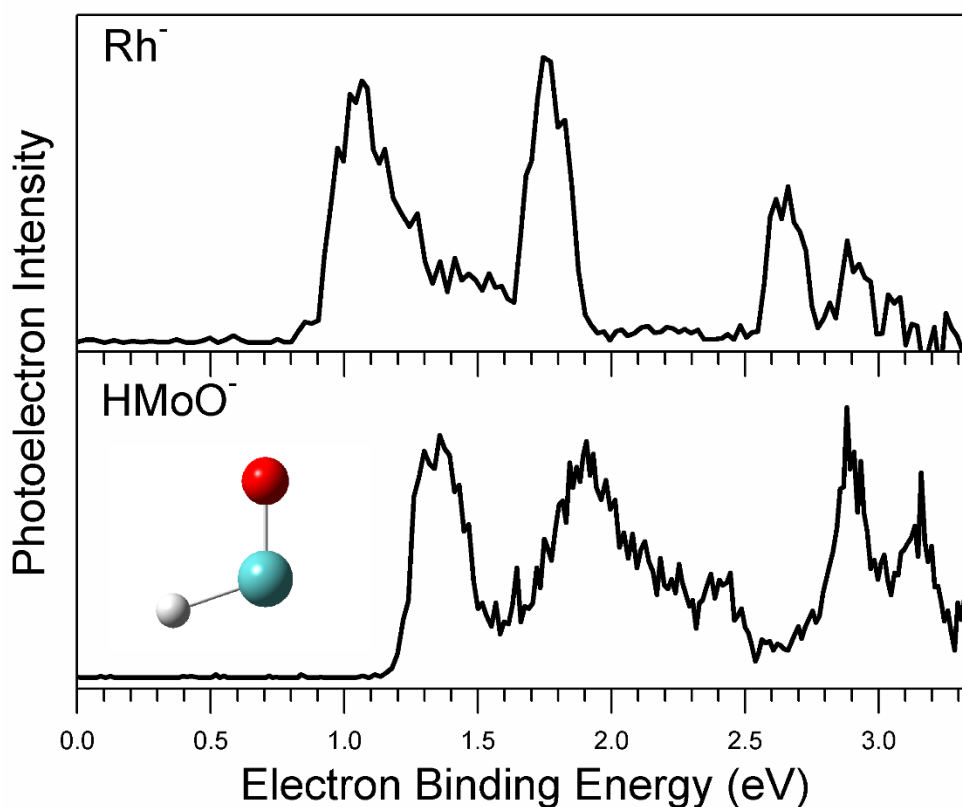

Figure A.28. PES of Rh^- and $HMoO^-$. The structure of $HMoO^-$ was obtained at B3LYP/SDD (Mo) and 6-311++ G (3df, 3pd) (O, H) level of theory. EA and VDE match experiment very well.
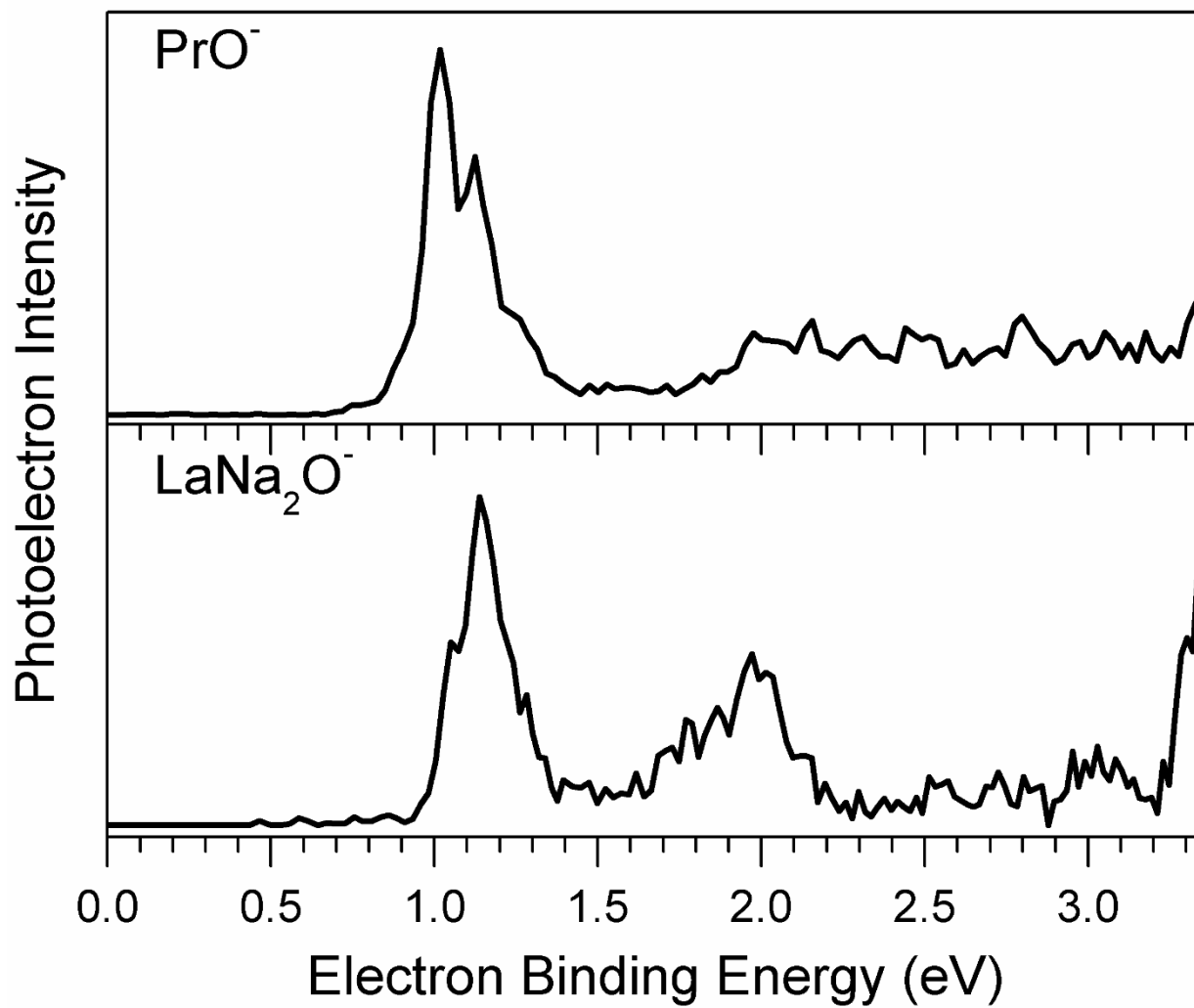
271

Figure A.29. PES of PrO$^-$ and LaNa$_2$O$^-$.

IX. Bimetallic transition metal cluster anions

Bimetallic transition metal clusters are good candidates to study mixed metal catalysts, which could be much better than single-metal catalysts. In this section, Ag-Mn, Pd-Cu, Pd-Mg, Pd-Zn, Pt-Mo, Pt-Ni, and Pt-Si systems will be presented.
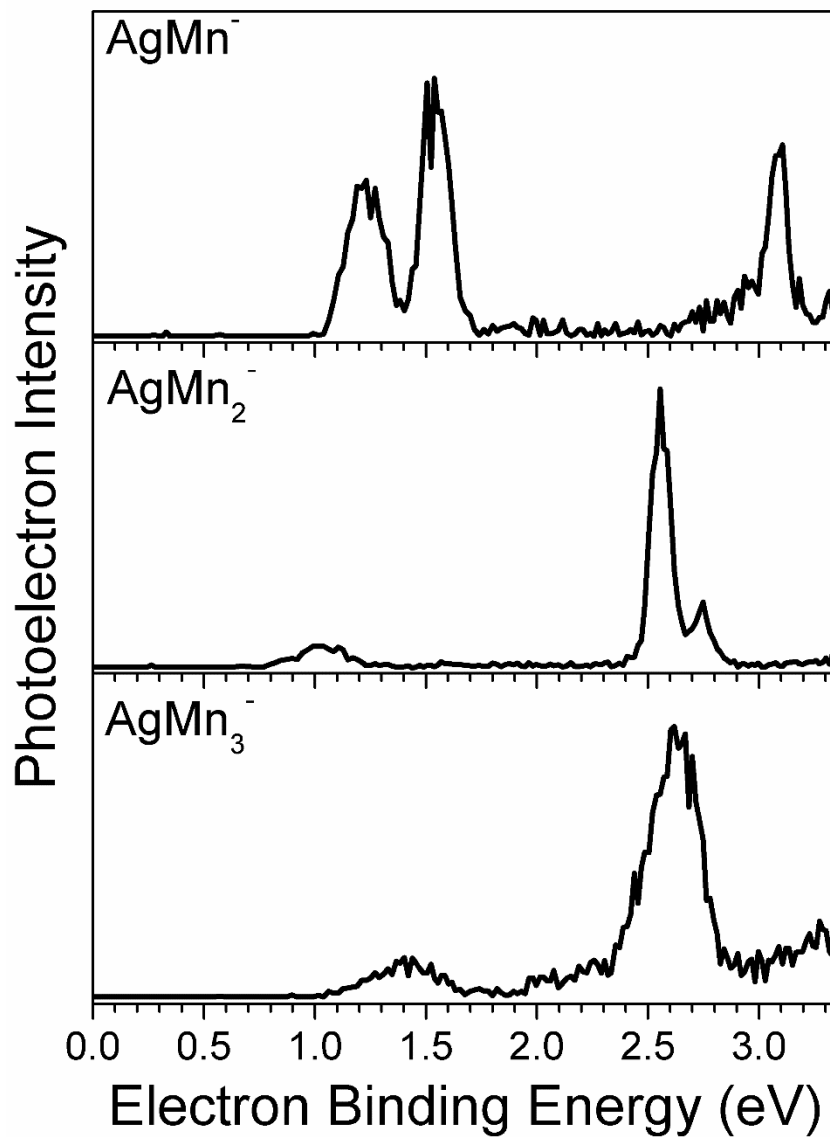

Figure A.30. PES of $AgMn_{1-3}^-$. Please note that these cluster might have very interesting magnetic properties.
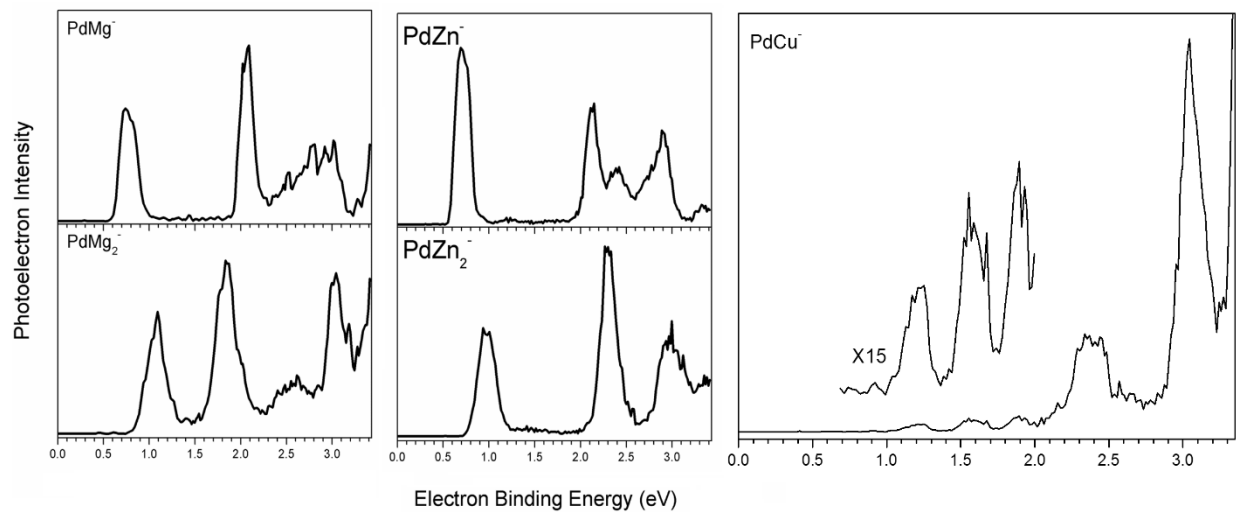
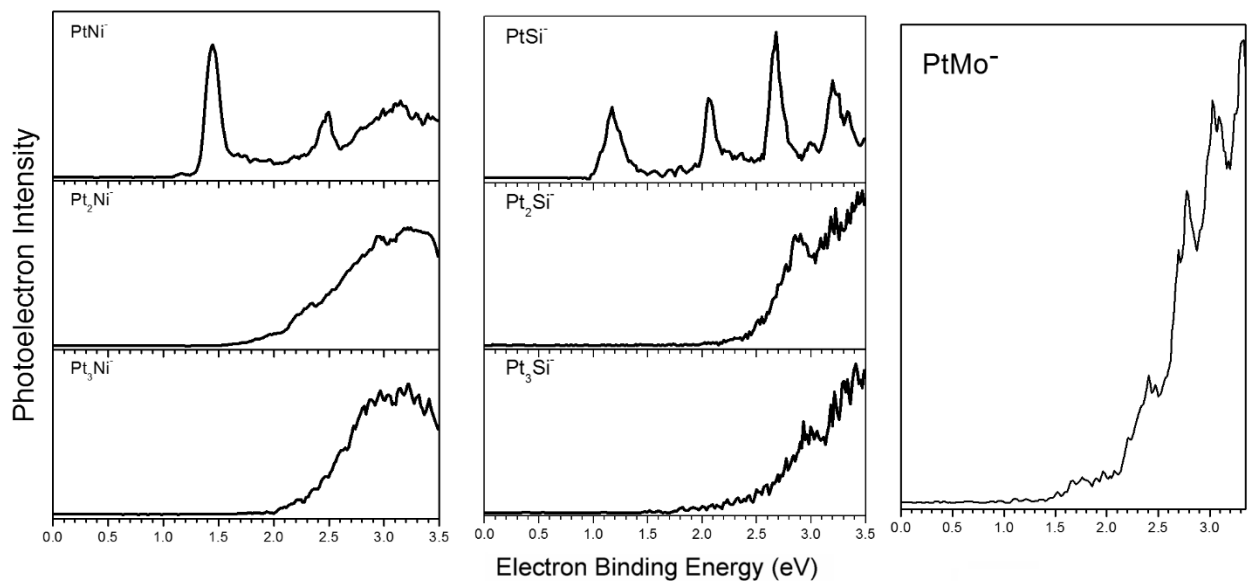Figure A.31. PES of $PdMg_{1,2}^-$, $PdZn_{1,2}^-$ and $PdCu^-$.

Figure A.32. PES of $Pt_{1-3}Ni^-$, $Pt_{1-3}Si^-$ and $PtMo^-$.

274

X. Transition metal hydrides

Certain transition metals are very good catalysts for hydrogenation and dehydrogenation. Understanding the electronic structure of these hydrides will facilitate the understanding of catalysis mechanism and further help designing good catalysts. In this section, some hydrides of Ag, Cu, Fe and Pd will be presented.
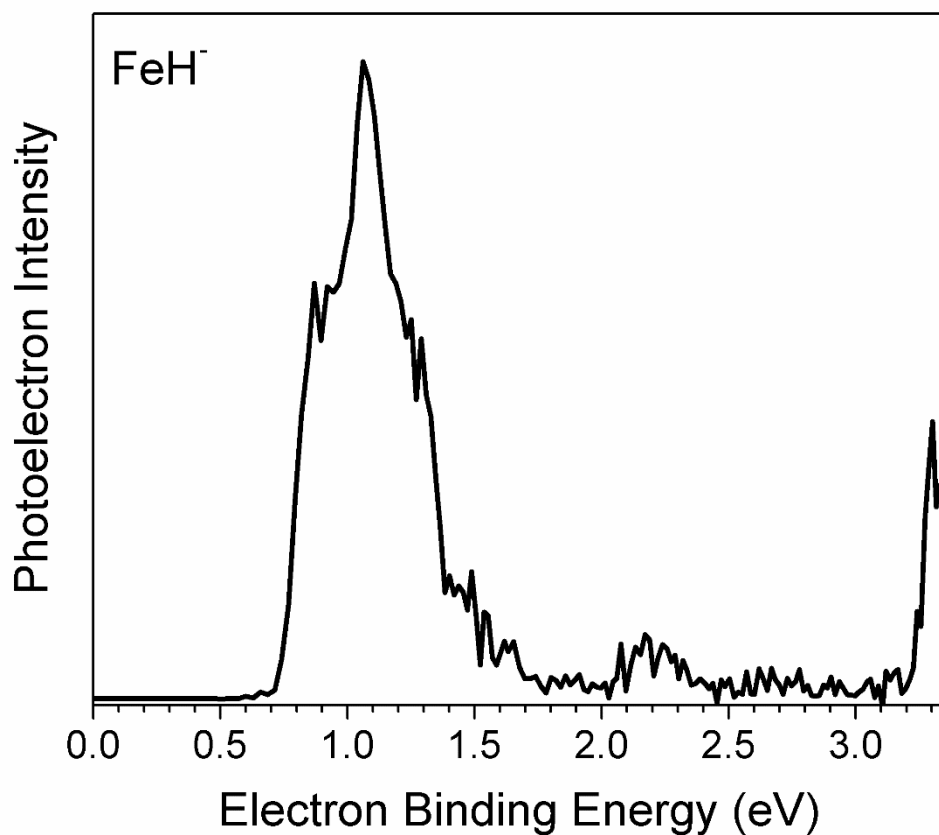

Figure A.33. PES of FeH⁻.
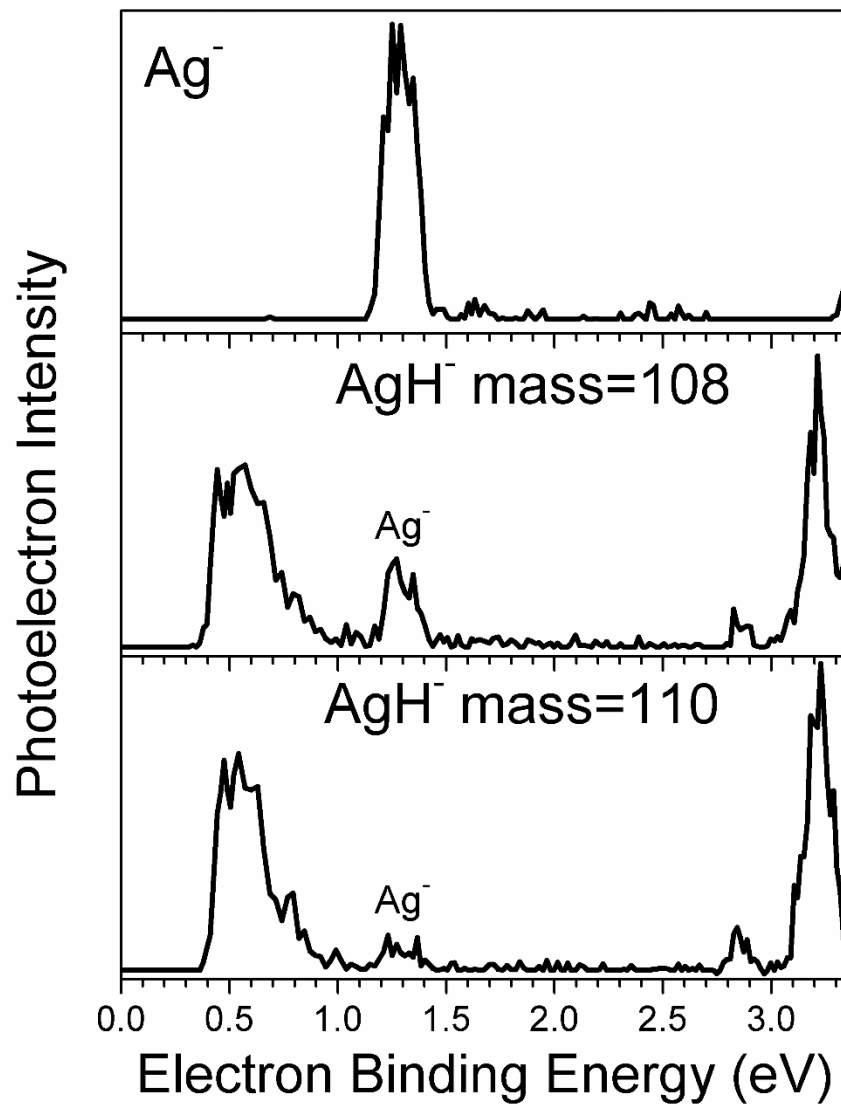
Figure A.34. PES of Ag⁻ and AgH⁻. Please note that some features in the spectrum of AgH⁻ belong to Ag⁻.
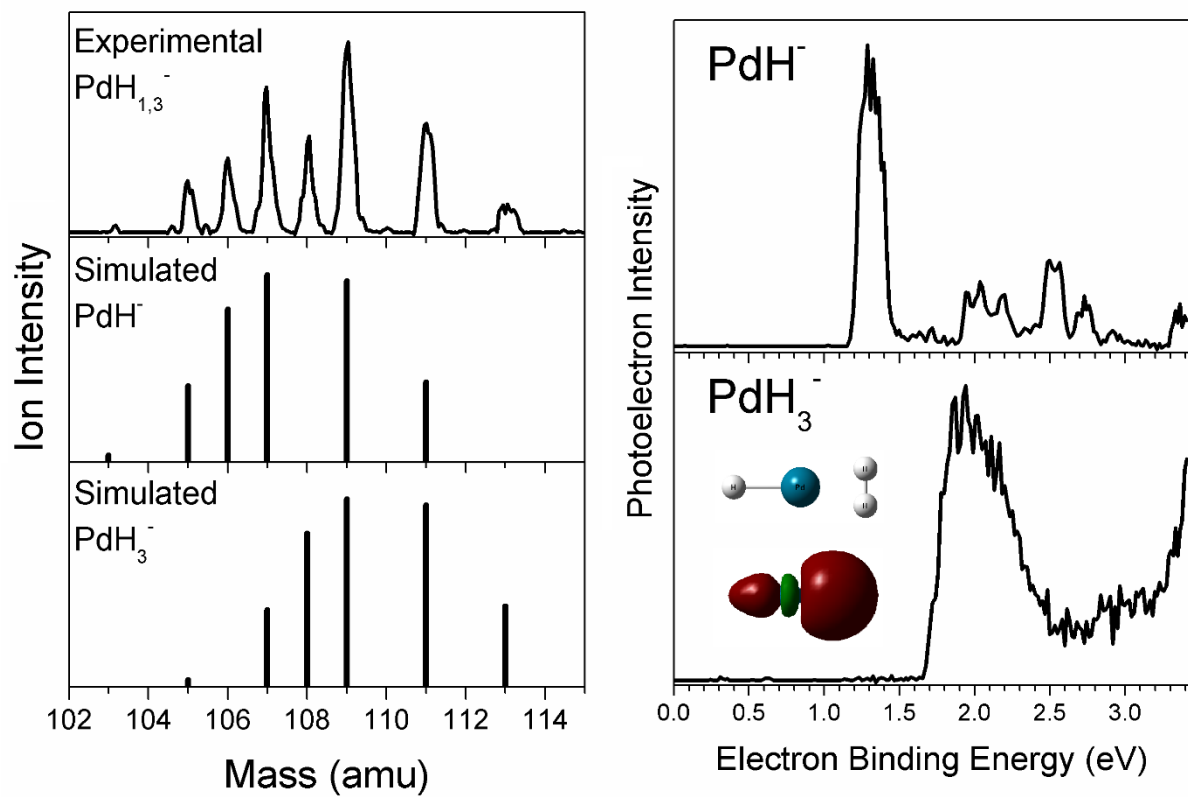
Figure A.35. Mass spectra and PES of PdH$_{1,3}^-$. Calculated structure of PdH$_3^-$ and the molecular

orbital of the bonding between H$_2$ molecules and PdH$^-$ moiety is also presented. PdH$_3^-$ is an

interesting cluster due to this unique structure. Calculations were performed at PBEPBE/SDD

(Pd) and 6-311+ G (3pd) (H) level of theory.

Figure A.36. PES of $Cu_2H_{1,2}^-$. Details about Cu_2H^- can be found in reference 9. Unlike the published work in which they only found one isomer, [9] we observed two isomers. $Cu_2H_2^-$ was observed by us for the first time. The structure was calculated at CCSD(t)/SDD (Cu) and 6-311+ G (3pd) (H) level of theory.

XI. Electron induced proton transfer in formic acid trimer

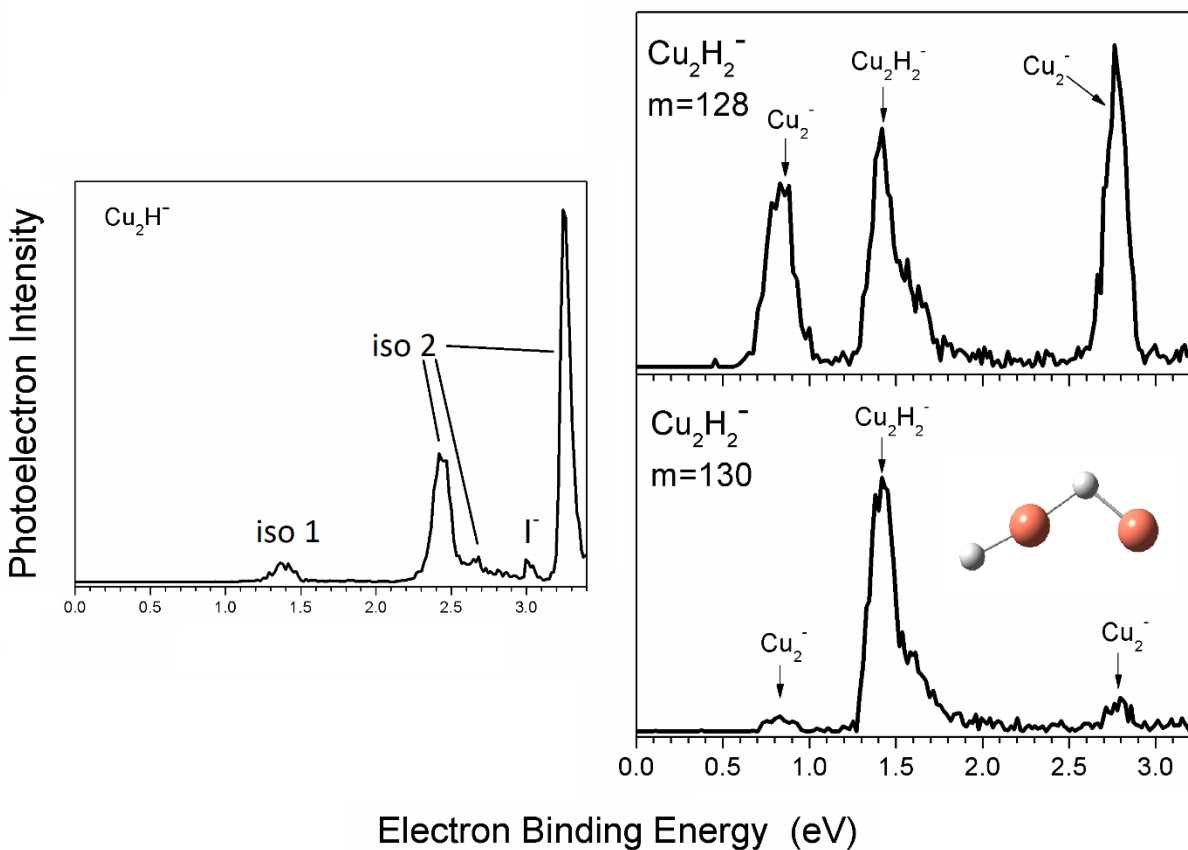Electron induced proton transfer occurs in formic acid dimer anion,[10] (the reported VDE of formic acid dimer anion in reference 10 might be wrong due to insufficient photon energy.) and in the trimer anion, the third formic acid molecule serves as a solvation molecule. Mass spectrum and photoelectron spectrum are presented in Figure A.37 and calculation results are shown in Figure A.38. Calculations were performed at wb97xd/6-31+ G(d, p) level of theory. Rigid scan means only the O-H coordinate is changing while the rest of the cluster remains unchanged.

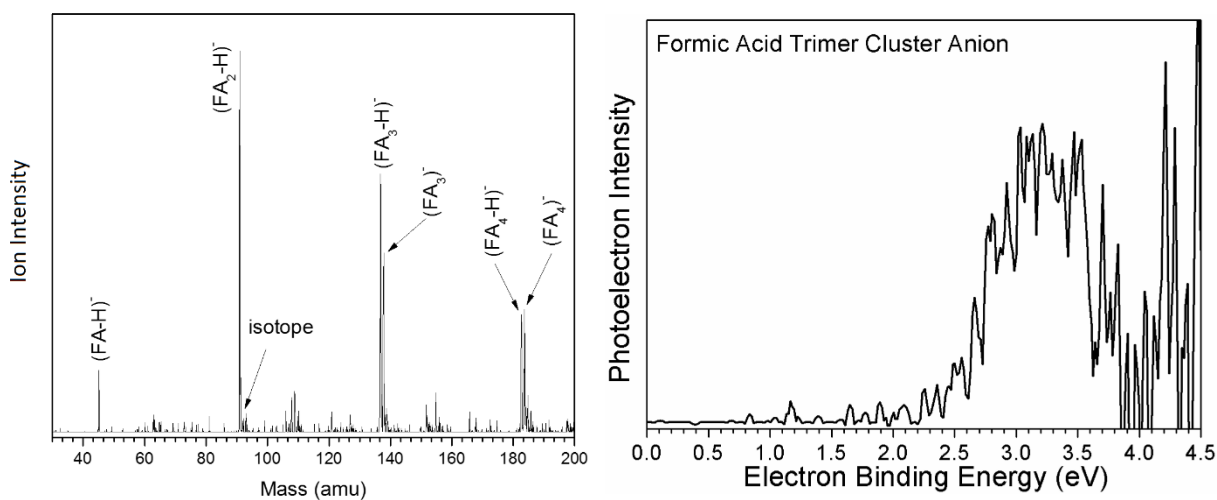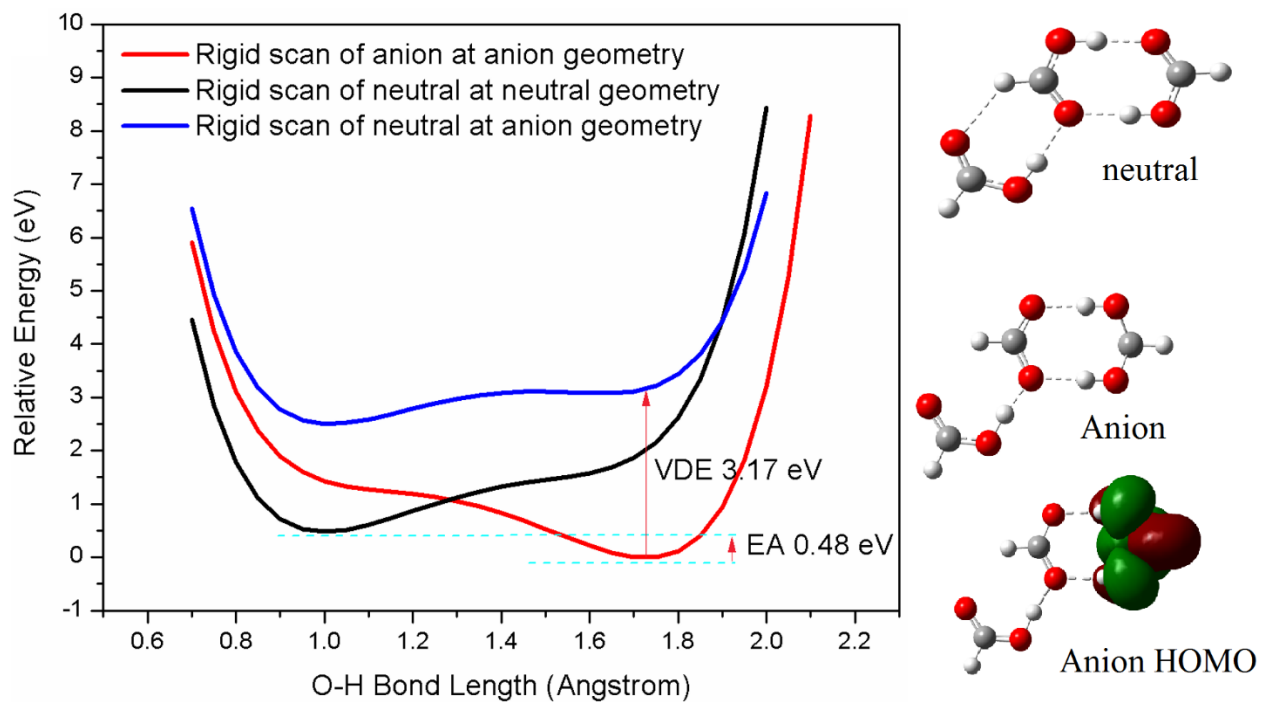
Figure A.37. Mass spectrum and PES of formic acid trimer.

Figure A.38. Rigid scan potential energy surfaces, neutral structure, anion structure and anion HOMO are presented. Calculated VDE matches experiment perfectly, and one can observe that there is no Frank-Cotton overlap between the ground state of the anion and ground state of the neutral, therefore EA cannot be observed experimentally.

XII. Anionic resonance of azobenzene parent anion

Azobenzene anion has resonance from 2.2 eV to 2.8 eV, so we expect special peaks when photodetachment photon energy falls into that region. Figure A.39 shows the photoelectron spectra of azobenzene anion taken at different photon energies. The 3.49 eV and 4.66 eV spectra are normal photodetachment spectra since there is no resonance. The vibrational progression is due to the C-N stretch mode, which is consistent with my calculations. The 2.54 eV, 2.41 eV and 2.33 eV spectra are mixtures of normal photodetachment and autodetachment after anionic resonance. Hence, the left three peaks are still the C-N vibrational progression, and the peak marked by R is due to the anionic resonance and it changes with photon energy. The right side of Figure A.39 shows the schematic energy diagram of the resonance absorption --- autodetachment process. This is a shape resonance, which is ultrafast. No Feshbach resonance is observed because Feshbach resonance involves two electrons but our spectra are relative simple. For detailed knowledge please refer to references 11 and 12. Since the shape resonance and autodetachment are ultrafast, the positions of peak Rs should be corresponding to the vertical autodetachment, therefore, their positions are determined by their own Frank-Condon overlap. Apparently 2.54 eV photon energy makes the Frank-Condon overlap the worst in the three cases, therefore its R peak is the widest. Besides, one would expect that the structural difference between T^{-*} and T^0 is smaller than that between T^- and T^0, because the excess electron in T^{-*} should have less influence to the T^0 core. Therefore, due to the similar slope of T^{-*} and T^0 on their potential energy surfaces, one would also expect similar kinetic energies caused by autodetachment in these three cases. When our machine recorded the kinetic energies, it still took them as normal photoelectrons and recorded the corresponding EBE, therefore, EBEs will be different when photon energies are different and kinetic energies are similar.
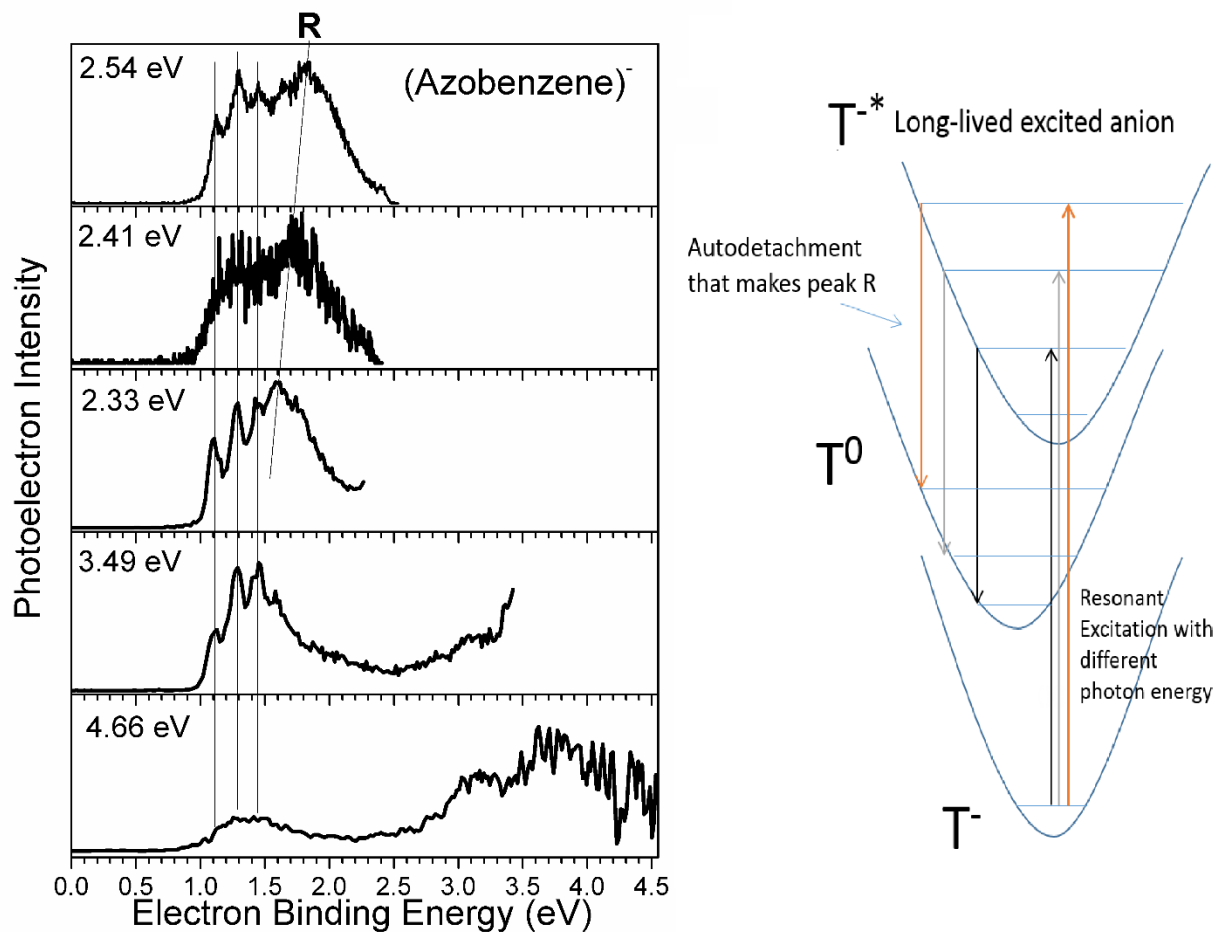
Figure A.39. Photoelectron spectra of azobenzene anions taken from different photon energies. The schematic energy diagram showing the anionic resonance and autodetachment is also presented on the right.

XIII. Transition metal anions solvated by water

When transition metal anions are solvated by one or more water molecules, all the peaks gradually shift to the high EBE end, but the spacing between peaks, the number of peaks, the nature of the transition of each peak do not change. Besides the shift, the major changes could only be peak width caused by Frank-Condon overlap change and sometimes, one might observe some vibrational features caused by water O-H stretch and bending. Next I will present the spectra of $M(H2O)_n^-$ where M = Au, Ag, Cu, Co, V, Fe. All of them follow the above protocol. This is a boring section, however, all of these systems are just to emphasize that how special Li^-, Ni^-, Pd^- and Pt^- are, because when they interact with water, they don't follow the above protocol.
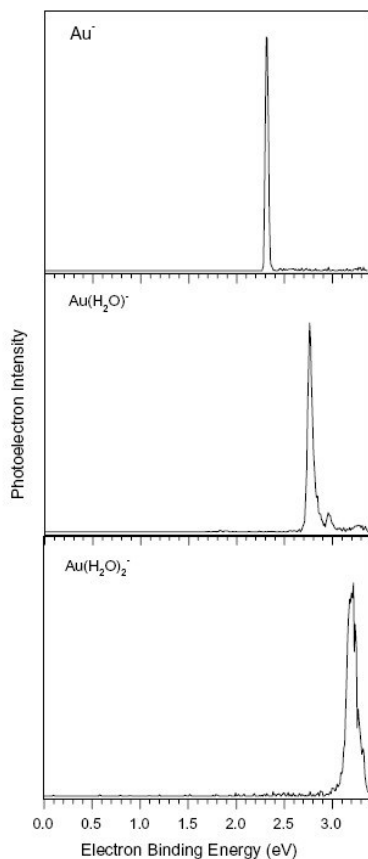
Figure A.40. PES of $Au(H_2O)_n^-$ (n = 0-2).

Figure A.41. PES of $Ag(H_2O)_n^-$ (n = 0-3).

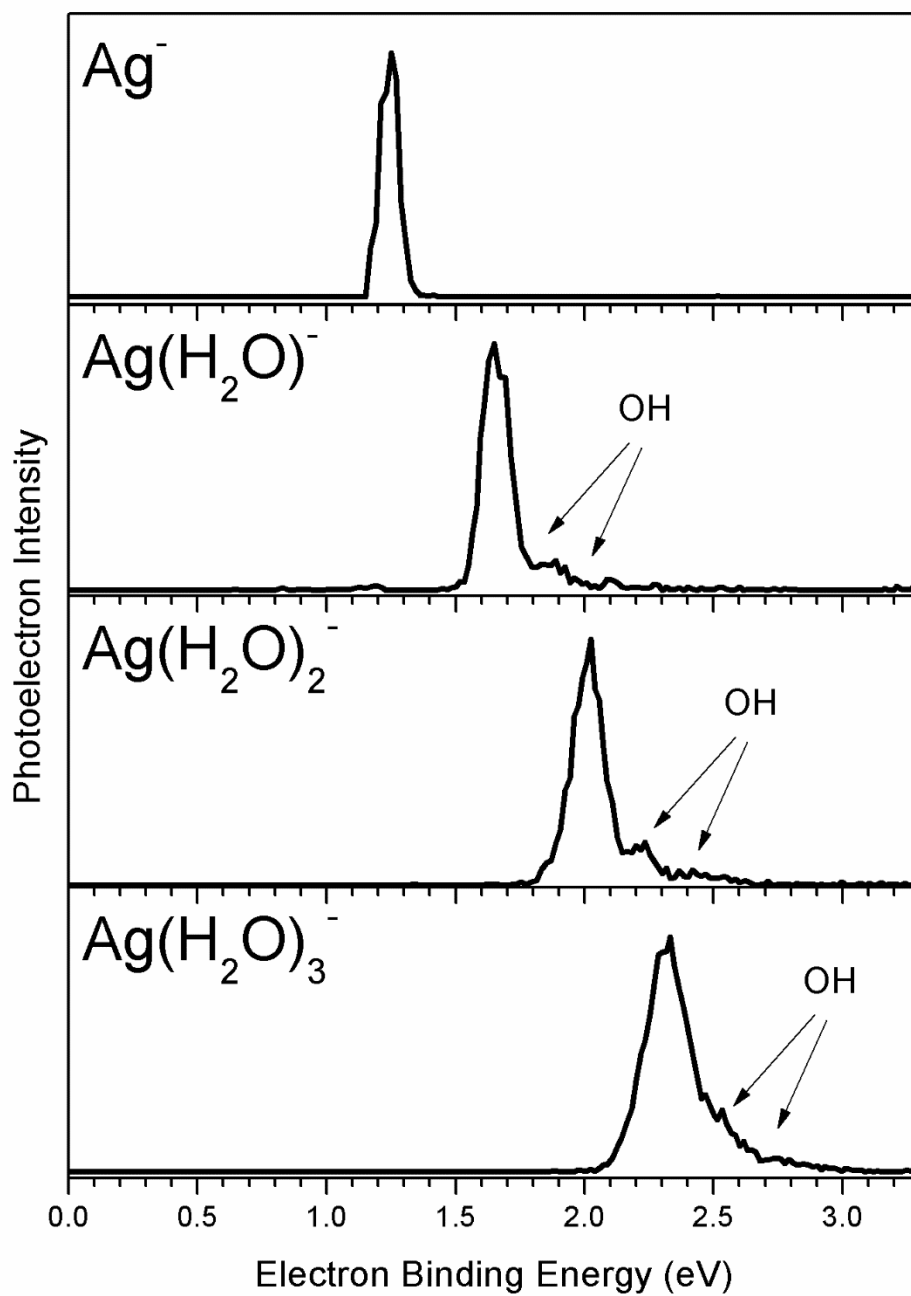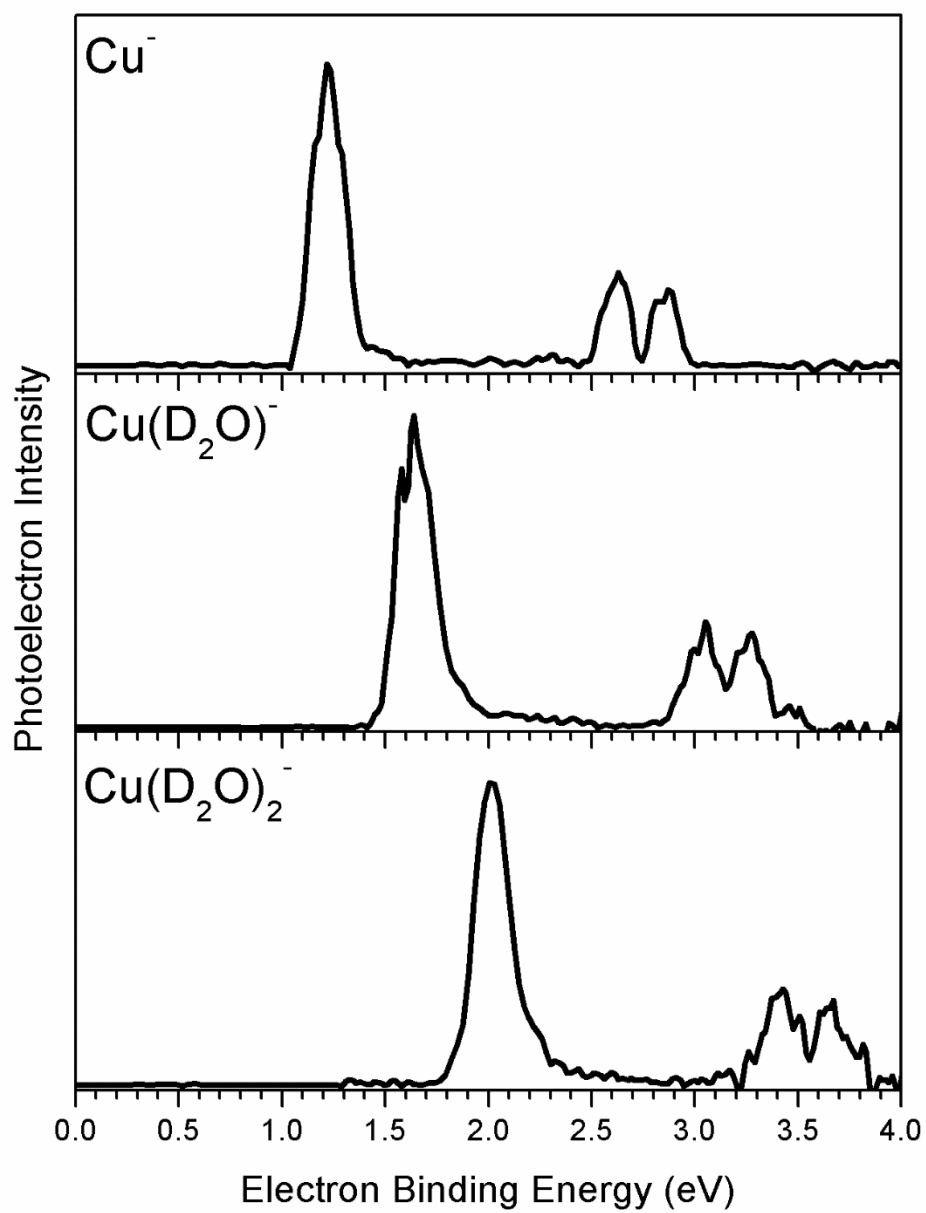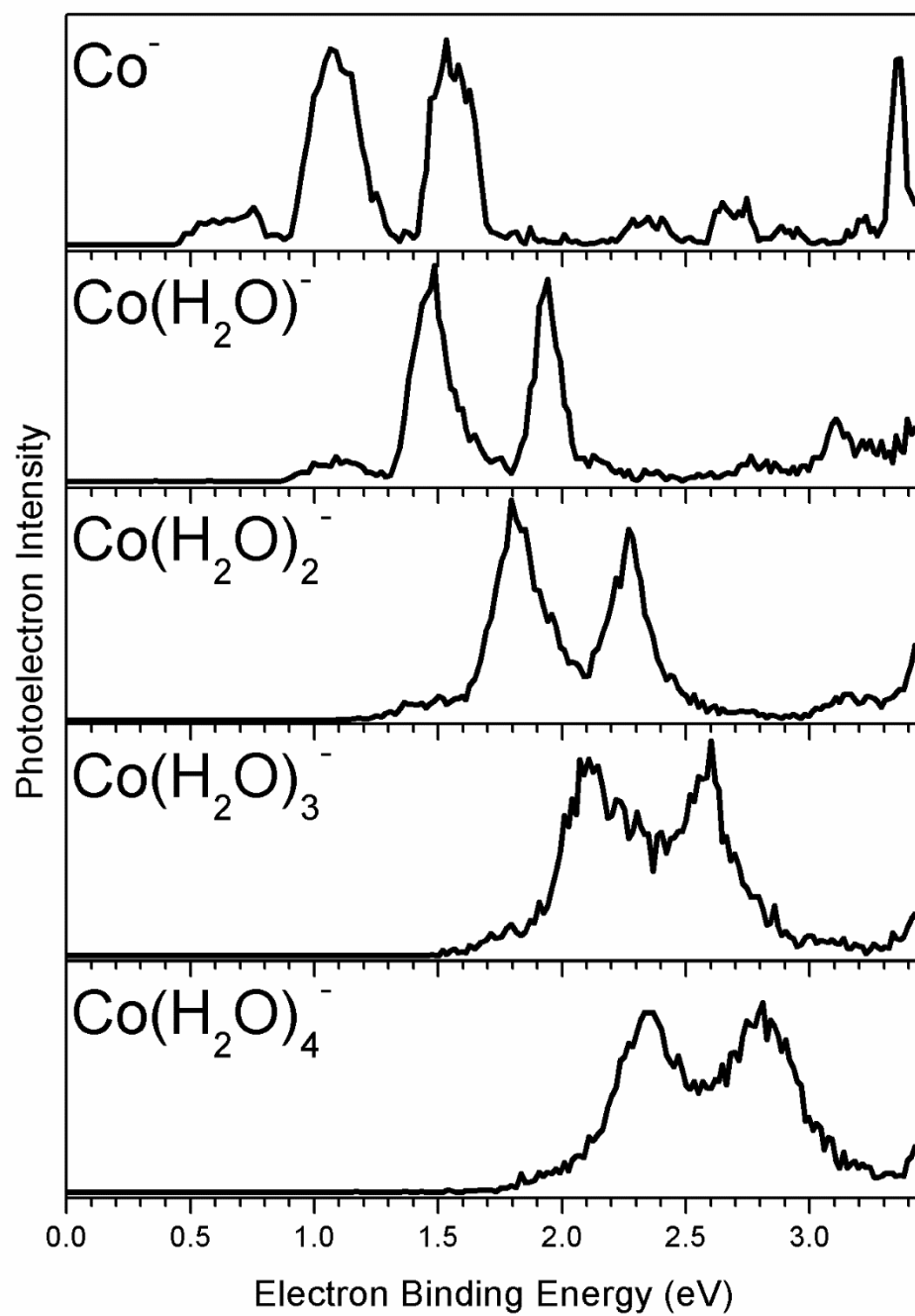Figure A.42. PES of $Cu(D_2O)_n^-$ (n = 0-2).

Figure A.43. PES of $Co(H_2O)_n^-$ (n = 0-4).
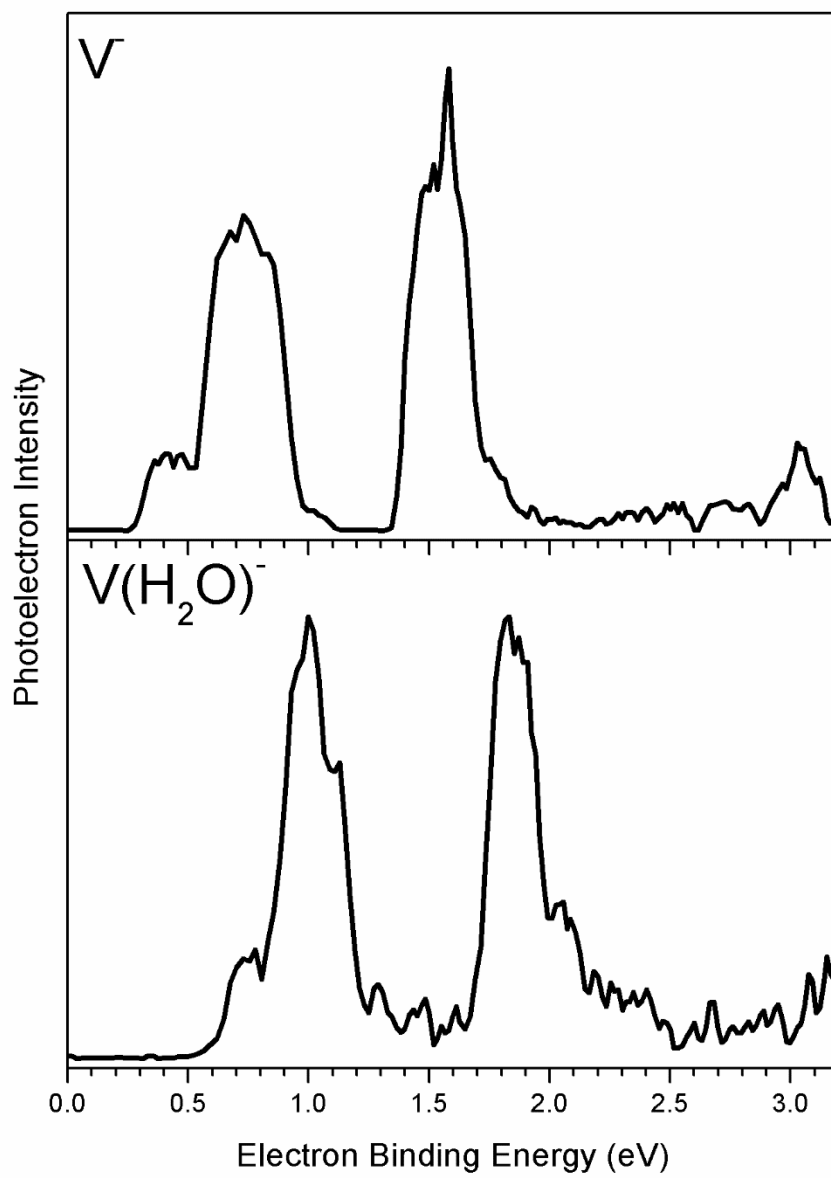
Figure A.44. PES of $V(H_2O)_n^-$ (n = 0-1).
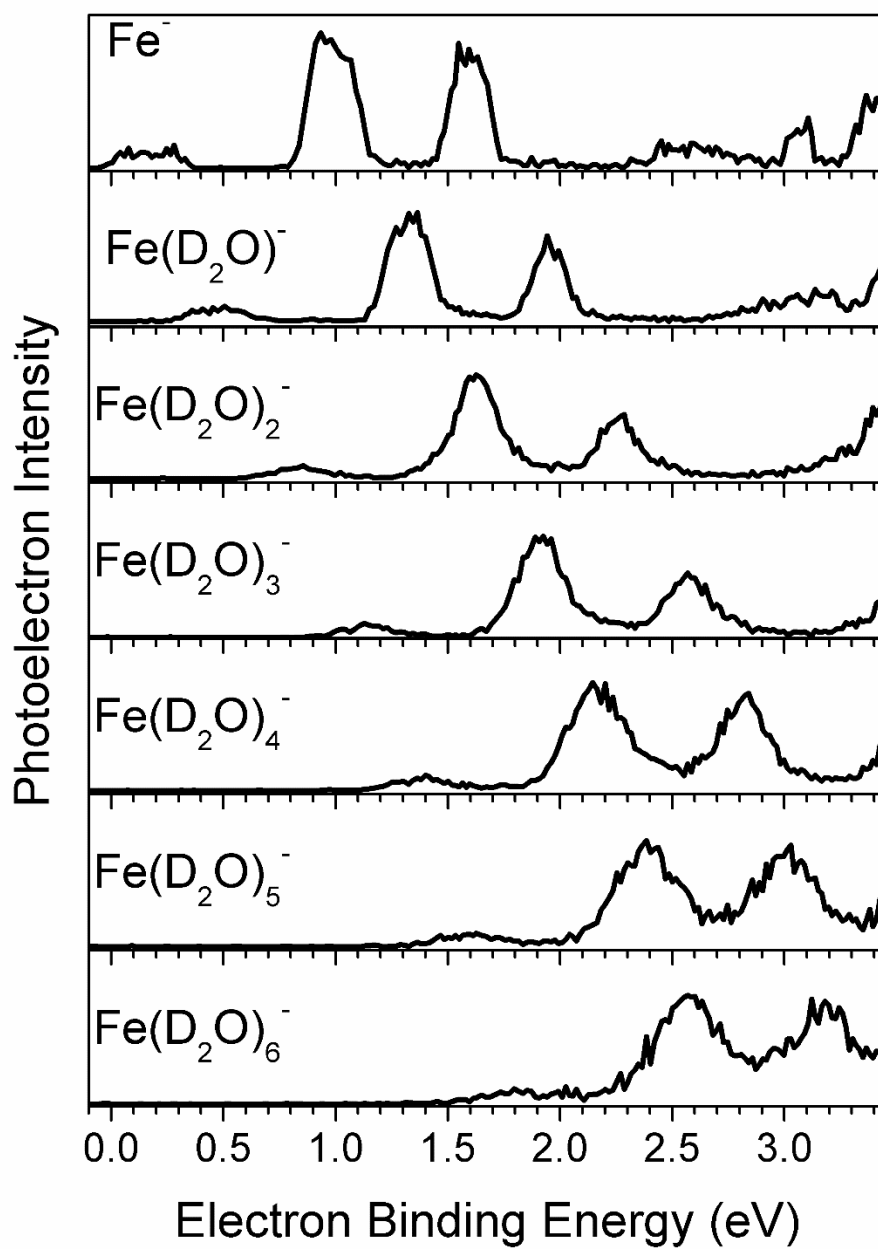
Figure A.45. PES of $Fe(D_2O)_n^-$ (n = 0-6).

XIV. Microsolvation of HCl

When acids, bases and salts dissolve in water, what is the mechanism of ionic dissociation? How many water molecules are needed to pull apart the cation and anion parts? As for the anions, after dissociation, where does the electron dwells? Is there a H_3O Rydberg molecule? Could this be a model of studying the nature of solvated electron (is it possible that the nature of solvated electron is H_3O---OH^- but not the electron occupying a cavity surrounded by a lot of water molecules)? How much can we stretch the electron induced proton transfer (EIPT) theory? This simple system is so interesting that we can look at it from so many perspectives. Anion photoelectron spectroscopy is a powerful tool for studying this kind of problems. In this section, I observed that the smallest $HCl(H_2O)_n^-$ cluster has 6 water molecules. Calculations are needed to reveal the actual structures of $HCl(H_2O)_n^-$ and to confirm that there is H_3O Rydberg molecule involved, but one can imagine that the calculation could be tedious because water molecules could have many different orientations. The way I did the experiment is using HCl solution, in which HCl is already dissociated. Hence, the onset of mass spectrum is smallest cluster with HCl dissociated, in other words, the H---Cl dissociated isomer of $HCl(H_2O)_n^-$ (n<6) cluster anions might have negative EAs. Vitaly's neutral molecule dipole moment experiment shows that six water molecules are needed to dissociate DCl.[13] Martina Havenith's work shows that only four water molecules are needed to dissociate HCl. [14] This difference might be another example of isotope kinetic effect. Then, why our system needs six water molecules to dissociate HCl? Is it because anion needs more water molecules to be stabilized than the neutral? Is it simply because our system has higher temperature?
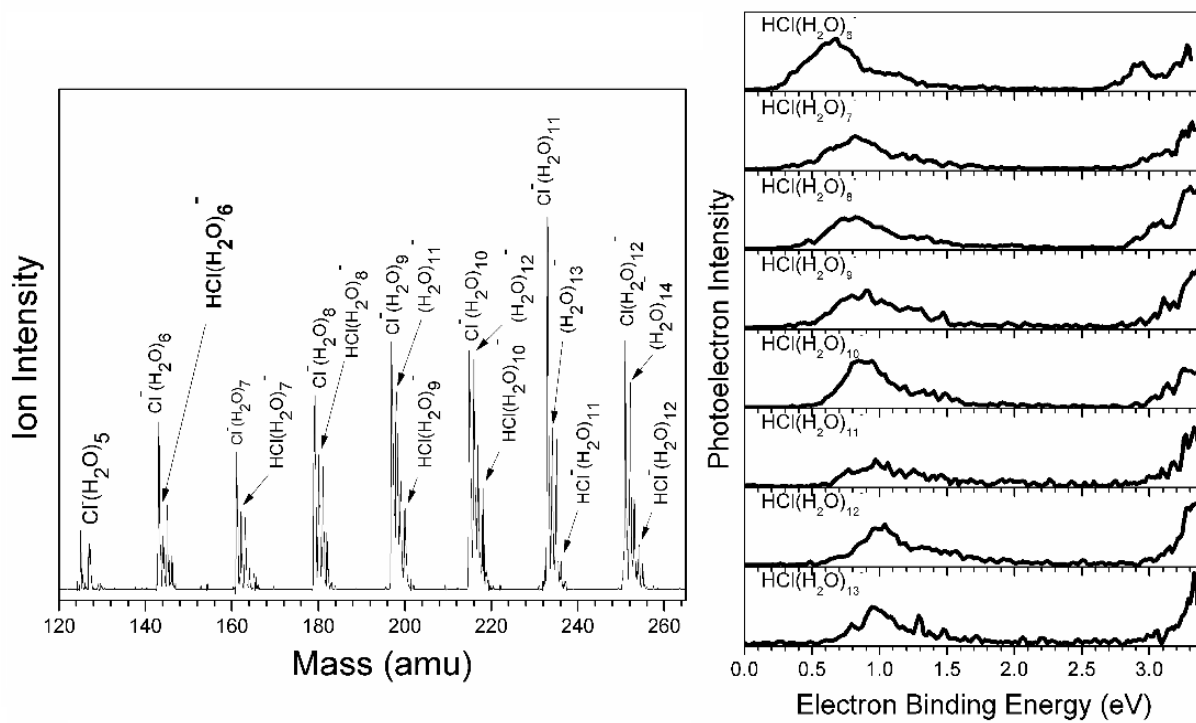
Figure A.46. Mass spectrum and PES of $HCl(H_2O)_n^-$ (n = 6-13).

XV. PES of organic anions

Electron delocalization, electron-withdrawing functional group, radical anion, etc. are very basic concepts in organic chemistry. Study of organic (radical) anions in the gas phase to obtain the electronic structure information help understanding the behaviors of certain organic compounds/functional groups/radicals in the bulk. Some of these works have been published by us.[15,16] In this section, the PES of radical anion of benzophenone, closed shell triphenylmethyl carbanion and its monoxide, nitrobenzene radical anion, and $CH_3COCH=C=O$ radical anion are presented. Benzophenone's very high electrophilicity explains its reaction with sodium to form a radical anion in solution. Triphenylmethyl anion on the other hand, is stable due to the electron delocalization in the three benzene rings. This stable carbanion is a good candidate for fixating CO_2: $Ph_3C^- + CO_2 = Ph_3CCO_2^-$. The high electrophilicity of nitrobenzene explains its role as electron scavenger.
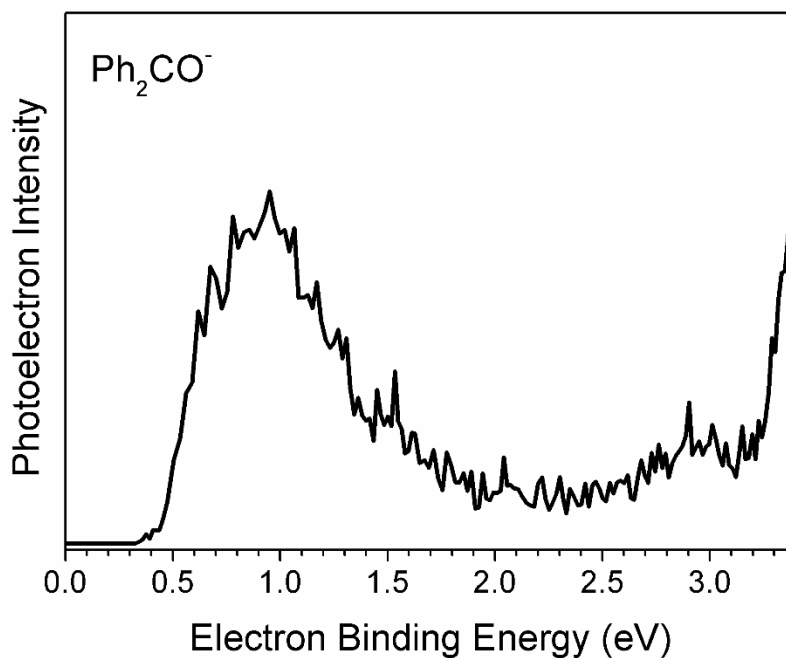
Figure A.47. PES of benzophenone radical anion, Ph_2CO^-.
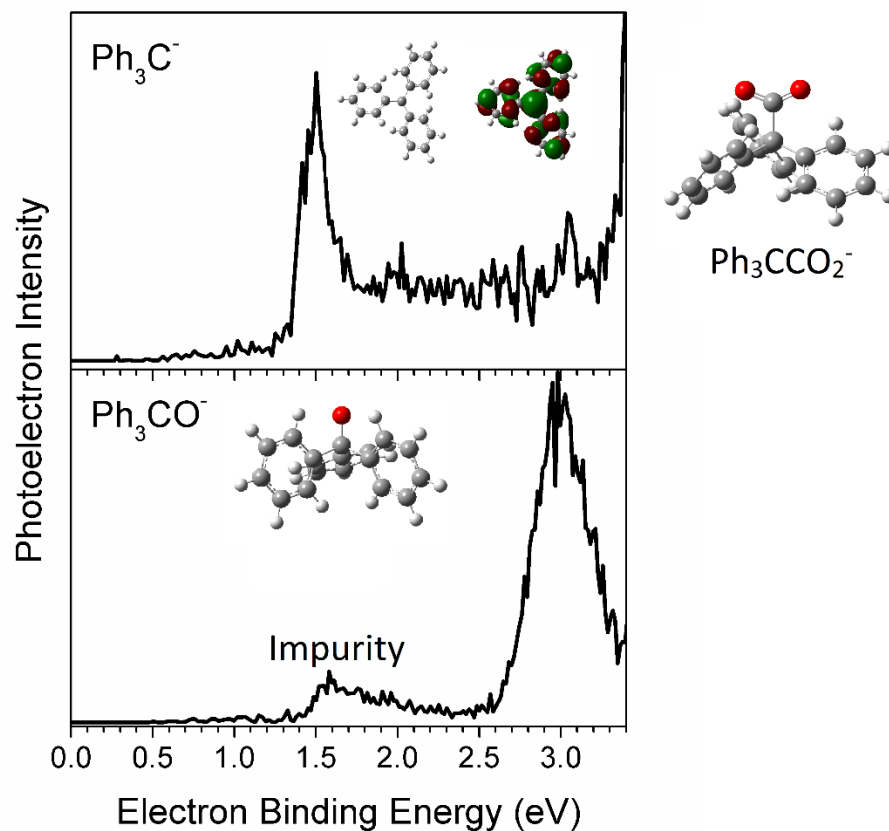
Figure A.48. PES of triphenylmethyl carbanion and its monoxide. Their calculated structures and

HOMO are also presented. One can observe that in Ph_3C^- the excess electron is highly

delocalized. Please note that the structure of Ph_3C^- is spiral but not planar due to steric hindrance.

The CO_2 fixation product of Ph_3C^- is shown on the right. More experiments are needed to

explore the CO2 fixation feasibility. All the calculated results match experiments very well.
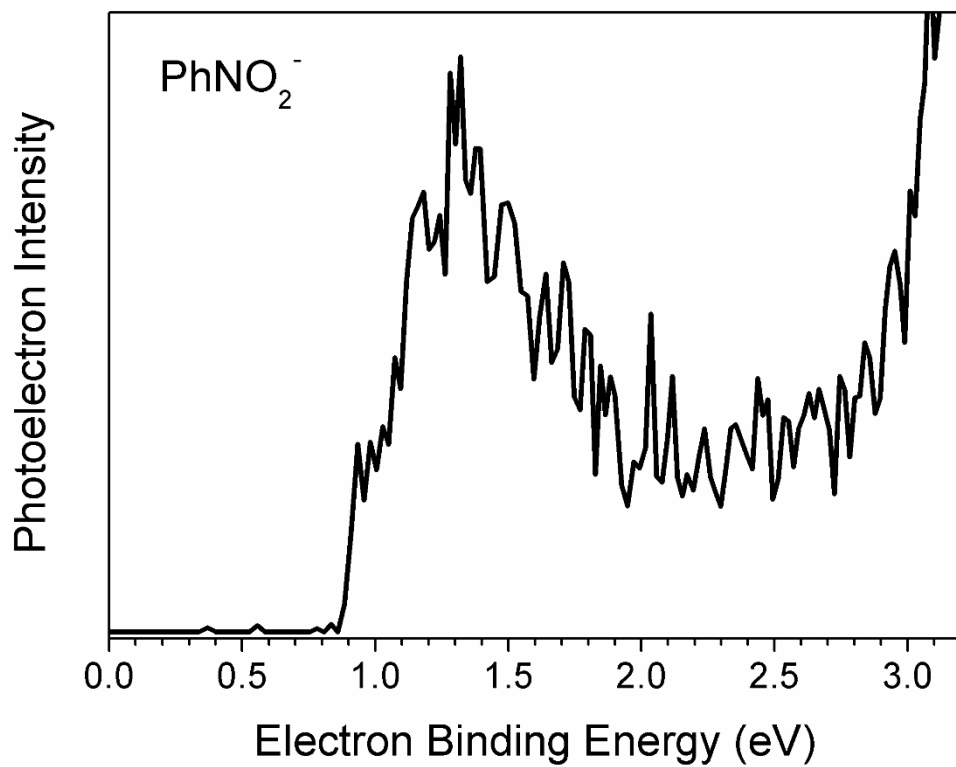
Figure A.49. PES of nitrobenzene radical anion.
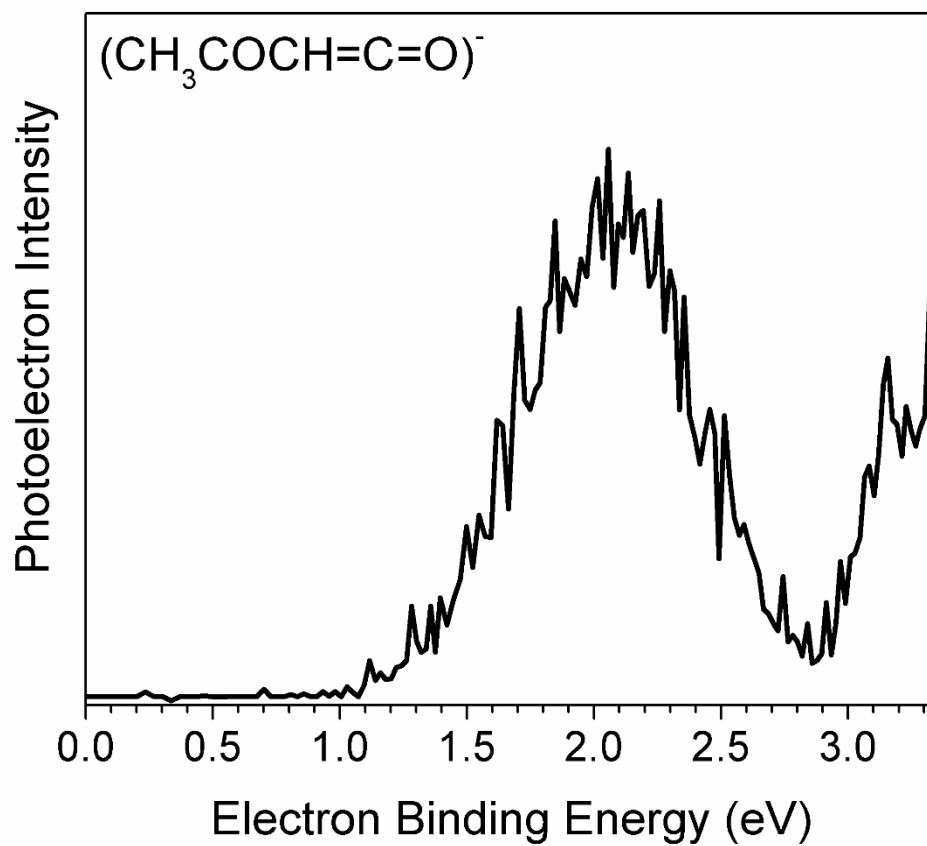
Figure A.50. PES of CH₃COCH=C=O radical anion.

XVI. Water activation by a single atom

In this section, the interaction between water molecule and Ni⁻, Pd⁻ and Pt⁻ are presented. Calculations give evidence that $M(H_2O)^-$ and HMOH⁻ coexist in the photoelectron spectra. Figure A.51 shows the PES of $M(H_2O)^-$ and HMOH⁻. The peaks in red circles belong to HMOH⁻. Figure A.52 presents the calculated structures of $M(H_2O)^-$ (a) and HMOH⁻ (b) and the transition state (c) in between $M(H_2O)^-$ and HMOH⁻. Figure A.53 displays the energy levels of these three systems, one can observe that HMOH⁻ has lower energy than $M(H_2O)^-$.

To confirm that the following reactions: $M(H_2O)^- \rightarrow$ HMOH⁻ indeed happen, but not the ion source simply makes HMOH⁻, an isotopic kinetics experiment was performed and presented in Figure A.54. One can observe that the peak of HPtOH⁻ is three times of the peak of DPtOD⁻, and the peak of HPtOD⁻/DPtOH⁻ is in between, which is due to the activation energy difference caused by zero-point energy difference. By calculating the activation energy (with zero point energy correction) and with the help of Arrhenius Equation, one can estimate the reaction rate. The calculation is as follows:

The reaction rate constant is k, and kH is the reaction rate constant using H_2O, kD is the reaction rate constant using D_2O. EH is the activation energy using H_2O and ED is the activation energy using D_2O. [A] is the concentration of reactant, [B] is the concentration of product. The reaction is as follows: $A \rightarrow B$. This is a first order reaction, because no other reactant is involved. Then $d[B]/dt = -d[A]/dt$, $d[A]/dt = -k[A]$, therefore, $[A] = [A]_0\, e^{-kt}$. Since $[B] = [A]_0 - [A]$, $[B] = [A]_0\, (1 - e^{-kt})$.

Then assume that for the H_2O and D_2O experiments the reaction time is the same, because the source conditions are the same. The final concentrations of the reactant [A] is also the same,

because their PES intensities are similar. Therefore, $[BH]/[BD] = (1 - e^{-kHt})/(1 - e^{-kDt})$. According to the relative intensities of BH and BD in the PES, $[BH]/[BD] = 3$, so $(1 - e^{-kHt})/(1 - e^{-kDt}) = 3$. Accroding to Taylor Series, $e^x = 1 + x + x^2/2 + x^3/6\ldots$, hence, $1 - e^{(-kt)} = kt - (kt)^2/2 + (kt)^3/6\ldots$, omit the second and higher order terms, we get $1 - e^{(-kt)} = kt$. Therefore, $kH/kD = 3$.

According to Arrnius Equation, $k = Ae^{-E/kT}$, where A is the total number of collisions and $e^{-E/kT}$ is the probability that any given collision will result in a reaction. Hence, $kH/kD = e^{(ED-EH)/kT}$, where EH and ED are the activation energies, k is the Boltzmann constant and T is the reaction temperature. Calculation reveals that $ED = 0.837$ eV and $EH = 0.768$ eV. Therefore, $kH/kD = e^{800/T}$.

Finally, we have $kH/kD = 3$ and $kH/kD = e^{800/T}$. Therefore, the reaction temperature T is 728 K. Put these numbers into the Arrnius Equation, the probability that any given collision will result in a reaction, $e^{-E/kT}$, is 4.88×10^{-6} for H_2O and 1.63×10^{-6} for D_2O. In this case, the total collision number, A, is actually the number of $Pt(H_2O)^-$ or $Pt(D_2O)^-$ clusters, which can easily vary a lot by changing source conditions, but the probability, $e^{-E/kT}$, is a much more essential and important factor in this study. A is in the order of 10^9-10^{13} per laser shot.[17]
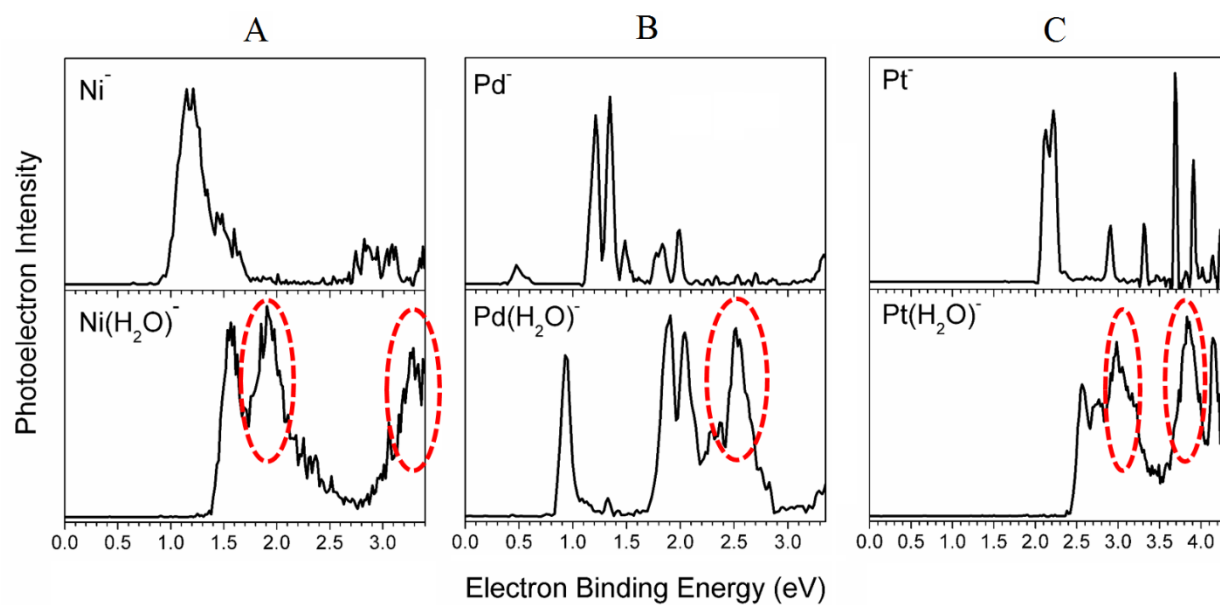
Figure A.51. PES of M(H$_2$O)$^-$ and HMOH$^-$. The peaks in red circles belong to HMOH$^-$. M = Ni, Pd and Pt.
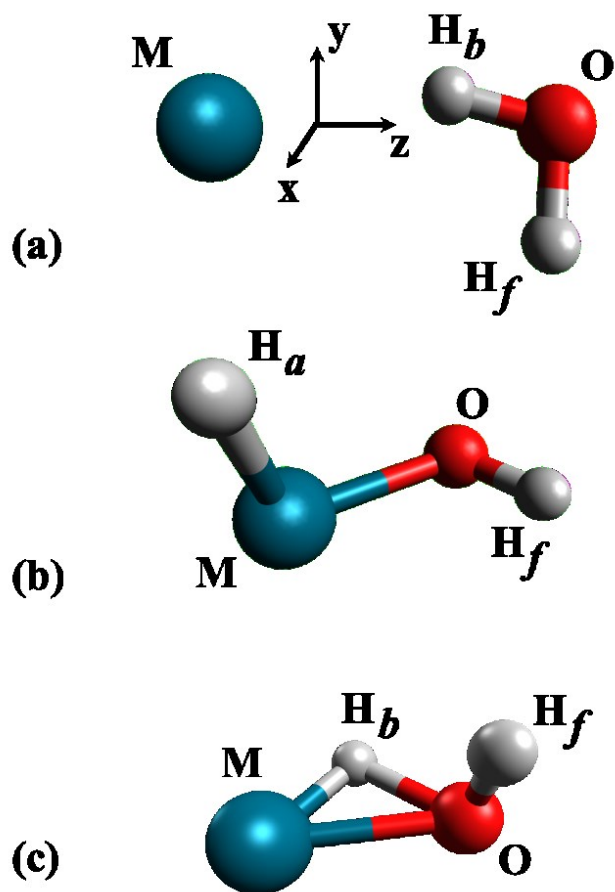
Figure A.52. Calculated structures of M(H$_2$O)$^-$ (a) and HMOH$^-$ (b) and the transition state in

between (c)
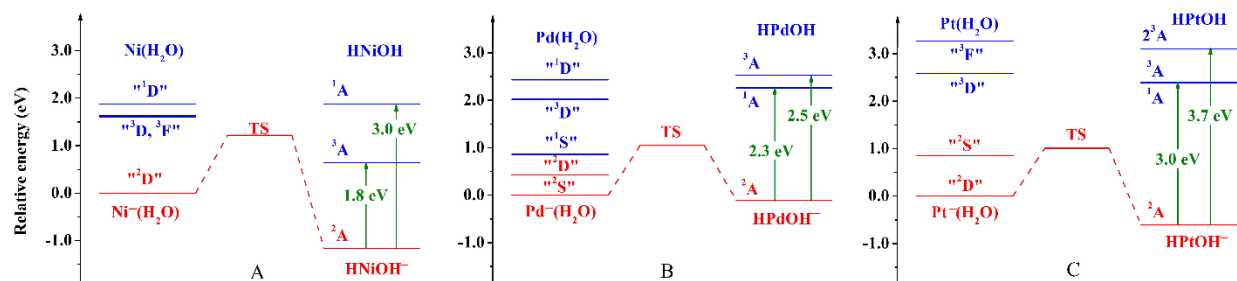
Figure A.53. Energy levels of these three systems.
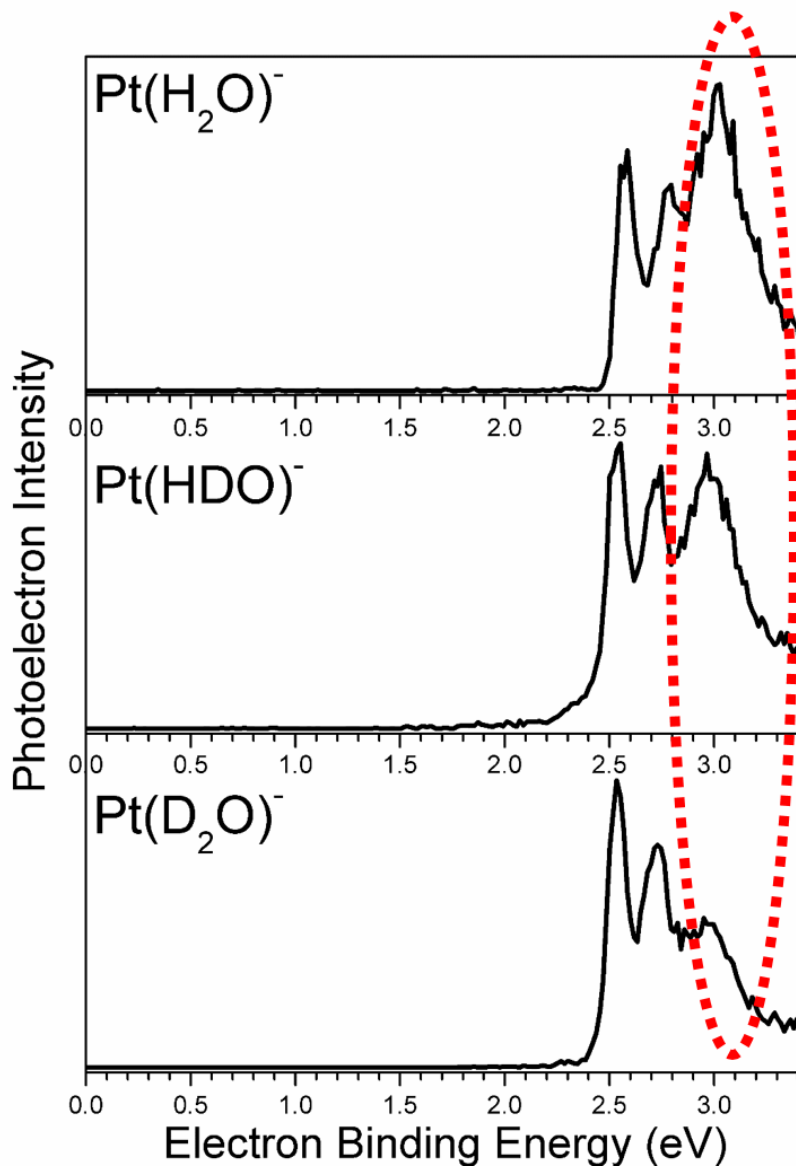
Figure A.54. PES of (Pt-H$_2$O)$^-$, (Pt-HDO)$^-$ and (Pt-D$_2$O)$^-$. The peaks in red circle belong to the water-activated cluster.

XVII. Miscellaneous

In this section, all the spectra are not categorized in any of the above sections. They are mainly "byproducts" of other experiments. Hopefully they can find their own use in the future.
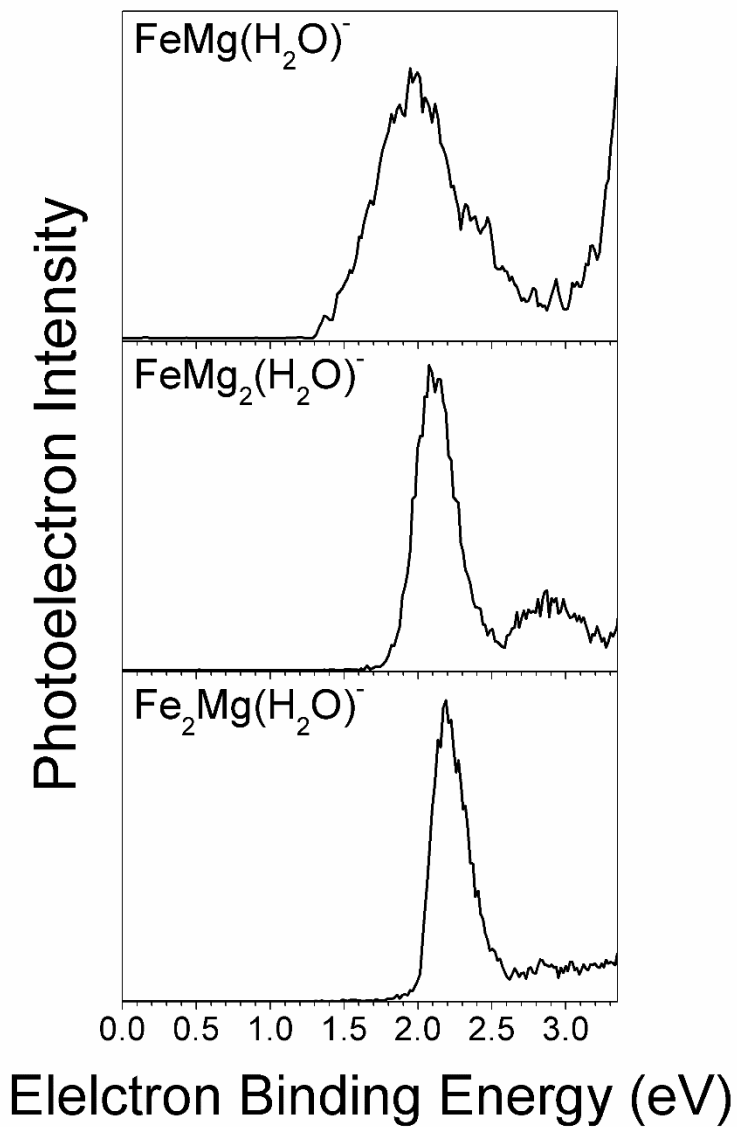
Figure A.55. PES of solvated Fe-Mg systems
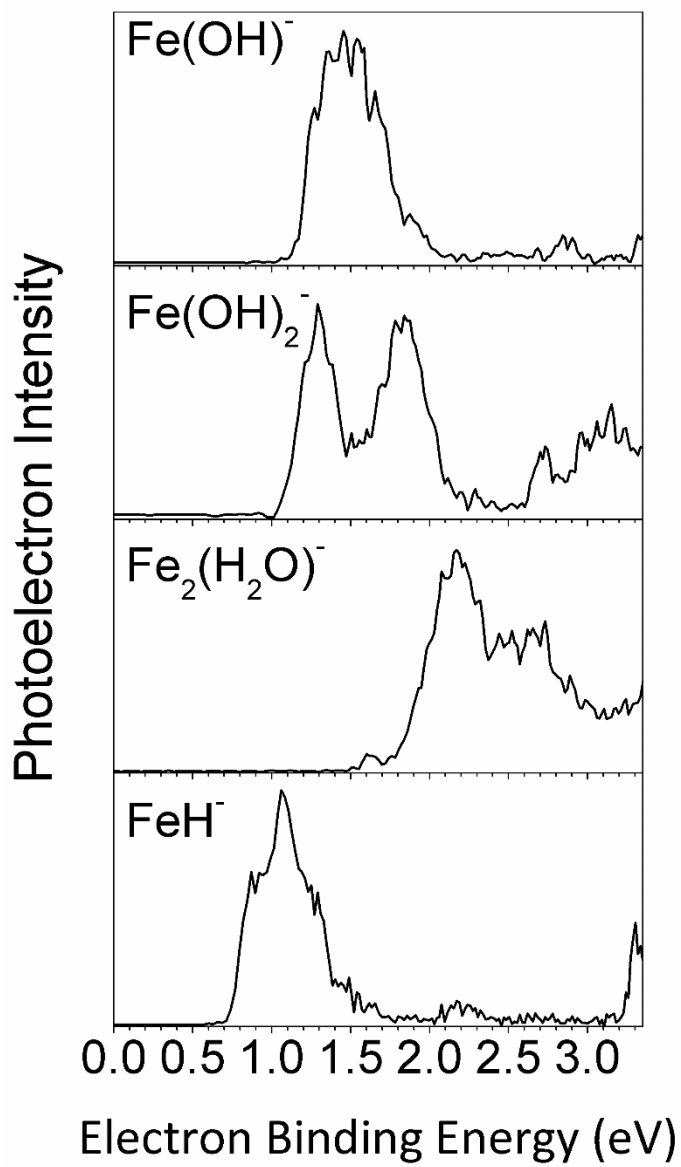
Figure A.56. PES of $Fe(OH)_{1,2}^-$, $Fe_2(H_2O)^-$ and FeH^-
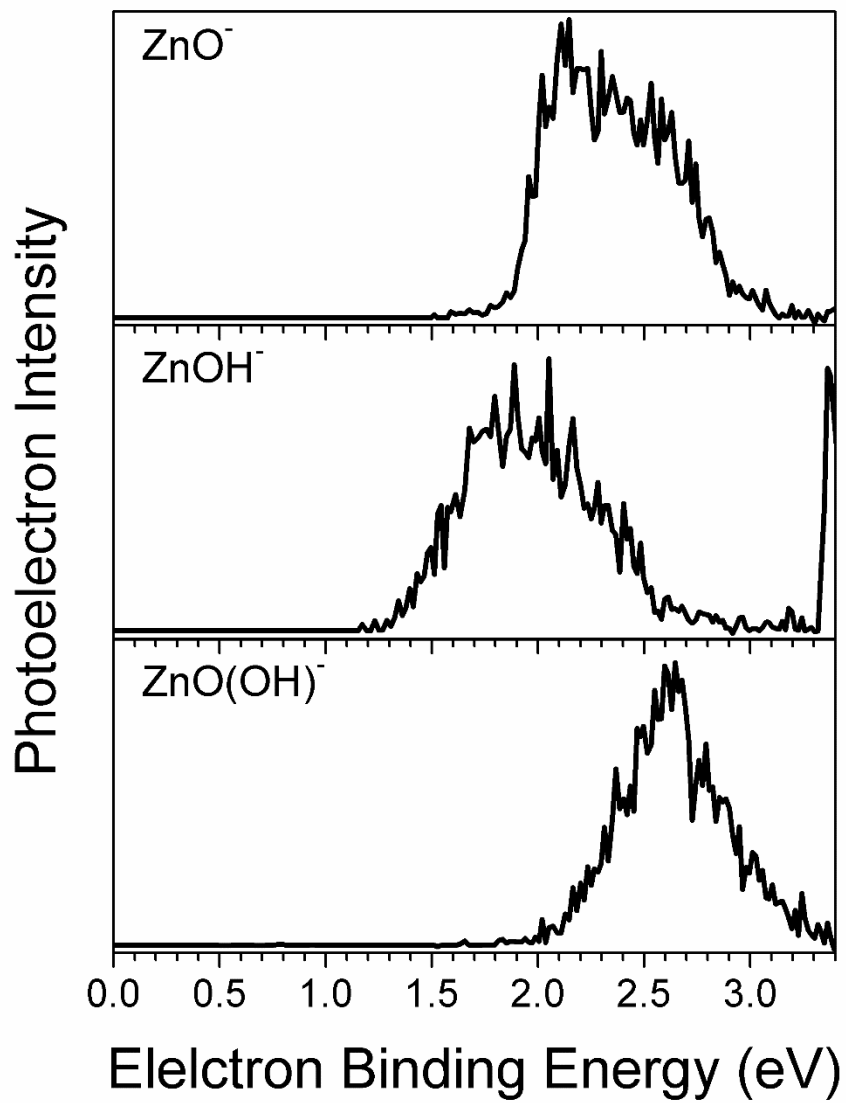
Figure A.57. PES of ZnO⁻, ZnOH⁻, ZnO(OH)⁻.
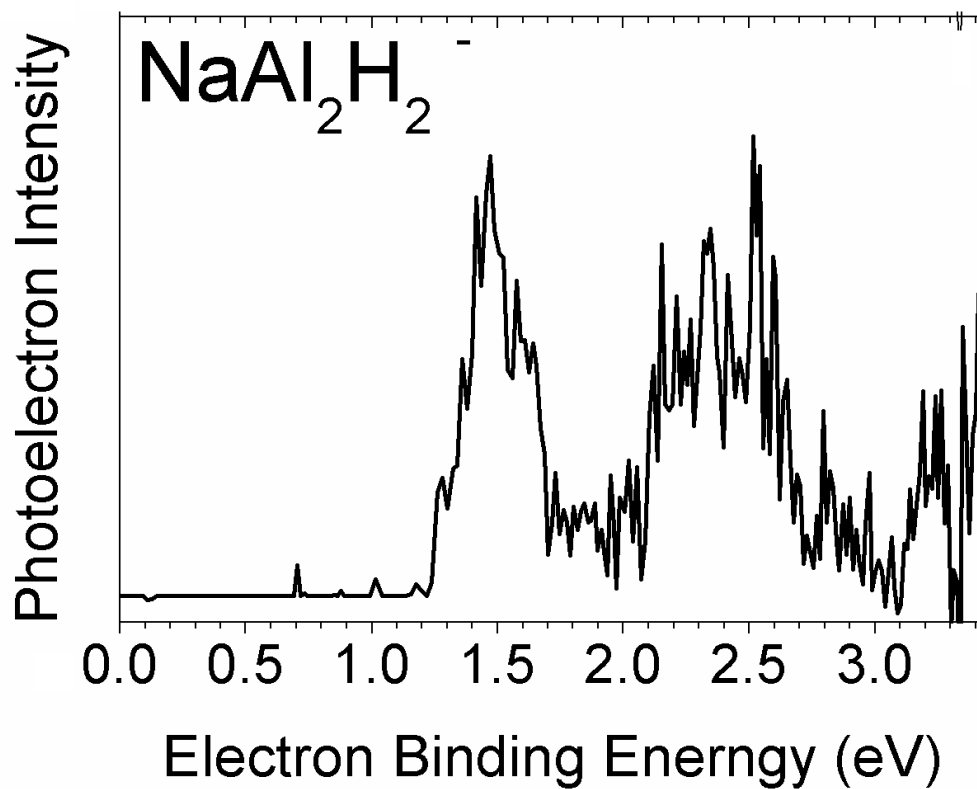
Figure A.58. PES of NaAl$_2$H$_2^-$. Please note that Al$_2$H$_2^{2-}$ kernel might mimic C$_2$H$_2$, therefore there could be Al-Al triple bond involved.
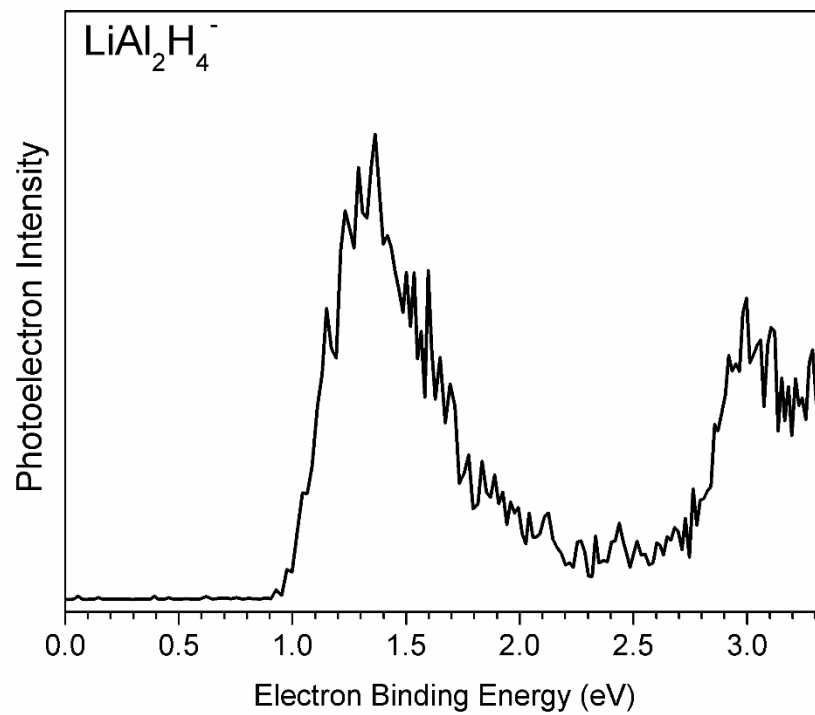
Figure A.59. PES of LiAl$_2$H$_4^-$. Please note that Al$_2$H$_4^{2-}$ kernel might mimic C$_2$H$_4$, therefore there could be Al-Al double bond involved.

References

1. B. Kiran, A.K. Kandalam, R. Rallabandi, P. Koirala, X. Li, X. Tang, Y. Wang, H. Fairbrother, G. Gantefoer and K.H. Bowen, *J. Chem. Phys.*, **136**, 024317 (2012).

2. O. C. Thomas, W. -J. Zheng, S. -J. Xu and K. H. Bowen, *Phys. Rev. Lett.*, **89**, 213403 (2002).

3. P. Syers, D. Kim, M. S. Fuhrer and J. Paglione, *Phys. Rev. Lett.* **114**, 096601 (2015).

4. J. C. Nickerson, R. M. White, K. N. Lee, R. Bachmann, T. H. Geballe and G. W. Hull, Jr. *Phys. Rev. B* **3**, 2030 (1971).

5. S. Tencé, O. Janson, C. Krellner, H. Rosner, U. Schwarz and F. Steglich, Y Grin, *J. Phys.: Condens. Matter* **26**, 395701 (2014).

6. U. Schwarz, S. Tencé, O. Janson, C. Koz, C. Krellner, U. Burkhardt, H. Rosner, F. Steglich and Yuri Grin, *Angew. Chem. Int. Ed.* **52**, 9853 (2013).

7. S. E. Waller, J. E. Mann, E. Hossain, M. Troyer and C. C. Jarrold, *J. Chem. Phys.* **137**, 024302 (2012).

8. J. E. Mann, S. E. Waller and C. C. Jarrold*, J. Phys. Chem. A* **117**, 12116 (2013).

9. H. Xie, X. Li, L. Zhao, Z. Liu, Z. Qin, X. Wu, Z. Tang and X. Xing, *J. Phys. Chem. A* **117**, 1706 (2013).

10. H. K. Gerardi, A. F. DeBlase, C. M. Leavitt, X. Su, K. D. Jordan, A. B. McCoy and M. A. Johnson, *J. Chem. Phys.* **136**, 134318 (2012).

11. J. H. Kim, S. Hak Lee and J. K. Song, *J. Chem. Phys.* **130**, 124321 (2009).

12. J. Schiedt and R. Weinkauf, *J. Chem. Phys.* **110**, 304 (1999).

13. N. Guggemos, P. Slavicek and V. V. Kresin, *Phys. Rev. Lett.* **114**, 043401 (2015).

14. A. Gutberlet, G. Schwaab, Ö. Birer, M. Masia, A. Kaczmarek, H. Forbert, M. Havenith and D. Marx, *Science* **324**, 1545 (2009).

15. X. Zhang, X. Tang, K.H. Bowen, *Chem. Phys. Lett.* **582**, 21(2013).

16. X. Zhang, X. Tang, D. H. Mayo, S. DeCarlo, B. Eichhorn, K. H. Bowen, *Chem. Phys. Lett. ,* **597**, 110 (2014).

17. N. R. Hutzler, H.-I Lu, and J. M. Doyle, Chem. Rev. **112**, 4803 (2012).

Appendix B. The Development of Theoretical Calculation

Capabilities in the Bowen Research Lab

In our lab, a computer cluster, as shown in Figure B.1, has been built by Evan Collins. Currently this cluster has 6 nodes. On each node, there are 8 processors and 1 TB hard drive space. Two computational software, Gaussian09 and Gamess are currently installed. The JHU Chemistry Department has the Gaussian09 license, and Gamess is free for everyone to use. Simple calculations are performed on this system, but complicated systems as well as very high level of theory calculations can be very time consuming.

In this section, I will present how to be a user, but not an administrator, of this system.

Login

We use WinSCP ftp software as the login media. The Host name is *bowen.chm.jhu.edu*. Please ask our group members for username and password. After login, our commanding tool is PuTTY. PuTTY is an SSH and telnet client, developed originally by Simon Tatham for the Windows platform. PuTTY is an open source software that is available with source code and is developed and supported by a group of volunteers. One can download PuTTY freely on the internet. After downloading, one needs to place it in the local Program Files. PuTTY can be activated by clicking the PuTTY button on WinSCP. If you are a MAC user, the Terminal App on MAC can also be used. Two files, for Gamess and Gaussian, respectively, are created for all the users. A Bowen Group Wiki is also built, one can login with the same user name and password as WinSCP.

The address is http://bowenlab.chm.jhu.edu/index.php/Main_Page. Some basic information about our group can be found there.

Software information

Gaussian09 and GaussView 5.0 can be downloaded from our group FTP, whose IP address is 128.220.169.11. Please ask a group member for the username and password. Gaussian09 is needed in your personal computer if you want to read the molecular orbitals with GaussView, even though you don't use it to run a real job. GaussView is the visualization software of Gaussian. One can generate input file (*.com), read the output file (*.log), view molecular orbitals (*.fchk) with GaussView.

Gamess software for different operating systems can be downloaded for free from http://www.msg.ameslab.gov/gamess/. Its corresponding visualization software, MacMolPlt, can be downloaded from http://wiki.wxmacmolplt.googlecode.com/git/MacMolPlt_Manual.html. The operation of MacMolPlt is similar to GaussView.

Basic command lines in PuTTY

After login to PuTTY, one can use the following command lines to perform basic operations.

cd file name: Change directory to a certain file.

qstat: to view all the running jobs.

watch qstat: to view all the running jobs with a refreshing rate of 2 seconds.

tail –f file name.filetype: to view the end of a certain file at the real time. One can read the output file of a certain job with this command.

bash gaussrun Gaussian input file name n: to run a certain job with Gaussian with n processors. With Gaussian, one can only use one node for each job, therefore the maximum n is 8. Please note that ".com" is not needed to specify the Gaussian input file name.

bash gmsrun Gamess input file name m n: to run a certain job with Gamess with m nodes and n processors. Different from Gaussian, one can use several nodes to run Gamess at the same time. ".inp" is not needed to specify the Gamess input file name.

Ctrl + z: to terminate reading and come back to command mode.

qdel job number: to terminate a job when it is running or queued.

formchk scratch file name.chk scratch file name.fchk: the molecular orbital information is stored in .chk file in Gaussian. To convert a .chk file into a GaussView readable .fchk file, one need to perform the above command.

Input examples for Gaussian

Please refer to Gaussian official website for detailed examples. Here I only present our frequently used operations. Please note that the Italic font in parentheses are my explanations.

1. To optimize a structure:

%chk=SF6neutral.chk *(The directory of saving the scratch file)*
%mem=4GB *(The memory given to this job)*
%nprocshared=4 *(The number of processors given to this job)*
opt b3lyp/6-311++g(3df,3pd) geom=connectivity *(opt means optimization, method/basis set)*
                                        (An empty line here)

309

Title *(the tile of this job)*
        (An empty line here)
0 1   *(Charge and multiplicity)*
S   0.30195383   1.26998222   0.00000000   *(Cartesian coordinates)*
F   0.30195383   2.85998222   0.00000000
F   1.89195383   1.26998222   0.00000000
F   0.30195383   1.26998222   -1.59000000
F   0.30195383   -0.32001778   0.00000000
F   -1.28804617   1.26998222   0.00000000
F   0.30195383   1.26998222   1.59000000
                                                    (An empty line here)
 1 2 1.0 3 1.0 4 1.0 5 1.0 6 1.0 7 1.0*(Bond orders between each atom. 1 2 1.0 means there is a
single bond between atom 1 and 2)*
 2
 3
 4
 5
 6
 7
  (A space and an empty line here)

        2. To optimize a structure with CCSD(T). With Gaussian, if one wants to use the very high

level of theory, CCSD(T), to optimize a structure, one has to do it with the Z-matrix coordinates

system and use the opt=z-matrix command line. Z-matrix coordinate system is to only use bond

length, bond angle and dihedral angle to specify a 3-d geometry. Z-matrix coordinates can be

generated by GaussView.

%chk=Cu2H-2neutral.chk
%mem=4GB
%nprocshared=4
opt=z-matrix ccsd(t)/def2tzvpp geom=connectivity *(opt=z-matrix is requied)*

Title

0 2
H   *(This is the Z-matrix coordinate system)*
Cu   1   B1
Cu   1   B2   2   A1

  B1   1.56262655   *(B is the bond length)*
  B2   1.70528709
  A1   101.61589315   *(A is the bond angle)*

310

1
2
3

3. To scan a potential energy surface. Potential energy surface can be scanned along a certain bond length, or a bond angle, or a dihedral angle. To scan a potential energy surface, Z-matrix coordinate system is needed. One can scan the potential energy surface with rigid scan or relaxed scan. Rigid scan means only that coordinate is scanned while the rest of the molecule does not change. Relaxed scan means while scanning a certain coordinate, the rest of the molecule is relaxed to reach the lowest energy geometry.

Rigid scan:
%chk=ph2COAlscan.chk
%mem=4GB
%nprocshared=4
scan ub3lyp/6-31+g(d,p) geom=connectivity *(scan means rigid scan)*

Title Card Required

0 2   *(Z-matrix coordinate system)*

C									
C	1	1.44725195							
C	2	1.41192265	1	122.51187926					
C	2	1.41131601	1	120.25254977	3	-177.03614718	0		
C	3	1.38438999	2	121.14038139	1	-178.41996675	0		
H	3	1.07920938	2	119.63899827	1	-0.99616893	0		
C	4	1.38429353	2	121.33244768	1	178.84658775	0		
H	4	1.08005245	2	119.23177212	1	-2.34905243	0		
C	7	1.39246246	4	120.53417131	2	-0.81087087	0		
H	5	1.08204212	3	119.33235554	2	179.12816147	0		
H	7	1.08207466	4	119.48753526	2	179.08910073	0		
H	9	1.08129513	7	120.45052786	4	-179.75333447	0		
C	1	1.44723033	2	126.29951838	4	158.11893483	0		
C	13	1.41192978	1	122.51239501	2	-24.82501818	0		
C	13	1.41132360	1	120.25253231	2	158.13816440	0		
C	14	1.38438571	13	121.14054629	1	-178.42106631	0		
H	14	1.07920875	13	119.63919504	1	-0.99749891	0		
C	15	1.38429116	13	121.33250531	1	178.84716504	0		
H	15	1.08005056	13	119.23158435	1	-2.34712999	0		
C	18	1.39246361	15	120.53441082	13	-0.81035899	0		

```
H          16   1.08204211   14   119.33225997   13   179.12857259   0
H          18   1.08207450   15   119.48740503   13   179.08973852   0
H          20   1.08129464   18   120.45059850   15   -179.75375197   0
O           1   1.33685900   13   116.85069538   15   -21.86283762   0
Al         24   B1           1   179.98850786   13   144.37434166   0   (The coordinate that is
scanned is specified with a variable, B1 means bond length here.)

B1 3.00 40 -0.05   (B1 is scanned from 3.00 Å, for 40 steps, with a -0.05 Å step width.)

1 2 1.5 13 1.5 24 1.5
2 3 1.5 4 1.5
3 5 2.0 6 1.0
4 7 2.0 8 1.0
5 9 1.5 10 1.0
6
7 9 1.5 11 1.0
8
9 12 1.0
10
11
12
13 14 1.5 15 1.5
14 16 2.0 17 1.0
15 18 2.0 19 1.0
16 20 1.5 21 1.0
17
18 20 1.5 22 1.0
19
20 23 1.0
21
22
23
24 25 1.0
25




Relaxed scan:
%chk=AgCO2scan5-1.chk
%mem=2GB
%nprocshared=2
# opt=ModRedundant rccsd/def2tzvpp geom=connectivity  (opt=ModRedundant is needed)

title

-1 1
 Ag                                              (Z-matrix coordinate system)
```

C   1   B1   *(B1, the bond between Ag and C, is the coordinate scanned)*
O   2   1.20253 1 107.8832
O   2   1.20253 1 107.8832 3 180.00

B1 1.7   *(B1 starts from 1.7 Å)*

1
2 3 2.0 4 2.0
3
4

 1 2 S 40 0.1   *(The bond between 1 and 2, which is B1, is scanned with the S method, for 40
steps, with a 0.1 Å step width. Method S means relaxed scan. Other methods can be found here:
http://www.gaussian.com/g_tech/g_ur/k_opt.htm)*

4. To use effective core potential for transition metals. Core electrons of transition metals

have strong relativistic effect. Models called effective core potential (ECP) have been built for

these transition metals, and relativistic effect is included in the ECP. Los Alamos National

Laboratory 2 Double Zeta (LANL2DZ) and Stuttgart/Dresden (SDD) are both very good ECPs.

%chk=HMoOsddneutraloptiso2.chk
%mem=2GB
%nproc=4
opt b3lyp/Gen Pseudo=Read   *(Gen Pseudo=Read is the language to use ECP)*

HMoOsddneutraloptiso2

0 2
 Mo   0.01785300 -0.34486200   0.00000000
 O   0.01785300   1.57044200   0.00000000
 H   -0.89264400   1.92065400   0.00000000

 1 2 1.0
 2 3 1.0
 3

O H 0   *(O and H use 6-311++g(3df,3pd) basis set)*
6-311++g(3df,3pd)
****
Mo 0   *(Mo uses SDD ECP)*
SDD
****

Mo 0
SDD

5. To calculate charge distribution. Mulliken charge distribution is the default method built in Gaussian, however, this method is very sensitive to method and basis set, and sometimes it might give highly wrong results. Natural population analysis (NPA), on the other hand, is very trustworthy. To perform NPA calculation, one just needs to add pop=npa in the method line.

6. To read the atomic orbital composition of a molecular orbital. MO is the linear combination of AOs. It is important to know that how a certain MO is obtained, especially when special chemical bonding is formed, such as those in Chapter 1 in this thesis. Sometimes by simply looking at the visualized MOs, one still can hardly tell how a MO is formed. Therefore, calculations are needed to reveal the compositions of a certain MO.

%chk=LiOH2ccsdnbo.chk
%mem=4GB
%nprocshared=4
ccsd(t)/6-311++g(3df,3pd) geom=connectivity pop=nboread (*Nbo is short for natural bond orbital)*

Title

-1 1
H   0.76368700 -0.77128700   0.34711900
H   0.77324600   0.76570000   0.34987700
Li   -1.52755300   0.00090500   0.04721100
O   0.38071600   0.00035900 -0.10482900

1 4 1.0
2 4 1.0
3 4 1.0
4

$NBO NAOMO $END   (*NAOMO means output AO to MO transformations*)

After the calculation, one needs to open the *.log file and find the "MOs in the NAO basis" section. For example, in the data below, the column marked by 1 means the first MO has

314

the composition of the below AOs. At column 1, row 76, the *s* orbital of O atom has a number of

0.9944, which means $(0.9944)^2$ of this MO is from the *s* orbital of O.

NAO	1	2	3	4	5	6	7	8
1. H 1 (S)	0.0257	0.0149	0.2764	0.3421	-0.1817	0.0174	0.1462	-0.1136
2. H 1 (S)	-0.0055	-0.0032	-0.0049	0.0158	-0.0245	0.0036	-0.0571	0.2192
3. H 1 (S)	0.0001	0.0002	-0.0129	0.0049	-0.0057	0.0052	0.0052	0.0410
4. H 1 (S)	-0.0026	-0.0014	-0.0003	0.0002	-0.0005	-0.0018	0.0005	-0.0457
5. H 1 (px)	0.0000	0.0000	-0.0062	-0.0100	0.0031	0.0000	-0.0065	0.0193
6. H 1 (px)	0.0000	-0.0001	0.0013	0.0051	0.0084	0.0139	-0.0021	-0.0013
7. H 1 (px)	0.0000	0.0001	0.0009	0.0007	-0.0011	-0.0002	-0.0024	0.0089
8. H 1 (py)	-0.0001	0.0000	0.0138	0.0184	-0.0075	-0.0032	0.0162	-0.0094
9. H 1 (py)	0.0001	0.0000	-0.0018	-0.0026	0.0082	-0.0016	0.0105	0.0278
10. H 1 (py)	-0.0001	0.0000	-0.0022	-0.0003	0.0014	-0.0012	0.0028	-0.0186
11. H 1 (pz)	0.0000	0.0000	0.0071	0.0120	-0.0064	-0.0013	0.0088	-0.0139
12. H 1 (pz)	0.0000	0.0000	-0.0029	-0.0048	-0.0097	0.0174	0.0018	0.0038
13. H 1 (pz)	0.0000	0.0000	-0.0004	-0.0016	0.0022	-0.0023	0.0034	-0.0080
14. H 1 (d1)	0.0000	0.0001	-0.0009	-0.0004	-0.0012	-0.0020	-0.0043	0.0091
15. H 1 (d2)	0.0000	0.0000	-0.0026	0.0027	0.0022	0.0010	-0.0032	0.0021
16. H 1 (d3)	0.0000	0.0001	0.0019	-0.0001	0.0030	-0.0035	0.0062	-0.0107
17. H 1 (d4)	0.0000	0.0000	-0.0016	0.0000	0.0037	0.0004	-0.0027	0.0018
18. H 1 (d5)	0.0000	0.0000	-0.0005	-0.0018	0.0021	-0.0004	-0.0007	0.0007
19. H 2 (S)	0.0257	0.0148	0.2764	-0.3428	-0.1814	0.0177	0.1448	-0.1133
20. H 2 (S)	-0.0054	-0.0032	-0.0050	-0.0155	-0.0242	0.0036	-0.0565	0.2189
21. H 2 (S)	0.0001	0.0002	-0.0128	-0.0048	-0.0057	0.0052	0.0052	0.0407
22. H 2 (S)	-0.0026	-0.0014	-0.0003	-0.0002	-0.0004	-0.0018	0.0005	-0.0464
23. H 2 (px)	0.0000	0.0000	-0.0064	0.0103	0.0031	0.0000	-0.0067	0.0195
24. H 2 (px)	0.0000	-0.0001	0.0013	-0.0051	0.0083	0.0139	-0.0023	-0.0015
25. H 2 (px)	0.0000	0.0001	0.0009	-0.0007	-0.0011	-0.0001	-0.0024	0.0091
26. H 2 (py)	0.0001	0.0000	-0.0137	0.0183	0.0074	0.0031	-0.0160	0.0094
27. H 2 (py)	-0.0001	0.0000	0.0017	-0.0025	-0.0083	0.0015	-0.0105	-0.0276
28. H 2 (py)	0.0001	0.0000	0.0022	-0.0002	-0.0014	0.0012	-0.0028	0.0184
29. H 2 (pz)	0.0000	0.0000	0.0072	-0.0121	-0.0064	-0.0013	0.0088	-0.0141
30. H 2 (pz)	0.0000	0.0000	-0.0029	0.0047	-0.0097	0.0174	0.0018	0.0038
31. H 2 (pz)	0.0000	0.0000	-0.0004	0.0016	0.0022	-0.0023	0.0034	-0.0081
32. H 2 (d1)	0.0000	-0.0001	0.0009	-0.0004	0.0011	0.0020	0.0044	-0.0091
33. H 2 (d2)	0.0000	0.0000	-0.0026	-0.0027	0.0021	0.0010	-0.0033	0.0023
34. H 2 (d3)	0.0000	-0.0001	-0.0019	-0.0001	-0.0030	0.0035	-0.0061	0.0107
35. H 2 (d4)	0.0000	0.0000	-0.0016	0.0001	0.0037	0.0005	-0.0025	0.0016
36. H 2 (d5)	0.0000	0.0000	-0.0005	0.0018	0.0021	-0.0004	-0.0007	0.0007
37. Li 3 (S)	-0.0006	0.9960	-0.0245	-0.0003	-0.0336	-0.0328	-0.0716	-0.0035
38. Li 3 (S)	0.0057	0.0722	0.0564	-0.0001	0.0555	0.0174	0.9505	0.1183
39. Li 3 (S)	0.0000	0.0007	0.0030	0.0000	0.0116	0.0102	-0.0011	0.0902
40. Li 3 (S)	0.0000	0.0000	0.0014	0.0000	0.0012	-0.0018	-0.0001	0.0766
41. Li 3 (S)	-0.0001	0.0000	-0.0013	0.0000	0.0008	-0.0005	0.0000	-0.0620
42. Li 3 (px)	-0.0043	0.0025	-0.0256	-0.0001	-0.0218	-0.0235	0.0976	-0.1114
43. Li 3 (px)	-0.0001	0.0000	-0.0013	0.0000	-0.0084	0.0009	-0.0296	0.7238
44. Li 3 (px)	0.0002	0.0012	0.0019	0.0000	-0.0135	-0.0074	-0.0032	0.1927

```
45. Li 3 (px)   0.0014 -0.0004  0.0055  0.0000 -0.0022  0.0052  0.0022 -0.4413
46. Li 3 (py)   0.0000  0.0000  0.0000 -0.0079 -0.0001  0.0000  0.0006  0.0003
47. Li 3 (py)   0.0000  0.0000  0.0000 -0.0068  0.0000  0.0000  0.0004  0.0005
48. Li 3 (py)   0.0000  0.0000  0.0000  0.0032  0.0000  0.0000  0.0000 -0.0002
49. Li 3 (py)   0.0000  0.0000  0.0000  0.0008  0.0000  0.0000  0.0000  0.0002
50. Li 3 (pz)  -0.0005  0.0000 -0.0099  0.0001 -0.0050  0.0221  0.0441  0.0082
51. Li 3 (pz)   0.0000  0.0000 -0.0008  0.0000 -0.0016  0.0053  0.0570 -0.1823
52. Li 3 (pz)   0.0000 -0.0001 -0.0001  0.0000 -0.0030  0.0021 -0.0034 -0.0389
53. Li 3 (pz)   0.0002  0.0000  0.0025  0.0000 -0.0024 -0.0008  0.0010  0.0834
54. Li 3 (d1)   0.0000  0.0000  0.0000 -0.0074  0.0001  0.0000 -0.0002 -0.0001
55. Li 3 (d1)   0.0000  0.0000  0.0000  0.0003  0.0000  0.0001  0.0001  0.0000
56. Li 3 (d1)   0.0000  0.0000  0.0000 -0.0007  0.0000  0.0000  0.0000  0.0001
57. Li 3 (d2)   0.0000  0.0000  0.0009  0.0000  0.0033 -0.0099 -0.0173  0.0039
58. Li 3 (d2)   0.0000  0.0001 -0.0023  0.0001  0.0080  0.0031 -0.0062 -0.0154
59. Li 3 (d2)   0.0000 -0.0001  0.0004  0.0000  0.0008 -0.0010  0.0005  0.0031
60. Li 3 (d3)   0.0000  0.0000  0.0000  0.0045  0.0000  0.0000  0.0000  0.0001
61. Li 3 (d3)   0.0000  0.0000  0.0000 -0.0042  0.0000  0.0000  0.0000  0.0000
62. Li 3 (d3)   0.0000  0.0000  0.0000  0.0001  0.0000  0.0000  0.0000  0.0000
63. Li 3 (d4)   0.0000 -0.0003 -0.0022  0.0000 -0.0048  0.0017 -0.0116  0.0286
64. Li 3 (d4)   0.0000  0.0002  0.0059  0.0000  0.0040  0.0005  0.0045  0.0102
65. Li 3 (d4)   0.0000 -0.0003 -0.0008  0.0000  0.0022  0.0007 -0.0005 -0.0031
66. Li 3 (d5)   0.0000  0.0001  0.0010  0.0000  0.0031 -0.0002 -0.0094 -0.0211
67. Li 3 (d5)   0.0000 -0.0001 -0.0032  0.0000 -0.0015  0.0004 -0.0012 -0.0083
68. Li 3 (d5)   0.0000  0.0001  0.0006  0.0000 -0.0010 -0.0007  0.0005  0.0028
69. Li 3 (f1)   0.0000  0.0000  0.0004  0.0000 -0.0031 -0.0007  0.0015  0.0017
70. Li 3 (f2)   0.0000  0.0000 -0.0013  0.0001  0.0016 -0.0004  0.0040  0.0033
71. Li 3 (f3)   0.0000  0.0000  0.0000 -0.0011  0.0000  0.0000  0.0000 -0.0001
72. Li 3 (f4)   0.0000  0.0000 -0.0015  0.0000  0.0051 -0.0017 -0.0045 -0.0057
73. Li 3 (f5)   0.0000  0.0000  0.0000 -0.0086  0.0001  0.0000  0.0000 -0.0001
74. Li 3 (f6)   0.0000  0.0001  0.0035  0.0001  0.0006 -0.0017  0.0022  0.0004
75. Li 3 (f7)   0.0000  0.0000  0.0000 -0.0015  0.0000  0.0000  0.0000  0.0001
76. O 4 (S)     0.9944 -0.0023 -0.1041  0.0000 -0.0178  0.0043  0.0009  0.0018
77. O 4 (S)     0.0990  0.0167  0.9008  0.0000  0.2405 -0.0516 -0.1422  0.0589
78. O 4 (S)     0.0004 -0.0003  0.0041  0.0000 -0.0004 -0.0061  0.0279 -0.0681
79. O 4 (S)     0.0000 -0.0001  0.0009  0.0000 -0.0043 -0.0022 -0.0007  0.0085
80. O 4 (S)     0.0000  0.0000 -0.0001  0.0000  0.0002 -0.0005 -0.0001  0.0007
81. O 4 (px)    0.0018  0.0454 -0.0750  0.0059  0.7063  0.6622  0.0064 -0.0340
82. O 4 (px)    0.0002  0.0008  0.0047 -0.0001  0.0050  0.0076 -0.0059  0.0022
83. O 4 (px)   -0.0003 -0.0017 -0.0068  0.0001 -0.0136 -0.0058  0.0008  0.0664
84. O 4 (px)   -0.0005 -0.0007  0.0027  0.0000 -0.0003  0.0008 -0.0015 -0.0012
85. O 4 (py)    0.0000  0.0000  0.0009  0.8724 -0.0059 -0.0030 -0.0004  0.0003
86. O 4 (py)    0.0000  0.0000  0.0000 -0.0167  0.0000  0.0000  0.0001  0.0006
87. O 4 (py)    0.0000  0.0000  0.0000  0.0192  0.0000  0.0000  0.0001 -0.0004
88. O 4 (py)    0.0000  0.0000  0.0000  0.0005  0.0000  0.0000  0.0000 -0.0001
89. O 4 (pz)   -0.0020  0.0023  0.1147 -0.0016 -0.6066  0.7438 -0.0458  0.0345
90. O 4 (pz)   -0.0003 -0.0001 -0.0026  0.0000 -0.0099  0.0034  0.0423  0.0391
91. O 4 (pz)    0.0004 -0.0001 -0.0041 -0.0001  0.0003 -0.0034  0.0112 -0.0602
92. O 4 (pz)    0.0007 -0.0001 -0.0043  0.0000  0.0003  0.0002 -0.0006 -0.0053
93. O 4 (d1)    0.0000  0.0000  0.0001 -0.0178  0.0001  0.0001  0.0000  0.0003
94. O 4 (d1)    0.0000  0.0000  0.0000 -0.0101  0.0000  0.0000 -0.0001 -0.0002
95. O 4 (d1)    0.0000  0.0000  0.0000 -0.0004  0.0000  0.0000  0.0000  0.0000
```

96. O 4 (d2)   0.0000 0.0002 -0.0129 0.0002 0.0321 0.0110 -0.0014 -0.0216
97. O 4 (d2)   0.0000 0.0000 -0.0008 0.0001 -0.0037 -0.0050 0.0034 0.0176
98. O 4 (d2)   0.0000 0.0000 0.0006 0.0000 0.0000 -0.0001 -0.0004 -0.0023
99. O 4 (d3)   0.0000 0.0000 0.0001 0.0320 -0.0003 0.0001 -0.0001 0.0001
100. O 4 (d3)   0.0000 0.0000 0.0000 0.0070 0.0000 0.0000 0.0000 -0.0001
101. O 4 (d3)   0.0000 0.0000 0.0000 0.0004 0.0000 0.0000 0.0000 0.0000
102. O 4 (d4)   0.0000 0.0006 -0.0081 -0.0003 0.0104 -0.0045 -0.0049 -0.0302
103. O 4 (d4)   0.0000 0.0001 -0.0031 -0.0001 -0.0047 -0.0027 0.0057 0.0269
104. O 4 (d4)   0.0000 -0.0001 0.0005 0.0000 0.0008 0.0002 -0.0005 -0.0037
105. O 4 (d5)   0.0000 -0.0004 -0.0076 -0.0001 -0.0143 0.0250 0.0005 -0.0086
106. O 4 (d5)   0.0000 -0.0001 0.0010 0.0000 0.0068 -0.0037 0.0005 0.0070
107. O 4 (d5)   0.0000 0.0000 0.0002 0.0000 0.0003 -0.0004 -0.0003 -0.0010
108. O 4 (f1) -0.0001 -0.0001 -0.0037 0.0000 0.0034 -0.0012 -0.0008 0.0073
109. O 4 (f2)   0.0000 -0.0002 -0.0011 0.0000 0.0011 -0.0057 0.0004 0.0005
110. O 4 (f3)   0.0000 0.0000 0.0000 -0.0040 0.0000 0.0000 0.0000 0.0000
111. O 4 (f4) -0.0001 0.0000 -0.0028 0.0000 -0.0016 -0.0060 -0.0009 0.0069
112. O 4 (f5)   0.0000 0.0000 0.0000 -0.0014 0.0000 0.0001 0.0000 -0.0001
113. O 4 (f6)   0.0001 0.0002 0.0045 -0.0001 -0.0017 -0.0031 0.0007 -0.0093
114. O 4 (f7)   0.0000 0.0000 -0.0001 -0.0037 0.0001 0.0001 0.0000 0.0002

7. To perform Franck-Condon analysis with Gaussian. FC analysis is useful to simulate experimental spectra, to obtain hot band and vibrational progression information, and to calculate the temperature of a certain system. In order to perform FC analysis, one needs to have the *.chk files of both the anion and the neutral with frequency calculations in them. To perform frequency calculation, just add "freq" in the command line. Then, perform the following calculation:

%chk=AuOHa.chk *(the .chk file of the anion)*
#P Geom=AllCheck Freq=(ReadFC,FC,SaveNM) NoSymm
     (An empty line here)
AuOHn.chk   *(the .chk file of the neutral)*
   Figure B.2 presents the simulated spectrum of AuOH⁻.

8. To perform excited states calculations. Sometimes our photoelectron spectra have the information of the excited states of the neutral. To calculate these transitions, one needs to use the structure of the anion to obtain vertical transitions, and then calculate the excited states. Different multiplicities need to be included. TDDFT, EOM-CCSD are all very good methods.

9. To calculate a transition state. A transition state can be generated between two structures.

```
%chk=CoCO2ts.chk
# opt=QST2 b3lyp/def2tzvpp geom=connectivity (opt=QST2 is the TS calculation method)

Title

-1 1            (The coordinates of the first structure)
C            0.00000000    0.87904000    0.00000000
O            1.17737900    0.32596400    0.00000000
O           -0.39785600    2.02369200    0.00000000
Co          -0.23097000   -0.89153700    0.00000000

1 2 1.5 3 2.0 4 1.0
2 4 1.0
3
4

Title

-1 1            (The coordinates of the second structure)
C            0.00235800   -1.34818200    0.00000000
O           -0.00390100    2.10128800    0.00000000
O            0.00213300   -2.52021800    0.00000000
Co           0.00000000    0.42372300    0.00000000

1 3 2.0 4 1.0
2 4 1.0
3
4
```

Commonly used theoretical methods and basis sets

Density functional theory is widely used. It has many functionals, and they all have different advantages. B3PW91 and B3LYP are good for general use. CAM-B3LYP, M06-2X, WB97XD, LC-WPBE are good in describing long distance interactions, such as hydrogen bond. PBEPBE or PBE0 is good for transition metals.

Hartree-Fock method is a low level of theory, but sometimes using it will give very good results, such as description of the pyridine-CO_2 anionic complex.

CCSD or CCSD(T) can be very time consuming, but they are more reliable than DFT.

Complete Active Space Self-Consistent Field (CASSCF) can be used for multi-reference systems, such as heavy metals.

I personally don't like MP2/4, but they are better than DFT sometimes.

For the information of basis sets, please refer to https://bse.pnl.gov/bse/portal.

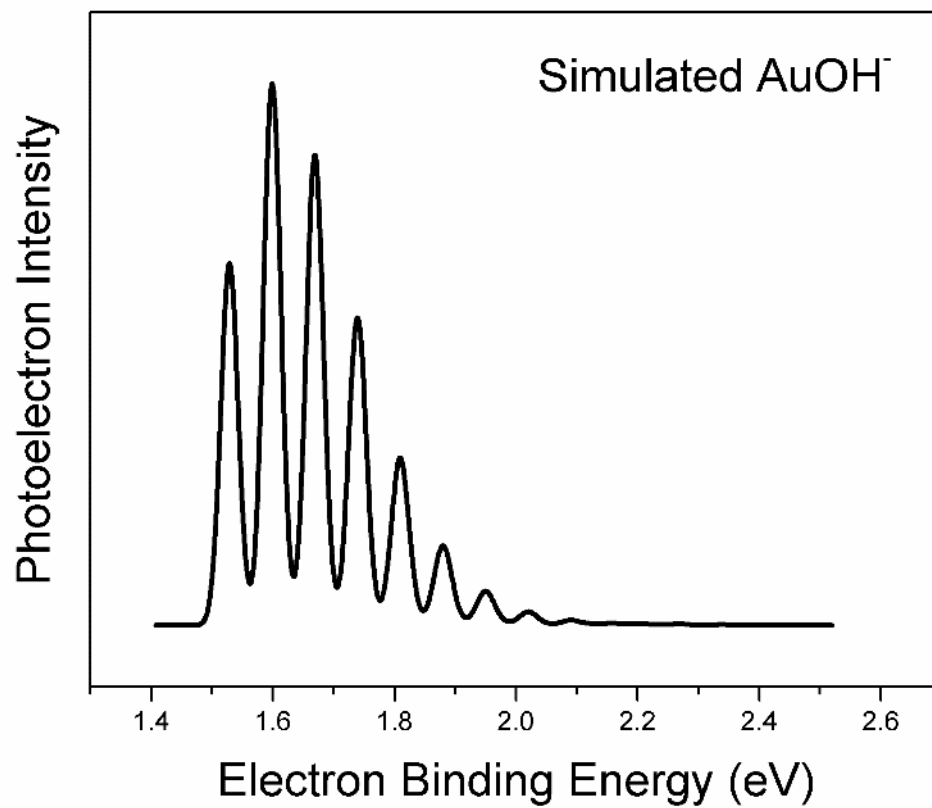Figure B.1. The computer cluster in Bowen Research Lab

Figure B.2. Simulated PES of AuOH⁻.

Appendix C. Cryopump Regeneration Log

Regeneration of the cryopump on PIPES is a routine maintenance, scheduled every six months even though the manual suggests every three months. After absorbing too much gas in the pump, the pump temperature might begin to rise, and Chamber 4 pressure might be higher than 3×10^{-8} torr. Should one observes the above phenomenon, a regeneration needs to be performed.

Day 1

On the first day of regeneration, begin with pumping CH1 and CH2 to a very good pressure. Typically 1×10^{-6} torr should be good enough to start the regeneration. During the whole cryopump warming up time (usually 6 hours), all the gas released from the cryopump will be pumped by, and only by the diffusion pumps and turbo pumps attached to CH1 and CH2.

When CH2 pressure reaches 1×10^{-6} torr, open the VAT valve between CH2 and CH3, and then turn off the ion pump on CH3 and the cryopump on CH4 at the same time. From this moment, several waves of gases will be released from the cryopump during the warming up. Monitor the pressure on CH2 all the time. Figure C.1 shows the pressure change on CH2 when the cryopump is warming up. One can observe that as soon as turning off the cryopump, a sharp wave of gas is released (A), which is He. The second wave (B), occurring between 10 to 60 minutes, is a wave of H_2. The third wave (C), which takes the longest time and reaches the highest pressure, is N_2. The fourth wave (D), which is also very wide, is speculated to be H_2O vapor. After 6-7 hours, the pressure of CH2 will go back to 1×10^{-6} torr.

Please note that the pattern in Figure C.1 is highly reproducible at every regeneration. Even though the highest pressure each wave reaches might be different, the pattern and the time taken have been repeatedly recorded on PIPES.

At the end of day 1, turn off the diffusion pumps on CH2, but leave the turbo pumps on, and leave the green VAT valve open. During the night, the whole system is only pumped by turbo pumps.

Day 2

On the second day, the first thing is still turning the diffusion pumps on CH2 back on. Monitor the pressure on CH2. Figure C.2 presents the pressure on CH2 on day 2. When pressure of CH2 reaches 5×10^{-6} torr, one can attempt to turn on the ion pump on CH3. However, the ion pump might not be turned on due to its high current protection. One can try several times to turn it on. The sudden pressure drop marked by A in Figure C.2 is due to the turning on of the ion pump.

Figure C.3 shows the pressure change on CH4. Point 1 is the starting point, and from point 1 to the end of this figure, the total time is about 16.4 hours. Between point 1 and point 2, Ch3 and Ch4 are only pumped by CH1 and CH2, and one can observe a very slow pressure drop from 2×10^{-5} to about 8×10^{-6}. The several spikes are due to the attempts of turning on the ion pump, because when turning on the ion pump, there is always gas release. However, due to the self-protection of the ion pump, if the current is too high, it will shut off by itself.

At point 2, after successfully turning on the ion pump, one can observe a sudden pressure rise due to the gas release from the pump, instantly after which the pressure quickly drops to 10^{-6} region. Shortly after turning on the ion pump, turn on the cryopump. Please note that at the moment

cryopump is turned on, it is not working yet, because it needs some time to cool down and begin to absorb gas. Between point 2 and point 3, Ch4 pressure drops from 8×10^{-6} to 4.5×10^{-7}, which is due to the working of both ion pump and cryopump. The pumping speed from point 2 to point 3 is getting lower and lower. At point 3, there is a sudden boost of pumping speed, which is because, I reckon, the temperature of the CP is lower than 77 K, and it begins to absorb nitrogen, which is the main gas from the air. Therefore, from point 3 to point 4, the pressure quickly drops from 4.5 $\times 10^{-7}$ to 4.8×10^{-8}. At point 4, degas the system for 5 minutes, and this makes the pressure drop to 3×10^{-8}. At point 5, which is the second day already, degas the system for another 5 minutes, and the pressure drops to 2.5×10^{-8}. In the next few months, the pressure can gradually drop to around 1×10^{-8}, or it just stays around 2~3 $\times 10^{-8}$. Over history, the lowest pressure that I have observed is 8.1×10^{-9} on 02/13/2012.

Figure C.4 shows a typical pressure change when a degassing is performed. Point 1 is the start of the degassing, point 3 is the end.
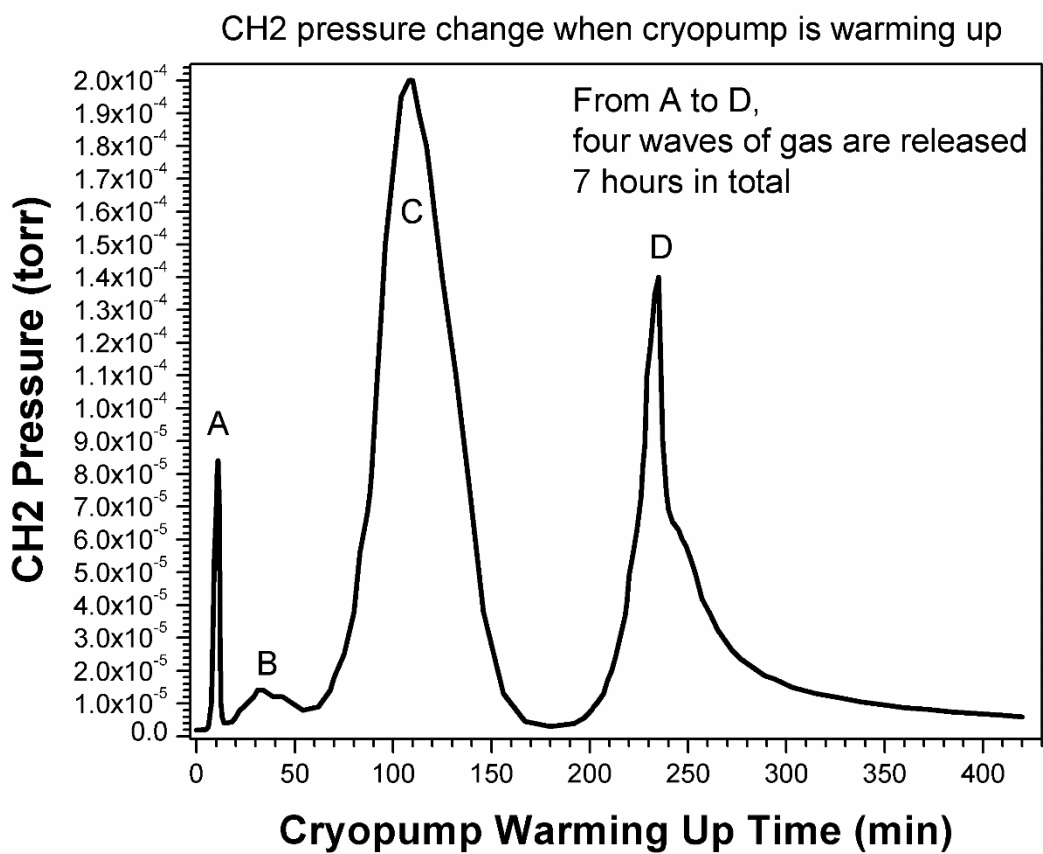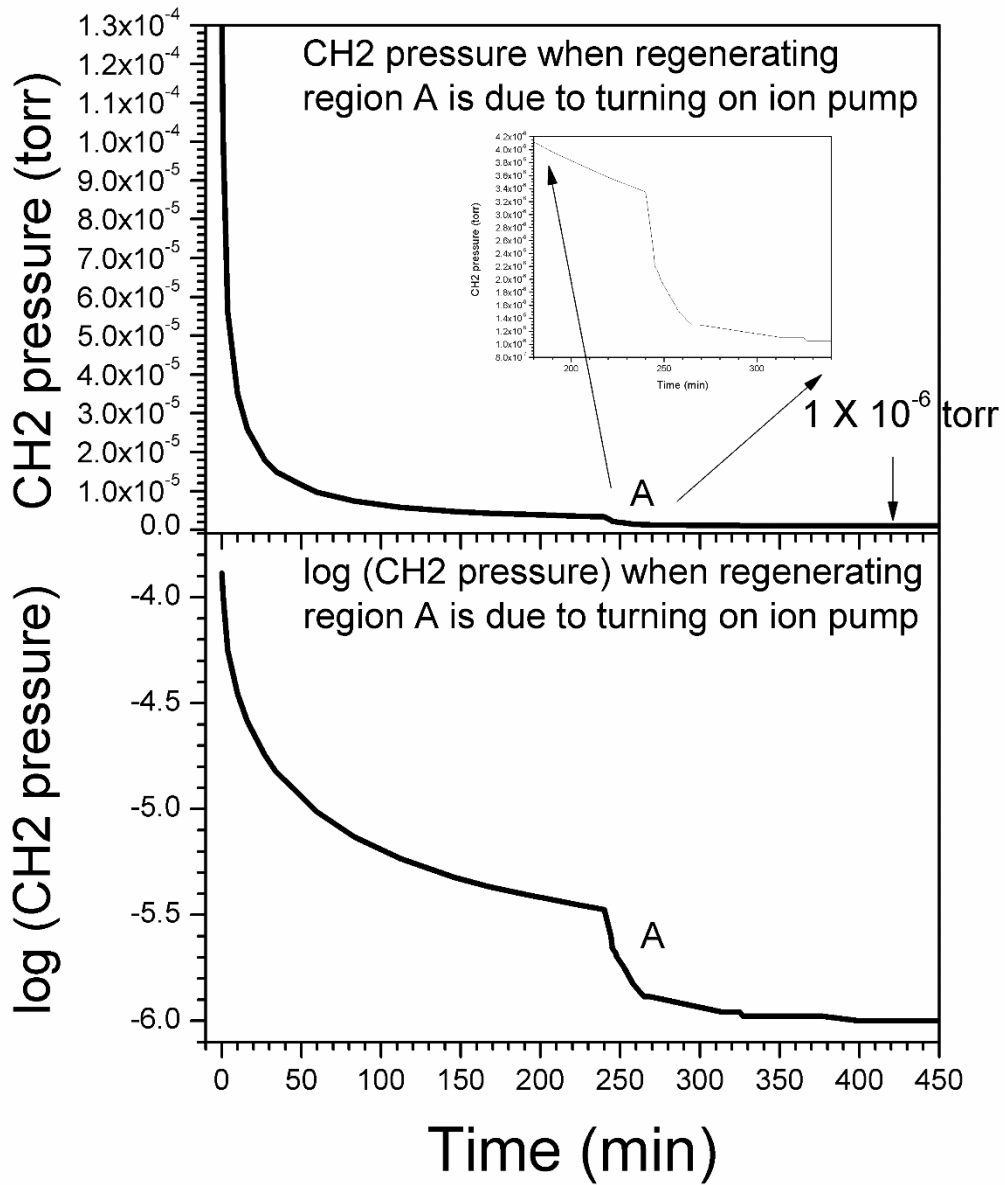
Figure C.1. CH2 pressure on day 1.

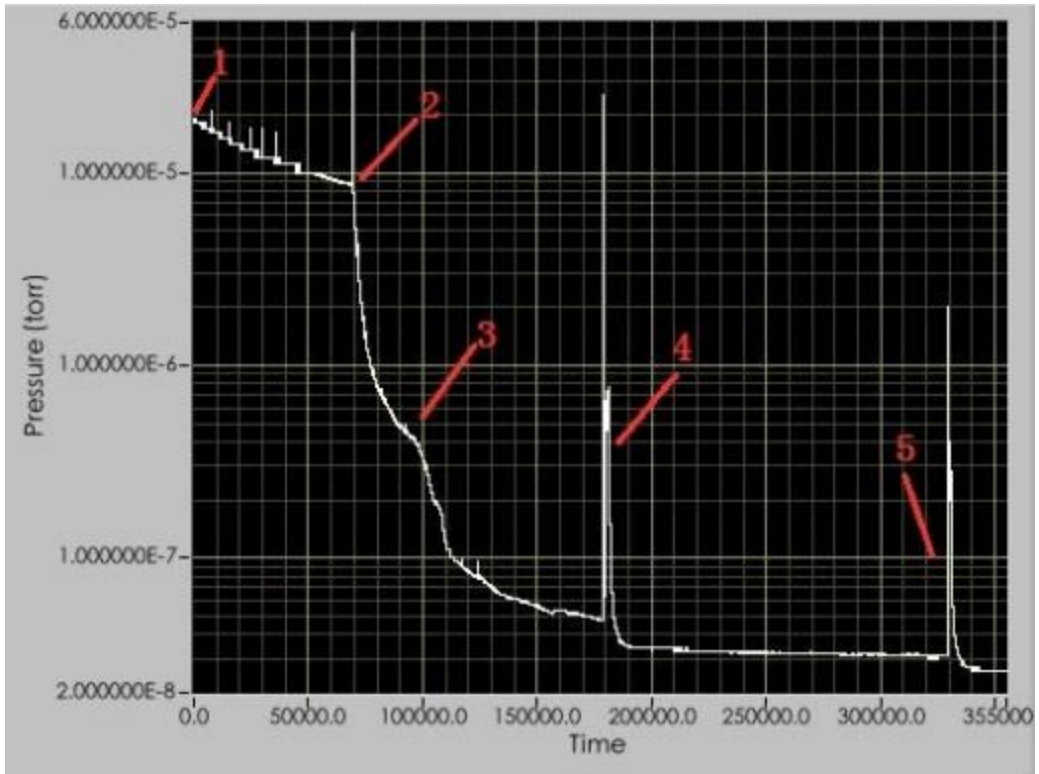Figure C.2. CH2 pressure on day 2.
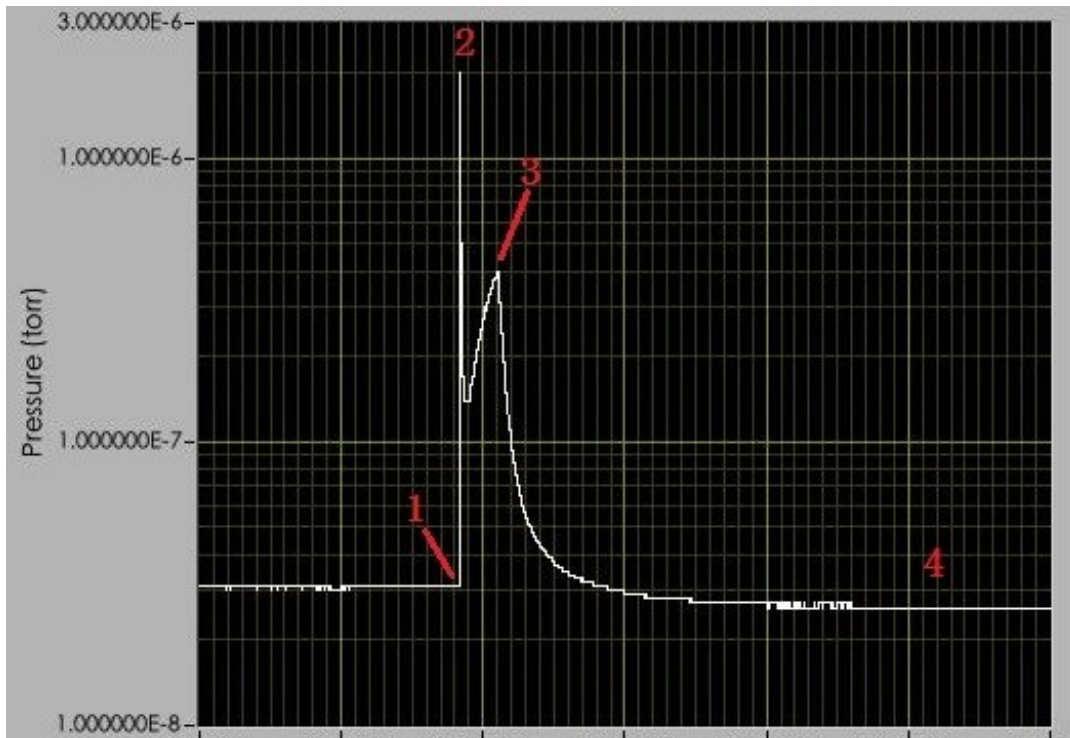
Figure C.3. CH4 pressure on day 2.

Figure C.4. A typical pressure change during degassing.

Curriculum Vitae

Zhang, Xinxing (张新星) Johns Hopkins University, Post-doc

Address: 3400 N. Charles Street, Johns Hopkins University, Baltimore, MD, 21218, USA

Email: xzhang54@jhu.edu, idea.then.diligence@gmail.com

Education and work

2015 ~ now   Johns Hopkins University, post-doc

2009 ~ 2015   Johns Hopkins University, PhD, GPA: 3.93/4.00

2005 ~ 2009   Fudan University, Shanghai, China. Bachelor of Science. GPA: 3.70/4.00

Honors

2015   Best poster award in China's 14th National Conference on Chemical Dynamics

2014   Chinese government award for outstanding self-financed students abroad

2013   Johns Hopkins University Owens Fellowship

2010   Johns Hopkins University Arthur D. Chambers scholarship

2009   Fudan University excellent BS thesis

2008   Fudan University People's scholarship first prize (top 5%)

2007   Fudan University scholarship first prize (DOW's award, top 2%)

2006   Fudan University scholarship first prize (DOW's award, top 2%)

2006   "Excellent Student" of Fudan Chemistry Department's 80th anniversary

2006   "Excellent Student" of Fudan University

Invited Talk

01/07/2013 State Key Lab. of Molecular Reaction Dynamics, Chinese Academy of Sciences, Beijing.

03/24/2014 Institute of Laser Chemistry, Department of Chemistry, Fudan University, Shanghai.

01/05/2015 State Key Lab. of Molecular Reaction Dynamics, Chinese Academy of Sciences, Beijing.

08/26/2015 Institute of Chemistry, Chinese Academy of Sciences, Beijing.

08/28/2015 State Key Lab. of Molecular Reaction Dynamics, Dalian Institute of Chemical Physics, Dalian.

Publications

26. "Carbon Dioxide is Tightly Bound in the [Co(Pyridine)(CO$_2$)]$^-$ Anionic Complex", J. Graham, A. Buytendyk, **X. Zhang,** S. Kim, and K. Bowen. *J. Chem. Phys.* submitted (2015).

25. "On the Importance of Time Scale and Local Environment in Electron-Driven Proton Transfer. The Anion of Acetoacetic Acid", Z. Keolopile, M. Gutowski, A. Buonaugurio, E. Collins, **X. Zhang,** J. Erb, T. Lectka, K. Bowen, and M. Allan, *J. Am. Chem. Soc.* Submitted (2015).

24. "Anion Photoelectron Spectroscopy and CASSCF/CASPT2/RASSI Study of Lan- (n=1, 3-7)", A. S. Ivanov, **X. Zhang, (co-first author)** H. Wang, A. I. Boldyrev, G. Gantefoer, K. H. Bowen and I. Černušák, *J. Phys. Chem. A* In press (2015).

23. "Photoelectron Spectroscopic and Theoretical Study of the [HPd(η^2-H$_2$)]$^-$ Cluster Anion", **X. Zhang,** P. J. Robinson, A. Alexandrova and K. H. Bowen, *J. Chem. Phys.* **143**, 094307 (2015).

22. "Photoelectron Spectroscopic and Computational Study of (M-CO$_2$)$^-$ Anions, M = Cu, Ag, Au", **X. Zhang,** E. Lim, S. K. Kim and K. H. Bowen, *J. Chem. Phys.* In press (2015).

21. "Aluminum chain in Li$_2$Al$_3$H$_8^-$ as suggested by photoelectron spectroscopy and ab initio calculations ", I. A. Popov, **X. Zhang**, **(co-first author)** B. W. Eichhorn, A. I. Boldyrev and K. H. Bowen, *PCCP*. DOI: 10.1039/C5CP04148A (2015).

20. "Negative ion properties of trans-2,2′,6,6′-tetrafluoroazobenzene: Experiment and Theory", M. Rezaee, Y. Wang , **X. Zhang,** G. Liu , K. Bowen , A. Bayer , M. D. Best , and R. N. Compton, *J. Chem. Phys.* **143**, 114303 (2015).

19. "The Onset of Electron-Induced Proton-Transfer in Hydrated Azabenzene Cluster Anions", Y. Wang, **X. Zhang,** S. Lyapustina, M. M. Nilles, S. Xu, J. D.Graham, K. H. Bowen, J. T. Kelly, G. S. Tschumper and N. I. Hammer, *PCCP*, DOI: 10.1039/C5CP02746B (2015).

18. "Photodetachment Velocity Map Imaging of the 1 A′← 2 A′ Transition in the AuOH Anion", B. Visser, M. Addicoat, J. R. Gascooke, **X. Zhang**, K. Bowen, W. Lawrance, and G. Metha, *Chem. Phys. Lett.* **625,** 164 (2015)

17. "Ab initio and Anion Photoelectron Study of Au$_n$Rh$_m$ (n=1−7,m=1−2) clusters", F. Buendia, M. Beltran, **X. Zhang**, G. Liu, A. Buytendyk, K. Bowen. *PCCP*. DOI: 10.1039/C5CP00115C (2015).

16. "The Photoelectron Spectrum of the Benzaldehyde Anion", A. Buonaugurio, **X. Zhang**, S. T. Stokes, Y. Wang, G. B. Ellison, and K. H. Bowen, *Int. J. of Mass Spectrom.* **377,** 278 (2015).

15. "PtZnH$_5^-$, A σ-Aromatic Cluster", **X. Zhang**, G. Liu, G. Gantefoer, K. H. Bowen, and A. N. Alexandrova, *J. Phys. Chem. Lett.* **5**, 1596–1601 (2014). This work was reported by *Chemistry World* from Royal Society of Chemistry and Bang! Science.

14. "The PtAl- and PtAl2- Anions: Theoretical and Photoelectron Spectroscopic Characterization ", **X. Zhang**, G. Gantefoer, K.H. Bowen, and A. Alexandrova , *J. Chem. Phys.* **140, 1**64316(2014)

13. "Photoelectron Spectroscopic Study of the Diphenylphosphide Anion and Its Oxide", **X. Zhang**, X. Tang, D. H. Mayo, S. DeCarlo, B. Eichhorn, and K. Bowen, *Chem. Phys. Lett. ,* **597**, 110 (2014)

12. "Photoelectron Spectroscopy of Boron Aluminum Hydride Cluster Anions ", H. Wang, **X. Zhang,** Y. Ko, G. F. Gantefor, K. H. Bowen, X. Li, K. Boggavarapu, and A. Kandalam , *J. Chem. Phys.* **140**, 164317 (2014)

11. "Aluminum Zintl Anion Moieties within Sodium Aluminum Clusters", H. Wang, **X. Zhang**, J. Ko, A. Grubisic, X. Li, G. Ganteför, H. Schnöckel, B. Eichhorn, M. Lee, P. Jena, A. Kandalam, B. Kiran, and K. H. Bowen, *J. Chem. Phys.* **140,** 054301 (2014)

10. "The Viability of Aluminum Zintl Anion Moieties within Magnesium-Aluminum Clusters", H. Wang, Y. J. Ko, **X. Zhang**, G. Gantefoer, H. Schnoeckel, B. W. Eichhorn, P. Jena, B. Kiran, A. K. Kandalam, and K. H. Bowen, Jr., *J. Chem. Phys.* **140**, 124309 (2014)

9. "The Alanate Anion, AlH4-: Photoelectron Spectrum and Computations", J. D. Graham , A. M. Buytendyk , **X. Zhang** , E. Collins , K. Boggavarapu , G. Gantefoer , B. W. Eichhorn , G. L. Gutsev , S. Behera , P. Jena , and K. H. Bowen, *J. Phys. Chem. A,* **118**, 8158 (2014)

8. "Photoelectron Spectra of the MgH$^-$ and MgD$^-$ Anions ", A. Buytendyk, J. Graham, H. Wang, **X. Zhang**, E. Collins, Y. J. Ko, G. Gantefoer, B. Eichhorn, A. Regmi, K.Boggavarapu, K. H. Bowen, *Int. J. of Mass Spectrom.,* **365-366**, 140 (2014).

7. "On the Existence of Designer Magnetic Superatoms ", **X. Zhang**, Y. Wang, H. Wang, A. Lim, G. Gantefoer, K.H. Bowen, J. U. Reveles, and S. N. Khanna, *J. Am. Chem. Soc.,* **135**, 4856 −4861 (2013) This work was reported/highlighted by C&EN news, JACS spotlight, Phys.org, People.com.cn, VCU news.

6. "Photoelectron Spectroscopic Study of the Ethyl Cyanoacrylate Anion", **X. Zhang**, X. Tang, K.H. Bowen, *Chem. Phys. Lett.* **582**, 21(2013)

5. "In Search of Four-Atom Chiral Metal Clusters ", **X. Zhang**, B. Visser, M. Tschurl, E. Collins, Y. Wang, Q. Wang, Y. Li, Q. Sun, P. Jena, G. Gantefoer, U. Boesl, U. Heiz, and K. H. Bowen, *J. Chem. Phys.* **139**, 111101 (2013)

4. " Photoelectron spectroscopy of the aluminum hydride anions: AlH$_2^-$, AlH$_3^-$, Al$_2$H$_6^-$, Al$_3$H$_9^-$, and Al$_4$H$_{12}^-$ ", **X. Zhang**, H. Wang, E. Collins, A. Lim, G. Ganteför, B. Kiran, H.Schnöckel, B. Eichhorn, and K.H. Bowen , *J. Chem. Phys.* **138**, 124303 (2013)

3. "Evolution of superhalogen properties in PtCl$_n$ clusters", J. Joseph, K. Pradhan, P. Jena, H. Wang, **X. Zhang**, Y. J. Ko, and K. H. Bowen, *J. Chem. Phys.*, **136**, 194305 (2012)

2. "Pd–CNT-catalyzed ligandless and additive-free heterogeneous Suzuki–Miyaura cross-coupling of arylbromides" P. Zhang, **X. Zhang, (Co-first author)** H. Sun, R. Liu, B. Wang, Y. Lin. *Tetrahedron Letters,* **50**, 4455 (2009)

1. "Suzuki-Miyaura Cross-Coupling of Aryl Bromides with Pd-CNT" P. Zhang, **X. Zhang**, H. Sun, R. Liu, B. Wang, Y. Lin. *Synfacts* **2009**, 1056 (2009)

Patents and Conference Abstracts

1. "Assembly of single-metal nanoparticle on carbon nanotube through metal organic chemical deposition method with acetyl acetonate", **X. Zhang,** Y. Lin, *Faming Zhuanli Shenqing*, CN Patent CN 101830429 (2010)
2. "Photoelectron spectroscopy of aluminum-containing cluster anions" K. H. Bowen, H. Wang, **X. Zhang**, and E. Collins, *68th Southwest Regional Meeting of the American Chemical Society,* SWRM-161 (2012)
3. "Photoelectron Spectroscopy of the Aluminum Hydride Anions: AlH$_3^-$, Al$_2$H$_6^-$, Al$_3$H$_9^-$ and Al$_4$H$_{12}^-$", K. Bowen, **X. Zhang**, E. Collins, *Symposium on Size Selected Clusters, Davos, Switzerland* 67 (2013)

4. "Cluster catalysis: Gas phase and surface studies", K. H. Bowen, X. Tang, S. Proch, J. Schneider, **X. Zhang,** G. Gantefoer, *247th ACS National Meeting & Exposition, Dallas, TX, United States*, PHYS-104 (2014)
5. "Photoelectron Spectroscopy of Transition Metal Hydride Cluster Anions", **X. Zhang*** and K. Bowen, *National Conference on Chemical Dynamics, Xi'an, China* (2015).
6. "Cluster catalysis: Gas phase and surface clusters", X. Tang, **X. Zhang**, Z. Hicks, G. Liu, Gao, K. H. Bowen. *250th ACS National Meeting & Exposition, Boston, MA, United States,* August 16-20, 2015, PHYS-90 (2015)